



TECHNISCHE UNIVERSITÄT MÜNCHEN

Ingenieur fakultät Bau Geo Umwelt

Lehrstuhl für Ingenieurgeologie

The Influence of Geotechnical Parameters on Penetration Prediction in TBM Tunneling in Hard Rock

**Special focus on the parameter of rock toughness and discontinuity pattern in
rock mass**

Lisa Steffi Franziska Wilfing

Vollständiger Abdruck der von der Ingenieur fakultät Bau Geo Umwelt der
Technischen Universität München zur Erlangung des akademischen Grades eines

Doktor-Ingenieurs (Dr.-Ing.)

genehmigten Dissertation.

Vorsitzender:

Prüfer der Dissertation:

1. Univ.-Prof. Dr. rer. nat. Kuroschi Thuro
2. Univ.-Prof. Dr. mont. Robert Galler, Montanuniversität Leoben / Österreich
3. em. O. Univ. Prof. Dr. Ewald Tentschert, Technische Universität Wien / Österreich

Die Dissertation wurde am 23.03.2016 bei der Technischen Universität München
eingereicht und durch die Ingenieur fakultät Bau Geo Umwelt am 03.05.2016
angenommen.

Abstract

Performance prediction is one of the crucial issues for estimating excavation costs and construction time of tunnel projects. In mechanized tunneling, TBM performance highly depends on an achieved penetration rate and cutter wear. The aim of this thesis is to illustrate the improvement of the GEHRING (1995) penetration prediction model by investigating two parameters that significantly influence the penetration. These are namely the toughness of rocks and the discontinuity pattern in rock mass.

Analysis is done by performing an extensive laboratory program (uniaxial compression tests, Brazilian tensile tests, point load tests, Cerchar abrasivity tests, LCPC abrasivity tests, thin sections) and on-site penetration tests. Laboratory testing aims to obtain a deep understanding of the deformation behavior of rocks under load. In addition, several characterization and classification methods for rock toughness are analyzed since neither have yet to gain complete acceptance. The commonly used toughness index, described by the ratio of uniaxial compressive strength and Brazilian tensile strength shows inappropriate results. Conversely, the ratio of uniaxial compressive strength and point load index yields best results regarding accuracy of laboratory parameters and applicability in practice. Therefore, this index seems suitable for an implementation into penetration prediction models.

In order to investigate the influence of discontinuities on TBM penetration, estimated parameters by two existing prediction models (**Gehring** model, **Colorado School of Mines** model) are compared with the results of 30 penetration tests and geological mapping at two tunnel projects. Penetration tests are a common tool to determine the performance of a TBM in certain geological environments. During a test, the TBM is operated under defined conditions that allow the comparison of different tunnel projects and machine types in analogous geological conditions. Results show that only for a narrow scope, considered prediction models reveal appropriate fitting. Once the rock mass is fractured or the stress level within the rock mass changes, existing models are not applicable. Based on this fact, the necessity to update penetration prediction models by implementing a correction factor for discontinuities can be clearly shown. The correction factor suggested by GEHRING (1995) does not reflect actual conditions, since only one discontinuity system is considered and the enhanced effect of intersecting systems on the penetration is neglected. Hence, this factor has to be revised. For this purpose, a combination with the fracturing factor originating from the prediction model of NTNU (BRULAND 2000) seems to be suitable, since it yields a good correlation with the obtained data. The rock fracturing index incorporates the parameter of rock mass fabric into the CSM prediction model. However, analyses reveal that results are not satisfying and the applicability of this index is additional limiting factor.

The general relation between force and resulting penetration is also in the focus of this thesis. It has been proven that force-penetration graphs can be described best by a linear function with certain y-axis offset. Consequently, CSM and Gehring prediction models are based on an inappropriate mathematical equation. The offset is characterized by the point of subcritical penetration and depends highly on the Brazilian tensile strength and the LCPC breakability coefficient. Incorporation of the critical y-axis offset, as well as of correction factors for rock toughness and discontinuity pattern result in a new prognosis tool called the 'Alpine model' which is based on the existing Gehring model.

Zusammenfassung

Die Leistungsprognose ist einer der wichtigsten Aspekte, wenn es um die Kalkulation von Baukosten und Bauzeiten bei Tunnelprojekten geht. Die Leistung einer TBM wird von der erreichten Penetration sowie dem auftretenden Werkzeugverschleiß bestimmt. Ziel dieser Dissertation ist es, das existierende Penetrationsprognosemodelle von GEHRING (1995) zu verbessern, indem zwei wesentliche Einflussfaktoren auf die Penetration untersucht werden. Diese sind zum einen die Zähigkeit von Gesteinen und zum anderen das Trennflächengefüge im Gebirge. Die Faktoren sollen mit Hilfe von einem umfangreichen Laborprogramm (Einaxiale Druckversuche, Spaltzugversuche, Punktlastversuche, Cerchar Abrasivitätsversuche, LCPC Abrasivitätsversuche, Dünnschliffe) sowie Penetrationsversuchen auf Tunnelbaustellen analysiert werden. Das Laborprogramm zielt darauf, ein detailliertes Verständnis über das Deformationsverhalten von Gesteinen unter Last zu erhalten. Zusätzlich werden eine Vielzahl an Charakterisierungs- und Klassifikationsmöglichkeiten für die Gesteinszähigkeit analysiert, da bisher keiner der existierenden Ansätze allgemein anerkannt ist. Der am meisten gebräuchliche Zähigkeitsindex, berechnet über das Verhältnis von Druck- zu Spaltzugfestigkeit, zeigte eine unzufriedenstellende Korrelation. Im Gegensatz dazu ergab das Verhältnis von Druckfestigkeit zu Punktlastindex das beste Ergebnis, sowohl auf die Genauigkeit der Laborparameter als auch auf die Anwendbarkeit in der Praxis gesehen. Dieser Index scheint demnach für eine Einarbeitung in Penetrationsprognosemodelle sinnvoll zu sein.

Um den Einfluss des Trennflächengefüges auf die Penetration zu untersuchen, wurden die prognostizierten Penetrationswerte von zwei gebräuchlichen Modellen (**Gehring** Modell, **Colorado School of Mines** Modell) mit den Ergebnissen von 30 Penetrationsversuchen sowie der geologischen Dokumentation an zwei Tunnelprojekten verglichen. Der Penetrationsversuch ist eine häufig angewandte Methode, um die Leistung einer TBM in einem spezifischen geologischen Umfeld zu bestimmen. Hierbei wird die Maschine unter definierten Bedingungen gefahren, wodurch ein Vergleich unterschiedlicher Tunnelprojekte sowie Maschinentypen bei entsprechenden geologischen Verhältnissen ermöglicht wird. Die Ergebnisse zeigen, dass die untersuchten Prognosemodelle nur für einen sehr engen Anwendungsbereich zuverlässige Werte liefern. Sobald das Gebirge Trennflächen oder einen veränderten Spannungszustand aufweist, sind beide Ansätze nicht mehr brauchbar. Diese Tatsache zeigt deutlich, dass die existierenden Modelle adaptiert werden müssen, indem beispielsweise ein Korrekturfaktor für das Trennflächengefüge im Gebirge eingebaut wird.

Der vorgeschlagene Korrekturfaktor von GEHRING (1995) spiegelt die Realität nur unzulänglich wider, da nur das Haupttrennflächensystem betrachtet und die verstärkende Wirkung von sich schneidenden Systemen vernachlässigt wird. Der Faktor muss daher überarbeitet werden. Hierfür eignet sich eine Kombination mit dem Gebirgszerlegungsfaktor des NTNU Prognosemodells (BRULAND 2000), welcher eine gute Korrelation mit den gewonnenen Daten aufweist. Auch das CSM Modell kann mit einem Parameter erweitert werden, welcher die Eigenschaften des Gebirgsgefüges berücksichtigen soll. Die Ergebnisse dieses Zerlegungsfaktors sind jedoch nicht zufriedenstellend. Ein weiterer limitierender Punkt ist der Aspekt der Anwendbarkeit, da die komplizierte Vorgehensweise viele Nachteile birgt.

Neben den Korrekturfaktoren wurde im Rahmen dieser Dissertation auch der grundsätzliche Zusammenhang zwischen Anpresskraft und resultierender Penetration betrachtet. Hierbei zeigte sich, dass

der Verlauf am besten mit einer linearen Funktion mit y-Achsenabschnitt beschrieben werden kann. Demnach werden beide Prognosemodelle, das CSM als auch das Gehring Modell, von der unzutreffenden mathematischen Funktion aufgebaut. Der Achsenabschnitt wird durch den Grenzwert der subkritischen Penetration definiert und zeigt eine starke Abhängigkeit von der Spaltzugfestigkeit sowie dem LCPC Brechbarkeitskoeffizienten. Die Implementierung dieses kritischen Achsenabschnittes sowie der Korrekturfaktoren für Gesteinszähigkeit und Trennflächengefüge soll in einem neuen Prognosewerkzeug, dem sogenannten „Alpine Modell“ resultieren, welches ein modifiziertes Gehring Modell darstellt.

Acknowledgement

First of all I would like to thank Prof. Dr. Kurosch Thuro for giving me the opportunity to work in the fascinating sector of TBM tunneling and to write this thesis under his supervision. I strongly appreciate the boundless support and professional advices during the whole PhD period and I am very pleased having him as doctoral father. Special thanks are offered also to Prof. Dr. Robert Galler and Prof. Dr. Ewald Tentschert for their co-supervision and review of this thesis where they contributed with valuable advices, especially in the final phase of this work.

Furthermore, I would like to thank the members of the ABROCK research group, represented by Prof. Eckart Schneider, Prof. Dr. Kurosch Thuro and Prof. Dr. Robert Galler, for the support and the helpful role they played in terms of providing professional connections to the construction sites. This opens the way to the required field investigations which is an important pillar of this work.

The performance of penetration tests would have not been possible without a good cooperation with the construction sites. Here, I would like to thank Dietmar Schubel and Dr. Bernd Moritz from the ÖBB-Infrastruktur AG and all the staff of the ARGE KAT2 (STRABAG SE & Jäger Bau GmbH) at the Koralm tunnel construction lot 2. My special thanks go to Manfred Köpf, Robert Uschan, Robert Goliasch, Wolfgang Stüttler and Michaela Pucher for supporting me during the visits at the Koralm tunnel. I am very grateful for the open and smooth cooperation with the Statkraft Energi AS and the LNS Group, represented by Tobias Andersson, at the Røssåga hydropower project in Norway. This project also created the contact to the NTNU and Prof. Amund Bruland who gave me a warm welcome in Trondheim. The teamwork with his PhD student Javier Macias persists even beyond the project and it was a pleasure working with him.

Furthermore, I would like to extend my thanks to all my colleagues at the Technical University of Munich. I am thankful for the constructive and critical discussions with Dr. Heiko Käsling which sometimes steered me back on the right track. A very special thank you goes to my office colleagues Peter Ellecosta and Carola Wieser for the divertive and entertaining talks if the writing work advanced only haltingly. I totally agree that working with a team makes things easier than struggling on your own. Peter gave a helping hand at the Koralm tunnel and Carola was a huge support when I was lost in the MATLAB jungle.

All students who contributed to this work either by helping in the laboratory or by writing their theses deserve a special mention. These are namely Tobias Zaegel, Rosa Bögle, Franz Weigert, Christian Leisch, Julia Gruber, Marian Hornung and Roman Rauch. Many thanks also to Friedrich Ettl who prepared hundreds of specimens for my laboratory program.

Last but not least my very special thanks go to my family and friends. Without the help of my parents throughout all those years, this work would have not been possible. Especially in the last month, their catering was irreplaceable when my refrigerator was empty again. In addition, they became acquainted with my topic even with no background in this field and gave valuable advices. I sincerely thank my partner who endured all the whining when I didn't gain the desired results. He spent a lot of time proof-reading the work and his insightful criticism supported this thesis in innumerable ways.

Table of contents

Abstract	I
Zusammenfassung	II
Acknowledgement	IV
List of figures	VIII
List of tables	XIII
List of acronyms and abbreviations	XIV
List of symbols	XV
1. Introduction	1
1.1 Motivation.....	1
1.2 Scope of study.....	2
2 State of the art	4
2.1 Penetration prediction – basic information	5
2.1.1 Rock parameters.....	6
2.1.2 Rock mass parameters.....	6
2.1.3 Machine parameters	6
2.1.4 Field penetration index.....	7
2.2 Penetration tests.....	8
2.3 Existing penetration prediction models	10
2.3.1 Ernst Büchi model (1984)	10
2.3.2 Michael Alber model (2000)	11
2.3.3 Q_{TBM} by Nick Barton (2000).....	12
2.3.4 NTNU model by Amund Bruland (2000)	13
2.3.5 RME indicator by Z.T. Bieniawski (2006).....	14
2.3.6 BI by Qiu Ming Gong and Jian Zhao (2009).....	15
2.3.7 CSM model by Levent Ozdemir (1977) and Jamal Rostami (1997).....	17
2.3.8 Gehring model by Karlheinz Gehring (1995).....	18
2.4 Influence of rock toughness on TBM penetration	25
2.4.1 Deformation behavior of rocks.....	26
2.4.2 Rock toughness – a brief introduction.....	32
2.4.3 Toughness definition – strain and energy based approach.....	33
2.4.3.1 Strain based approach – parameter plastic deformation	36
2.4.3.2 Energy based approach – parameter post-failure region	38
2.4.4 Toughness definition – strength based approach	40
2.4.5 Toughness definition – special test based approach	43
2.5 Influence of discontinuity pattern on TBM penetration	45
2.5.1 Ernst Büchi model (1984)	49
2.5.2 NTNU model by Amund Bruland (2000)	49
2.5.3 BI by Qiu Ming Gong and Jian Zhao (2009).....	51

2.5.4	Modified CSM model by Saffet Yagiz (2002)	56
2.5.5	Gehring model by Karlheinz Gehring (1995).....	56
3	Study sites	57
3.1	Koralm tunnel project	57
3.1.1	Machine design KAT2	58
3.1.2	Project geology KAT2	59
3.2	Røssåga tunnel project.....	63
3.2.1	Machine design Røssåga.....	64
3.2.2	Project geology Røssåga	65
4	Methodology	68
4.1	Laboratory testing.....	68
4.1.1	Uniaxial Compression Test.....	68
4.1.2	Brazilian Tensile Test	75
4.1.3	Point Load Test	75
4.1.4	Cerchar Abrasivity Test	77
4.1.5	LCPC Abrasivity Test.....	78
4.1.6	Thin section.....	81
4.2	Field investigation	82
4.2.1	Penetration test.....	82
4.2.2	Geological mapping and sample acquisition	84
5	Results and discussion of laboratory testing	86
5.1	Results.....	86
5.1.1	Petrographic analysis of tested samples	86
5.1.1.1	Magmatic rocks.....	87
5.1.1.2	Metamorphic rocks	90
5.1.1.3	Sedimentary rocks.....	96
5.1.2	Standard laboratory testing.....	99
5.1.3	Uniaxial Compression Tests: detailed analysis	102
5.2	Discussion.....	107
5.2.1	Toughness definition – strain and energy based approach.....	112
5.2.2	Toughness definition – strength based approach	116
5.2.3	Toughness definition – special test based approach.....	119
6	Results and discussion of field investigations	124
6.1	Results.....	124
6.1.1	Influence of discontinuities on TBM penetration	124
6.1.2	Penetration test.....	127
6.1.2.1	Field penetration index FPI	128
6.1.2.2	Penetration prediction models (Gehring & CSM)	130
6.1.2.3	Variation of cutterhead rotational speed	138

6.2	Discussion.....	140
6.2.1	General investigations on force – penetration graphs	140
6.2.2	Parameter - rock toughness.....	149
6.2.3	Parameter - discontinuity pattern in rock mass	151
7	Conclusions.....	156
8	Bibliography	160
9	URL Resources	168

Appendix A:

Summary of laboratory test results (project data excluded)

List of figures

Fig. 1:	Schematic figure of the fragmentation process during rock excavation with disc cutters (...)	4
Fig. 2:	Thrust-penetration curve derived from a penetration test after BRULAND at Atlanta West Side (...)	9
Fig. 3:	Thrust-penetration curve including measured friction derived from a penetration test performed after FRENZEL et al. (2012) at the Koralm tunnel.	9
Fig. 4:	Schematic timeline for TBM performance prediction models. The CSM and Gehring model, as well as the newly suggested Alpine Model (...) are highlighted.	10
Fig. 5:	Probability density functions of the nine suggested advance rate classes by ALBER (2000: 60).	12
Fig. 6:	Influence of uniaxial compressive strength and volumetric joint count on the penetration rate (...)	16
Fig. 7:	Basic penetration p depending on uniaxial compressive strength σ_u for a mean thrust force of 200 kN per cutter, recalculated from approaches by GRAHAM, FARMER, HUGHES, SANIO and NTH (...)	20
Fig. 8:	Correction factor k_1 as a function of specific failure energy w_f (mod. from GEHRING 1995: 443)	22
Fig. 9:	Correlation diagram of correction factor k_5 and cutter spacing as a function of drillability (...)	24
Fig. 10:	Penetration rate variations depending on rock brittleness index $B_1 = UCS / BTS$ (...)	26
Fig. 11:	Schematic stress-strain relations for various rheological models (...)	27
Fig. 12:	Influence of loading rate on the uniaxial compressive strength (mod. from VARDAR 1977: 17)	29
Fig. 13:	Variation of compressive strength depending on different loading rates (A). Relation between the increment of compressive strength (...) and the porosity of tested samples (B) (...)	29
Fig. 14:	Loading rate dependence of five rock types: a) marble, b) andesite, c) tuff, d) granite and e) sandstone. Samples were tested at loading rates of 10^{-6} , 10^5 , 10^{-4} and 10^{-3} (mm/mm)/s (...)	30
Fig. 15:	Stress-strain curves of Plexiglas at four different loading rates (ZHOU et al. 2013)	31
Fig. 16:	Schematic stress-strain curves: A) typical tough failure behavior with high plastic deformation and distinct post-failure range and B) typical brittle failure behavior with infinitesimal plastic deformation and no post-failure range.	33
Fig. 17:	Stress-strain diagram of a uniaxial compression test showing lateral, volumetric, axial strain and corresponding thresholds for crack closure, crack initiation, and crack damage (...)	35
Fig. 18:	Schematic stress-strain curve showing three different curve sections A-C. In addition, elastic / plastic deformation ranges and corresponding elasticity moduli E_t and E_{pl} are plotted.	36
Fig. 19:	Three schematic shapes of stress-strain curves belonging to different rock categories (...)	37
Fig. 20:	Schematic stress-strain curves for class I and II rock failure behavior in uniaxial compression (...)	38
Fig. 21:	Schematic stress-strain curve including the parameters of failure work W_b , destruction work W_z and post-failure modulus P_f .	40
Fig. 22:	Rock specimens of calcareous mica schist as representative of a tough rock type after uniaxial compression testing and Brazilian tensile testing (...)	40
Fig. 23:	Relation between compressive and tensile strength of rock. A) concept considering the slope of relation line; B) concept considering the area under the relation line (...)	42
Fig. 24:	Rock specimens of basalt as representative of a brittle rock type after uniaxial compression testing and point load testing. The ratio of UCS and I_s can be used to classify rock toughness.	42
Fig. 25:	A) Schematic figure of the brittleness test (...). B) Schematic figure of the punch penetration test (...). Both tests are used to investigate rock brittleness.	43
Fig. 26:	A) Schematic figure of the miniature drill test (...). B) LCPC testing device at the Chair of Engineering Geology (TUM). Both tests might be used to investigate rock toughness.	45
Fig. 27:	Schematic figures (cube with 1 m edge length) for the characterization of joint frequency d [m^{-1}] proposed by WANNER & AEBERLI (1979: Fig. 5).	47
Fig. 28:	Definition of α' and β' determining the orientation of anisotropy planes (...)	47

Fig. 29: Dependency of specific penetration on the orientation of schistosity relative to cutting direction in phyllite (solid line) and phyllite-carbonate alternation (dashed line) (...).	48
Fig. 30: Correction factor k_s for rock mass fracturing at the NTNU prediction model, depending on the angle α and the fracture class (mod. from BRULAND 2000c: 8; BRULAND 2000d: 72).	50
Fig. 31: Influence of joint volumetric count J_v (left) and angle α (right) on predicted penetration rate for the GONG prediction model (...).	52
Fig. 32: Numerical model of failure pattern in granite with $\alpha = 15^\circ$. Crushed zone shows an asymmetric shape (a), then the initial crack propagates asymmetrically to the joint plane (b, c, d) (...).	53
Fig. 33: Numerical model of failure pattern in granite with $\alpha = 75^\circ$. First failure takes place at the joint plane (a), then the initial crack propagates to the free surface (b, c) (...).	53
Fig. 34: Effect of the angle α on the penetration rate for joint spacing of 20 cm. α is plotted against the ratio of the penetration at certain α angle (P_α) and the penetration at $\alpha = 0$ (P_0) (...).	54
Fig. 35: Numerical model of failure pattern in granite with different joint spacing of 40 mm (a), 60 mm (b), 80 mm (c), 90 mm (d), 200 mm (e) and 500 mm (f) (...).	55
Fig. 36: Effect of joint spacing on the penetration rate for vertical joint orientation. Spacing is plotted against the ratio of the penetration at certain spacing and the penetration in unfractured rock mass (...).	55
Fig. 37: Geographic location of the Koralm railway track with the Koralm tunnel as centerpiece.	57
Fig. 38: Schematic figure of the three construction lots at the Koralm tunnel with a rough geological classification into tertiary sediments and crystalline basement (...).	58
Fig. 39: Cutterhead design of Aker Wirth doubleshield TBMs used at KAT2 (...).	59
Fig. 40: Geological overview of the Styrian part of the project area with planned tunnel route in grey (...).	61
Fig. 41: Schematic geological longitudinal section through the Koralm tunnel showing the construction lots KAT 1-3 and the major geological elements (mod. from MORITZ et al. 2011: 306).	61
Fig. 42: Mica schist KAT2: specimen for uniaxial compression testing (A) and thin section analysis under plane polarized light (B) (...).	62
Fig. 43: Fine-grained gneiss KAT2: specimen for uniaxial compression testing (A) and thin section analysis under plane polarized light (B) (...).	62
Fig. 44: Geographic location of the Røssåga hydropower project in Nordland County, Norway.	63
Fig. 45: Robbins open gripper TBM used at Røssåga tunnel (www-06).	64
Fig. 46: Geological overview of the Røssåga tunnel project with planned tunnel route in rose (...).	65
Fig. 47: Calcareous mica schist: specimen for uniaxial compression testing (A) and thin section analysis under plane polarized light (B) (...).	66
Fig. 48: Quartzite: specimen for uniaxial compression testing (A) and thin section analysis under crossed polarized light (B) (...).	67
Fig. 49: Front view of “ToniNorm” Compression Testing Machine at the Chair of Engineering Geology (...).	69
Fig. 50: Schematic stress-strain curve showing the determination of the Young’s modulus (E_t) and the Young’s modulus including plastic deformation range (E_{pl}).	70
Fig. 51: Schematic stress-strain curve including the parameters of failure work W_b and destruction work W_z .	71
Fig. 52: Classification of the uniaxial compressive strength of hard rocks adapted from the ISRM suggested method (1978: 348) with chosen rock type examples by THURO 1996 (: 55).	72
Fig. 53: Failure modes of tested rock samples after uniaxial compression (mod. from SZWEDZICKI 2007: 99).	72
Fig. 54: Stress-strain diagram showing lateral, volumetric and axial strain and corresponding thresholds for crack closure, crack initiation and crack damage (mod. from MARTIN 1993: 77) (...).	73
Fig. 55: Axial stiffness curve calculated by first derivation of axial stress-strain curve using moving point regression. Crack damage threshold is set by the inflection point in axial stiffness.	74
Fig. 56: Experimental setup of Brazilian Tensile Test with loading direction F.	75
Fig. 57: Cerchar-device for the determination of the Cerchar abrasivity index (mod. from WEST 1989).	78

Fig. 58: LCPC testing device with a 700 W electric motor (1), funnel tube (2), metal impeller (3) and dismantled sample container (4) (KÄSLING 2009: 67).	79
Fig. 59: Thin section analysis of calcareous mica schist under plane (A) and crossed (B) polarized light.	81
Fig. 60: Thrust-penetration curve including measured friction derived from a penetration test (left) and corresponding plot with normal force per disc cutter (right).	83
Fig. 61: Geological face documentation and structure model at the Koralm tunnel with mapped discontinuity systems (S = schistosity, J = joint).	84
Fig. 62: Penetration test at chainage 1865 in quartzite at Røssåga hydropower project with mapped discontinuity systems (J = joint, F = fissure).	85
Fig. 63: Flossenbürg: granite under reflected-light microscope.	87
Fig. 64: Tittling: granite under reflected-light microscope.	87
Fig. 65: Brixen: granite under reflected-light microscope.	88
Fig. 66: Metten: granite under reflected-light microscope.	88
Fig. 67: Nittenau: diorite under reflected-light microscope.	89
Fig. 68: Pechbrunn: basalt under reflected-light microscope.	89
Fig. 69: Koralm tunnel: schistose gneiss under reflected-light microscope.	90
Fig. 70: Koralm tunnel: gneiss under reflected-light microscope.	90
Fig. 71: Malta Valley: Augen gneiss under reflected-light microscope.	91
Fig. 72: Humpelgraben: granitic gneiss under reflected-light microscope.	91
Fig. 73: Pfunderer Valley: greenschist under reflected-light microscope.	92
Fig. 74: Limberg hydropower plant: calcareous mica schist under reflected-light microscope.	92
Fig. 75: Røssåga hydropower plant: calcareous mica schist under reflected-light microscope.	93
Fig. 76: Oberbaumühle: amphibolite under reflected-light microscope.	93
Fig. 77: Humpelgraben: amphibolite under reflected-light microscope.	94
Fig. 78: Gleinalm tunnel: amphibolite under reflected-light microscope.	94
Fig. 79: Røssåga hydropower plant: quartzite under reflected-light microscope.	95
Fig. 80: Laas marble under reflected-light microscope.	95
Fig. 81: Koralm tunnel: marble under reflected-light microscope.	96
Fig. 82: Rothenfels: sandstone under reflected-light microscope.	96
Fig. 83: Posta: sandstone under reflected-light microscope.	97
Fig. 84: Abtswind Castell: sandstone under reflected-light microscope.	97
Fig. 85: Wiesenhofen: limestone under reflected-light microscope.	98
Fig. 86: Dietfurt: limestone under reflected-light microscope.	98
Fig. 87: Moosegg: anhydrite under reflected-light microscope.	99
Fig. 88: Uniaxial compressive strength of tested rock types with strength classification acc. to ISRM (1978).	102
Fig. 89: Uniaxial compressive strength σ_u plotted against tangent Young's modulus E_t of tested samples (...)	103
Fig. 90: Variations in stress-strain curves of tested granite TIT-5 (A) and anhydrite MO-6 (B) at five different loading rates from $\frac{1}{3}$ - to 10-fold of recommended rate acc. to DGGT (2004).	107
Fig. 91: Exemplary stress-strain curves of three different types of tough failure behavior. A) High plastic deformation & no post-failure range. B) Minor plastic deformation & major post-failure range. C) High plastic deformation & major post-failure range.	109
Fig. 92: Special stress-strain curves of tough failure behavior. A) Sandstone reveals extremely high deformation relative to its strength due to existing porosity. B) Marble shows major post-failure behavior and plastic deformation due to twin gliding.	110

Fig. 93: Exemplary stress-strain curves of basalt and augen gneiss with brittle failure behavior showing minimal plastic deformation and no post-failure range.	110
Fig. 94: Strain based approach: Tangent Young's modulus E_t is plotted against deformation modulus E_{pl} (A) resp. strain at failure ϵ_u is plotted against strain at crack damage ϵ_{cd} (B). Energy based approach: Relation of specific destruction work W_z is plotted against specific failure work W_b (C) (...).	113
Fig. 95: Influence of loading rate on the uniaxial compressive strength of five rock types (...).	114
Fig. 96: Influence of loading rate variations on the Young's modulus (A) and the crack damage strength (B).	115
Fig. 97: (A) Toughness coefficient T_z . Uniaxial compressive strength vs. Brazilian tensile strength with the existing classification (...). (B) In addition, failure behavior of tested rock samples under uniaxial compression is considered (...).	117
Fig. 98: Calculation of toughness indices T_d (A) and T_e (B) depending on the rock type. The failure behavior of tested rock samples under uniaxial compression is considered by colored crosses (...).	117
Fig. 99: (A) Toughness index T_{PLT} . Uniaxial compressive strength σ_u vs. point load index I_s . Threshold for tough failure behavior are adopted from KLEIN et al. (1995) and BARTON (2000). (B) Failure behavior of tested rock samples under uniaxial compression is considered (...).	118
Fig. 100: Brazilian tensile strength σ_t vs. point load index I_s of tested rock samples (...).	118
Fig. 101: Calculation of the punch penetration toughness index T_{ppT} depending on the rock type (...).	119
Fig. 102: Force – penetration graphs as results of punch penetration test. A) shows augen gneiss (AG) as brittle rock with highly fluctuating curve and B) calcareous mica schist (KGS) as tough rock (...).	120
Fig. 103: Uniaxial compressive strength (A), point load index (B) and Brazilian tensile strength (C) of tested rock samples plotted against LCPC breakability coefficient.	121
Fig. 104: Uniaxial compressive strength (A), point load index (B) and Brazilian tensile strength (C) plotted against LCPC breakability coefficient (...).	122
Fig. 105: TBM data analysis at the Røssåga hydropower project. Mean penetration rate is plotted against 1,000 m tunnel length. Additionally, predicted values from the basic CSM (blue) and basic Gehring (orange) model are displayed (...).	125
Fig. 106: TBM data analysis at the Koralm tunnel. Marked force drop is accompanied with an increase in penetration rate (black rectangles). In addition, calculated forces from the CSM (blue) and Gehring (orange) model are displayed (...).	126
Fig. 107: Field penetration index FPI of penetration tests at the Koralm tunnel and Røssåga hydropower project (...).	129
Fig. 108: Actual measured penetration rate plotted against predicted penetration rate of the basic CSM (blue) and Gehring (orange) model of performed penetration tests at Koralm and Røssåga tunnel (...).	131
Fig. 109: Schematic profile of the studied tunnel section at the Koralm tunnel with actual encountered formation boundaries (...).	131
Fig. 110: Penetration test type 1– Left: Normal force per cutter is plotted against resulting penetration rates of start and stop test. In addition, CSM (blue) and Gehring (orange) models are displayed (...).	132
Fig. 111: Penetration test type 2– Left: Normal force per cutter is plotted against resulting penetration rates of start and stop test. In addition, CSM (blue) and Gehring (orange) models are displayed (...).	133
Fig. 112: Penetration test type 3 – Left: Normal force per cutter is plotted against resulting penetration rates of start and stop test. In addition, CSM (blue) and Gehring (orange) models are displayed (...).	135
Fig. 113: Penetration test type 4 – Left: Normal force per cutter is plotted against resulting penetration rates of start and stop test. In addition, CSM (blue) and Gehring (orange) models are displayed (...).	136
Fig. 114: Friction 5,500 kN: Force – penetration graphs of start / stop test including CSM (blue) and Gehring (orange) models. (...). Friction force is considered by 50 % (A) and 100 % (B) of measured value leading to divergence in force per cutter of about 15 %.	138
Fig. 115: Friction 3,500 kN: Force – penetration graphs of start / stop test including CSM (blue) and Gehring (orange) models. (...). Friction force is considered by 50 % (A) and 100 % (B) of measured value leading to divergence in force per cutter of about 10 %.	138

Fig. 116: Variation of cutterhead rotational speed at the Koralm tunnel. (A) Penetration rate increases with de-creasing cutterhead speed in predominantly massive (...) rock mass. (B) Penetration rate de-creases with decreasing cutterhead speed in rock mass with distinctive discontinuity pattern (...). ..	139
Fig. 117: Field penetration index at subcritical penetration FPI_{3mm} plotted against chosen geotechnical parameters (...).	141
Fig. 118: Schematic figure of the contact area between disc cutter and rock (...).	143
Fig. 119: Result of a penetration test at cross passage No. 18 at the Koralm tunnel. Besides force-penetration graph (green & red), also the applied stress under the cutter is plotted (purple & rose) (...).	143
Fig. 120: Results of penetration tests at Koralm tunnel. Besides force-penetration graphs (...), also the applied stress under the cutter is plotted (...). Stress under cutter depends on penetration rate, resulting in either positive (A) or negative (B) slope in the range of effective rock cutting.	144
Fig. 121: Investigations on the correlation between the stress under disc cutters and corresponding penetra-tion for penetration tests at the Koralm tunnel. (...). The gradient of regression lines seems to be affected by rock mass properties such as fracturing degree or in-situ stress.	145
Fig. 122: Stress under disc cutter at subcritical penetration plotted against uniaxial compressive strength, destruction work, point load index, Brazilian tensile strength and LCPC breakability coefficient (...). 146	146
Fig. 123: Field penetration index at subcritical penetration FPI_{3mm} is plotted against the toughness coeffi-cient T_{LBC}^{-1} (A) and T_z (B) (...).	150
Fig. 124: Corrected Gehring model including correction factors for rock mass fabric compared to basic Gehring model (dashed line) of penetration test No. 24. (A) $k_2 = 1.3$ acc. to proposed factors by Gehring. (B) $k_{s-tot} = 3.3$ based on suggested NTNU total fracturing factor.	152
Fig. 125: Predicted correction factors k_2 and k_{s-tot} for the Gehring model compared with actual deviation of predicted to measured data determined by penetration tests at the Koralm tunnel.	153
Fig. 126: Modified CSM model including correction factors for rock mass fabric and rock brittleness compared to basic CSM model (dashed line) of penetration test No.24.	154

List of tables

Tab. 1: Main parameters for the prediction of penetration rates in TBM tunneling.	5
Tab. 2: Input parameters for the RME index with corresponding rating (BIENIAWSKI et al. 2006: Tab. 2).	14
Tab. 3: Classification system for the applicability of double-shield TBMs based on RME index (...).	15
Tab. 4: Penetration coefficient a and exponent b (...) and resulting Gehring factors (...).	20
Tab. 5: Correction factor k_2 depending on spacing and orientation of discontinuity relative to tunnel axis in terms of α angle (GEHRING 1995: 447).	23
Tab. 6: Toughness classification depending on the ratio of uniaxial compressive strength to Brazilian tensile strength (SCHIMAZEK & KNATZ 1976, extended by THURO 1996).....	41
Tab. 7: Suggested rock brittleness classification based on measured or predicted brittleness index which are determined by punch penetration test or calculated by strength and density of the rock (...).	44
Tab. 8: Short key information for construction lot KAT2 at the Koralm tunnel.	58
Tab. 9: Short key information on the machine design of Aker Wirth double shield TBM used at KAT2.	59
Tab. 10: Short key information for the New Nedre Røssåga hydropower plant.	64
Tab. 11: Short key information on the machine design of (...) open gripper TBM used at Røssåga tunnel.	64
Tab. 12: Classification of destruction work according to THURO (2000).	72
Tab. 13: Abrasiveness classification using the Cerchar Abrasivity Test (acc. to CERCHAR 1986: 7).	78
Tab. 14: Classification of the LCPC abrasivity coefficient LAC in accordance to the Cerchar abrasivity index CAI with chosen rock type examples (mod. from THURO et al. 2006: 40).	80
Tab. 15: Number of performed laboratory tests depending on different rock types (...).	100
Tab. 16: Summary of basic laboratory results: uniaxial compressive strength, Brazilian tensile strength, point load index, Cerchar abrasivity index, LCPC abrasivity coefficient and LCPC breakability coefficient. .	101
Tab. 17: Summary of laboratory results from Uniaxial Compression Tests in detail.	104
Tab. 18: Summary of laboratory results from Uniaxial Compression Tests with varying loading rate.	106
Tab. 19: Results of toughness defining indices of tested rock samples (...).	111
Tab. 20: Summarized results of performed penetration tests and corresponding laboratory program (...). ...	128
Tab. 21: Machine input parameters at the Koralm and Røssåga tunnel project for penetration prediction models.	130
Tab. 22: Summarized results of penetration tests at the Koralm tunnel concerning the correction factor for discontinuities for the Gehring model (...).	153
Tab. 23: Final outcomes of the existing and newly developed characterization possibilities for rock toughness concerning the accordance of laboratory results and the applicability of the testing method (...). ...	156

List of acronyms and abbreviations

AFNOR	Association Française de Normalisation (French Institute for Standardization)
ARA	Average advance rate
ASTM	American Society for Testing and Materials
BTS	Brazilian tensile strength
CAI	Cerchar abrasivity index
CLI	Cutter life index
CSM	Colorado School of Mines
DGGT	Deutsche Gesellschaft für Geotechnik e.V. (German Society for Geotechnics)
DI	Deformation index
DIN	Deutsches Institut für Normung (German Institute for Standardization)
DRI	Drilling rate index
FPI	Field penetration index
FS	Factor of safety
ISRM	International Society for Rock Mechanics
KAT2	Koralm tunnel – construction lot 2
LAC	LCPC abrasivity coefficient
LBC	LCPC breakability coefficient
LCPC	Laboratoire central des Ponts et Chaussées (French Public Scientific and Technical Research Establishment)
LNS	Leonhard Nilsen & Sønner AS (Norwegian construction company)
MCSM	Modified Colorado School of Mines model
NTNU	Norwegian University of Science and Technology
ÖBB	Österreichische Bundesbahnen (Austrian Federal Railways)
PLT	Point load test
PPT	Punch penetration test
RFI	Rock fracture index
RME	Rock mass excavatability
RMR	Rock mass rating
RQD	Rock quality designation
SI	Strain index
SRMBI	Specific rock mass boreability index
TBM	Tunnel boring machine
UCS	Uniaxial compressive strength
UDEC	Universal Distinct Element Code
WI	Work index

List of symbols

B_i	Brittleness coefficients	α	Smallest angle between discontinuity and tunnel axis
E_{pl}	Deformation modulus	ϵ_{cd}	Strain at crack damage
E_t	Young's modulus	ϵ_{el}	Elastic strain
F_N	Normal force per cutter	ϵ_{pl}	Plastic strain
I_s	Point load index	ϵ_u	Strain at maximum strength
J_v	Volumetric joint count	σ_{cc}	Stress at crack closure
k_{1-5}	Correction factors Gehring model	σ_{cd}	Stress at crack damage
k_{s-tot}	Total fracturing factor	σ_{ci}	Stress at crack initiation
p	Penetration rate	σ_t	Brazilian tensile strength
R	Radius of disc cutter	σ_u	Uniaxial compressive strength
T	Cutter tip width		
T_d	Toughness coefficient – difference approach		
T_e	Toughness coefficient – energy approach		
T_{LBC}	Toughness coefficient – LCPC approach		
T_{PLT}	Toughness coefficient – point load approach		
T_{PPT}	Toughness coefficient – punch penetration approach		
T_z	Toughness coefficient – 'Zähigkeit' approach		
W_b	Failure work		
W_z	Destruction work		

1. Introduction

1.1 Motivation

For a long time, the construction of tunnels is of major importance in the transportation sector. In the beginning, tunnels have been constructed mainly by drill and blast. Over time, technique evolved and larger distances needed to be overcome. This was the beginning that tunnel boring machines (TBM) gained wide acceptance and their utilization in tunnel projects increased rapidly. Nowadays, TBMs are a common tool to excavate ground, independent whether the tunnel is situated in soft or hard rock. Since then, a lot of research has been carried out to investigate the interaction between the rock mass and the excavation tool. These investigations should conduce to one special topic – estimating the performance of TBMs in advance of a tunnel project to allow calculations on construction time and costs. Good predictions of TBM performance facilitate the control of risk, as well as avoiding delays and budget overruns. This focus is even more important today than in the past since tunnel boring machines made larger infrastructure projects such as Alpine Transit Routes possible. Exact predictions are absolutely essential for such large and long-term projects. First prediction models were published about 40 years ago and over time, a large number of models emerged that are based on different scientific background, either empirical by analyzing data from tunnel projects or theoretical by performing laboratory tests to simulate reality. Nowadays, also numerical approaches are used to reflect reality. However, each prediction model can only be as precise as its input parameters are. First, models depended simply on two parameters. Over the years, the models got more complex resulting in multi factor models up to numerical simulations. Today commonly used prediction models (CSM model, NTNU model) were developed about 20 years ago. Since then, TBM technique and tunnel dimension developed significantly which leads to inaccuracies of these prediction models. This fact emphasizes the need of an updated model that incorporates the current state of the art, resulting in predictions of higher accuracy.

This problem has been seized by the research group ABROCK where this thesis is part of (SCHNEIDER & THURO 2007, SCHNEIDER et al. 2011, www-01). The research group has been formed in 2006 and is the collaboration between five universities (Technische Universität München, Montanuniversität Leoben, Universität Innsbruck, ETH Zürich, EPF Lausanne), clients, contractors, TBM manufacturers and TBM experts. ABROCK approaches the analysis and prediction of TBM performance by improving the existing prediction model of Dr. Karl-Heinz Gehring and consequently develop a new, so called ‘**Alpine model**’.

1.2 Scope of study

Performance prediction in TBM tunneling can be divided into two main pillars. These are on one hand the prediction of achievable penetration rates and on the other hand calculations of expected cutter wear. This thesis focusses on the aspect of penetration prediction for hard rock tunnel boring machines. Achieved penetration rates are characterized by the interaction between the cutting tool, in case of hard rock TBMs disc cutters, and the rock mass. Therefore, parameters that influence the penetration are of mechanical and geotechnical aspects. Input parameters for existing prediction models vary significantly, especially in terms of incorporated geotechnical parameters. The aim of this work is to compare estimated parameters by penetration prediction models with results of penetration tests during excavation by a TBM at actual tunnel projects. Penetration tests are a common tool to determine the performance of a TBM in certain geological environments. During a test, the TBM is operated under defined conditions that allow the comparison of different tunnel projects and machine types in analogous geological conditions. For the validation, two existing models have been picked out. First the Colorado School of Mines (CSM) model, which is one of the most often used models to estimate achievable penetration in advance of a tunnel project (ROSTAMI 1997). Compared to this, the less known Gehring model is validated (GEHRING 1995). This model has been chosen by the ABROCK research group as basis for further development since it provides several advantages. It is of modular structure and each factor can be considered and improved individually and back-incorporated again into the model. The structure also allows an implementation of new parameters in relatively straightforward way. Furthermore, geotechnical input parameter originate from standard laboratory testing and are already available in the phase of preliminary investigations. However, some of the input parameters are based on limited data sets or are not state of the art anymore.

This is why this work deals with the improvement of two factors that are incorporated in the Gehring model, but are of major importance for all prediction models and can be transferred in a second step. These are namely the parameter of **rock toughness** and the **discontinuity pattern** in the rock mass which both influence the penetration rate significantly.

The **toughness of rocks** is in the researchers' focus for long time. Nevertheless, no commonly accepted definition and classification is available. The broad consensus is that tough rocks require more energy to be excavated and result in low boreability. The opposite is given by the term of rock brittleness. The scope of this study is a consistent definition of rock toughness to enable investigations on the influence of toughness on the boreability (penetration rate) in mechanical tunneling and in a second step an implementation into penetration prediction models. Therefore, an extensive laboratory program shall investigate the deformation behavior of rocks. Results are then evaluated by several classification possibilities used to characterize rock toughness. The final step is to select the best determination formula which reveals high accuracy for obtained laboratory results and is easy to apply in practice. The chosen formula may then be incorporated into the prediction model via correction factor for rock toughness.

The **discontinuity pattern** in the rock mass affects the performance of TBMs to a large extent. Investigations on the influence of planes of weaknesses on the penetration are rather complicated as the scale effect is of major importance. No laboratory test can simulate actual geological conditions at a

tunnel face and the interaction of the whole TBM with surrounding rock mass properly. Therefore, in-situ penetration tests are conducted in this thesis to diminish the scale effect and to obtain data directly from the tunnel face. Beside actual TBM data, a geological documentation of the tunnel face and side walls is performed at each test with a special focus on existing discontinuity systems. Corresponding sample acquisition shall provide information about the mineralogy of the rock and its geotechnical parameters. Measured data is then compared with estimated data to validate the CSM and Gehring prediction model. If the rock mass is fractured, the influence on the penetration can be directly determined by means of penetration test results. The final step is to adapt the existing Gehring model by a correction factor that incorporates the influence of discontinuities on penetration.

Conclusively, existing penetration prediction models shall be improved by updating the correction factor for rock toughness, as well as for discontinuities in the rock mass. These results in a new prognosis tool called '**Alpine model**' enhancing penetration prediction significantly.

2 State of the art

The fragmentation process of rock by disc cutters has been investigated intensively by researchers over the last 40 years (BENJUMEA & SIKARSKIE 1969, ROXBOROUGH & PHILLIPS 1975, OZDEMIR et al. 1977, WANNER & AEBERLI 1979, SANIO 1983, LINDQVIST & LAI 1983, BÜCHI 1984, ROSTAMI 1997, GEHRING 1997 etc.). All authors agree that the fragmentation is divided into two parts (Fig. 1): a zone of crushed material beneath the cutter (**crushed zone**) and the formation of rock chips (**chipping**).

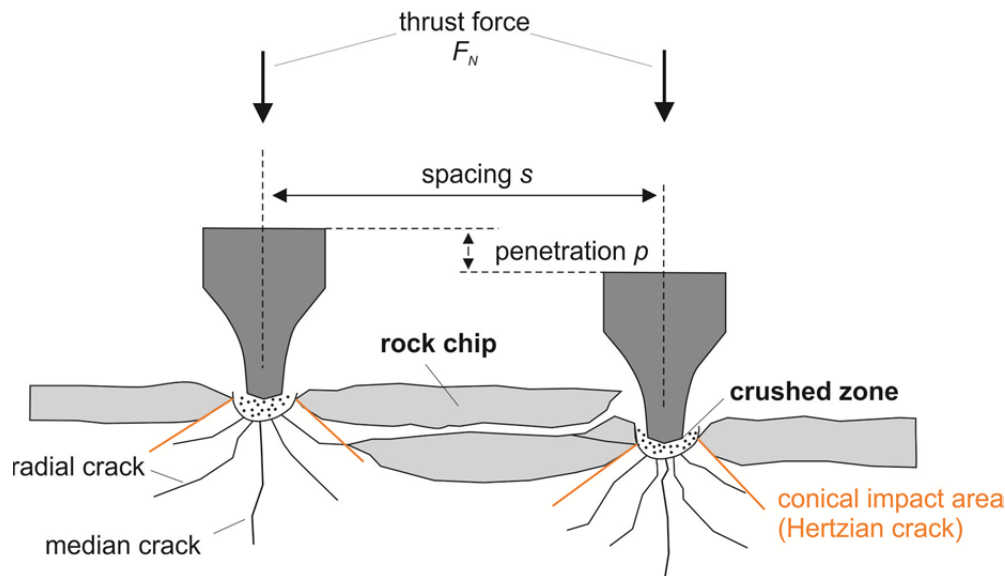


Fig. 1: Schematic figure of the fragmentation process during rock excavation with disc cutters (mod. from ROSTAMI 1997: 23).

The force that is applied by a disc cutter causes an indentation into the rock surface and forms a fan-shaped zone of crushed material beneath the cutter. Penetration can only be possible, when the applied forces exceed the uniaxial compressive strength of the rock (ROXBOROUGH & PHILLIPS 1975: 362). Excavation by disc cutters is not a continuous process, since the rock surface is irregular leading to a high variation of cutter load during the rolling process. The indentation into the rock mass takes place under sudden stress peaks. At these peaks, the cutter tip is subject to very high contact stresses resulting in the crushing of the rock material and the formation of a high pressure zone which shows plastic flow properties (BÜCHI 1984: 28). Crushed rock powder is displaced to the side and when the pressure level is sufficient to exceed the shear or tensile strength of the rock, new cracks develop (LINDQVIST & LAI 1983: 200). At the cutter edge, GONG et al. (2005) proved that a conical crack (Hertzian crack) is initiated which agrees with the theory of contact mechanics between a rigid indenter and brittle material. Furthermore, radial cracks and a median crack develop. If these cracks grow and coincide with cracks from adjacent cuts reaching free rock surface, rock chips are formed and chipping takes place. In terms of chipping, two mechanical theories exist. It is not definitely known whether the formation of rock chips is contingent on the development of shear or tension cracks or a combination of both. Nowadays researchers tend to prefer the mechanical approach of tension cracks since the cutter induces high stresses on a single spot at the tunnel face which is more likely compared to tensile or point load forces than to shear forces (SANIO 1985, BARTON 2000, GERTSCH 2000, KÄSLING 2009,

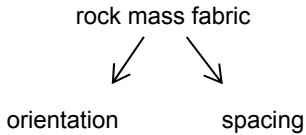
SCHNEIDER et al. 2011). Depending on geotechnical parameters of the rock and applied thrust force, cutters have to pass the same position at the tunnel face two or three times until a rock chip is being formed (LISLERUD 1997: 129). The shape and size of the rock chips for anisotropic rocks are highly dependent on the orientation of the anisotropy planes that may influence the excavation process to a great extent (ROXBOROUGH & PHILLIPS 1975).

To sum up, the formation of a **crushed zone** is mainly controlled by the **uniaxial compressive strength**, whereas the formation of **rock chips** is controlled by the **tensile strength** of rocks. Therefore, both factors are main input parameters for most of the penetration prediction models explained in chapter 2.3. By analyzing the grain size distribution of muck from linear cutting test, the ABROCK research group could prove that 80 - 90 % of the applied energy is needed to generate the crushed zone where fine grained material is dominant (GEHRING 1997, SCHNEIDER et al. 2011: 4). This coincides with the formulas of commonly used prediction models, where uniaxial compressive strength has higher impact than Brazilian tensile strength.

2.1 Penetration prediction – basic information

The performance of a TBM can be divided into two main issues that significantly influence the costs of a tunnel project – the penetration rate of a disc cutter into the rock mass and the expected cutter wear. To estimate either the penetration or the wear, different prediction models are in use. The focus of this thesis is the prediction of penetration rates in mechanized tunneling with hard rock TBMs. The penetration rate is influenced by a number of parameters that have to be considered for a precise prediction. There are on one hand rock parameters and on the other hand machine parameters that affect the efficiency of TBM excavation. Nowadays, also the influence of rock mass parameters is moving to focus which is discussed in the following chapters. In chapter 2.3, several penetration prediction models are described in detail. Since the models were developed in different countries, input parameters vary in some degree. This is particular the case for rock parameters as diverse laboratory tests exist for characterizing rock properties. Tab. 1 shows the most important input factors that are used in the majority of penetration prediction models, keeping in mind that it may vary depending on the applied model. These parameters are either input parameters for prediction models themselves or have to be considered before using predictor formulas.

Tab. 1: Main parameters for the prediction of penetration rates in TBM tunneling.

Intact rock parameters	Rock mass parameters	Machine parameters
uniaxial compressive strength (UCS)	rock mass fabric 	total thrust force (F)
Brazilian tensile strength (BTS)		normal force per cutter (F_N)
drilling rate index (DRI)		friction force (F_f)
		cutter diameter
		cutter tip width
		cutter spacing
		number of cutters

2.1.1 Rock parameters

To characterize the behavior of rocks in terms of cuttability, a number of parameters exist. Some are to be mentioned as representative. Often the **uniaxial compressive strength** (UCS) and **Brazilian tensile strength** (BTS) are implemented in prediction models since they are responsible for the formation of the crushed zone and rock chips. Beside UCS and BTS, the **drilling rate index** (DRI) has been introduced by the *Norwegian University of Science and Technology* which describes the required boring energy for certain rock types (s. chapter 2.3.4). DRI is a combination of the brittleness value S_{20} that expresses the amount of energy required to crush the material and the Sievers J-value SJ that characterizes the depth a cutter can be thrust into the rock (BRULAND 2000a: 7). A similar approach of using a factor for energy consumption has been presented by GEHRING (1995) who implemented the term of **specific failure energy** (W_f). It describes the energy that is needed to cause the failure of rock samples under uniaxial compression (s. chapter 2.3.8). W_f might also characterize the deformation behavior of rocks under compression and correspond to whether a rock behaves brittle or ductile. The brittleness of rocks has been addressed in the several prediction models. For example, GONG & ZHAO (2009) incorporates the **brittleness index** (Bi) as quotient of UCS and BTS (s. chapter 2.3.6).

Besides abovementioned parameters one must be aware that the penetration rate may be significantly influenced by petrographic characteristics such as rock type, mineral composition, texture, grain size, porosity and many others.

2.1.2 Rock mass parameters

Besides rock properties, the characteristic of the rock mass is of major influence for the penetration of a TBM. This fact has been disregarded in early-stage research, but became more and more important in current studies. Rock mass properties are heavily influenced by the fabric which is described by discontinuity or cleavage characteristics. Main aspect is hereby the orientation of joints, fissures and faults relative to the direction of tunnel advance. The parameter includes the strike direction and the dipping angle of discontinuities. Furthermore, the distance between these planes of weakness must be considered. Of minor importance are geotechnical properties of discontinuities such as surface conditions in terms of joint roughness, aperture and filling material, friction angle, cohesion and many more. One is aware that these factors may also affect the penetration, but until now, no implementation into prediction models was considered necessary.

Besides rock mass fabric, also the primary state of stress and the water inflow within the rock mass influence the performance of tunnel boring machines. However, these parameters have not yet been investigated adequately and are until now not implemented into prediction models.

2.1.3 Machine parameters

The **normal force per cutter** can be considered as indicator whether disc cutters are over- or under-loaded during excavation. Depending on the diameter, cutters are able to retain different loading forces. For example, the maximum force per cutter is assumed with 267 kN at 17'' cutters and 300 kN at 19'' cutters (GIRMSCHIED 2013: 452). Calculation of force per cutter is performed by dividing the **total thrust force** (minus friction force) by the numbers of cutters on the cutterhead. This underlines the need for conducting a friction stroke to determine friction force acting on the cutterhead and shield. However, it must be noted that not all cutters receive equal loading during the rotation of

the cutterhead, since gauge cutters are not in same contact with the rock mass like center cutters. This must be considered with a theoretical reduction of the number of cutters individually for particular TBM setup. To obtain detailed information about the different loading conditions during the excavation process, researchers are working on force measurement systems on individual disc cutters (e.g. ENTACHER 2013).

The **friction force** reflects the contact area between the shield and surrounding rock and is dependent on rock mass quality and weight of the cutterhead. High friction values caused by low rock mass strength and blocking of the annular gap by rock fragments reduce the applied thrust force respectively the force per cutter significantly. Since different tunnel routes (straight line or curve) and machine types cause varying friction values, this parameter must be considered to ensure comparability of different prediction models. Therefore, a friction stroke has to be performed where the cutterhead rotates in unobstructed space without touching the tunnel face and performing active excavation. The detail procedure is described in chapter 4.2.1. During the friction stroke, the shield of a TBM is in full contact with the surrounding rock mass. But not the entire cutterhead is, since the TBM is not penetrating the face and only gauge cutters are affected by the testing procedure. Consequently, measured values reflect the friction of the shield, but not of the cutterhead. During the excavation process, thrust force is pushing the machine against the face. This leads to high friction at the cutterhead and lower friction at the shield. Another aspect that may reduce friction during the continuous boring process is cutterhead vibration (FRENZEL et al. 2012, GONG et al. 2007). In the process of pushing the cutterhead forward, the fringe of the cutterhead, as well as gauge cutters may cause instabilities at the tunnel wall leading to rock chips falling into the gap between tunnel wall and shield. This may lead to increasing friction force. Still there is no agreement within the community to what percentage the determined friction value has to be taken into account for predicting the penetration. Commonly, value ranges from 50 % to 100 % (BÜCHI 1984, FRENZEL et al. 2012). GONG et al. (2007) carried out a series of retracting and pushing test to determine the friction at certain chainage of a tunnel system in Singapore granite. The study revealed that at the same chainage, measured values of the retracting tests (~ 100 kN) are 10-times lower than the one for pushing the cutterhead forward (~ 1,050 kN). Based on these results, GONG et al. assumed the force measured during retraction test since the true friction force. This might overestimate the benefit of continuous boring.

Cutter spacing has an impact on the fracture propagation and the rock chip formation between two adjacent cuts. Numerical modelling of GONG et al. (2005) illustrates this effect quite clearly (s. chapter 2.5.3). This is why the parameter plays an important role in penetration prediction and is implemented in most prediction models.

Furthermore, the **geometry of the cutter** respectively the characteristic of the cutter tip width during excavation respectively have an influence on the performance since worn disc cutters show larger contact area to the rock mass and thus, for a given thrust force, resulting in lower contact stresses which are essential for forming a crushed zone and rock chips. As a consequence, the size of the crushed zone, the indentation depth and the penetration rate decrease.

2.1.4 Field penetration index

To quantify the cuttability of a rock mass by tunnel boring machines, KLEIN et al. (1995) defined a **field penetration index (FPI)** which is a basic tool (Eq. 2-1). It depends on the force per cutter and

resulting penetration rate. Low values indicate high boreability since lower thrust forces are required to obtain acceptable penetration rates. In contrast, high values correspond to low boreability of a rock mass. This index can give a first impression of the boreability of a rock mass during the excavation itself, but may not predict the performance. Furthermore, it is based on the assumption that the relation between force and penetration is linear and intersects at the origin. This statement is being analyzed in detail in terms of this thesis.

$$\text{FPI} = \frac{F_N}{p} \quad \text{Eq. 2-1}$$

FPI	field penetration index [(kN/cutter) / (mm/rev)]
F_N	normal force per cutter [kN]
p	penetration rate [mm/rev]

Since the calculation of excavation costs and construction time is mainly based on performance prediction, the development of TBM performance prediction models has been addressed by a number of researchers over the last decades (s. Fig. 4). For penetration prediction, more complex models than the field penetration index have been developed to simulate reality more precisely (s. chapter 2.3).

2.2 Penetration tests

Various researchers have tried to investigate the excavation and fragmentation process of rock mass with tunnel boring machines by means of penetration tests on-site. These tests seem to be the right tool to study the interaction between rock mass and cutting tool. In addition, existing penetration prediction models can be validated. It reveals the relation between the applied thrust force and resulting penetration rate. The range, where low penetration rates cause relatively high thrust forces is defined as **subcritical penetration**. Once a certain penetration rate is exceeded, the relation between penetration and thrust becomes linear and the gradient of the function diminishes. This is due to the rock fragmentation process described in the introduction of chapter 2. At low penetration rates, the induced force is not sufficient for causing tension cracks that coincide with each other and only a crushing of the material beneath the cutter occurs (FRENZEL et al. 2012: 559, ROSTAMI 1997: 23). When a critical thrust level is not exceeded, no rock chips are formed and the penetration rate remains low. Since the formation of the crushed zone consumes high levels of energy, high thrust force values illustrated in Fig. 2 and Fig. 3 can be explained. FRENZEL et al. (2012) defined the threshold of subcritical penetration at 2 mm/rev (Fig. 2). However, analyses in terms of this thesis showed that subcritical penetration might rather range from 0 to 3 mm/rev which revealed good correlation with conducted penetration tests (Fig. 3). GONG et al. (2007: 310) set the critical point of penetration rates at 0.5 – 1 mm/rev according to his penetration test results with an EPB machine in weathered granite and alluvium. The main strength of the penetration test is that it is a full scale cutting tests directly on the TBM construction site. Therefore, the scale effect can be eliminated that one might get when performing small scale cutting in the laboratory. Small scale cutting tests are a useful instrument for obtaining an initial impression of the expected penetration rate in given geology (e.g. LORENZ 2013), but they do not reflect actual conditions at the tunnel face.

There are several methods and philosophies for conducting a penetration test and investigating the relationship between the thrust force and the penetration rate of a TBM. BRULAND (2000C) was one of the first to address this topic. He conducted an incremental test with at least four different thrust levels between the ranges of 70 % - 100 % of thrust used prior to the beginning of the test. At least 30 revolutions per level should be made. This time consuming method leads to only a few data points, since only few thrust levels are performed (Fig. 2). To maintain one thrust level constant during the test, thrust-controlled TBMs are preferred. As modern TBMs are commonly speed-controlled, this leads to an inaccuracy of obtained data set. Furthermore, the range for thrust forces lower than 70 % and corresponding penetration rates is not investigated with this method.

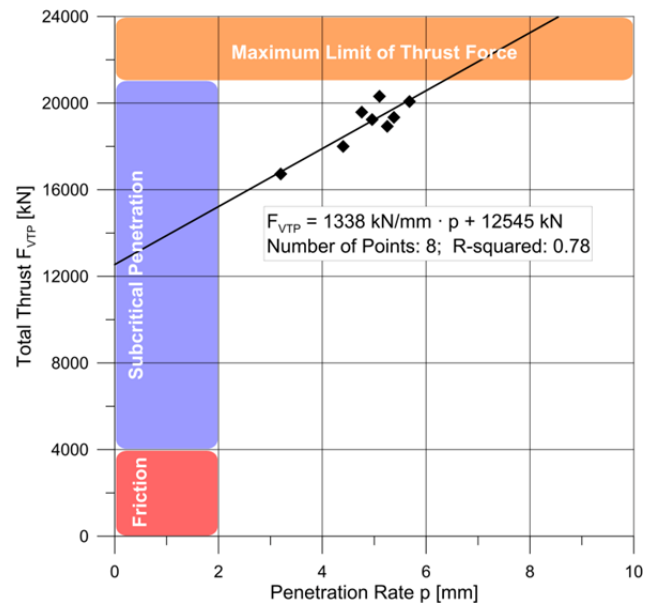


Fig. 2: Thrust-penetration curve derived from a penetration test after BRULAND at Atlanta West Side CSO tunnel (FRENZEL et al. 2012: Fig. 4, data by KÄSLING 2009: 106 ff.).

Another testing procedure arose in cooperation with Herrenknecht AG. VILLENEUVE (2008) described this approach of recording thrust-penetration data during machine start-up to interpret the cutter-rock relationship over a very short distance at the Gotthard base tunnel. Therefore, the thrust is slowly increased from zero to maximum. This leads to a denser data set in a short time period which is an advantage for the applicability at construction sites. The same procedure has also been used by GONG et al. (2007) at a Singaporean tunnel project where he compared both testing procedures. The incremental penetration test with 7 thrust levels took about 80 minutes whereas the start-up test needed only 10 minutes. Nevertheless, the writer found that similar results could be obtained by both methods.

The start-up approach has been adopted and expanded by the ABROCK research group leading to the publication of FRENZEL et al. (2012). The new testing procedure can be described as start-stop tests, meaning that the TBM starts from zero thrust to the maximum possible, given by the geological environment,

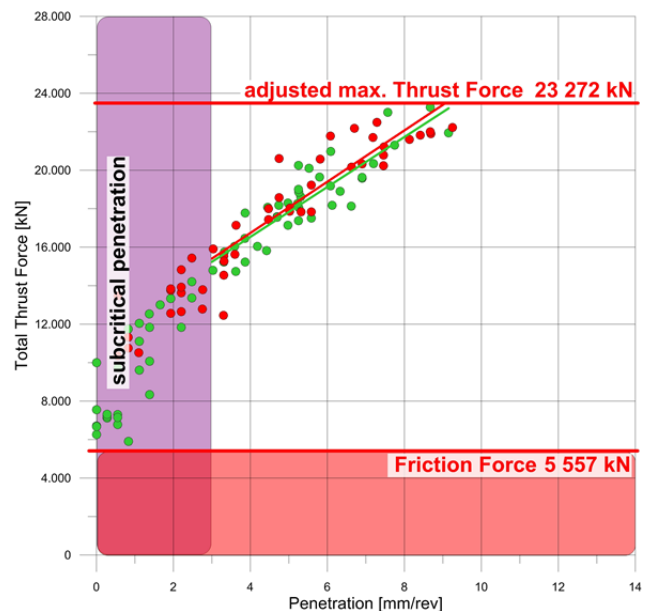


Fig. 3: Thrust-penetration curve including measured friction derived from a penetration test performed after FRENZEL et al. (2012) at the Koralm tunnel.

and back to zero thrust in very small steps. This results in a sufficient number of cutterhead revolutions to simulate the fragmentation process during active excavation. Furthermore, this quick method leads to an adequate data set to analyze the cutter-rock interaction, since it produces data points from zero to maximum possible thrust and corresponding penetration rates (Fig. 3). In addition, the stop test can provide a validation of the recorded data from the start test.

Since the start-stop tests illustrate main advantages in contrast to the BRULAND method, this approach is used as basis for further research in this thesis. In terms of this work, the testing procedure is modified in some points. A detailed description of the testing methodology and modifications is explained in chapter 4.2.1.

2.3 Existing penetration prediction models

The estimation of penetration rates in advance of a tunnel project has been the main focus of researchers over the last decades. A number of models exist that are based on different scientific backgrounds, either **empirical** by analyzing data from tunnel projects or **theoretical** by performing laboratory tests to simulate reality. More recently, also numerical approaches are used to reflect reality. GRAHAM (1976) and FARMER & GLOSSOP (1980) already started 40 years ago to develop models that estimated the penetration rate depending simply on two parameters. Throughout the years, the models became more and more complex resulting in multi factor models up to numerical simulations. Fig. 4 shows a summary of the most important prediction models, some of them are also explained in the following chapters illustrating also the strengths and weaknesses of each model. The CSM (s. chapter 2.3.7) and Gehring model (s. chapter 2.3.8) are highlighted in orange. Both are used for further research in this thesis, since they appear to be most suitable for predicting the penetration rate in alpine tunnel projects. The aim of this thesis is the development of an updated CSM and Gehring model that meets all the requirements that have to be taken into account at large alpine tunnels and combines the strengths of each model into one (**Alpine Model**).

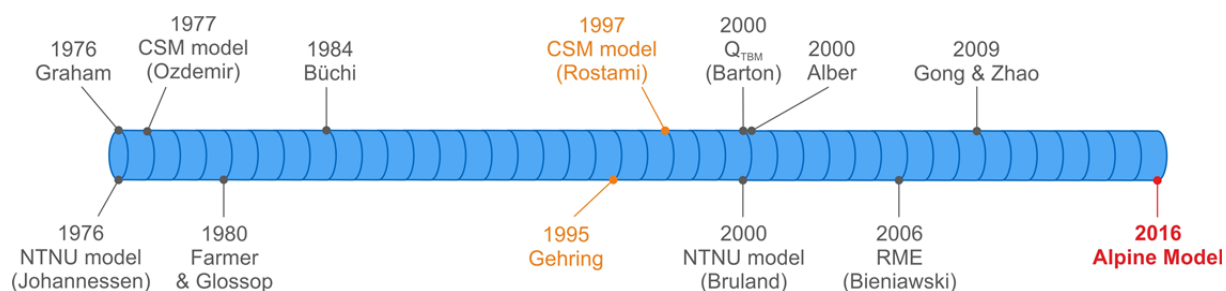


Fig. 4: Schematic timeline for TBM performance prediction models. The CSM and Gehring model, as well as the newly suggested Alpine Model, which are used for further research in this thesis, are highlighted.

2.3.1 Ernst Büchi model (1984)

BÜCHI (1984) developed in his PhD thesis a new prediction model that mainly derives from the Colorado School Mines model (s. chapter 2.3.7.) and is extended in terms of rock anisotropy and rock mass fracturing. His research is based on field observations of 9 tunnel projects with a total length of more than 38 km. Furthermore, geological mapping and sampling to determine the geotechnical parameters were performed. The formula of the CSM model is used to estimate the basic net penetration rate for isotropic and unfractured rock mass. The geotechnical input parameters for the CSM model

are uniaxial compressive strength and Brazilian tensile strength that have to be implemented with their maximum value (perpendicular to possible anisotropies). The second step is a correction for rock anisotropy (e.g. schistosity) since BÜCHI observed an increase in penetration rates of 33 % for an angle of 90° between tunnel axis and orientation of anisotropy of a 7.1 km long sample area. If the schistosity is parallel to the tunnel axis ($\cong 0^\circ$), the increase was observed with 0 %. Taking the schistosity into account, an anisotropy factor is calculated which can be determined by the ratio of maximum (perpendicular to schistosity) to minimum (parallel to schistosity) strength. Rock mass fracturing is considered by measuring the mean spacing of fractures relating to the direction of the tunnel axis. This parameter is stated more in detail in chapter 2.5.

The BÜCHI model is based on the evaluation of field performance data in comparison with geological back mapping. Thus, it features a good practical application and large number of laboratory testing results. The development of this model dates back to 1984 and since then tunnel dimensions and TBM technique evolved. Furthermore, the thesis is only available in German which minimizes the use in countries worldwide. An additional disadvantage of the model is the handling of a correction for rock mass fracturing. The recommendation might be useful for back analyzing the fracturing degree, but not for making predictions. To solve this problem, BÜCHI (1984: 56) suggested making use of the RQD index from drill core analysis as it gives a first impression of the fracture frequency in advance of a tunnel project. Until now, no update has been published.

2.3.2 Michael Alber model (2000)

ALBER (2000) published a system to estimate the advance rate of TBMs by the classification of rock mass strength and rock mass behavior. **Rock mass strength (σ_{cm})** combines the commonly used uniaxial compressive strength and rock mass characteristics by implementing RMR index to Hoek-Brown failure criterion (Eq. 2-2). Using the RMR index has the advantage that discontinuity spacing, surface condition and groundwater inflow are already included. By contrast, this value is accompanied with high uncertainties and a very subjective determination, since the system gives the user a high variance of interpretation possibilities. Furthermore, the RMR system has to be transferred to TBM tunneling by an empirical formula (ALBER 1996).

$$\sigma_{cm} = \sigma_c \cdot \sqrt{s} \quad \text{Eq. 2-2}$$

σ_{cm}	rock mass strength [MPa]		
σ_c	uniaxial compressive strength [MPa]		
s	Hoek-Brown failure criterion	=	$\exp\left(\frac{\text{RMR} - 100}{9}\right)$

Rock mass behavior is the second parameter that is required to determine suggested stability classes. It is characterized by the **Factor of Safety (FS)** (Eq. 2-3). ALBER shows a good correlation between FS at the centerline of the roof and TBM utilization.

$$\text{FS} = \frac{\sigma_{cm}}{\sigma_\theta} \quad \text{Eq. 2-3}$$

FS	Factor of Safety
σ_{cm}	rock mass strength [MPa]
σ_θ	tangential stress at side wall [MPa]

To estimate the advance rate, ALBER categorized each parameter (σ_{cm} and FS) into three classes (A-C and I-III) and combined them to nine possible advance rate classes. Each class reflects specific tunneling condition and a certain effort of the TBM to excavate the ground. By analyzing the variability of each parameter, one may calculate probability density functions for each advance rate class (Fig. 5). Based on this figure, the user can estimate the minimum and maximum, as well as the most probable advance rate for certain ground conditions (ALBER 2000: 60).

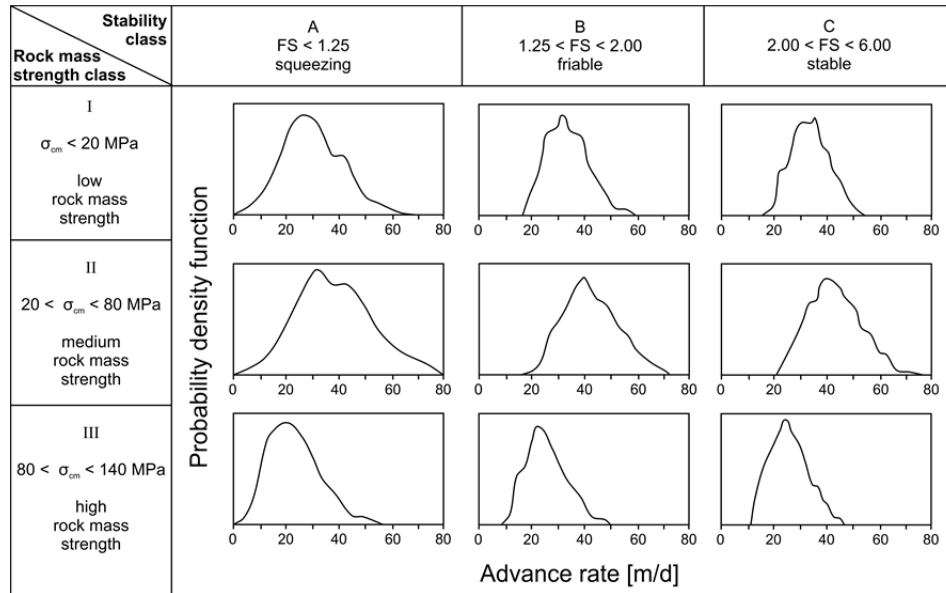


Fig. 5: Probability density functions of the nine suggested advance rate classes by ALBER (2000: 60, mod.).

Until recently, the prediction model has not been applied frequently in practice since the determination of the parameters bears uncertainties and the result is only a range of advance rates. Consequently, the model has not found its way to the construction sites yet.

2.3.3 Q_{TBM} by Nick Barton (2000)

BARTON (2000) suggested a TBM performance prediction model for hard rock that is based on previously developed Q-system for rock classification in NATM tunneling. The modification of this index system for TBMs is called Q_{TBM} and contains the orientation and material property of discontinuities, rock mass strength, cutter wear and force, as well as the stress level at the tunnel face (Eq. 2-4).

$$Q_{TBM} = \frac{RQD_0}{J_n} \cdot \frac{J_r}{J_a} \cdot \frac{J_w}{SRF} \cdot \frac{SIGMA}{F^{10}/20^9} \cdot \frac{20}{CLI} \cdot \frac{q}{20} \cdot \frac{\sigma_\theta}{5} \quad \text{Eq. 2-4}$$

RQD_0	RQD for orientation II to tunnel direction [%]
J_n	joint set number [-]
J_r	joint roughness number [-]
J_a	joint alteration number [-]
J_w	joint water reduction factor [-]
SRF	stress reduction factor [-]
SIGMA	rock mass strength [MPa]
F^{10}	cutter force [kN]
CLI	cutter life index [-]
q	quartz content [%]
σ_θ	biaxial stress on tunnel face [MPa]

To estimate the performance of the TBM, particularly the penetration rate, case records of 145 tunnels with a total length of 1,000 km have been analyzed leading to a relationship as seen in Eq. 2-5.

$$PR \approx 5 \cdot (Q_{TBM})^{-0,2} \quad \text{Eq. 2-5}$$

PR penetration rate [m/hr]

To gain a better matching of the Q_{TBM} system, the RQD (Rock Quality Designation) value has been modified to RQD_0 . The modified parameter addresses the spacing of discontinuities at the tunnel level by analyzing rock cores from boreholes parallel to the tunnel axis and not from vertical boreholes. J_n , J_r , J_a , J_w and SRF ratings are equal to the original Q-system, except that J_r and J_a should refer to the joint set that most influences the boring process.

The concepts behind this approach steps in the right direction, but the technical implementation is complicated and expensive. In sum, this model based on Q_{TBM} did not gain acceptance in the construction industry in Central Europe since it contains an abundance of required input parameters, some of them are commonly not determinable outside of Norway (e.g. cutter life index CLI), or are not strictly defined (e.g. rock mass strength SIGMA).

2.3.4 NTNU model by Amund Bruland (2000)

BRULAND (2000) developed a prediction model to estimate time consumption and costs for mechanical tunneling which includes the prediction of the penetration rate, as well as cutter wear. The empirical model is based on the results of penetration tests and analyzed data from various tunnel projects. The **basic penetration rate** (i_0) can be calculated by using Eq. 2-6.

$$i_0 = \left(\frac{M_{ekv}}{M_1} \right)^b \quad \text{Eq. 2-6}$$

i_0	basic penetration [mm/rev]
M_{ekv}	equivalent thrust per cutter [kN/cutter]
M_1	critical thrust for 1 mm/rev penetration [kN/c]
b	penetration coefficient

The term of **equivalent thrust per cutter** (M_{ekv}), characterizes the influence of machine parameters on the penetration and includes gross average cutter thrust, cutter diameter and cutter spacing. Parameters M_1 and b are highly influenced by the factor k_{ekv} , which describes rock and rock mass properties such as spacing and orientation of discontinuities, drillability (DRI - Drilling Rate Index) and porosity of the material (BRULAND 2000a). The prediction of cutter wear is separated in machine and rock mass parameters and uses input parameters like Cutter Life Index (CLI), quartz content, number of cutters, cutter and TBM diameter and cutterhead rotational speed. Since the focus of the thesis is penetration prediction, cutter wear is not addressed any further, but can be read in detail in BRULAND (2000c).

The advantage of the NTNU model is based on a large and high quality data set from former tunnel projects that lead to a very practical application. It offers a huge amount of input parameters and thus a high flexibility which, as a consequence, is not easy to handle for average customers. The very detailed manner of characterizing the rock mass properties such as fracturing degree or type of fracture is on one hand highly desirable. On the other hand, this possibility leads to greater uncertainty and

lesser reproducibility since geological mapping is still a subjective matter. By providing the geologist with a greater choice, the more likely it is that different people will tend to choose different classes or types of fractures. In addition, some input parameters are only determinable at the laboratory at NTNU / Sintef, and thus not commonly recorded by the geological preliminary investigation (DRI, CLI). BARTON (2000:16) suggested a possible correlation between DRI and UCS for metamorphic rock types (quartzite, gneiss, schist), granites, sandstone and siltstone. These values can be used as an approximation. Ongoing PhD thesis of MACIAS aims to an update of the existing NTNU model to account for the further development in TBM techniques since the first publication (MACIAS et al. 2014a, MACIAS et al. 2014b).

2.3.5 RME indicator by Z.T. Bieniawski (2006)

BIENIAWSKI et al. (2006) introduced a **rock mass excavability indicator (RME)** to predict the performance of a TBM. The authors aim was to combine established drill and blast rock mass characterization concepts, like RMR, and TBM parameters. The system for the determination of the new RME indicator is the same as RMR. Input parameters are rated with certain values and then summed up. Data for RME was derived from field investigations at four tunnel projects in Spain (mainly double-shield TBMs) with a cumulative length of 23 km. A linear discriminant analysis selected 5 input parameters as most influencing TBM advance rates: abrasivity (expressed by DRI), discontinuity spacing, stand-up time, uniaxial compressive strength and groundwater inflow. Afterwards, these parameters were weighted by statistical methods resulting in the following ratings (Tab. 2).

Tab. 2: Input parameters for the RME index with corresponding rating (BIENIAWSKI et al. 2006: Tab. 2).

Uniaxial compressive strength of intact rock [0 – 10 points]											
c _{ri} (MPa)		< 5	5-30		30-90		90-180		> 180		
Ratings		0 (*1)	5		15		10		0		
Abrasive – Drilling Rate Index [0 – 15 points]											
DRI		> 80	80-65		65-50		50-40		< 40		
Ratings		15	10		7		3		0		
Discontinuities at excavation front [0 – 40 points]											
Homogeneity			No. of joints per meter				Orientation w.r.t. tunnel axis				
Homogeneous		Mixed	0-4	4-8	8-15	15-30	>30	Parallel	Oblique	Perpendicular	
Ratings		10	0	20	15	10	5	0	10	5	0
Stand up Time [0 – 25 points]											
hours		< 5	5-24		24-96		96-192		> 192		
Ratings		0	2		10		15		25		
Groundwater inflow [0 – 10 points]											
litres/min		> 100	70-100		30-70		10-30		< 10		
Ratings		0	1		2		4 (**0)		5		

* For double-shield and single shield. ** For argillaceous rocks.

RME values show a good correlation with **average advance rates (ARA)** of chosen tunnel projects. With the help of this relation, equations can be set to predict the performance for two ranges of RME values (BIENIAWSKI et al. 2006: 4). Eq. 2-7 is valid for RME > 75 which corresponds to high advance rates up to 30 m/day. Eq. 2-8 is valid for RME < 75 with corresponding lower advance rates.

$$ARA \text{ [m/day]} = 0.56 \times RME - 26 \quad \text{Eq. 2-7}$$

$$ARA \text{ [m/day]} = 0.213 \times RME \quad \text{Eq. 2-8}$$

Based on these results, BIENIAWSKI suggested a classification system which describes the applicability of double-shield TBMs for certain tunnel projects (Tab. 3).

Tab. 3: Classification system for the applicability of double-shield TBMs based on RME index (BIENIAWSKI et al. 2006: 5).

RME [-]	Classification	Average advance rate ARA [m/day]
> 75	very high preference	> 16
50 – 75	good preference	10 – 16
25 – 50	fair preference	5 – 10
< 25	TBM not suitable	< 5

Conclusively, the rating system seems to be a good approach, but the determination of the stand-up time implies uncertainties into the model. This parameter must be estimated from an RMR chart, which has been developed by BIENIAWSKI for drill and blast tunneling. Additionally, an equation derived from case studies has to be used to convert $RMR_{D\&B}$ to RMR_{TBM} (ALBER 1996). It is worth considering an adaption of the abrasivity factor, now determined with DRI, by implementing a rating for the Cerchar abrasivity index (CAI) which is used worldwide.

2.3.6 BI by Qiu Ming Gong and Jian Zhao (2009)

The authors proposed a conceptual model of rock mass properties that results in a **boreability index (BI)** to predict the penetration rate (GONG & ZHAO 2009). During the construction of sewerage tunnel systems in Singapore, TBM data, geological face mapping and geotechnical parameters have been recorded and analyzed. Rock mass properties are addressed by implementing uniaxial compressive strength (UCS), brittleness, joint spacing and joint orientation. The influence of rock brittleness on the TBM performance has been studied by GONG & ZHAO (2007). The brittleness index (Bi), defined as ratio of UCS and BTS, was compared with TBM data from a project in Singapore granite. The results reveal that with increasing rock brittleness, the indentation process, as well as the formation of a crushed zone becomes easier and also the penetration rate increases. For a detailed description of the brittleness index and its influence on the penetration see chapter 2.4.

Joint spacing is taken into account by determining the volumetric joint count (J_v) which is the sum of the number of joints per cubic meter for each joint set (s. chapter 2.5.3, Eq. 6-5). Joint orientation is considered by the angle (α) between tunnel axis and discontinuity. However, only the orientation of the most frequent joint set is implemented in the prediction model.

Due to the influence of operating machine parameters such as thrust force and rotational speed of the cutterhead, the penetration rate can vary even in the same rock mass condition. To eliminate these effects and to ensure an evaluation of rock mass boreability in the same tunnel or in tunnels excavated by similar TBMs, the authors proposed a **specific rock mass boreability index (SRMBI = BI₍₁₎)** (GONG et al. 2007, GONG & ZHAO 2009). The SRMBI is defined as the boreability index equal to a penetration of 1 mm/rev and can be calculated by Eq. 2-9. Furthermore, the penetration rate of 1 mm/rev is close to the critical penetration value (0.5 - 1 mm/rev) defined by GONG at which chipping takes place. Therefore, the SRMBI does not change at different operating thrust forces. However,

it must be noted that even with the SRMBI, the effect of machine parameters (cutter geometry, cutter spacing) still exists.

$$BI_{(1)} = 37.06 \cdot UCS^{0.26} \cdot Bi^{-0.1} \cdot (0.84 e^{-0.05 \cdot J_v} + e^{-0.09 \cdot \sin(\alpha+30)}) \quad \text{Eq. 2-9}$$

$BI_{(1)}$	specific rock mass boreability index [kN/cutter/mm/rev]
UCS	uniaxial compressive strength [MPa]
Bi	brittleness index = UCS/BTS [-]
J_v	volumetric joint count [-]
α	angle between tunnel axis & joint orientation [°]

By analyzing data from penetration tests at a tunnel system in Singapore, the following relationship (Eq. 2-10) has been established, which describes the **boreability index (BI)** of a rock mass depending on $BI_{(1)}$. The formula refers to the field penetration index (FPI) mentioned in chapter 2.1.4.

$$BI = BI_{(1)} \cdot p^{-0.75} = \frac{F_N}{p} \quad \text{Eq. 2-10}$$

BI	boreability index [kN/cutter/mm/rev]
$BI_{(1)}$	specific rock mass boreability index [kN/cutter/mm/rev]
p	penetration rate [mm/rev]
F_N	normal force per cutter [kN]

Statistical evaluation of the data reveals that uniaxial compressive strength and volumetric joint count have a predominant effect on the penetration rate (Fig. 6), whereas joint orientation and rock brittleness have a minor influence (GONG & ZHAO 2009: 15). This statement is not in agreement with common research opinions, since joint orientation is attributed to having a profound effect on TBM performance.

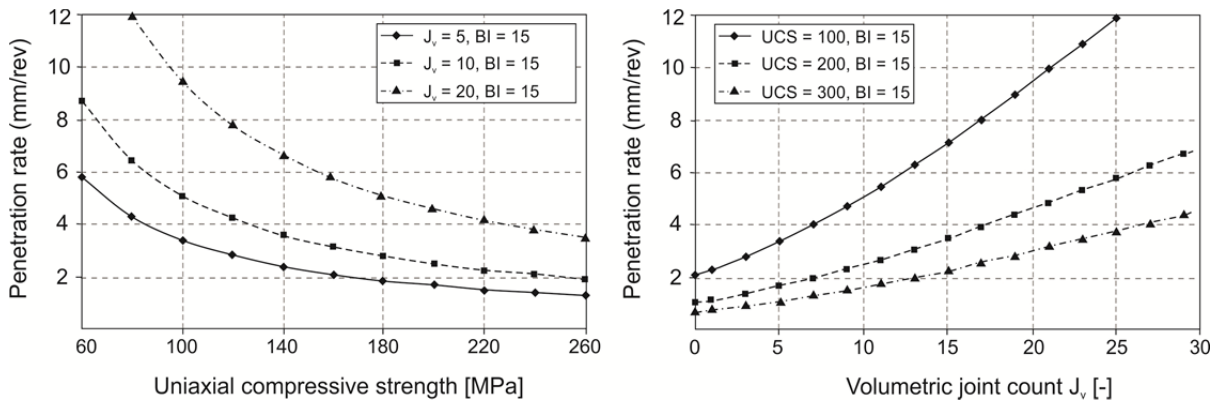


Fig. 6: Influence of uniaxial compressive strength (UCS) and volumetric joint count (J_v) on the penetration rate at constant thrust force of 200 kN/cutter (mod. from GONG & ZHAO 2009: Fig. 8 & 10).

One main limitation on the model is that it is based on only one tunnel project where an EPB machine is used to excavate granite. All machine parameters (e. g. cutter diameter, cutter tip width, cutter spacing) are considered constant. Hence, the model might not be applicable to predict the penetration at tunnel projects that are not situated in granite, and that are not using 17'' cutters. This is why the boreability index is not commonly used to predict the penetration, but the author's investigation

concerning the effect of various rock mass parameters on the penetration, provides some useful information (s. chapter 2.5.3).

2.3.7 CSM model by Levent Ozdemir (1977) and Jamal Rostami (1997)

The Colorado School of Mines (CSM) model is an analytical penetration prediction model that has been developed by performing laboratory testing at the Earth Mechanics Institute in Golden. Formulas of the model are based upon results from linear cutting tests by which the estimation of cutting forces for disc cutters can be investigated. These results have been subsequently compared with TBM field data to include the practical aspect. The first version of the model was published in 1977 by OZDEMIR et al. and describes force as a product of crushed zone pressure and cutter-rock contact area. At that time, tests were conducted with V-shaped disc cutters, but today constant cross-section geometries are used. ROSTAMI (1997) tackled this problem in his PhD thesis and updated the original model resulting from new data with constant cross-section cutters. In addition, ROSTAMI revised the base formula of OZDEMIR since it was dimensionally not correct.

The final result of the CSM model is the normal force per cutter that is needed for a certain penetration (Eq. 2-13) using a power function. Input parameters for this calculation are the angle and the pressure of the contact area between cutter and rock (Eq. 2-11, Eq. 2-12). These parameters are characterized by the cutter and cutterhead geometry (cutter diameter, cutter tip width and spacing), as well as by geotechnical parameters of the rock (UCS, BTS).

It is an important aspect that both, uniaxial compressive strength and Brazilian tensile strength, appear in the formula for the pressure calculation, since UCS seems to control the formation of a crushed zone and BTS the formation of tension cracks and rock chips. The ‘cutting constant c’ describes the ratio of rolling to normal force, since both forces occur during the cutting process. The value has been set with 2.12 based on the results of linear cutting tests.

In certain rock types using a certain tunnel boring machine, all these parameters are fixed. The only variable of this model is the penetration which is increased until one of the machine limits (e.g. cutter load, thrust, torque) is reached.

$$\Phi = \cos^{-1} \frac{R - P}{R} \quad \text{Eq. 2-11}$$

Φ	angle of the arc of contact [rad]
R	cutter radius [mm]
P	penetration rate [mm/rev]

$$P' = c \cdot \sqrt[3]{\frac{\sigma_u^2 \cdot \sigma_t \cdot s}{\Phi \cdot \sqrt{(R \cdot T)}}} \quad \text{Eq. 2-12}$$

P'	pressure of contact area [MPa]
c	cutting constant = 2,12 [-]
σ_u	uniaxial compressive strength [MPa]
σ_t	Brazilian tensile strength [MPa]
s	spacing of cutters [mm]
T	cutter tip width [mm]

$$F_N = \left(\frac{T \cdot R \cdot \Phi \cdot P' \cdot \cos\left(\frac{\Phi}{2}\right)}{1000} \right) \quad \text{Eq. 2-13}$$

F_N normal force per cutter [kN]

The main advantage of this model is that cutterheads and disc cutters with different geometries can be individually implemented with a high accuracy. Notwithstanding, no rock mass characteristics such as discontinuities, stress conditions, ground water etc. are taken into account in the basic model of OZDEMIR and ROSTAMI. These parameters seem to highly influence the penetration rate. Therefore, YAGIZ (2002), and prior to that CHEEMA (1999), upgraded the basic model by rock mass characteristics. CHEEMA developed a **rock mass boreability index (RMBI)**, while YAGIZ found a linear equation by combining **rock fracture index (RFI)** and **brittleness index (BI)** with the penetration rate of the basic CSM model as best fitting for a new **modified CSM (MCSM)** model. The approach by YAGIZ is explained in detail in chapter 2.5.4. It is worth mentioning that the determination of the BI is based on results from the punch penetration test which is rarely used in European rock laboratories. This may explain why the modified CSM model has not gained such wide acceptance as the basic model by ROSTAMI. In total, the basic CSM model is one of the most widely used prediction model which is why further investigations and analysis of penetration tests in this thesis are carried out using the CSM model.

2.3.8 Gehring model by Karlheinz Gehring (1995)

Dr. Karlheinz Gehring was a well-known Austrian expert for tunnel boring machines. He worked over 30 years at *Voest-Alpine Bergtechnik* and gained a lot of experience with TBMs at different tunnel projects all over the world. He published the first version of the model in 1995 (GEHRING 1995) and enhanced it during the following years (GEHRING 1997). He was member of the research group ABROCK, from which this thesis is part of. Therefore, a special focus in terms of evaluating penetration tests is based on the Gehring model which is, in a second step, compared with the CSM model.

GEHRING's formula is empirical and derives from the analysis of different tunnel projects from *Voest-Alpine* with a certain machine setup (17'' cutters, 80 mm spacing). The final result is the maximum penetration for a certain normal force per cutter. The formula has a modular structure and a simple linear function with independent correction factors that allow the consideration of rock mass properties, as well as different cutterhead types and geometries (Eq. 2-14). At the time of its development, a scientifically proof model, in terms of correct dimensions, had not been considered as crucial.

$$p = \frac{F_N}{\sigma_u} \cdot k_i \quad \text{Eq. 2-14}$$

p	penetration rate [mm/rev]
F_N	normal force per cutter [kN]
σ_u	uniaxial compressive strength [MPa]
k_i	correction factors [-]

The basic formula includes the following correction factors:

- k_0 = basic penetration factor = 4.0 (at 432 mm / 17'' cutterring Ø, 80 mm spacing)
- k_1 = factor specific failure energy
- k_2 = factor rock mass fabric
- k_3 = factor state of stress in rock mass
- k_4 = factor for cutter diameters \neq 432 mm
- k_5 = factor for cutter spacing \neq 80 mm

All factors are explained below. This thesis focusses on the validation and improvement of two correction factors (k_1 and k_2). The factor for specific failure energy includes the term of rock toughness, whereas the factor for rock mass fabric describes characteristics of discontinuity systems. Both parameters influence penetration rates significantly and are discussed in detail in chapter 2.4 and 2.5.

k_0 = basic penetration factor

The basic equation of GEHRING reveals the relation between penetration and uniaxial compressive strength. It originates in the approach of various researchers combined with the analysis of actual TBM data from *Voest-Alpine* projects (Eq. 2-15).

$$p = a \cdot \sigma_u^{-b} \quad \text{Eq. 2-15}$$

p	penetration rate [mm/rev]
a	penetration coefficient [-]
σ_u	uniaxial compressive strength [MPa]
b	penetration exponent [-]

GEHRING aimed to develop a model for 'average' rock strength and thrust forces that can be easily applied and meet the conditions at most of existing tunnel projects. This means uniaxial compressive strength from about 100-250 MPa and a mean thrust force of 200 kN per cutter. Most of the data from other researchers are also available for rocks with these strength values. GEHRING performed a regression analyses for the basic penetration depending on different strength values on the basis of approaches by GRAHAM (1976), FARMER et al. (1979), HUGHES (1972), SANIO (1983) and NTH (now NTNU). Fig. 7 reveals that especially in the range of 100-250 MPa (grey rectangle), all results show low divergence.

The two unknown variables **a** and **b** have been recalculated for comparable boundary conditions (17'' cutterring Ø, 80 mm cutter spacing) on the basis of the abovementioned approaches. The results are shown in Tab. 4. Approaches by HUGHES and NTH show a significant increase in penetration rates at UCS values lower than 100 MPa. This leads to *coefficient a* larger 2,000 and unrealistic high penetration rates of more than 20 mm/rev. Therefore, both approaches are excluded for the calculation of average values for *coefficient a* and *exponent b* which set up the Gehring model.

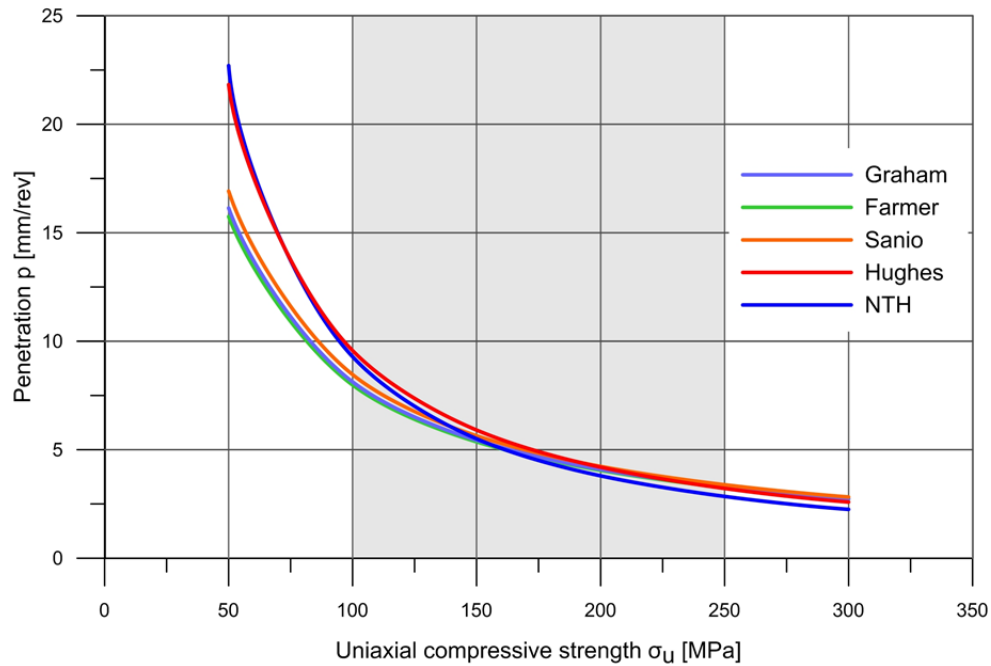


Fig. 7: Basic penetration p depending on uniaxial compressive strength σ_u for a mean thrust force of 200 kN per cutter, recalculated from approaches by GRAHAM, FARMER, HUGHES, SANIO and NTH (mod. from GEHRING 1995: 441).

It must be mentioned, that the NTH approach uses DRI (s. chapter 2.3.4) instead of UCS. BARTON (2000: 16) suggested a possible correlation between DRI and UCS for metamorphic rock types, granites, sandstone and siltstone. These values can be used as an approximation, but are not to be considered as a reliable correlation. This may explain the deviation at low UCS values (SCHNEIDER et al. 2011: 7).

Tab. 4: Penetration coefficient a and exponent b originating from different approaches and resulting Gehring factors (after GEHRING 1995: 441).

Source	Coefficient a	Exponent b
Graham	778	0.99
Farmer	729	0.98
Sanio	846	1.00
Hughes	2295	1.19
NTH	3530	1.29
Gehring	785	0.99

GEHRING simplified following equation (Eq. 2-16) as sufficient precise for practical use: coefficient $a = 800$ and exponent $b = 1$. The formula was developed for a thrust force of 200 kN/c. For a generalization, a **basic penetration factor** like *coefficient a* has been introduced - named k_0 . This factor is set at 4.0 for machines with a certain setup of 17'' (432 mm) cutters and 80 mm spacing. In a second step, GEHRING developed correction factors to consider conditions deviating from those abovementioned to establish a broad applicability (s. next paragraphs).

$$p = 800 \cdot \sigma_u^{-1} = 4 \cdot 200\text{kN} \cdot \sigma_u^{-1} = 4 \cdot \frac{F_N}{\sigma_u} \quad \text{Eq. 2-16}$$

p	penetration rate [mm/rev]
σ_u	uniaxial compressive strength [MPa]
F_N	normal force per cutter [kN]

$k_1 =$ factor for specific failure energy

GEHRING's own experience, as well as data from the literature showed that **fracture energy** W_f is a parameter that influences the penetration of rocks significantly (GEHRING 1995). In general, the term describes the energy that is needed to cause failure of a specimen under uniaxial compression. It is similar to the term of failure work (W_b), which is used in this thesis (s. chapter 4.1.1). GEHRING found a coefficient of determination of about 0.9 for a correlation of penetration and failure energy at four different tunnel projects. Since failure energy is dependent on the uniaxial compressive strength of particular rock, he introduced a new parameter called **specific failure energy** w_f which is normalized by UCS (Eq. 2-17). It must be mentioned that the suggested unit of w_f (acc. to GEHRING) does not conform to Eq. 2-17 as the division units in $[\text{m}^3 10^{-6}]$. Furthermore, it is not fully clear, how the specific failure work was calculated concerning the results from uniaxial compression tests. It appears that the parameter cannot be equated to the failure work, which is used in recent rock mechanics (s. chapter 4.1.1). The correction factor k_1 that is based on w_f has been set by a regression analysis of existing TBM data (Eq. 2-18).

$$w_f = \frac{W_f}{\sigma_u} \quad \text{Eq. 2-17}$$

w_f	specific failure energy $[\text{m} 10^{-6}]$ $[\text{m}^3 10^{-6}]$
W_f	failure energy [Nm]
σ_u	uniaxial compressive strength [MPa]

$$k_1 = 0.475 \cdot w_f^{-0.56} \quad \text{Eq. 2-18}$$

k_1	factor for specific failure energy [-]
w_f	specific failure energy $[\text{m} 10^{-6}]$ $[\text{m}^3 10^{-6}]$

Regarding the analysis of certain tunnel projects, according to the author, the specific failure energy can influence the penetration rate by approximately $\pm 20\%$ leading to correction factors k_1 of 0.7 to 1.2 (Fig. 8). This assumption will be analyzed throughout of this thesis. The definition of k_1 is rarely used, and must therefore be validated by more data from actual tunnel projects.

Another aspect that captures this idea of energy consumption as an influencing factor for penetration rates is the parameter of **destruction work** W_z . In contrast to failure energy, this parameter also counts for the post-failure range of rocks and may characterize the rock toughness (s. chapter 2.4). THURO (2002: 60) could prove a clear correlation between penetration and destruction work in his post-doctoral thesis.

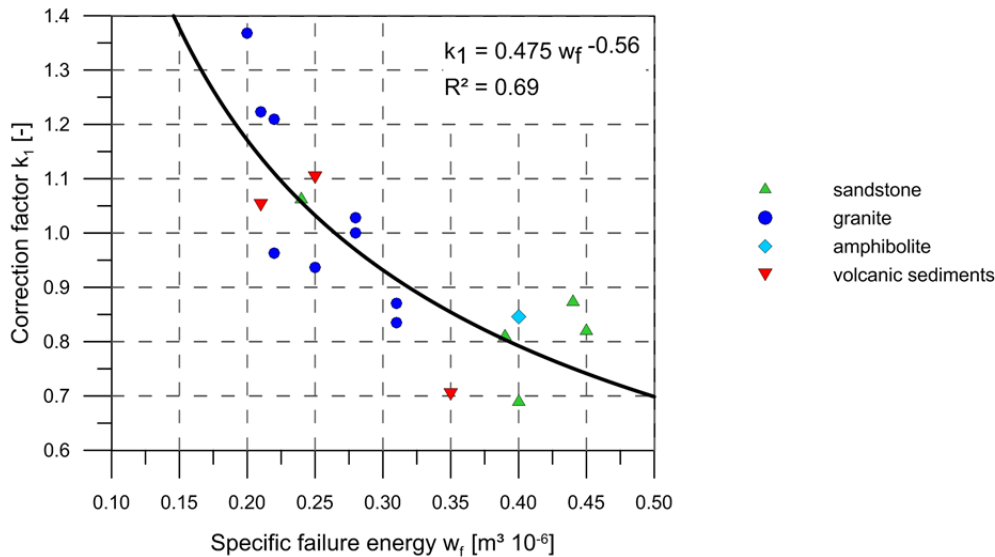


Fig. 8: Correction factor k_1 as a function of specific failure energy w_f (mod. from GEHRING 1995: 443).

Both parameters have advantages and disadvantages. W_f is easy to determine in the laboratory in terms of UCS testing, but doesn't consider post-failure range, whereas W_z requires a more complex determination which not all testing machines can perform. This issue is discussed more in detail in chapter 2.4.

$k_2 =$ factor for rock mass fabric

Characteristics of discontinuities are taken into account by correlating **spacing** and **orientation** of schistosity, foliation, joints or other planes of weaknesses. Suggested correction factors according to GEHRING are based on data of WANNER & AEBERLI (1979), combined with results of NTNU reports (Tab. 5). GEHRING considers spacing and orientation only of the major plane of weakness and not of intersecting discontinuity systems, which might not reflect actual rock mass characteristics. Furthermore, only spacing < 50 cm are assumed to influence the penetration rate. In GEHRING (1997), the author pointed out that distances between planes of weakness up to 160 cm might influence the performance. However, this value is not considered in the following determination table. By contrast, the NTNU model counts for spacing up to 160 cm (BRULAND 2000d: 8). In reference to BRULAND (2000d: 16), the orientation of discontinuities is described in the Gehring model by the smallest **angle α** between tunnel axis and plane of weakness (Eq. 2-19). At an angle of $\alpha = 60^\circ$, the greatest influence is observed resulting in a very high correction factor k_2 of 3.0. This value corresponds more or less to the maximum correction factor at the NTNU model, which is 4.0 (s. Fig. 30). A detailed comparison of the Gehring model and the NTNU model in terms of discontinuities is given in TÜRSCHER (2012: 169ff.). The major influence at an angle of $\alpha = 60^\circ$ has also been confirmed by other authors (THURO 2002, BARTON 2000, GONG et al. 2005, SANIO 1985).

$$\alpha = \sin^{-1}(\sin \alpha_f \cdot \sin(\alpha_t - \alpha_s)) \quad \text{Eq. 2-19}$$

α	smallest angle between tunnel axis and discontinuity [°]
α_f	dip angle discontinuity [°]
α_s	strike angle discontinuity [°]
α_t	tunnel direction [°]

Tab. 5: Correction factor k_2 depending on spacing and orientation of discontinuity relative to tunnel axis in terms of α angle (GEHRING 1995: 447).

Spacing of discontinuity	Correction factor k_2 at $\alpha =$			
	0°	30°	60°	90°
> 50 cm	1.0	1.0	1.0	1.0
10 – 50 cm	1.2	1.3	1.6	1.3
5 – 10 cm	1.4	1.8	2.3	1.6
< 5 cm	1.7	2.3	3.0	2.0

The main disadvantage of this correction factor is the small data base which has to be extended by new data. Furthermore, only one plane of weakness is considered and the spacing must be less than 50 cm to influence penetration. Hereby, also single marked discontinuities such as faults are excluded from the consideration. These assumptions are not correct and must be revised for an accurate penetration prediction (s. chapter 6).

$k_3 =$ factor for state of stress in rock mass

A factor for the stress field at the tunnel face and side walls could not be determined by GEHRING since the author only analyzed tunnel projects with overburdens of lower than 250 m and no horizontal stress regime expected. Especially at large base tunnels crossing the Alps (Lötschberg, Gotthard, Koralm, etc.), instabilities at the face and side walls could be observed causing blocky faces. Therefore, at tunnel projects with higher overburden or horizontal stress, an influence on the penetration rate is to be expected, but no formula is available, yet.

$k_4 =$ factor for cutter diameters $\neq 432$ mm (17'')

GEHRING performed a regression analysis for constant section cutters with diameters of 432 mm (17'') and cutter tip widths of 15.875 mm (5/8''). Field data showed that the relation between cutter diameter and penetration rate is linear resulting in Eq. 2-20 (GEHRING 1995: 444). The linear correlation is based on the results of LISLERUD et al. (1983) and verified by BRULAND (2000d: 20).

$$k_4 = \frac{430}{d_c} \quad \text{Eq. 2-20}$$

k_4 factor for cutter diameters $\neq 432$ mm [-]
 d_c cutter diameter [mm]

TÜRSCHER (2012) from the ABROCK research group suggested an extension of Eq. 2-20 by a quotient which also considers different cutter tip widths (Eq. 2-21). An application of the extended formula raised some doubt if the quadratic approach for the cutter tip width is overestimating this influence (SCHNEIDER et al. 2011). Further research appears to be required.

$$k_4 = \frac{430}{d_c} \cdot \left(\frac{15.875}{b_c} \right)^2 \quad \text{Eq. 2-21}$$

k_4 factor for cutter diameters $\neq 432$ mm [-]
 d_c cutter diameter [mm]
 b_c cutter tip width [mm]

$k_5 =$ factor for cutter spacing $\neq 80$ mm

This correction factor is based on research at the NTNU concerning the relation between cutter spacing and penetration (LISLERUD et al. 1983). It has been proven that, for constant thrust force, smaller spacing cause higher penetration rates. The suggested correlation diagram for k_5 considers the influence of cutter spacing $\neq 80$ mm, depending also on the cuttability of the rock.

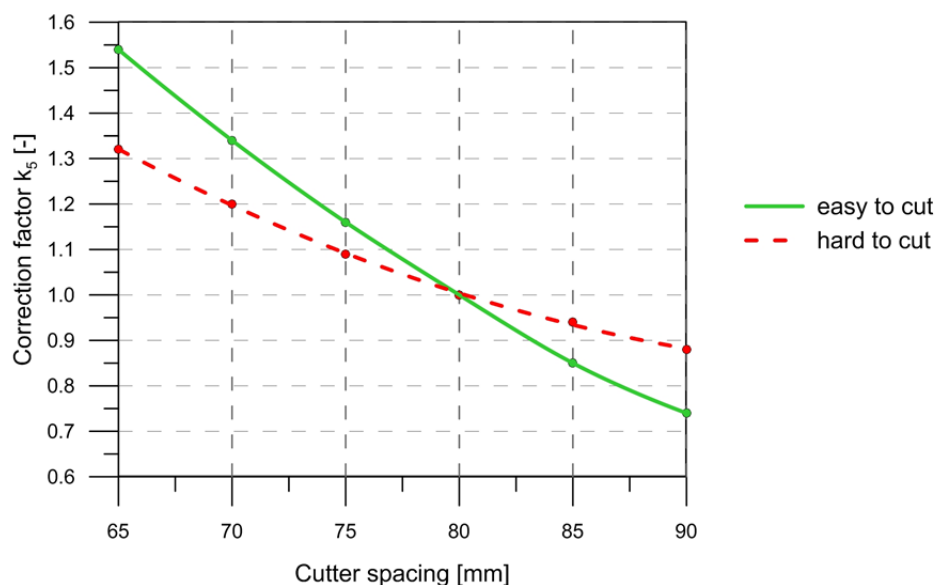


Fig. 9: Correlation diagram of correction factor k_5 and cutter spacing as a function of drillability (mod. from GEHRING 1995: 444).

Weakness and strength of the Gehring model

The basic approach of the model seems very reasonable, but the main weakness is the small data set for GEHRING's original regression analysis. Only four tunnel projects with a certain machine setup, in addition to more research in the literature have been taken into account. The model was developed in the 1990s with literature and data not later than 1995. Since then, tunnel dimension and TBM technique have evolved, developed further suggesting the necessity for revision. Validation with more data from actual tunnel projects is obligatory to develop a new, adapted Gehring model.

The adapted Gehring model leads to the main strength of the model. Because of its modular structure, each correction factor can be considered independent from each other. A factor can be improved and afterwards re-implemented again in the formula. This makes the revision flexible and it can be achieved step by step. The model has an empirical origin which leads to results close to reality and all of the input parameters are easy to determine since they are based on standard laboratory tests.

2.4 Influence of rock toughness on TBM penetration

Toughness, respectively brittleness is an important research topic in rock mechanics and many scientists have been working on a simple way to measure and quantify their findings. However, until now, no standardized definition has been provided. People from different industries use the word toughness to describe different material properties, but even within one sector such as rock mechanics, the term is not consistently used. Moreover, the unanimous opinion is that it is a rock property that is very close to the real fragmentation process and affects excavatability significantly. It is said that cutting or boring tough rock needs a lot more energy than the destruction of brittle rock. But the positive effect of increasing rock brittleness on cutting efficiency is not yet fully understood. Basically rock brittleness is defined by MORLEY (1944) as “the lack of ductility” which means that rock toughness can be defined by the significant amount of ductility and plastic deformation. HUGHES (1972) describes the process of rock cutting as follows. Once the cutting tool is indented into the rock, the introduced energy is converted into strain. If strain energy becomes too excessive, fracturing takes places by propagating pre-existing cracks. This process causes a release of strain energy that is converted into the following:

1. surface energy of freshly formed cracks (GRIFFITH 1921: 165 f)
2. work of plastic deformation in zones adjacent to propagating cracks (esp. ductile material) (OROWAN 1949)
3. kinetic energy of rock fragments (esp. brittle material) (MOTT 1948)
4. chemical reactions in thermally unstable materials (esp. carbonates) (FOX & SORTA-RUIZ 1970)

This means that brittle rocks require less energy to fail as few less energy is absorbed in plastic deformation and more energy remains for kinematic processes such as rock chips to be expelled from the tunnel face.

The aspect of rock brittleness and its influence on the boreability of rocks has been in the focus of researchers for a long time. Due to the lack of information on rock toughness, existing knowledge concerning rock brittleness is analyzed and in a second step transferred to rock toughness in this thesis. Several approaches for defining brittleness indices were developed all over the world (e.g. EVANS & POMEROY 1966, HUCKA & DAS 1974, BRULAND 2000b, YAGIZ 2002, ALTINDAG 2010). Analysis on the influence of rock brittleness on the penetration rate has been carried out by GONG & ZHAO (2007) and KAHRAMAN (2002) focusing on the simplest brittleness index B_1 that is the ratio of uniaxial compressive strength and Brazilian tensile strength. Investigations reveal that there is a strong correlation between penetration rates in TBM tunneling and rock brittleness. Numerical simulations by GONG & ZHAO (2007) based on data from a 42 km long tunnel project in granite shows that with higher brittleness index B_1 the penetration also increases (Fig. 10). This effect is even more obvious for rocks with lower uniaxial compressive strength (Fig. 10, upper line).

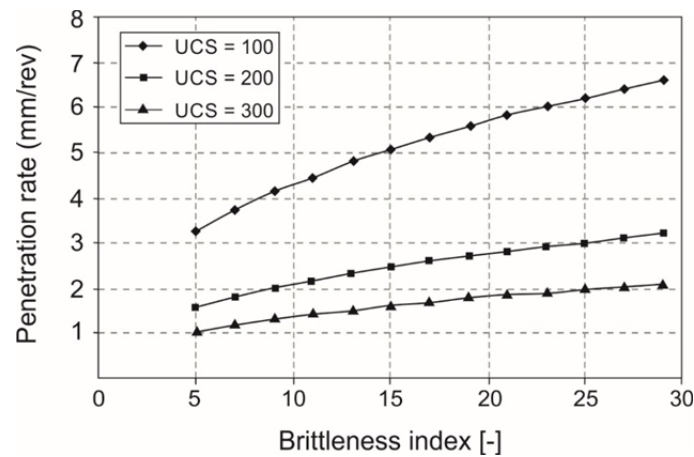


Fig. 10: Penetration rate variations depending on rock brittleness index $B_1 = UCS / BTS$ based on numerical simulations (mod. from GONG & ZHAO 2007: 320).

Numerical modelling of GONG & ZHAO reveals that tough rocks, with a low brittleness index, show less developed crushed zones and the number and length of main cracks outside the crushed zone also decreases. This observation coincides with investigations of BRULAND (2000a). He stated that high brittleness leads to most crack formation and chipping to cutter sides, whereas low brittleness causes less crack formation and chipping. KAHRAMAN (2002: 270) found a strong correlation between penetration rates and brittleness index B_1 in TBM tunneling and rotary drilling. However, the correlation result indicates an inverse tendency meaning that the penetration rate increases with decreasing brittleness. The result is based on model TBM data in different rock types. In addition to rock brittleness, other material or rock mass properties may also influence the penetration rate which leads to uncertainties and reveal the inverse tendency in the results by GONG & ZHAO (2007) and BRULAND (2000a). By performing linear cutting tests, ENTACHER found that cutting brittle rocks result in very irregular force graphs with a number of sudden force drops. These drops are attributed to the formation of rock chips. In contrast, ductile rocks result in smooth force graphs and less rock chip formation took place (ENTACHER 2013: 83ff.).

The abovementioned analysis emphasizes the necessity to investigate rock deformation in more depth in order to gain a better understanding about the influence on penetration rates in TBM tunneling.

On the basis of existent research concerning rock brittleness, this thesis will focus on the contrary term, namely rock toughness. The aim is to provide a consistent definition that enables investigations on the influence of rock toughness on the boreability (penetration rate) in mechanical tunneling, and in a second step, an implementation into penetration prediction models.

The following chapters will give a brief introduction on the deformation behavior of rocks and the term of rock toughness, followed by several definition possibilities.

2.4.1 Deformation behavior of rocks

To understand the mechanical behavior of rocks under load, it is important to analyze the characteristics of rocks from **small scale** (single crystal) to **large scale** (rock mass). Particularly, deformation characteristics of rocks are of interest since they control the resistance against indentation by a cutting tool and thus also the boreability of a rock.

The mechanical properties of a **rock crystal** are defined by its chemical composition and the lattice structure (HAWKES & MELLOR 1970: 184). Depending on the lattice structure, the crystal tends to

glide easily along sliding planes such as mica or calcite crystals do. The gliding process causes a distinct ductile deformation behavior under load and may therefore be related to tough failure. The deformation behavior of crystals under load also associates with their orientation relating to the loading direction.

The next scale is a **rock specimen** for laboratory testing. Here, not only a single crystal defines the deformation behavior under load, but also the way in which they are connected. The petrographic structure includes mineralogical composition, cementing material, grain size/shape and the texture of the rock (HAWKES & MELLOR 1970: 184). Grain size is an important parameter as it controls the length of the predominant defect structure, the so called Griffith crack. This crack leads to failure of the specimen and under uniaxial compression, and it seems likely that the Griffith crack develops within the grain or at grain boundaries (BRACE 1961). If the specimen already shows cracks, sealed joints, or inhomogeneity before testing, the strength may be reduced significantly and cause a certain failure mode. Therefore, these characteristics must be recorded in detail before testing. Special focus should be placed on the orientation of the crystals and, especially for anisotropic rocks, a detailed description of the structure since the orientation highly influences the deformation behavior and strength (THURO 1996). Dealing with sedimentary rocks, density, and porosity seem to be the crucial factors. They appear to have a high correlation with resulting strength and elastic modulus (MORGENSTERN & PHUKAN 1966).

Factors that emerge mainly on a large scale and influence the strength and excavatability of a **rock mass** respectively, are discontinuities and their mechanical properties, alteration processes, stress conditions and water. The strength of a rock mass is hard to determine because parameters that are measured in the laboratory cannot be transferred on a large scale without hesitation. Several approaches exist that attempt to characterize rock mass strength depending on a number of parameters (BIENIAWSKI 1989, HOEK & BROWN 1997, BARTON 2000). However, there is still a high degree of uncertainty that cannot be eliminated.

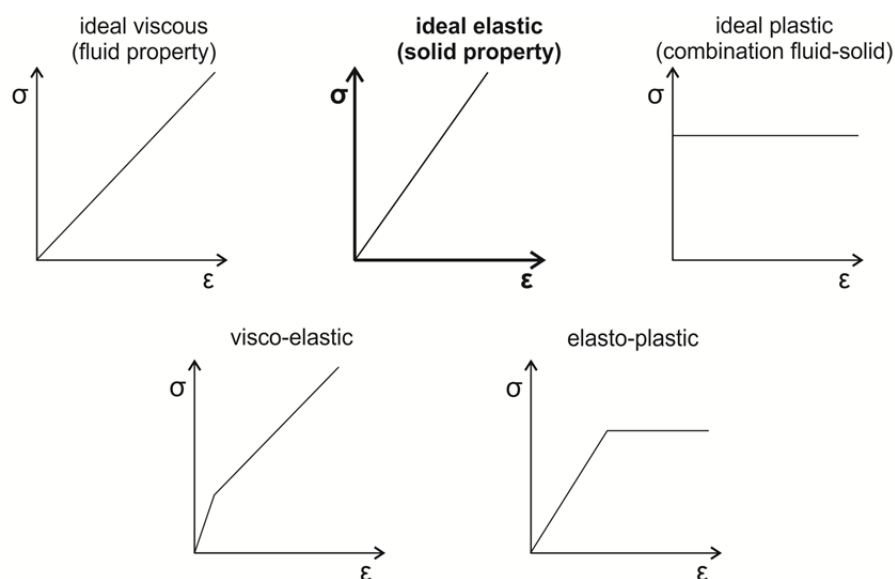


Fig. 11: Schematic stress-strain relations for various rheological models (mod. from HAWKES & MELLOR 1970: 197).

In general, rocks are assumed to behave like elastic material which is why physical approaches to rock mechanics derive from the Theory of Elasticity (Hooke's law) (HAWKES & MELLOR 1970: 195). Since rocks are a product of nature, they are not perfectly isotropic with linear elastic behavior under load. All rock types contain inherent flaws such as cracks, pores, or grain boundaries even before applying a load. Further it must be noted that rocks also possess rheological properties of viscosity and plasticity (Fig. 11). For **ideal elastic material**, the stress is directly proportional to the strain rate up to the failure of the specimen. This mechanical behavior remains constant, irrespective of loading rate or duration. The elastic behavior of rocks is described by the Young's modulus (ratio of axial stress to axial strain) and the Poisson's ratio (ratio of lateral to axial strain) which are directly given by uniaxial compression testing and therefore easy to determine (s. chapter 4.1.1). Actually, **viscosity** is a measure for the resistance of fluids to deformation by shear or tensile stresses. If the fluid layer is very thin, Newton's law is valid contending that stress is directly proportional to strain rate and the deformation proceeds continuously. Under certain conditions, such as high stresses and long testing period, many solids (even rocks) may flow like fluids, although very slowly. Such materials are best described as visco-elastic material. Conversely, **ideal plastic material** remains rigid under load up to a critical stress level. If the critical level is exceeded, the material deforms indefinitely without increasing stress. To characterize the plastic property of rocks, more complex yield criterion using stress tensors are necessary (HAWKES & MELLOR 1970: 196ff.).

Similar to other materials, all rocks show a time and temperature-dependent deformation behavior. If rocks were tested under sufficient stress over **long time**, creeping occurs and no ideal elastic behavior is observed. The process may mathematically best be described by visco-elastic or elasto-plastic models. In the practice of engineering geology and rock mechanics, an application of these models is complicated and not the intention of this work since a commonly used determination of rock toughness is the main focus. In addition, time-dependent behavior recedes into the background for moderate stress rate and standard loading rate (PRANDTL 1928: 86) at which laboratory tests are performed in this thesis.

At **high temperatures**, most materials tend to reveal plastic flow properties which are associated with very high deformation rates. During uniaxial compression, the temperature may be decisive as to whether a brittle or ductile failure occurs, since the ductile-brittle transition temperature is existent for all materials. Experiments performed at higher temperatures lead to an increase of dislocation activity and therefore to ductile deformation behavior (KOLYMBAS 2011: 168). However, the temperature must be significantly higher than room temperature to influence the deformation behavior of rocks. Thus, this aspect may be neglected for further research as all tests were performed at room temperature.

As rocks show only minor percentage of plastic deformation under load, it is mostly neglected when evaluating uniaxial compression tests. The aim of this research is to characterize the amount of plastic deformation that rocks may show under uniaxial compression at normalized testing conditions, since it is the direct link to the term of rock toughness which is described in detail in chapter 2.4.2.

Influence of loading rate on the deformation behavior of rocks

A number of researchers investigated how rocks change their deformation behavior under uniaxial compression when the loading rate is increased towards the recommended one of suggested methods by ISRM (1979) or DGGT (2004). If the loading rate is increased, the duration of the test is decreased and the maximum strength is reached in a shorter time. Since rocks show time-dependence in stress and strain, the variation of loading rate must lead to changes in the deformation behavior. Research that had been performed until the 1980s often resulted in two important findings (HAWKES & MELLOR 1970, MOKHNACHEV & GROMOVA 1969, VUTUKURI et al. 1974, CRUDEN 1974, KOBAYASHI 1971, VARDAR 1977).

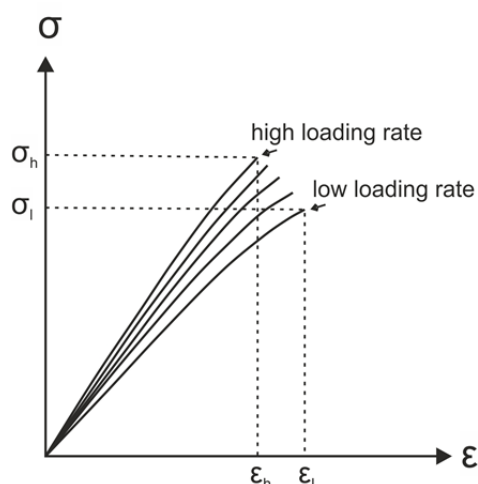


Fig. 12: Influence of loading rate on the uniaxial compressive strength (mod. from VARDAR 1977: 17).

First, it had been noticed that the **uniaxial compressive strength** of rocks increases by applying a higher loading rate (Fig. 12, σ_h). KOBAYASHI (1971) noticed that the increase reveals different dimensions for different rock types (Fig. 13A). The increment of compressive strength is dependent on the porosity of the rock and increases since the porosity decreases (Fig. 13B). This means that sandstone with a porosity of 30 % shows less increase of uniaxial compressive strength than andesite with a porosity of 5 %.

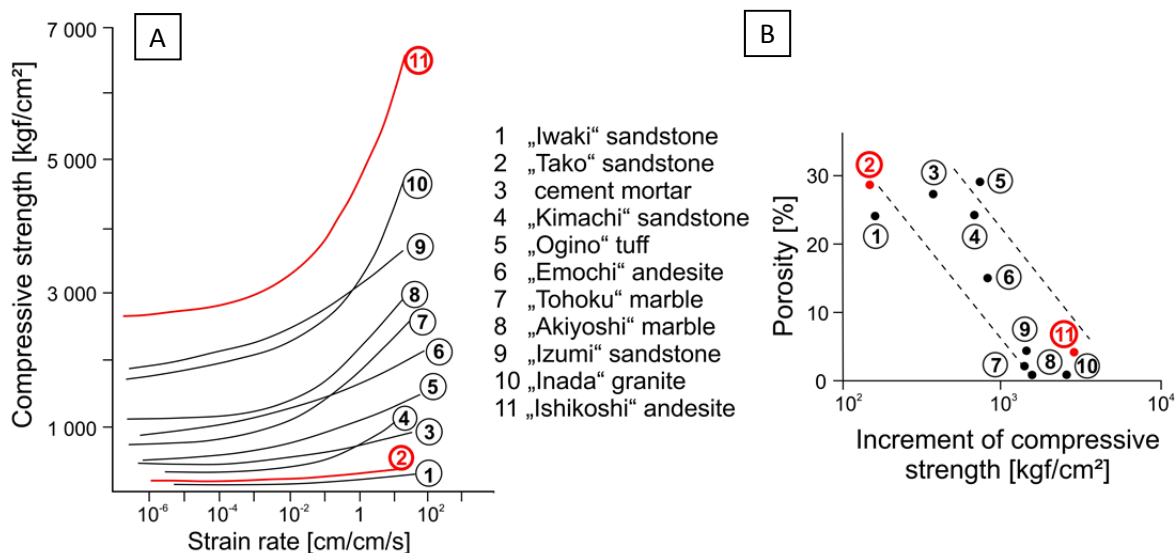


Fig. 13: Variation of compressive strength depending on different loading rates (A). Relation between the increment of compressive strength for different loading rates and the porosity of tested samples (B) (mod. from KOBAYASHI 1971: 169).

Second, also an increase of the **Young's modulus** has been recorded, showing lower total strain rates at the failure of the specimen (Fig. 12, ϵ_h). This means physically, that the rock behaves somehow more elastic since the stress-strain curve displays a straight line. It corresponds to the rheological

model of Maxwell which describes visco-elastic materials and consists of two terms – one for elasticity and one for viscosity. Since viscosity is time-dependent, high loading rates make this term relatively insignificant and only the linear-elastic term is relevant (HAWKES & MELLOR 1970:198). Conversely, low loading rates decrease the general slope of the stress-strain curve and introduce certain curvature. These findings have also been confirmed by research results from the civil engineering sector. MESECK (1987) and HEITFELD (1989) analyzed mechanical properties of diaphragm walls of mineral composition under uniaxial compression. Again increasing uniaxial compressive strengths and Young modulus have been measured at higher loading rates. The tests summarized by VUTUKURI et al. (1974: 44ff.) basically showed the same trend, but also revealed that not all rock types react to the same extent to loading rate variations. For example, an increase of loading rate at limestone samples did not change the Young's modulus at all, whereas sandstone, granite and marble react as described above. This aspect has already been mentioned before by HAWKES & MELLOR (1970). The authors analyzed that dense, hard, and fine-grained rocks are highly elastic, and that only changes of two or three orders of magnitude of loading rate affect the slope of the stress-strain curve. In contrast, some softer rocks such as marble, rock salt and anhydrite may creep quite easily, and doubling the loading rate may cause a significant change in the slope of the stress-strain curve.

The results of more recent investigation agree in terms of changing UCS, but they differ from the prior in terms of Young's modulus (OKUBO et al. 1990, NATAU et al. 1991, MISSBICHLER 1997, LI & XIA 2000). The authors showed that the deformation behavior does not change at varying loading rate. OKUBO et al. (1990) tested five rock types (andesite, tuff, granite, marble and sandstone) via constant strain rates under uniaxial compression at four different loading rates ranging from 10^{-6} to 10^{-3} /s. The loading rate of 10^{-3} /s signifies a strain-controlled speed of 0.01 (mm/mm)/s which corresponds to 0.06 mm/min. Since the samples were only 5 cm long, this loading rate is around twice as high as the standard rate according to ISRM (1978) and DGGT (2004). With increasing loading rate, the uniaxial compressive strength increases and stress-strain curves tend to shift to the right-hand side in the post-failure range (Fig. 14). The gradient of the curve in the pre-failure range does not change meaning that the Young's modulus is more or less constant.

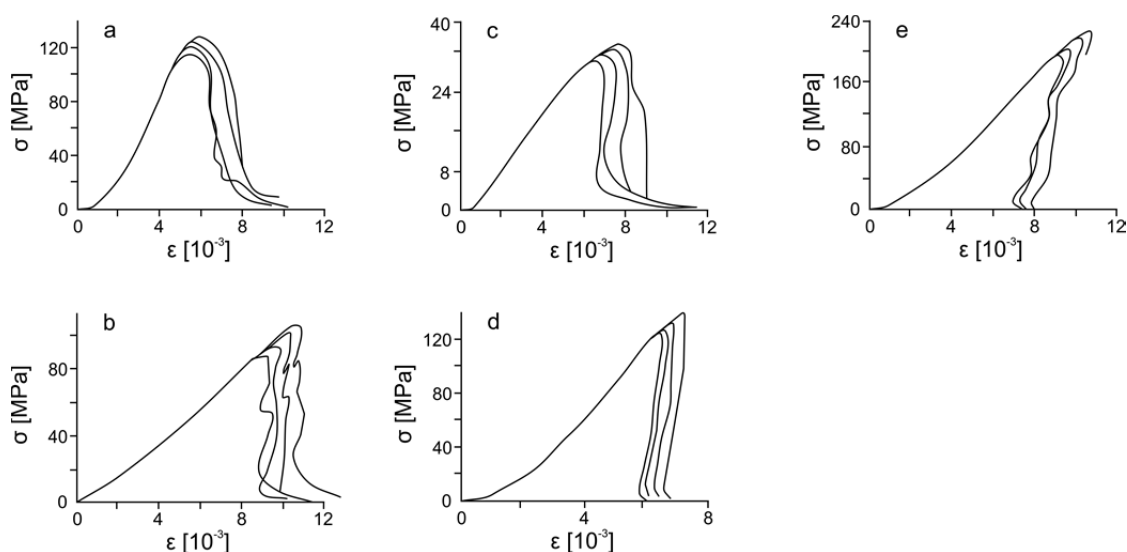


Fig. 14: Loading rate dependence of five rock types: a) marble, b) andesite, c) tuff, d) granite and e) sandstone. Samples were tested at loading rates of 10^{-6} , 10^{-5} , 10^{-4} and 10^{-3} (mm/mm)/s (mod. from OKUBO et al. 1990: 560).

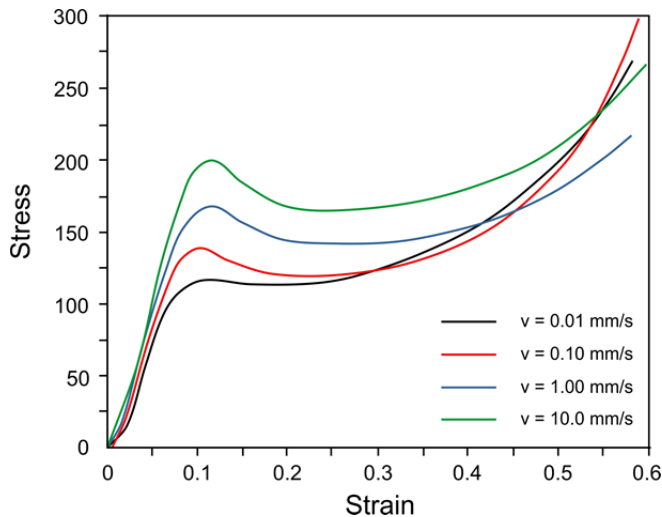


Fig. 15: Stress-strain curves of Plexiglas at four different loading rates (mod. from ZHOU et al. 2013).

The trend also coincides with tests performed by ZHOU et al. (2013) with polymethyl methacrylate (PMMA). The material represents the ideal isotropic medium. Loading rate varies from 0.01 mm/s up to 10 mm/s, and also the post-failure range has also been recorded. With increasing loading rate, the failure stress also increases and the stress-strain curves shift again to the right (Fig. 15). The gradient of the curve in the pre-failure range changes only slightly. The analysis of the post-failure range of tested Plexiglas showed a special property that has not been observed for rock samples. When reaching the failure

load, the stress level decreases only to increase again. This trend is more pronounced for lower loading rates (red and black line, Fig. 15).

The physical process behind time-dependent changes in the deformation behavior of rocks is not well defined, but it is rather likely that thermally activated processes such as vacancy diffusion and dislocation motion cause a deformation of the crystal lattice and grain boundaries may be displaced (HAWKES & MELLOR 1970). Therefore, a creeping of the material without crack formation is possible and the rock may behave more plastically at lower loading rates. SCHOLZ (1968) showed that even brittle rocks such as granite may creep at certain loading rates due to progressive internal cracking.

To guarantee a correct determination of deformation characteristics (Young's modulus) during compression, it is stated that the testing speed should be high enough to eliminate creeping and low enough to prevent thermal effects of contraction (ASTM 2010). This statement takes into account that during the compression, the rock changes its physical system which corresponds with the production of heat. If the compression test is performed too quickly, the heat cannot be transferred to the surrounding area and the system is adiabatically isolated. This may enhance thermal effects such as lattice deformation. However, it must be noted that exactly this process may occur during the excavation of rocks by TBM since the loading rates are around 1,000 times as high as the standard loading rate in the laboratory. Consequently, it is questionable if the investigation in the laboratory by uniaxial compression can be transferred properly to the loading conditions rocks are exposed during excavation.

Next to the change in the deformation behavior under uniaxial compression, MARTIN (1993) and SANGHA & DHIR (1972) showed a correlation of loading rate to modes of failure. Highest loading strain rates (2.5×10^{-3} /s) reveal consistent shear failure modes with clear evidence of sliding, planar surface and no slab formation. With decreasing loading rates, the size and number of slabs increased. At lowest loading rate (2.5×10^{-8} /s), samples mostly show failure by axial splitting and a high number of slabs. In this case, the least consistency in the failure modes could also be observed.

This may perhaps also coincide with the results by BASU et al. (2013: 461), who found a correlation of failure modes depending on uniaxial compressive strength. It was observed that the same rock type showed predominant axial splitting for lower UCS and shearing along a single plane for higher UCS.

2.4.2 Rock toughness – a brief introduction

Toughness describes the resistance of rocks against indentation, destruction and subsequently also against excavation by cutting or boring tools. ‘**Tough**’ behavior may be equated with the term ‘**ductile**’ and characterizes rocks that reveal appreciable plastic deformation under load (BIENIAWSKI 1967: 412). The opposite term is brittle which means that the rock behaves elastically up to failure and exhibits minor plastic deformation.

At **microscopic scale**, tough deformation behavior is caused either by dislocations, meaning crystallographic defects in the lattice structure or by minerals with existing cleavage planes and a tendency to glide along these (TAYLOR 1934). The minerals have a strong capacity of absorbing the introduced energy and initially responding by plastic deformation without actual failure of the crystal. Typical representatives are mica, feldspar, calcite, gypsum, anhydrite, and amphibole, or pyroxene. At **macroscopic scale**, tough failure may be caused if rocks possess a high percentage of the abovementioned minerals. Plastic deformation often takes place even if only one distinct layer of these minerals (e.g. mica) acts as anisotropy. Correspondingly, crack propagation mainly occurs along such layers. Of major importance is the size and percentage of cleavable minerals in relation to the surrounding rock matrix. It may be decisive whether a rock behaves tough or brittle like, for instance, augen gneiss with a porphyroblastic structure of coarse grained cleavable feldspar minerals in fine grained matrix. Another important factor at macroscopic scale is the bonding between the minerals since rocks are regarded as polycrystalline material (HAWKES & MELLOR 1970: 186). If individual grains show a strong bonding among each other, the mobility and dislocation activity is hindered. If the bonding is weaker, individual grains may glide along each other, or porous spaces are compressed and subsequently closed like it does with porous sandstones (KOLYMBAS 2011: 168). This correlates with an energy consuming process and plastic deformation. Such plastic, i.e., tough deformation behavior can be observed clearly by the results from uniaxial compression tests which reveal the deformation behavior of rock under load. In this manner, it is obvious that two different failure behaviors exist (Fig. 16). This topic had been in the focus of researchers over a long period, each of them designating it in different manner. It is the fact that there are rock types that somehow react in a ductile way, and show relatively high plastic deformation even after the maximum strength σ_u is reached (Fig. 16 A). This deformation behavior is accompanied by high energy consumption to cause final fracture of the rock and can be associated with rock toughness. The term toughness is contrary to rock brittleness. Brittle rocks reveal a violent rupture directly after maximum strength σ_u is reached due to an explosive propagation of cracks (Fig. 16 B) (OBERT & DUVALL 1967). Transferring the findings of HUCKA & DAS (1974: 389) concerning rock brittleness to rock toughness, the following statements can be made to characterize tough rocks:

- high values of elongation
- post-failure fracture
- reduced formation of crushed material
- reduced formation of cracks in indentation
- low ratio of compressive to tensile strength

The following figure shows two schematic stress-strain curves, whereby each of them stands for either typical tough (A) or typical brittle (B) failure behavior.

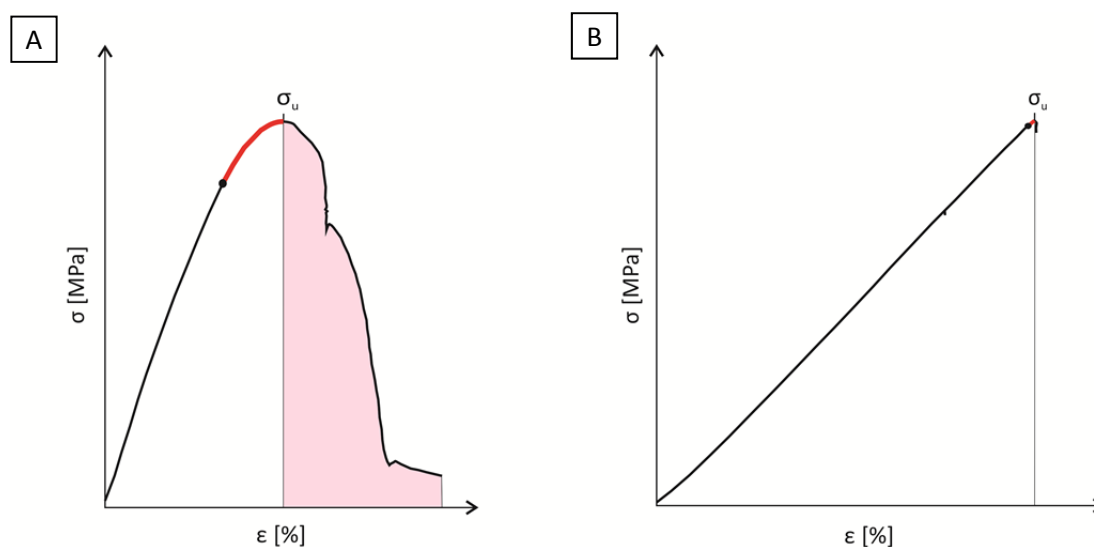


Fig. 16: Schematic stress-strain curves: A) typical tough failure behavior with high plastic deformation (red line) and distinct post-failure range (red area) and B) typical brittle failure behavior with infinitesimal plastic deformation and no post-failure range.

To define rock toughness respectively brittleness, a number of approaches exist, none of them gaining complete acceptance among experts. Three different basic concepts were favored during experimental time within which various different approaches exist. The basic ideas are transferred from definitions of rock brittleness and are as follows.

1. Toughness definition: **strain** or **energy** based approach
2. Toughness definition: **strength** based approach
3. Toughness definition: **special test** based approach

All principles have their strengths and weaknesses which are explained in detail in the following chapters. To briefly summarize, the approach via analyzing the deformation behavior under uniaxial compression is referred to be the more precise method, but requires a more complicated measurement system and data evaluation. In contrast, the ratio of compressive to tensile strength can be determined by performing two standard laboratory tests without any profound data analysis and can be used more extensive. A special test based approach has its constraints in terms of a wide used application since most of the existing tests are only applied in certain countries, and not worldwide.

2.4.3 Toughness definition – strain and energy based approach

The deformation behavior of rocks under load has been subject to a wide array of research, but analysis in the past mainly focused on the deformation behavior and fracture mechanisms of brittle rocks such as the research conducted by BIENIAWSKI (1967), MARTIN (1993), EBERHARDT (1998), AMANN et al. (2011), and many more. Their results are used as a framework for interpreting tough failure behavior. During unconfined compression, the rock passes through several stages of deformation depending on lateral, axial and volumetric strain. Lateral and axial strain values are recorded during uniaxial compression, whereas volumetric strain is calculated on the basis of lateral and axial strain measurements (s. Fig. 17). A detailed description of the testing methodology follows in chapter 4.1.1.

The deformation stages have been analyzed already in the 1970s by BRACE (1964) and BIENIAWSKI (1967):

1. Crack closure

Existing microcracks or flaws in the rock specimen, orientated at a certain angle to applied load, are closed. The extent of this stage is dependent on the initial crack density and crack geometry. This part of the stress-strain curve is nonlinear exhibiting an increase in deformation modulus which is represented by axial stiffness (EBERHARDT 1998: 225).

2. Linear elastic region

Once the existing cracks are closed, ideal elastic deformation occurs. Hereby the stress is directly proportional to the axial strain resulting in a linear portion of the axial stress-strain curve which is used to calculate elastic constants such as the Young's modulus (s. chapter 4.1.1).

3. Stable crack growth

Stable crack growth describes the region where progressive cracking takes place and new microcracks are formed. The formation of cracks is accompanied with the beginning of plastic deformation. At stable crack growth, the portion of plastic deformation is insignificant compared to elastic deformation and is therefore often neglected. The stress threshold between the elastic region and beginning crack propagation is called **crack initiation** σ_{ci} . In this deformation stage, cracks propagate in a stable manner and the growth can be stopped by controlling the applied load. This means that no failure of the specimen will occur and further load is required to cause final rupture. The cracks propagate parallel to the direction of the applied load which is indicated by the fact that mainly lateral strain measurements notice the cracking (MARTIN 1993: 90). The cracks are observed primarily within individual grains (cleavage planes) and no trans-granular cracks are noticed. The authors showed that cracks start to form at around 35 % of uniaxial compressive strength σ_u and it may be correlated with a stress level that is about eight times the Brazilian tensile strength σ_t .

4. Unstable crack growth

This stage marks the beginning of unstable crack propagation and sample dilatancy which subsequently leads to irreversible damage. Failure of the specimen is self-maintaining since the crack growth would continue even if the applied load is kept constant. The stress threshold between the stable and unstable crack growth is called **crack damage** σ_{cd} and coincides with the critical value of energy release. In this deformation stage, the axial stress-strain curve departs from linearity, and plastic deformation is the defining factor. This is caused by the introduction of shearing element and that sliding is now initiated along mineral cleavage cracks, flaws or grain boundaries. The cracks must grow parallel and inclined to the applied load since both, lateral and axial strain measurements notice cracking. This results in nonlinear behavior (MARTIN 1993: 90). It has been noted that exceeding the crack damage stress level results in an abrupt development of finite frictional slipping along flaws and grain boundaries (BOMBOLAKIS 1973). At this phase, the most significant changes in the structure of the sample take place, the density of microcracks increase by about sevenfold, and cracks also cross grain boundaries leading to a shattering of grains (HALLBAUER et al. 1973). This can be determined by simultaneous acoustic emission measurement which counts acoustic events that are caused by newly formed cracks. The authors showed that unstable crack propagation starts around 80 % of uniaxial compressive strength σ_u . The crack damage threshold σ_{cd} is one of the most important parameters

characterizing rock toughness since it determines the departure of the linear axial stress-strain curve and marks the beginning of **plastic deformation**. Furthermore, crack initiation σ_{ci} and crack damage σ_{cd} were found to be characteristic material properties that are independent of testing conditions (specimen shape, loading platens, and loading machine) contrary to the uniaxial compressive strength σ_u (MARTIN 1993: 91).

5. Post-failure range

This term describes the deformation stage after the maximum stress level is reached. Axial stress decreases, but axial and lateral strain still increases up to the maximum value. The threshold between unstable crack growth and post-failure range is set by the **uniaxial compressive strength σ_u** . A special feature in this deformation stage is the phenomenon of crack forking, meaning the splitting of one crack into two or more. It occurs if the maximum crack velocity is reached which is mostly the case at uniaxial compressive strength. Although distinctive damage occurs within the rock sample, certain strength and cohesion is maintained. Finally, the coalescence of crack forking, which runs intra and trans-granular, leads to macrocracks, rupture, and complete disintegration of the specimen. The process of crack coalescence is more dependent on the structure of the rock rather than on the material property. The point of rupture is therefore a significant parameter for the characterization of the stability of rock structure. The post-failure range is the part of the stress-strain curve that not all rock types must reveal. A post-failure part is existent and decisive for tough rocks and is nearly absent for brittle rocks. Tests performed by BIENIAWSKI show that the record of this phenomenon is highly affected by the testing machine, especially its stiffness.

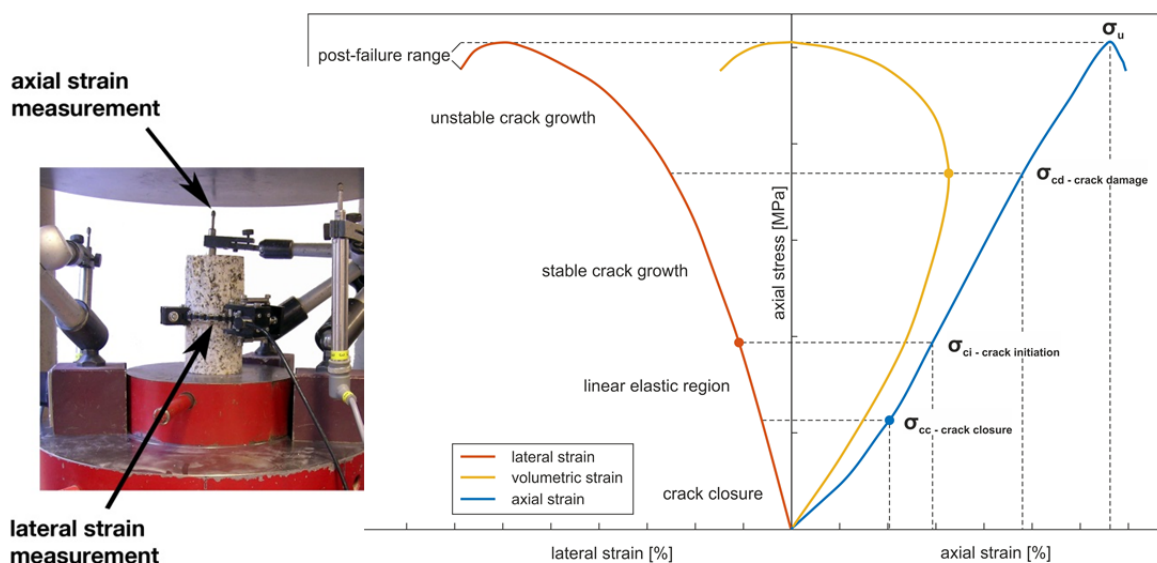


Fig. 17: Stress-strain diagram of a uniaxial compression test showing lateral, volumetric, axial strain and corresponding thresholds for crack closure, crack initiation, and crack damage (mod. from MARTIN 1993:77). In addition, the deformation stages according to BIENIAWSKI (1967) are plotted.

The detailed determination of the abovementioned thresholds and corresponding deformation stages is explained in chapter 4.1.1 at the data analysis of uniaxial compression tests. The following paragraphs will explain the current state of research concerning the two decisive parameters that may characterize rock toughness. These are, on the one hand, the existence of certain plastic deformation, and on the other hand, distinct post-failure range.

2.4.3.1 Strain based approach – parameter plastic deformation

Over a long period of time investigations on the deformation behavior of rocks have concentrated on characterizing brittle failure (BRACE 1964, HOEK & BIENIAWSKI 1965, BIENIAWSKI 1967, WAWERSIK & FAIRHURST 1970, BARRON 1971, HUCKA & DAS 1974, ANDREEV 1995, EBERHARDT 1998, ALTINDAG 2010, AMANN et al. 2011). Research trying to analyze the plastic deformation and tough failure in detail is very limited. Findings from investigations on brittle failure are therefore transferred to tough failure behavior in the following paragraph.

The existence of significant plastic deformation coincides with a process that requires more input energy to reach certain stress level since the slope of the stress-strain curve becomes flatter. Thus the pre-failure part of the axial stress-strain curve can roughly be divided into three different curve sections (Fig. 18). Section A equates to the crack closure part. The shape of the curve is nonlinear and elastic deformation takes place. Section B merges the region of linear elasticity and stable crack propagation. The curve shape is more or less linear and since the formation of cracks is reversible, the deformation is elastic with infinitesimal plastic deformation. This behavior can also be described as elasto-plastic. Section C describes the part of unstable crack growth and irreversible formation of cracks. The shape of the curve is nonlinear and plastic deformation occurs to a large extent.

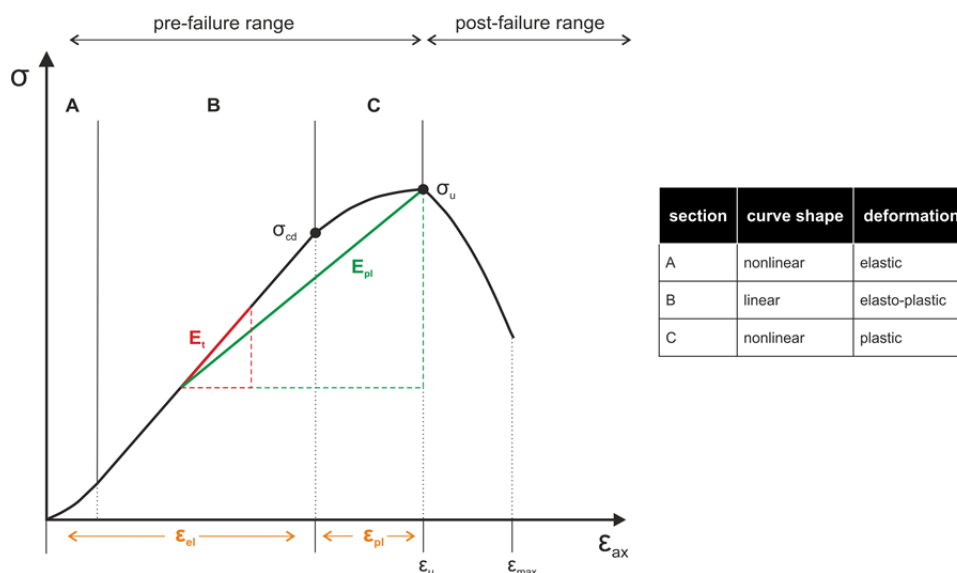


Fig. 18: Schematic stress-strain curve showing three different curve sections A-C. In addition, elastic / plastic deformation ranges (orange) and corresponding elasticity moduli E_t (red) and E_{pl} (green) are plotted.

To classify rock toughness in terms of plastic deformation two approaches are presented below.

Direct method by strain measurements

The crack damage threshold σ_{cd} marks the beginning of plastic deformation (Fig. 18). It can be calculated by a combined analysis of lateral and axial strain measurements during uniaxial compression. The detail data evaluation can be read in chapter 4.1.1 and in publications by BIENIAWSKI (1967), MARTIN (1993) and EBERHARDT (1998). In this way, the amount of plastic strain ϵ_{pl} relative to elastic strain ϵ_e can be directly determined. This approach has already been described by HUCKA & DAS (1974) for defining rock brittleness.

HANDIN (1966) and ANDREEV (1995) proposed a classification that describes whether a rock type behaves brittle or ductile, i.e., tough. It depends on the total axial strain which occurs until peak stress is reached. Both authors' conclusions resulted in different threshold values for brittle-ductile transition. One weakness of this approach is that it is an absolute index based on the absolute measured axial strain. This means that different specimen sizes are not considered and the classification thresholds are possibly not transferrable to recent testing techniques and results. Therefore, the classification method has never gained wide acceptance, but the aspect of total strain is subject to further research (s. chapter 5.1.3).

Indirect method by deformation moduli

An indirect method of determining the amount of plastic deformation is to calculate the slope of the stress-strain curve (Fig. 18, red and green). As a reference, the method for calculating the tangent Young's modulus E_t is used (ISRM 1979) which characterizes the slope between 40 % and 60 % of uniaxial compressive strength. To include the plastic deformation range, the modulus E_{pl} is calculated from 40 % to 100% in this thesis. The deformation modulus E_{pl} has not yet been mentioned in the literature in exactly this form, but may be attributed to the modulus of compressibility in soil mechanics which describes the nonlinear part of the stress-displacement curve (DIN 18135).

The indirect method by deformation moduli allows the determination of three different shapes of stress-strain curves attributed to distinct rock categories by VUTUKURI et al. (1974). **Type A** reveals ideal elastic behavior until failure and the E_t and E_{pl} modulus are the same. The behavior is typical for eruptive rock types (e.g. basalt) and very fine grained, hard rocks such as limestone or quartzite. Type A can be equated to brittle failure. **Type B** shows a concave shape. Here the deformation modulus is highest in the beginning and decreases continuously. Therefore, the E_t modulus is higher than the E_{pl} modulus and the behavior is called 'strain-softening'. It is often observed for tough rocks such as tuff, schist, and silt, or clay stones. Additionally, samples with lamination resp. foliation parallel to the loading direction, reveal Typ B. **Type C** is of convex shape and the deformation modulus is lowest in the beginning, but increases continuously until failure. Therefore, the E_t modulus is lower than the E_{pl} modulus and the behavior is called 'strain-hardening'. It is typical for rocks that react brittle and even before failure, no flattening of the curve which indicates plastic deformation, occurs. Also samples that are testes normal to existing lamination or foliation react with type C behavior. Most often, rocks fail under uniaxial compression by a combination of all three types, but the categories are useful for basic classification of brittle or tough failure behavior.

The sole value of the Young's modulus may be an indicator for the toughness of rocks against blasting. LEINS et al. (1973) found that the higher the Young's modulus the lower the toughness is. The authors stated that high Young's moduli (such as for basalt) are caused by dense lattice structure and strong bonding which reduce rock toughness.

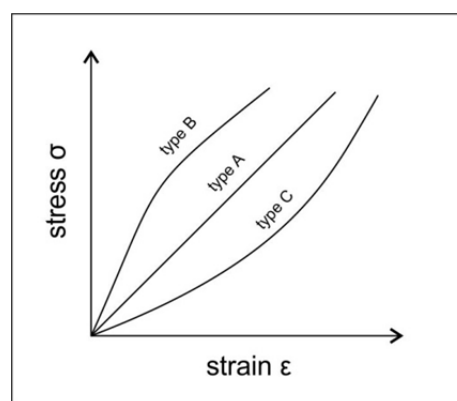


Fig. 19: Three schematic shapes of stress-strain curves belonging to different rock categories (mod. VUTUKURI et al. 1974).

2.4.3.2 Energy based approach – parameter post-failure region

The post-failure region has been in the focus of researchers since the 1960s. At this time, the main problem was the testing technology. Most of the testing machines were not able to record the range after maximum strength was reached, since release of excess energy from the testing machine led to a sudden and abrupt failure of the rock specimen (WAWERSIK & FAIRHURST 1970: 561). To solve this problem, stiff or servo-controlled machines have been used since then. If a machine is not sufficiently stiff, the elastic energy that is stored in the machine is released abruptly when the specimen reaches maximum stress. This means that the loading platens accelerate with a high velocity and the rock specimen is destroyed explosively. Nowadays, servo-controlled machines have become prevalent since this type allows higher flexibility of controlling the test. If the machine has a fast response time, a stable failure process in the post-failure range can be achieved and the stress-strain curve is recorded properly.

A number of researchers (e. g. WAWERSIK & FAIRHURST 1970, BIENIAWSKI 1967, BARRON 1971, VUTUKURI et al. 1974) noticed two different failure behaviors under uniaxial compression and attributed it as follows (Fig. 20):

- **Class I behavior:** After exceeding maximum load bearing capacity of the specimen, still more energy must be exerted to cause final failure and rupture of the specimen. Hence, these rocks retain a certain strength even after the compressive strength is reached and axial strain still increases.
- **Class II behavior:** After exceeding maximum load bearing capacity of the specimen, the amount of energy stored in the sample is sufficient to maintain crack propagation and growth until the specimen has lost virtually all strength. Hence, these rocks lose all their strength after compressive strength is reached and axial strain decreases.

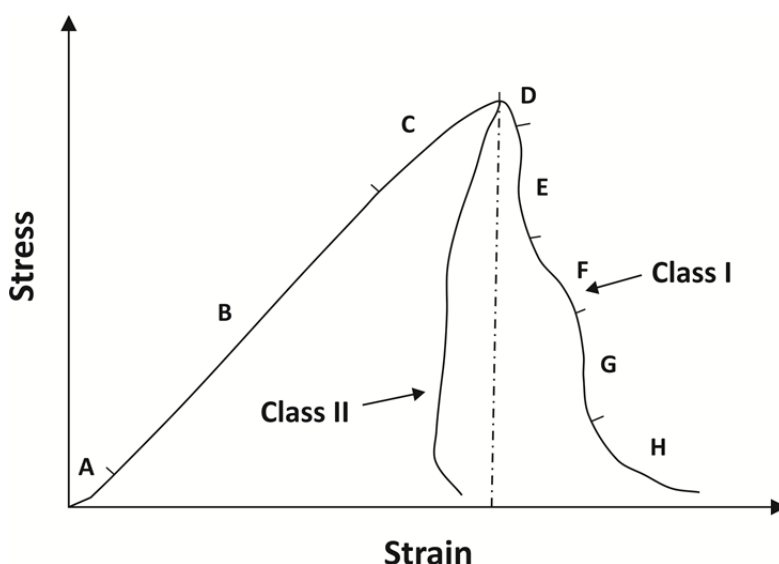


Fig. 20: Schematic stress-strain curves for class I and class II rock failure behavior in uniaxial compression (mod. from WAWERSIK & FAIRHURST 1970: Fig. 12).

VUTUKURI et al. (1974) already associated class I behavior to tough failure, followed by THURO (1996). Class II behavior is associated with brittle failure. But the results from former tests reveal significant difference concerning class II behavior compared to recent tests. Investigations from WAWERSIK & FAIRHURST (1970) showed that some rock specimens fail revealing a decrease in stress and strain which means that energy is released from the system. This energy could not be stored only in the specimen, but must also be derive from the testing machine. The process of energy release is only possible when elastic strain is stored in the testing machine during loading which is the case with machines that are too soft. This means that even WAWERSIK & FAIRHURST may have used a testing machine that was not stiff enough to record the post-failure range properly. Nowadays, class II behavior can be reflected by stress-strain curves like Fig. 16B, where the stress decreases abruptly after maximum strength, but strain remains more or less constant. HUDSON et al. 1971 found that specimen size and shape has a significant influence on the shape of the post-failure curve. The higher the length to diameter (l/d) ratio is, the lower is the maximum strain rate and the post-failure range is less pronounced. Marble specimens with (l/d) ratios of 1 result in maximum axial strain of 10^{-7} , whereas ratios of 3 reveal maximum strain of 10^{-3} . The size effect has less influence. It has been noted by the authors that specimens with larger diameters show steeper post-failure curves than smaller samples. To classify the post-failure range, two different approaches are worth mentioning.

Aspect of energy consumption

The analysis of the energy needed to cause final failure of the specimen is one of the most meaningful approaches. This can be achieved by the determination of the **destruction work W_z** (THURO 1996: 58). Compared to failure work, this parameter also accounts for the post-failure region (Fig. 21). Determination of the parameters is explained in chapter 4.1.1. The concept of considering the energy needed to cause failure has already been mentioned by HUGHES (1972) and GEHRING (1995) (specific failure energy), but focusing only on the pre-failure range. HUCKA & DAS already described a method in 1974 to determine rock brittleness by using the parameter of energy consumption. The aspect of energy seems meaningful in providing a link to excavatability of rocks. TEALE (1965), GEHRING (1995) and THURO (1996) found a significant correlation of specific failure energy, i.e., destruction work with drillability. Since the existence of a post-failure region stands for profounder stability of the rock structure (BIENIAWSKI 1967: 421), tough rocks reveal certain resistance against destruction and are thus harder to drill. This fact can best be described with the parameter of destruction work W_z .

Aspect of curve slope

A second approach is to analyze the slope of the stress-strain curve in the post-failure region similar to the deformation modulus in the pre-failure region (Young's modulus). The **post-failure modulus P_f** is therefore calculated by means of a regression line in the range between maximum strength and final failure of the specimen (Fig. 21). This method is often imprecise and not suitable for a detailed definition of the post-failure range. However, JAEGER & COOK (1979) already described the slope of the descending stress-strain curve in the post-failure range as mark for rock brittleness.

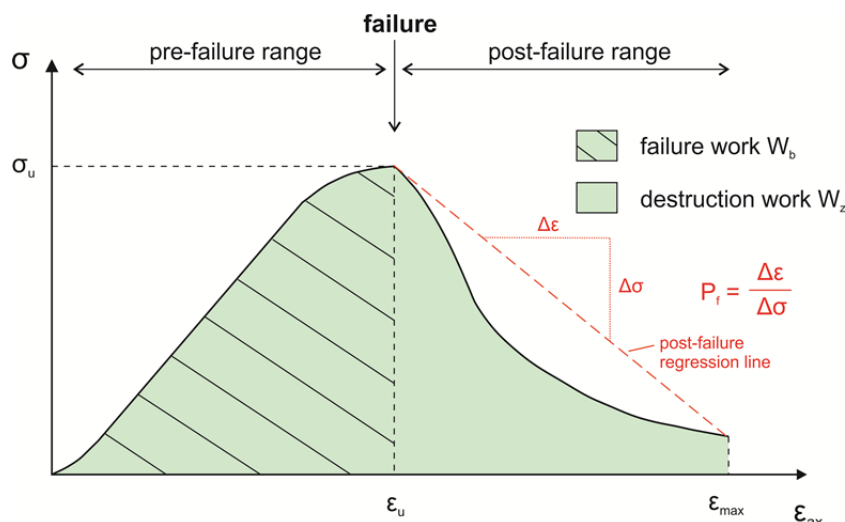


Fig. 21: Schematic stress-strain curve including the parameters of failure work W_b , destruction work W_z and post-failure modulus P_f .

In conclusion, the post-failure range is a distinct marker for characterizing rock toughness. The main problem with this approach might be the correct measurement and determination since it heavily depends on the testing machine.

2.4.4 Toughness definition – strength based approach

In engineering analysis, strength based approaches are often used to define rock toughness. The required parameters are mostly based on standard laboratory tests, are simply defined and easy to obtain. Various definition possibilities are based on the ratio of strength parameters from two different laboratory tests.

Ratio of uniaxial compressive strength to Brazilian tensile strength

The ratio of uniaxial compressive strength to Brazilian tensile strength must be most suitable theoretically to characterize the toughness or rather the resistance of rocks against cutting. Exemplary rock specimens of each test with a tough rock type (calcareous mica schist) are illustrated in Fig. 22. The detailed methodology of both testing procedures follows in chapter 4.1.1 and 4.1.2.



Fig. 22: Rock specimens of calcareous mica schist as representative of a tough rock type after uniaxial compression testing and Brazilian tensile testing. The ratio of UCS and BTS can be used to classify rock toughness.

The ratio combines both parameters that influence the fragmentation process of rock by disc cutters. On the one hand, the uniaxial compressive strength is decisive for the first indentation into the rock and the formation of a crushed zone. On the other hand, tensile cracks are responsible for the formation of rock chips. Both processes combined lead to effective rock cutting. Furthermore, HUCKA & DAS (1974: 390) observed that the difference between compressive and tensile strength increases with increasing brittleness. Therefore, the ratio is one of the most often used tools to classify rock brittleness and is transferred to rock toughness in this work. It has been described by EVANS & POMEROY (1966) and HUDSON (1993) in two different ways named brittleness index B_1 and B_2 (Eq. 2-22, Eq. 2-23). ALTINDAG (2003) modified existing definitions leading to a third determination possibility B_3 (Eq. 2-24). SCHIMAZEK & KNATZ (1976) were the first to also use term B_1 for rock toughness and published a corresponding classification system with thresholds for tough to brittle behavior based on the Z-coefficient (*Zähigkeit* = German for toughness) which is equal to B_1 . This classification has been extended by THURO (1996) (Tab. 6). Existing brittleness coefficients are renamed to fit to the aspect of rock toughness. B_1 is described as T_z since it is based on the Z-coefficient. B_2 is named T_d since it is calculated using the difference of compressive and tensile strength and B_3 is described as T_e since it accounts for the specific energy (s. Fig. 23).

$$B_1 = Z = \frac{\sigma_u}{\sigma_t} = T_z \quad \text{Eq. 2-22}$$

$$B_2 = \frac{\sigma_u - \sigma_t}{\sigma_u + \sigma_t} = T_d \quad \text{Eq. 2-23}$$

$$B_3 = \frac{\sigma_u \cdot \sigma_t}{2} = T_e \quad \text{Eq. 2-24}$$

B_i	brittleness coefficients [-]
T_i	toughness coefficients [-]
σ_u	uniaxial compressive strength [MPa]
σ_t	Brazilian tensile strength [MPa]

Tab. 6: Toughness classification depending on the ratio of uniaxial compressive strength to Brazilian tensile strength (SCHIMAZEK & KNATZ 1976, extended by THURO 1996).

Rock toughness $T_1 = Z = \sigma_u / \sigma_t$ [-]	Classification
< 5	very tough
5 – 10	tough
10 - 20	brittle
> 20	very brittle

Linking the existent definitions of B_1 and B_2 to the topic of rock cutting, one might notice the occurring problem. Clay stone may result in the same brittleness ratio than basalt, for example. However, everyone is well aware that cutting basalt requires more energy than cutting claystone. To solve this problem, ALTINDAG (2003) developed B_3 which considers the area under the $\sigma_u - \sigma_t$ relation line and

not the slope (Fig. 23). This brittleness index should therefore account for the specific energy needed to cut rocks.

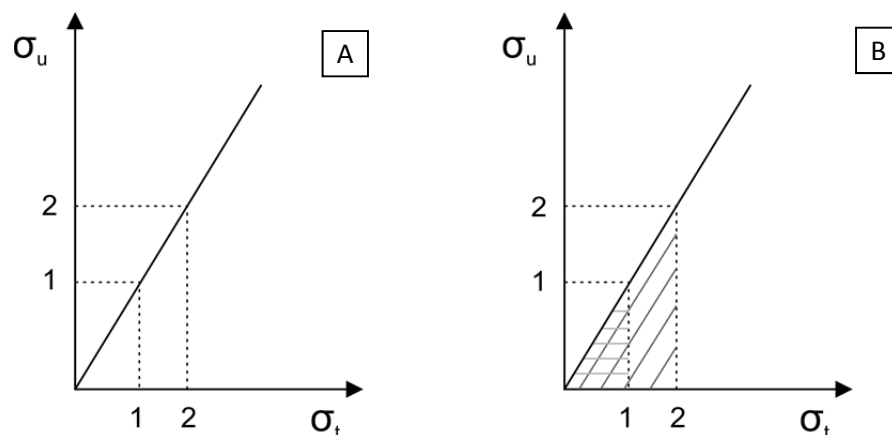


Fig. 23: Relation between compressive and tensile strength of rock. A) concept considering the slope of relation line; B) concept considering the area under the relation line (mod. from ALTINDAG 2003: Fig. 1).

Ratio of uniaxial compressive strength to point load index

Dividing the uniaxial compressive strength σ_u by the point load index I_s results in the **correction factor c** (Eq. 2-25). Fig. 24 illustrates exemplary rock specimens (basalt) of both testing methods that show typical brittle failure behavior. A detailed testing procedure follows in chapter 4.1.1 and 4.1.3.

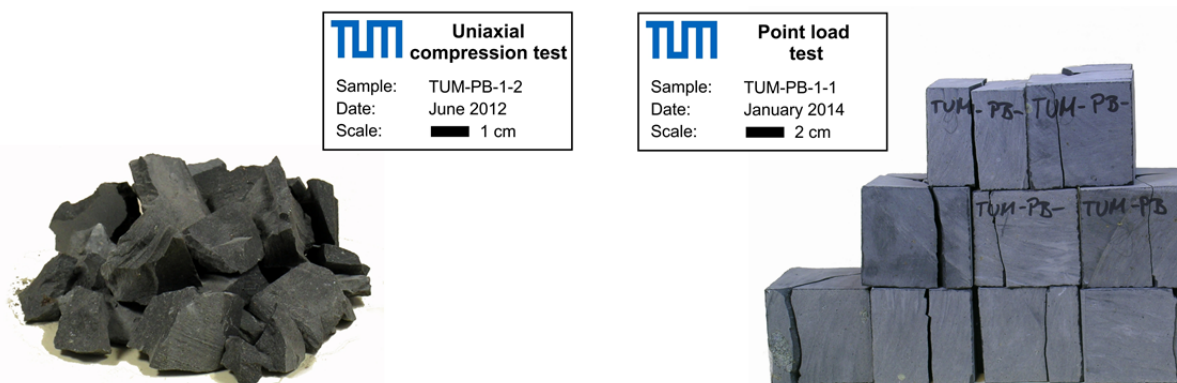


Fig. 24: Rock specimens of basalt as representative of a brittle rock type after uniaxial compression testing and point load testing. The ratio of UCS and I_s can be used to classify rock toughness.

This factor is mainly used to predict uniaxial compressive strength by the point load test which is easier to perform and a quick indirect testing method. KLEIN et al. (1995) and BARTON (2000) found another considerable coherence between both parameters. The authors pointed out the important role of tensile strength of rocks on the penetration rate which is hereby expressed by the point load index I_{50} . TBM data analysis reveals that low UCS/ I_{50} ratio results in low penetration rates and a low boreability class. The authors found evidence that this ratio describes the toughness of rocks and their resistance to the boring process. Ratios lower than the suggested conversion factor $c = 20-25$ (ISRM 1985) respectively $c = 20$ (DGGT in prep., THURO & PLINNINGER 2001), can be classified as tough and hard to bore, whereas higher ratios can be described as easy to bore (BARTON 2000: 28).

$$c = \frac{\sigma_u}{I_s} = T_{PLT} \quad \text{Eq. 2-25}$$

c	correction factor [-]
T_{PLT}	toughness coefficient point load test [-]
σ_u	uniaxial compressive strength [MPa]
I_s	point load index [MPa]

2.4.5 Toughness definition – special test based approach

Rock brittleness, or as the case may be, toughness can also be determined by several special tests that should reflect the destruction mechanisms occurring during the excavation by cutting or drilling tools. This chapter summarizes the most important laboratory tests for brittleness characterization which can be roughly divided into impact and rotary tests.

Impact test (brittleness value S_{20} , punch penetration index)

Impact tests reveal the resistance of rocks against indentation by an impactor tool. It is of interest for penetration prediction since the indentation into the rock is the first step to achieve effective rock cutting.

The first test that is used to obtain information about the impact resistance is the **brittleness test** developed in northern Europe (Fig. 25A). The test gives a good measure for the ability of rock to resist crushing by repeated impacts of an indenter (BRULAND 2000d: 8ff.). After 20 impacts, the percentage of fine grained material is determined leading to the brittleness value S_{20} . This value is commonly used in Norway and is also implemented in the NTNU prediction model.

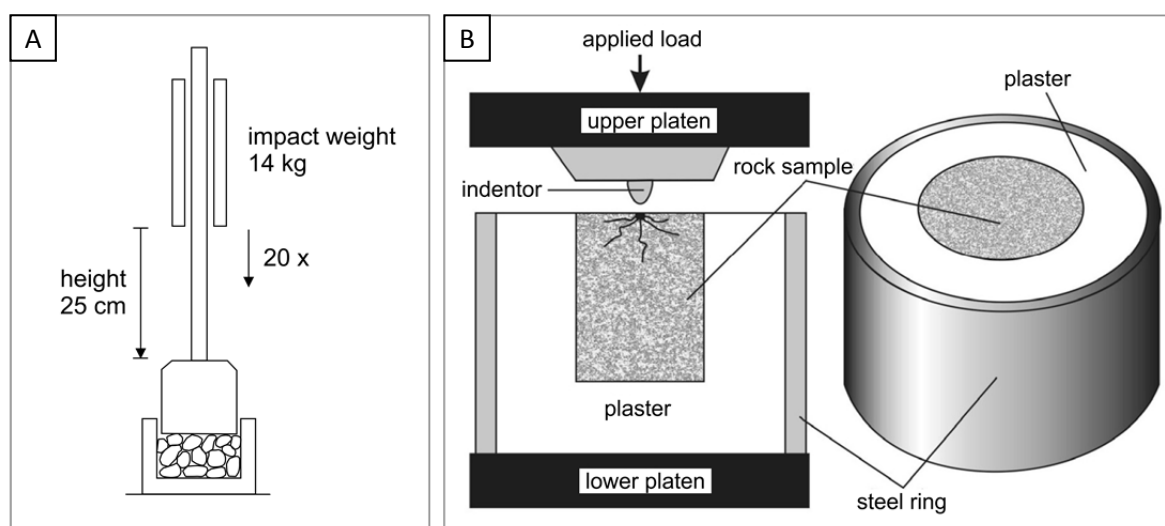


Fig. 25: **A)** Schematic figure of the brittleness test (mod. from BRULAND 2000d: Fig. 1.1). **B)** Schematic figure of the punch penetration test (mod. from YAGIZ 2009: Fig. 1). Both tests are used to investigate rock brittleness.

In North America, the **punch penetration test** is a common laboratory test to determine the rock brittleness used for boreability analysis (DOLLINGER et al. 1998, GERTSCH 2000, YAGIZ 2009). This test reflects the fragmentation process in rocks under load (such as disc cutters or indenters) and fracture pattern or chipping can be investigated. The conical indenter is pressed into a saw cut sample surface

and load and displacement of the indenter are measured and transferred to force - penetration graphs (Fig. 25B). The main result is a rock brittleness index BI_m (also peak slope index P_s) that is the ratio of maximum applied force and corresponding penetration (YAGIZ 2002: 69) (Eq. 2-26).

$$BI_m = \frac{F_{\max}}{P} = P_s \quad \text{Eq. 2-26}$$

BI_m	measured brittleness [kN/mm]
F_{\max}	max. applied force [kN]
P	penetration [mm]

The problem with this index is that it only considers the maximum force and does not account for the behavior of the force – penetration graph. There are tough/ductile rocks showing very high maximum forces and brittle rocks revealing low maximum forces at the same penetration rate. So it might be useful to analyze the shape of the curve since it gives evidence of the failure behavior. Brittle rocks reveal a highly fluctuating curve since a number of chips are formed that causes sudden force drops. Tough rocks show a smoother curve without sudden force drops (ERBEN 2013: 53). This aspect has already been mentioned by LINDQVIST et al. (1984) who recorded the force-displacement curve during indentation of wedges. Another weakness is that there is no approved standard procedure and the test is not internationally used. To overcome this problem, YAGIZ (2009: 72) proposed a conversion formula based on statistical analysis where the brittleness index can be predicted by standard laboratory parameters such as uniaxial compressive strength, Brazilian tensile strength and density (Eq. 6-5). Predicted results reveal good fitting with a regression coefficient of 0.94 and might be a suitable tool if the punch penetration test is not available. YAGIZ also suggested a classification system for rock brittleness which is presented in Tab. 7.

$$BI_p = 0.198 \cdot \sigma_u - 2.174 \cdot \sigma_t + 0.913 \cdot \rho - 3.807 = T_{PPT} \quad \text{Eq. 2-27}$$

T_{PPT}	toughness coefficient punch penetration test [-]
BI_p	predicted brittleness [kN/mm]
σ_u	uniaxial compressive strength [MPa]
σ_t	Brazilian tensile strength [MPa]
ρ	density [kN/m ³]

Tab. 7: Suggested rock brittleness classification based on measured or predicted brittleness index which are determined by punch penetration test or calculated by strength and density of the rock (YAGIZ 2009: 69).

Brittleness index $BI_{m/p}$ [kN/mm]	Classification
≥ 40	very high brittleness
35 – 39	high brittleness
30 – 34	medium brittleness
25 – 29	moderate brittleness
20 – 24	low brittleness
≤ 19	no brittleness (ductile)

It is questionable to what extent such small grading system for rock brittleness is reasonable. However, it can be concluded that the threshold for tough to brittle failure is at around $BI_{m/p} = 20$. Conclusively, this test reflects best the fragmentation process of rocks under impact. But it must be noted that excavating rock with disc cutters is not only based on impact force, but also on rolling force. This may be the reason why KAHRAMAN (2002) could not find a correlation of impact brittleness indices with TBM penetration and rotary drilling, but instead found significant correlation with percussion drilling.

Rotary tests (Sievers' J value, LCPC breakability coefficient)

Rock toughness can also be described by rotary testing, which reveals the failure behavior of rocks during the drilling process. In this work, exemplary two exemplary testing methods are mentioned.

The **Sievers value SJ** is determined by miniature drilling and results in the depth of penetration for certain number of rotations (Fig. 26A). This parameter characterizes the surface hardness and also the resistance against indentation (BRULAND 2000d: 18) and might be used to describe rock toughness. However, the test is not regarded as a standard laboratory test, but is commonly used in Norway. It is also implemented in the NTNU prediction model.

The **LCPC test** was actually developed to determine the abrasiveness of rocks (AFNOR 1990). A metal impellor is rotated in a sample container and the mass loss of the impellor is measured to determine the LCPC abrasivity coefficient (Fig. 26B). A detail testing procedure of the LCPC test is described in chapter 4.1.5. But the rock mechanical process underlying this test might also be useful as measurement for rock toughness since it reveals the resistance of rock fragments against destruction by a drilling tool (LCPC breakability coefficient).

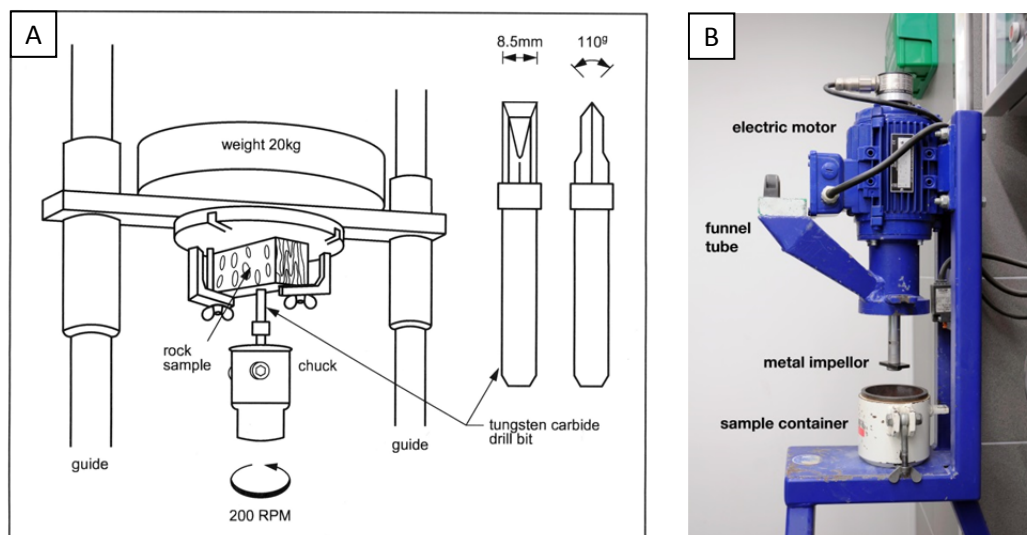


Fig. 26: **A)** Schematic figure of the miniature drill test (BRULAND 2000d: Fig. 1.2). **B)** LCPC testing device at the Chair of Engineering Geology (TUM). Both tests might be used to investigate rock toughness.

2.5 Influence of discontinuity pattern on TBM penetration

Besides rock toughness, most influencing parameters on the penetration rate of TBMs are the spacing and the orientation of discontinuities since they characterize the rock mass behavior. Up to certain spacing, jointing has a favorable effect on the daily performance (HOWARTH 1981, BRULAND 2000d).

When fracture spacing reaches the cutter spacing, two to three times higher penetration rates can be achieved (BARTON 2000: 35). If a critical spacing is undercut, the high fracturing hinders the formation of rock chips and leads to instabilities at the tunnel face and side walls. BÜCHI (1984: 53) set a critical threshold at a spacing of 10 cm, whereas GEHRING (1997), THURO (2002: 75) and AASEN (1980: 8) could observe the highest penetration rate at a spacing of around 5 cm. However, analysis reveals, that the influence of spacing is highly dependent on the rock type (TENTSCHERT et al. 2005, POISEL et al. 2010). It seems that the effect is highest for metamorphic rocks since foliated rocks show strongest increase in penetration rates. Analysis by fuzzy theory results in the finding that joint spacing is the dominant influencing factor for phyllites and joint orientation recedes into the background. The lamination of sedimentary rocks like limestones appears to have not the same effect as schistosity and the influence of the fracturing degree is less pronounced (TENTSCHERT et al. 2005).

However, fracture orientation seems to influence the penetration even more than fracture spacing for most rock types. It could be observed that some fracture orientations have greater impact on the penetration rate than others. Joints parallel to tunnel axis provide the least benefit to TBM performance whereas an orientation of about 60° to tunnel axis causes the highest increase in penetration rate (WANNER & AEBERLI 1978, BÜCHI 1984, SANIO 1985, GEHRING 1997, BRULAND 2000d, YAGIZ 2002, GONG et al. 2005, DELISIO et al. 2013). The dipping angle of discontinuities also affects the penetration. Dipping angles against the direction of tunnel advance leads to penetration rates which are 3-times higher than dipping in tunnel advance (TENTSCHERT et al. 2005). The influence of joint orientation diminishes with increasing fracturing degree. If several joint sets intersect each other, the intensity of fracturing appears to be the decisive parameter (GERSTNER et al. 2001).

One important aspect is considered by the term of potentially activated discontinuity plane (GEHRING 1997). It is of major significance if the planes of weakness are mechanically active and act as assisting feature in terms of excavatability. Not all distinguished planes can be activated and consequently don't facilitate the excavation. Typical examples are small fissures in Alpine dolomites which are interlocked and show no 'softening behavior' of the rock mass.

Besides joint spacing and orientation, geotechnical properties of joints such as surface quality, filling, aperture and roughness are affecting the penetration rate. Mylonites or joints filled with gauge material have greater impact on the penetration since they are often accompanied with many minor fissures and a wider range of rock mass may be disturbed than closed or unfilled joints (WANNER & AEBERLI 1979: 578).

Finally, it must be noted that in general, discontinuities increase the penetration rate. In the case of unfavorable joint spacing, orientation, and geotechnical property, the planes of weakness reduce TBM performance as a reduction of thrust force and cutterhead revolution is necessary to obtain stable side walls and tunnel face. Furthermore, great amounts of material have to be removed by the machine. Therefore, the TBM utilization is decreased since more time for mucking and rock support is needed.

In the following paragraphs, a short summary of selected research carried out in the last decades concerning the effect of discontinuities on the performance of TBMs is presented. Furthermore, it is highlighted, how some of the abovementioned prediction models (chapter 2.3) incorporate a discontinuity pattern.

Wanner & Aeberli (1979)

WANNER & AEBERLI (1979) investigated the influence of discontinuities by using a theoretical approach to characterize the joint frequency with the relation of total area of discontinuity planes [m^2] per unit volume [m^3]. A schematic figure for typical joint frequency is illustrated in Fig. 27.

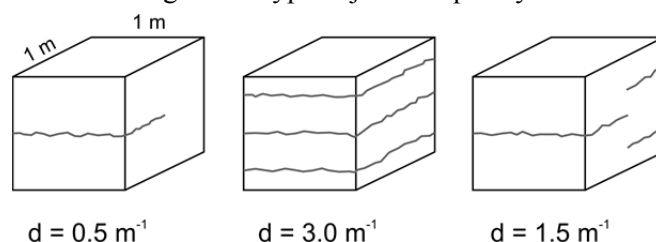


Fig. 27: Schematic figures (cube with 1 m edge length) for the characterization of joint frequency d [m^{-1}] proposed by WANNER & AEBERLI (1979: Fig. 5, mod.).

Since discontinuity planes intersect with the circular tunnel, the calculation of the joint frequency is mathematically not as easy as shown in the figure above. Thus, a number of geometric calculations have to be performed considering that only a part of the weakness plane is also excavated within one shift. Nowadays, especially for mechanical tunneling, this approach seems no longer practicable. Although the method may not be useful for predicting the penetration at actual tunnel projects, the conclusion WANNER & AEBERLI made when applying their method at five study sites provides some useful information.

- The trend shows that larger joint frequencies cause higher specific penetration rates.
- The rock type/grain size must also be considered, since the same joint frequency causes higher increase of penetration rate in coarse grained limestone than in fine grained.
- The type of discontinuity influences the penetration rate since open joints, mylonites, and cleavages change the penetration significantly whereas tight joints have a minor impact.

Sanio (1985)

SANIO (1985) investigated the performance of disc cutters in anisotropic rocks by theoretical analysis and subsequent laboratory experiments. The goal of this study was to develop predictor equations for rocks with bedding or schistosity since anisotropies influence the penetration. The author conducted wedge indentation and full-scale cutting tests on rock samples with certain orientations of the bedding or schistosity. The influence of different orientations on the penetration force has been analyzed by accounting for two different angles (Fig. 28):

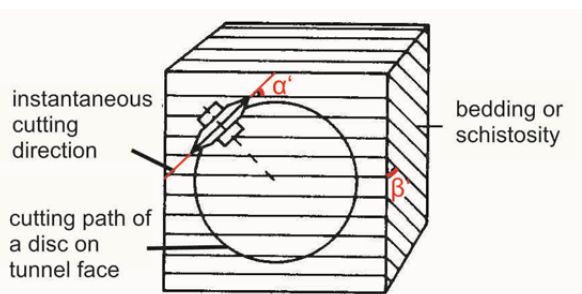


Fig. 28: Definition of α' and β' determining the orientation of anisotropy planes (mod. from SANIO 1985: Fig. 5).

- α' : angle between the momentary rolling direction of the cutter and the apparent strike of the anisotropy on the tunnel face
- β' : angle between the anisotropy planes (bedding, schistosity) and the tunnel face

For five rock types, wedge penetration tests were performed for every combination of α' and β' between 0° and 90° measuring the normal force for a fixed penetration. Tests reveal that α' has a rather small influence on the normal force. Only for highly schistose rocks, a distinct decrease of penetration force is measured. By contrast, the penetration force is highly dependent on β' . The force needed to penetrate rocks with horizontal anisotropy planes ($\beta' = 90^\circ$) is three times as high as for vertical ($\beta' = 0^\circ$). These testing results have also been proven by full-scale cutting tests.

Thuro (1996 & 2002)

THURO (1996, 2002) analyzed the influence of discontinuity spacing on the performance of drill and blast tunneling, of roadheaders and tunnel boring machines. The author showed that for spacing greater than 200 cm, the influence on the performance is marginal and the excavability is characterized by actual rock properties. A decrease of spacing leads to higher penetration rates up to a critical value of about 5 cm (THURO 2002: 75). Beyond this point, the rock is not cut anymore, but rather ripped and the total performance decreases again due to blocky tunnel face, stronger rock support and high amount of material that has to be handled by the conveyor belt.

The influence of the orientation of anisotropies such as schistosity on the penetration is analyzed by means of phyllite and phyllite-carbonate alternation (Fig. 29). Highest specific penetration has been achieved for a cutting direction perpendicular to schistosity and decreases constantly until cutting direction parallel to schistosity. This is contradicting to the results of abovementioned authors. THURO stated that the deviation may be caused by the consideration of different rock types since WANNER & AEBERLI (1978) analyzed very brittle rocks such as limestone, dolomite and siliceous limestone.

Tested phyllites showed a very narrow foliation at which the shear strength is reduced to a minimum which consequently facilitates the chipping process parallel to schistosity.

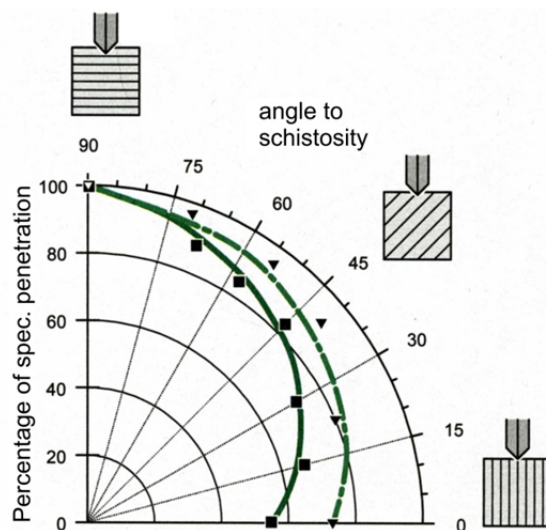


Fig. 29: Dependency of specific penetration on the orientation of schistosity relative to cutting direction in phyllite (solid line) and phyllite-carbonate alternation (dashed line) (mod. from THURO 2002: Fig. 85).

Ribacchi & Lembo Fazio (2005)

RIBACCHI & LEMBO FAZIO (2005) analyzed a 6.6 km long hydraulic tunnel in gneissic formation in terms of investigating the influence of rock mass parameters on the TBM performance. Therefore,

TBM data has been compared with geological investigations on the tunnel face and laboratory testing. It has been proposed that main influencing factors are rock toughness and joint characteristics.

Statistical analysis has been performed correlating the penetration only with selected single rating factors of the RMR (joint spacing, RQD, joint characteristics, rock strength). Results show, that RQD and compressive strength do not influence the penetration significantly. RIBACCHI et al. attributed this fact due to the close correlation of RQD with joint spacing and that compressive strength is almost constant over the whole tunnel length (100 – 200 MPa). Joint conditions reveal to have a significant impact, though most influencing is joint spacing. Joint spacing of 6 – 20 cm results in 3 m/h which is three times higher than the penetration rate for spacing > 200 cm. However, it must be noted that the regression coefficient for this parameter is only 0.44 and might not be reliable. Moreover, the rating factor for discontinuity orientation is neglected. Stated correlations of selected rock mass factors with penetration rates showing fairly low correlation coefficients, are only evaluated for one rock type and have to be treated with caution.

Entacher (2013), Lassnig (2012), Mori (2012) (Montanuniversität Leoben, ABROCK)

The influence of discontinuities and foliation has been investigated by several graduates from the *Montanuniversität Leoben* who joined the ABROCK research group (ENTACHER 2013, LASSNIG 2012, MORI 2012). Therefore, linear cutting tests were performed at the *Colorado School of Mines* and at the *Sandvik* laboratory. Furthermore, the crack pattern has been analyzed. Tests reveal that cutting parallel or oblique to foliation results in damage zone that is narrow, but deep. Conversely, perpendicular cutting shows a wide and thin damage zone (LASSNIG 2012: 106ff.). It could be proved that the cuttability increases from perpendicular orientation to oblique or parallel (MORI 2012). The same method should be used to identify the influence of discontinuities on the cutting performance. Therefore, linear cutting tests with artificially formed joints have been conducted in homogeneous granite (ENTACHER 2013). Rock cobbles from the exploratory tunnel Aicha (Brenner base tunnel) were cut into plates of different thickness and then arranged to smooth and closed joints perpendicular to the cutting direction. Unfortunately, the results vary to a high degree and no clear trend could be observed.

2.5.1 Ernst Büchi model (1984)

BÜCHI (1984: 51ff.) considers the frequency of joints in his prediction model by measuring the mean distance between them in the direction of tunnel axis. Only joints that appear over $\frac{2}{3}$ of the tunnel perimeter are counted. Surface condition and degree of opening are noted only for a general survey. This method is suitable for monitoring the influence of joints during construction, but not for a prediction since planners cannot rely on the existence of such detailed information on discontinuity patterns in advance of a tunnel project. Another disadvantage is that the orientation of discontinuities is not measured. By back-analyzing tunnel projects with this method, BÜCHI could show that highly fractured rock mass (< 5 cm spacing) can lead to an increase of penetration rates of more than 100 % in contrast to unfractured rock mass.

2.5.2 NTNU model by Amund Bruland (2000)

In contrast, to the research opinion of WANNER & AEBERLI, BRULAND (2000a: 18) investigated via geological back-mapping that even smallest fissures and mica layers act as planes of weakness. This is why the fracturing of rock mass is of major importance in the NTNU model like in no other prediction

model. Rock mass fracturing is described by the degree of fracturing (type and spacing) and the angle α between tunnel axis and discontinuity (s. chapter 2.3.4). BRULAND originally distinguishes two types of discontinuities – joints and fissures – that result in different correction factors k_s . **Joints** characterize continuous planes of weaknesses that can be observed all around the tunnel profile. They may be open or closed since they are filled with gauge material or other weak minerals. **Fissures** describe non-continuous joints that can only be detected partly over the tunnel profile. Filled joints with low shear stress and cleavage planes, like in mica schist, are included in this type. Nowadays, a third type is mentioned - **marked single joints**. This type describes distinctive discontinuities such as minor faults which occur as single phenomena at the tunnel level. Depending on the type, the orientation and the distance between the planes of weakness, BRULAND defines 7 fracture classes with corresponding correction factor k_s for the NTNU penetration prediction model (Fig. 30). Based on this, the fracturing factor can range from 0.36 for massive rock (fracture class 0) to greater than 4 for highly fractured rock mass (fracture class IV). Marked single joints are considered by an individual graph and taken into account by a maximum correction factor of k_{esp} of 1.4. The correction factor k_{esp} depends on the angle α , but instead of the distance between planes of weakness, the Drilling Rate Index is also included (BRULAND 2000d: 23). However, he noted that with the increase of joint spacing, the influence of joint orientation on the penetration rate decreases. Refinement and validation of suggested approach is currently done by MACIAS et al. (2014b) aiming to an update of existing NTNU prediction model.

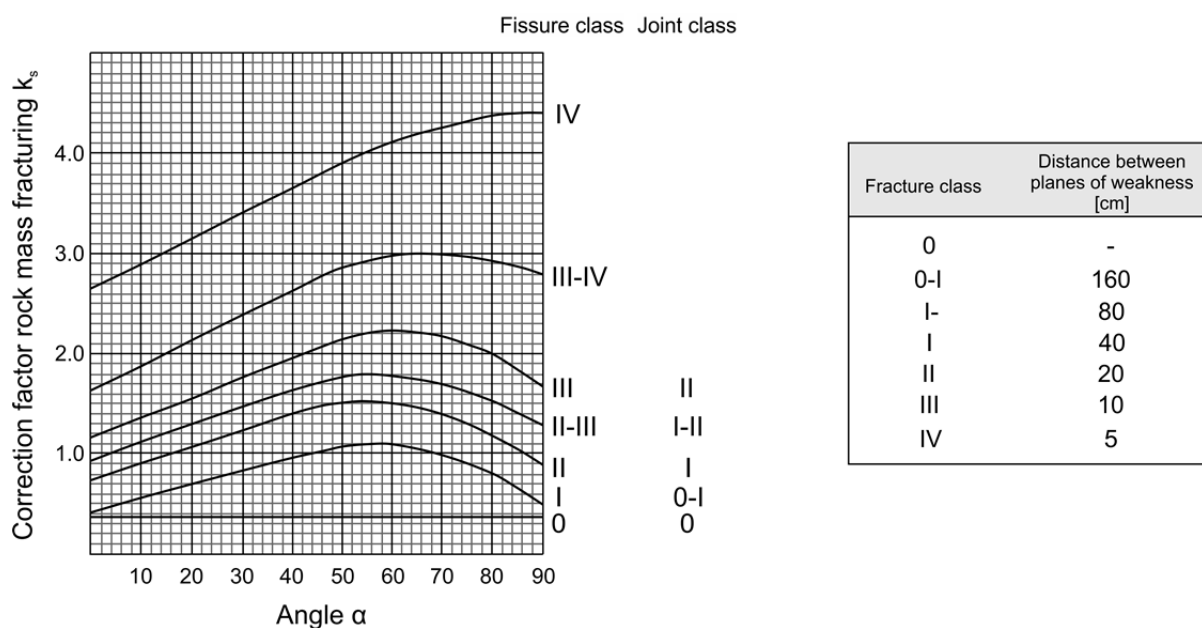


Fig. 30: Correction factor k_s for rock mass fracturing at the NTNU prediction model, depending on the angle α and the fracture class (mod. from BRULAND 2000c: 8; BRULAND 2000d: 72).

When several sets of weakness planes coincide, the total fracturing factor k_{s-tot} is defined as Eq. 2-28. The formula considers the effect that intersecting joint sets amplify the influence on the penetration rate since k_{s-tot} results in higher values than calculating the mean value of each correction factor.

$$k_{s\text{-tot}} = \sum_{i=1}^n k_{si} - (n - 1) \cdot 0.36 \quad \text{Eq. 2-28}$$

$k_{s\text{-tot}}$	total fracturing factor [-]
k_{si}	fracturing factor for set no. i [-]
n	number of fracturing sets [-]

Texture of metamorphic rocks is also assumed to act as planes of weakness, but this is not implemented in the correction factor for rock mass fracturing. The effect is accounted for in the Drilling Rate Index (DRI) where metamorphic rocks are assigned to lower DRI values than magmatic rocks. For example, gneisses with a UCS of about 100 MPa have equal DRI values, compared with granites with UCS of about 200 MPa.

2.5.3 BI by Qiu Ming Gong and Jian Zhao (2009)

In the prediction model of GONG & ZHAO (2009), joint spacing and joint orientation are implemented by the volumetric joint count J_v and the angle α .

Volumetric joint count (J_v) is the sum of the number of joints per cubic meter for each joint set (Eq. 2-29) (PALMSTRÖM 1982). To determine the volumetric joint count, the number of joints along certain distance (scan line) has to be counted. Since the shield of a TBM prevents the view on the tunnel side walls, a scan line analysis is not possible. Therefore, the measurement is constrained on tunnel face mapping including joint set spacing to calculate the volumetric joint count J_v . This may falsify the result since the joint spacing is not measured in the direction of tunnel advance.

$$J_v = \sum \left(\frac{1}{J_{si}} \right) + \left[\frac{N_{r(5)}}{5} \right] \quad \text{Eq. 2-29}$$

J_v	volumetric joint count [-]
J_{si}	joint spacing [m]
$N_{r(5)}$	number of joints along 5 meters [-]

To evaluate the influence of J_v - and consequently joint spacing - on predicted penetration rates in the GONG model, statistical analyses for three different uniaxial compressive strengths has been conducted with fixed thrust force of 200 kN/c and varying J_v from 0 to 30. Fig. 31 shows that independent of the rock strength, J_v has a great impact on predicted penetration. At UCS of 100 MPa, the penetration rate increases up to 10 times higher for $J_v = 30$ than for $J_v = 0$.

By contrast, **angle α** which describes the orientation of discontinuities does not influence the predicted penetration rate at all (Fig. 31 right). This is completely contradictory to the prevailing research opinions (WANNER & AEBERLI 1979, BRULAND 2000d, YAGIZ 2014) and also to the numerical results from GONG (s. next paragraph). This may be caused by the fact that the Gong model only considers the orientation of the minimum spacing joint set which is not automatically the one with unfavorable orientation. Furthermore, inaccuracies are incorporated by only estimating strike and dip of each joint set since no measurements have been performed.

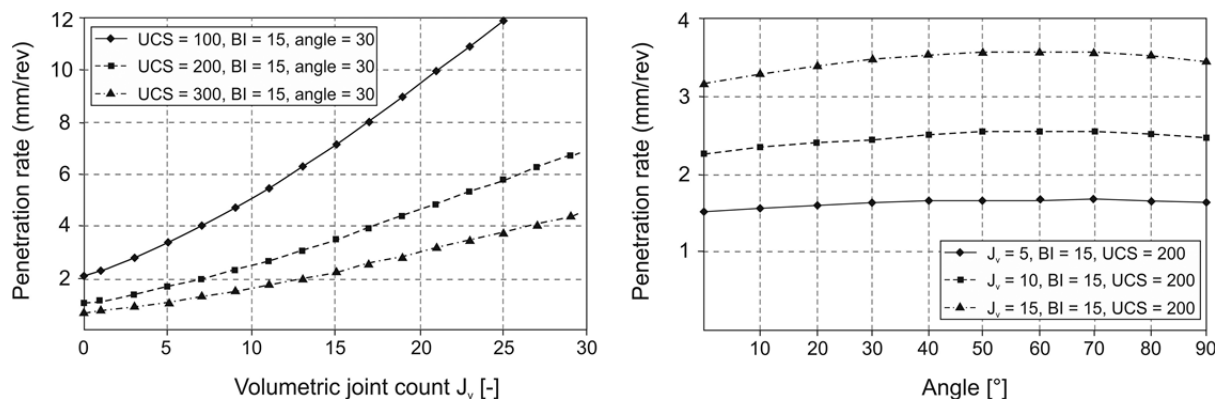


Fig. 31: Influence of joint volumetric count J_v (left) and angle α (right) on predicted penetration rate for the GONG prediction model with fixed thrust force of 200 kN/cutter. Additional input parameters are rock brittleness (Bi) and rock strength (UCS) (mod. from GONG & ZHAO 2009).

Researchers proved the significant influence of discontinuities on the TBM performance, but little experience is available on the fracture pattern induced by disc cutters in jointed rock mass. To address this topic, GONG et al. (2005, 2006) performed numerical modeling using the 2-D discrete element method UDEC from Itasca to investigate the influence of joint orientation on the one hand, and the influence of joint spacing on the other hand.

Numerical modeling of the effect of joint orientation

In the computational model for **joint orientation**, a block of granite with the size of 1.2 x 1.2 m and joint spacing of 20 cm is set where the load is applied over a 15 mm wide contact area. The dip direction of the joint is assumed to be the same for the tunnel advance and thus in direction of the cutter load. The dip angle (α angle) is varied from 0° to 90° and the fracture pattern is analyzed for each angle. Implemented rock and joint properties derive from tests in Singapore granite. Results show, that beneath the crushed zone, a zone with multiple cracks (radial and medial cracks) is formed. The cracks mainly propagate along the tensile failure elements. At joint orientations from $\alpha = 15^\circ$ to 45° , the crushed zone has an asymmetric shape and the cracks also propagate asymmetrically (Fig. 32). When the crack reaches the discontinuity plane, a rock chip is formed. For $\alpha = 60^\circ$ to 75° , fracture pattern is completely different. Since the distance between joint plane and induced force is less, no crushed zone is formed and the first failure occurs at the element closest to the joint plane (Fig. 33a). When the penetration is increased, the initial crack propagates from the failed element to the free surface and in a second step, cracks from the cutter edge are formed. 0° and 90° are special cases since the crack initially propagates like in unjointed rock mass.

For all numerical models of different joint orientations, the crack growth terminates at the joint surface which means that the fragmentation only takes place in the block directly beneath the disc cutter. This approach is justified with field observations from a tunnel project in Singapore granite where the same fragmentation process occurred in jointed rock mass. Since the crack propagation is influenced by the joint orientation, so does the rock chipping angle. GONG et al. (2005) revealed that with increasing angle α from 15° to 75° the rock chipping angle also increased. Modeling results show that smaller angle α facilitate rock fragmentation. When the joint orientation is 90° , the lateral crack propagation is not affected by the joint plane leading to a chipping angle of about 35° which agrees with the Hertzian cone crack ($30^\circ - 40^\circ$) (s. chapter 2.1).

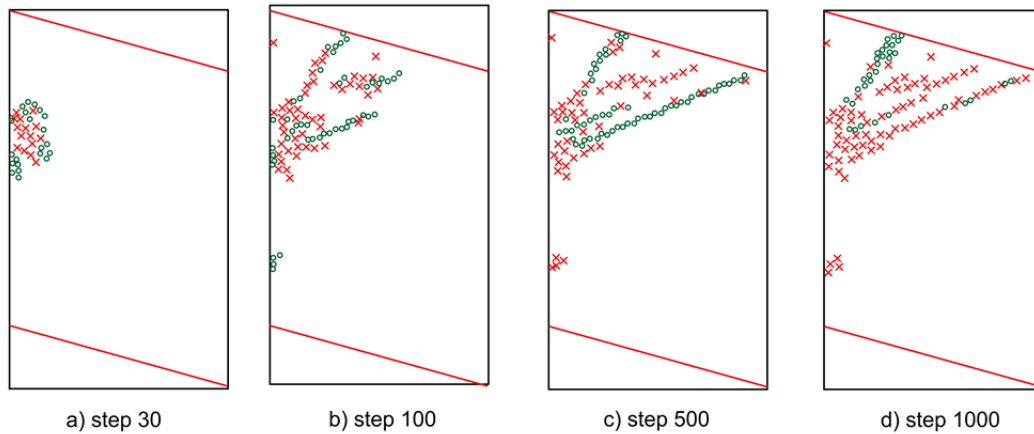


Fig. 32: Numerical model of failure pattern in granite with $\alpha = 15^\circ$. Crushed zone shows an asymmetric shape (a), then the initial crack propagates asymmetrically to the joint plane (b, c, d). Circles mark tensile failure; crosses mark compressive failure (mod. from GONG et al. 2005).

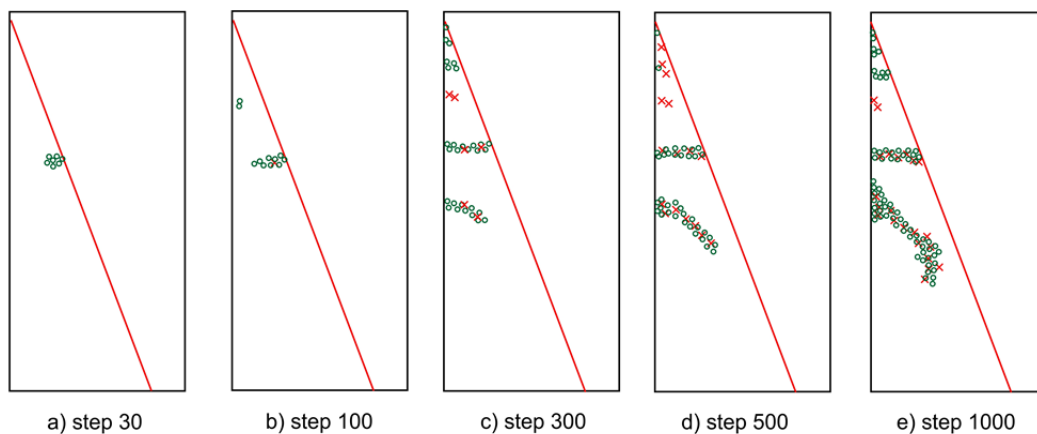


Fig. 33: Numerical model of failure pattern in granite with $\alpha = 75^\circ$. First failure takes place at the joint plane (a), then the initial crack propagates to the free surface (b, c). Circles mark tensile failure, crosses mark compressive failure (mod. from GONG et al. 2005).

To evaluate the numerical results, comparisons with field observation regarding the penetration have been performed. Therefore, the angle α is plotted against the ratio of the penetration rate at certain α angle (P_α) and the penetration at $\alpha = 0$ (P_0). Fig. 34A reveals that the penetration increases up to an angle of 60° where the penetration is twice as high as for $\alpha = 0$. This trend coincides with actual TBM data. It should be noted that the simulated results do not consider the effect of adjacent cutters since the numerical model is developed as single indenter.

TÜRTSCHER (2012) compared the abovementioned coherence of angle α and penetration rate with reference curves derived from the Gehring and NTNU models (Fig. 34B). To ensure comparability, input parameters by Gehring and NTNU were set to a minimum to reach a penetration factor of 1.0 for $\alpha = 0^\circ$. The analysis showed that numerical results from GONG overestimated the influence of α in comparison to Gehring and NTNU, especially for the critical angle of $\alpha = 60^\circ$, but the basic trend of the curves could be validated.

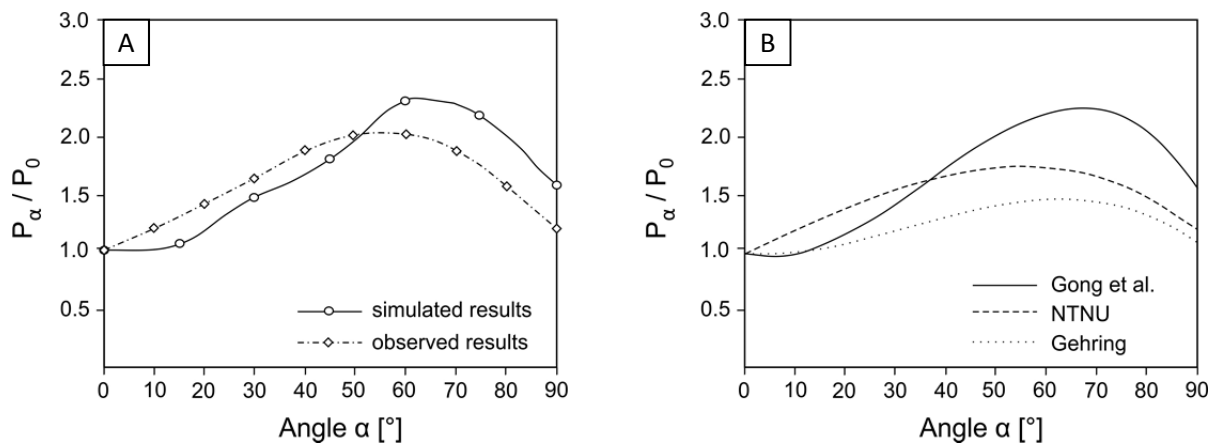


Fig. 34: Effect of the angle α on the penetration rate for joint spacing of 20 cm. α is plotted against the ratio of the penetration at certain α angle (P_α) and the penetration at $\alpha = 0$ (P_0).

Fig. 34A represents the simulated and observed results from GONG et al. 2005, whereas Fig. 34B shows a comparison of Gong (simulated), Gehring & NTNU models (mod. from TÜRTSCHER 2012: 205).

Numerical modeling of the effect of joint spacing

In the computational model for **joint spacing**, a block of granite with the size of 0.6 x 0.6 m and a vertical joint set is modelled where the spacing is varied from 10 to 500 mm (GONG et al. 2006).

Results reveal that, similar to the observations for joint orientation, two different crack initiation modes occur. At joint spacing less or equal than 40 mm, the first failure happens at the joint plane and the crack propagates to the free surface. Spacing more than 40 mm lead to joint initiation at the crushed zone and crack propagation towards the joint plane. The fracture pattern of different joint spacing is shown in Fig. 35. The model is designed in the way that propagating cracks terminate when reaching the joint plane. It is interesting to note, that the combination of median and lateral cracks only reaches the joint plane at spacing equal or less than 80 mm. At joint spacing > 80 mm, lateral cracks start to propagate towards the joint, but then change direction parallel (Fig. 35d). Therefore, the joint plane does not facilitate the chipping to the same extent as for spacing < 80 mm. At joint spacing > 200 mm, even the median crack doesn't reach the joint plane and the fragmentation pattern is the same as in unfractured rock mass (Fig. 35f).

On the basis of modeling results, GONG et al. set the favorable spacing for rock fragmentation between 50 and 80 mm which corresponds to very closely spaced (ISRM 1978), and to BRULANDS' high fracture classes (III-IV). These results seem quite impractical since the excavation of such fractured rock mass by TBM might be complicated and a lot of time is needed for rock support and mucking. A comparison of simulated results with in-situ measurements by BRULAND are shown in Fig. 36. It is evident that the simulation predicts less influence on the penetration rate than actually observed in tunnel projects, but the trend of the simulated curve agrees with in-situ measurements. The numerical research study by GONG et al. only covers a small range of joint spacing (up to 500 mm), whereas BRULAND analyzed spacing up to 1,600 mm. Furthermore, the intersection of discontinuity sets is not considered which leads to falsifies simulation, since especially in granite three or more joints sets are not unlikely.

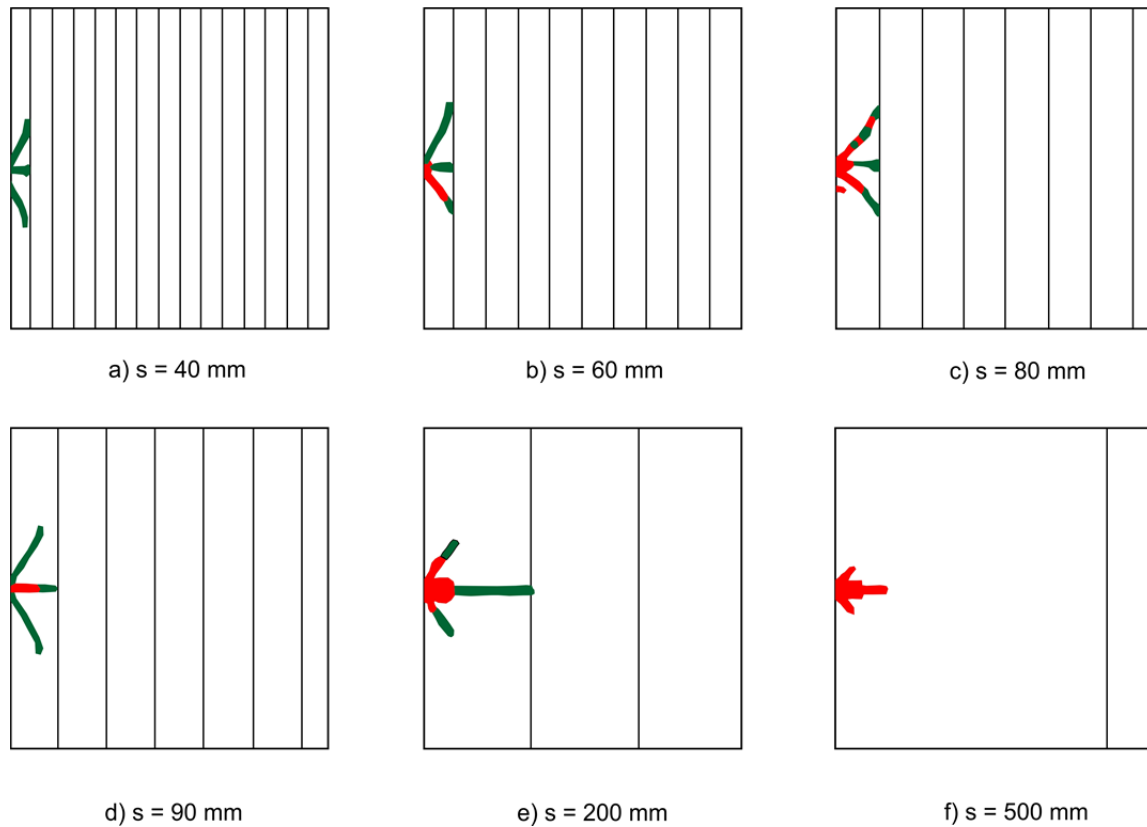


Fig. 35: Numerical model of failure pattern in granite with different joint spacing of 40 mm, 60 mm, 80 mm, 90 mm, 200 mm and 500 mm. Only in figure a-c, lateral cracks reach joint plane. Green areas mark tensile failure; red areas mark compressive failure (mod. from GONG et al. 2006).

In Fig. 36, the authors also implemented statistical results derived from his prediction model by transferring the volumetric joint count J_v into equivalent joint spacing (GONG & ZHAO 2009). The prediction model results are consistent with the numerical modeling, but again slightly smaller than the results by BRULAND. This is caused by the fact, that GONG did not incorporate joint properties such as filling, aperture, and length due to the time limit during geological face mapping.

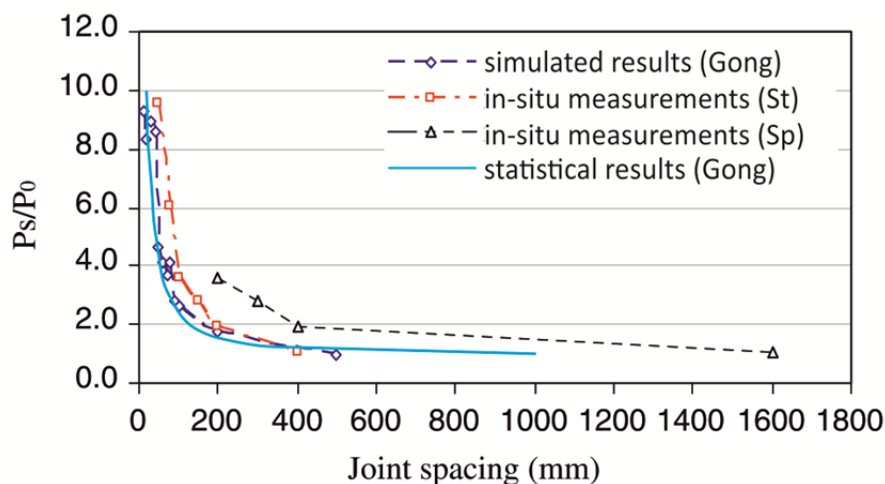


Fig. 36: Effect of joint spacing on the penetration rate for vertical joint orientation. Spacing is plotted against the ratio of the penetration at certain spacing (P_s) and the penetration in unfractured rock mass (P_0). In-situ results by BRULAND for joints (Sp) and fissures (St) are compared with simulated and statistical results by GONG (mod. from GONG et al. 2006, GONG & ZHAO 2009).

2.5.4 Modified CSM model by Saffet Yagiz (2002)

YAGIZ (2002, 2014) developed a modified CSM model to include the effect of rock mass fracture and brittleness to the basic prediction formula of ROSTAMI & OZEMIR. The modified CSM model (MSCM) is based on data from a 16 km long tunnel project where the author conducted geological mapping with a special focus on joint record, laboratory testing, and TBM data analysis. The research results in the implementation of three more parameters to consider rock mass characteristics: distance between discontinuities, orientation of discontinuities, and rock brittleness. For a quantitative description of discontinuities, YAGIZ goes back to BRULAND using abovementioned fracture spacing and angle α , combined as **rock fracture index (RFI)** (Eq. 2-30). The **rock brittleness index (BI)** is determined by the peak slope P_s measured by the punch penetration test (Eq. 2-31) (s. chapter 2.4.5). The author could prove a significant influence of RFI and BI on the penetration rate with regression coefficients of about 0.60. By multiple variable regression analysis, a linear predictor equation with a regression coefficient of 0.82 has been achieved depending on RFI, BI and basic CSM formulas (Eq. 2-32).

$$\text{RFI} = 1.44 \cdot \text{Log}(\alpha) - 0.0187 \cdot F_s \quad \text{Eq. 2-30}$$

RFI	rock fracture index [-]
α	smallest angle between tunnel axis and fracture orientation [°]
F_s	spacing between fractures [in; mm]

$$\text{BI} = 0.0157 \cdot P_s \quad \text{Eq. 2-31}$$

BI	brittleness index [-]
P_s	peak slope [-]

$$\text{ROP} = 0.859 - \text{RFI} + \text{BI} + 0.0969 \cdot \text{CSM}_{(\text{b-rop})} \quad \text{Eq. 2-32}$$

ROP	rate of penetration [ft/hr; m/hr]
RFI =	rock fracture index [-]
BI =	brittleness index [-]
$\text{CSM}_{(\text{b-rop})} =$	CSM model basic ROP [ft/hr; m/hr]

The MSCM is an important improvement for the basic model since it addresses the influence of discontinuities, but it has been developed and validated only on one tunnel project. The main weakness for using this model outside the United States is the need of performing punch penetration tests. The test is commonly not used in European rock mechanics laboratories which makes the determination of BI complicated. The proposed conversion formula by YAGIZ may provide a solution for this problem (s. chapter 2.4.5).

2.5.5 Gehring model by Karlheinz Gehring (1995)

The influence of the discontinuity pattern on predicted penetration rate for the Gehring model has already been explained in detail in chapter 2.3.8. To briefly summarize, the correction factor k_2 is implemented into the model. K_2 is determined by a table (GEHRING 1995: 445) and depends on joint spacing and orientation (angle α) in accordance with results by (BRULAND 2000d: 16).

3 Study sites

Two tunnel projects are subject to investigations to study the interaction between the tunnel boring machine and the surrounding rock mass. At both projects, penetration tests, a detailed geological mapping and laboratory tests have been performed. This provides the basis for further investigations concerning the general relation between the applied force and resulting penetration, and the influence of rock toughness and rock mass fabric on the penetration.

3.1 Koralm tunnel project

The 33 km long Koralm tunnel is the centerpiece of the Koralm railway track between Graz and Klagenfurt in Austria which is part of the Baltic-adriatic axis that leads from Tallinn (Estonia) to Venice (Italy). The tunnel cuts through the Koralm massif connecting Deutschlandsberg in Styria with St. Paul in Carinthia (Fig. 37). The mountain range has its highest peak at 2 140 m. a. A. (Großer Speikkogel) and is bordered by the Lavant valley in the west and by the Styrian upland in the east. As a result of this high-speed line project, the travel time from Graz to Klagenfurt is reduced from three to less than one hour (ÖBB-INFRA 2012).

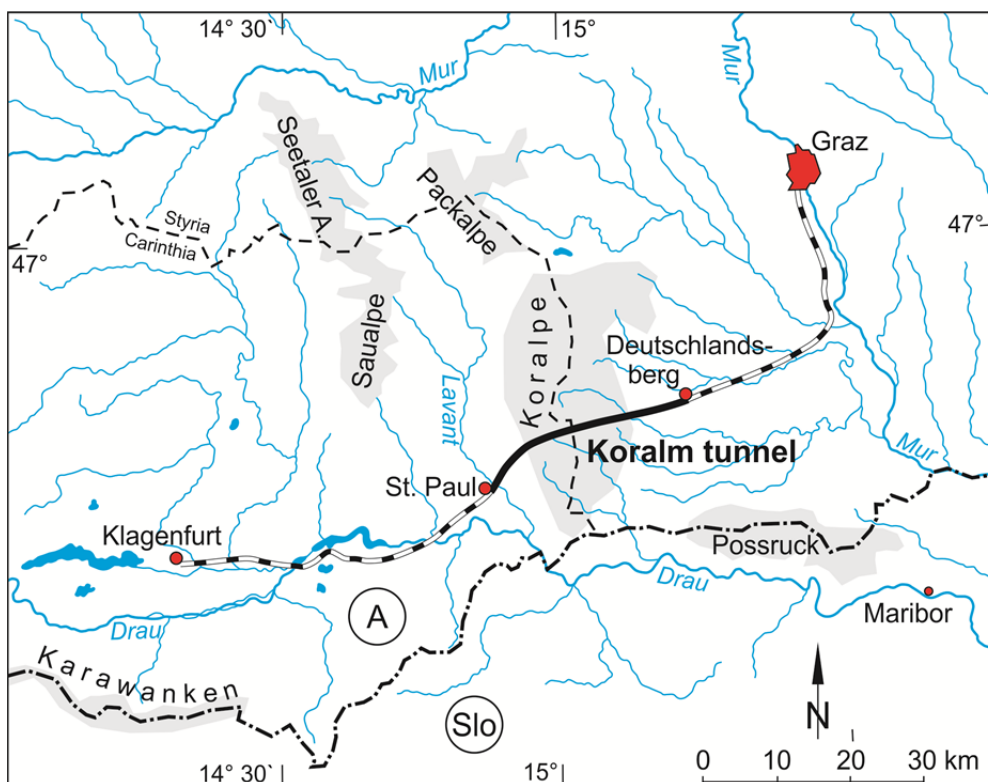


Fig. 37: Geographic location of the Koralm railway track with the Koralm tunnel as centerpiece.

It is designed as two single tube system (northern & southern tube) with cross-passages every 500 m and one emergency stop of about 1 km length in the middle. The total length of 32.9 km is divided into three construction lots (KAT1-3) whereby the focus of this thesis is on the northern tube of KAT2 (Fig. 38). Over a length of about 13 km, more than 20 penetration tests including geological mapping and laboratory testing have been performed. KAT2 is mainly constructed by two double shield TBMs with diameters of around 10 m. Only the first 3 km at the transition from KAT1, the cross passages

and one emergency stop in the middle of the lot are excavated by drill and blast (NATM). Key information of KAT2 is summarized in Tab. 8.

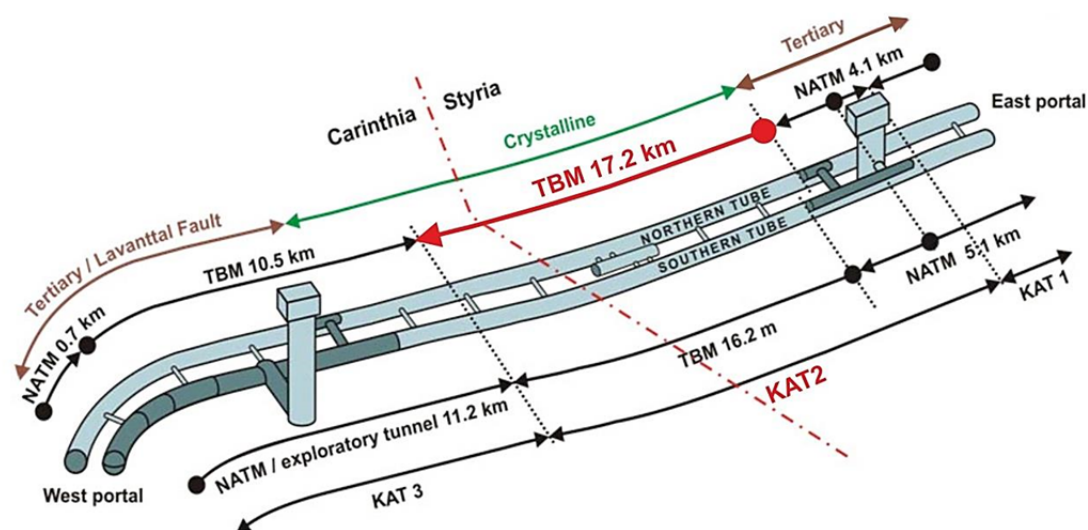


Fig. 38: Schematic figure of the three construction lots at the Koralm tunnel with a rough geological classification into tertiary sediments and crystalline basement. Highlighted in red is the northern tube of the section KAT2 where research focuses on (mod. from www-02).

Tab. 8: Short key information for construction lot KAT2 at the Koralm tunnel.

Construction lot KAT2	
length	17.2 km
diameter	10 m
excavation profile	80 m ²
max. overburden	1250 m
construction design	2 single tubes with axial distance ~ 40 m
construction time	2011 – exp. 2019
client	Österreichische Bundesbahnen Infrastruktur AG - ÖBB Infra
contractor	Strabag SE & Jäger Bau GmbH

3.1.1 Machine design KAT2

Construction lot KAT2 is excavated by two Aker Wirth double shield TBMs of the type TB 993E/TS with diameters of 9.93 m. The cutterhead is equipped with manholes, muck baskets and 80 cutters from which 67 are face cutters, 8 gauge cutters and 5 center cutters (Fig. 39). Constant cross section cutters with diameters of 17'' (432 mm) and mean cutter tip widths of 7/8'' (22 mm) are used. The average spacing of the cutters is 65 mm. Key information of the machine design at KAT2 is summarized in Tab. 9 (ÖBB-INFRA 2009a).

Calculating the force per disc cutter, the total number of cutters is reduced from 80 to 78 since gauge cutters only contribute to a small percentage of the penetration of the tunnel face. Their number is therefore just considered by factor 1/4 since their main goal is to ensure the tunnel's profile. Gauge

cutters show less force transmission than face cutters as well. For 17'' cutters, maximum force is set at 267 kN (GIRMSCHIED 2013: 452).

Tab. 9: Short key information on the machine design of Aker Wirth double shield TBM used at KAT2.

Machine design KAT2	
cutterhead diameter	9.93 m
max. thrust force	23 000 kN
max. revolution per minute	5.5 rpm
stroke length	1.9 m
no. of cutters	80 (red. 78)
cutter diameter	17'' (432 mm)
cutter spacing	65 mm
cutter tip width (mean)	7/8'' (22 mm)
max. force per cutter	267 kN

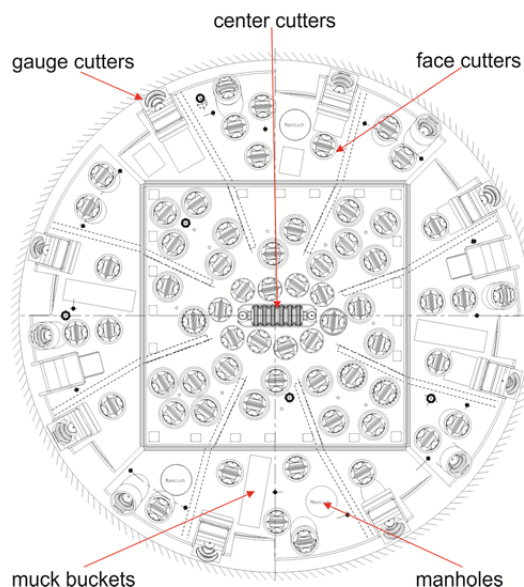


Fig. 39: Cutterhead design of Aker Wirth doubleshield TBMs used at KAT2 (www-03; mod. from ÖBB-INFRA 2009a).

3.1.2 Project geology KAT2

The tunnel project in the European Alps is geologically situated in the Upper Austro Alpine (Oberostalpin), more precisely in the East Alpine crystalline basement. This basement layer is divided into two subunits called Murids, including Glein- & Stubalpe, and Korids including Sau- & Koralpe. Murids describes the lower unit which surprisingly shows lower metamorphosis than the Korids which are the upper unit (TOLLMANN 1977: 20ff.).

The Korids, also called Koralm crystalline, are limited by neogenic sediments in the east and the west. The **Styrian basin** in the east is an inneralpine basin formed in Tertiary with depths up to 3 000 m in the eastern part. The basin is mainly filled with limnic fluvial sediments and in Miocene and

Pliocene volcanic activity also took place leading to spots with volcanic rocks such as tuff or trachyte (FLÜGEL & NEUBAUER 1984: 16ff.).

The **Lavant basin** in the west shows depths of about 800 m and is filled with debris from surrounding mountain ranges (BECK-MANNAGETTA 1952a, BECK-MANNAGETTA 1980). The valley originates in complex fault tectonics of the Lavanttal fault system with extreme high movement rates in Tertiary. The Lavanttal system can be associated with the main transversal fault zone of the eastern Alps, striking NNW-SSE and connecting with the Periadriatic fault in the south. Main activity occurred during the alpine orogeny and inducing Miocene (23 – 5 Myr) an abrupt offset of up to 5 000 m led to an uplift of the Koralpe massif. Subsequently, a subsidence of the southern and eastern part of the Koralpe caused a tilting of the rock layers in SE direction (BECK-MANNAGETTA 1952b: 3ff.).

The main part of the tunnel crosses the polymetamorphic basement of the Upper Austro Alpine. A simplified geological map of the Styrian part of the Koralm tunnel is shown in Fig. 40. For the Carinthian part, the directly adjacent geological map does not exist. Metamorphism in the **Koralm crystalline** took place during the variscan and alpine orogeny. The variscan metamorphism can be subdivided into two events where the first one has been temperature controlled leading to fluids percolating the rock and forming pegmatites. The second event has been temperature and pressure controlled reaching the amphibolite and eclogite facies. The alpine metamorphism is accompanied by high tectonic movement rate, but a low grade of metamorphism (greenschist facies) (FLÜGEL & NEUBAUER 1984: 60ff.). During this deformation phase, the predominant folding direction developed with fold axis striking W-E / WNW-ESE. According to TOLLMANN (1977: 236ff.) the Koralm crystalline is divided into several geological series where the ‘Koralpenserie’ and the ‘Schwanberger Serie’ are affecting the tunnel excavation most. However, the classification of TOLLMANN into suggested nappes is no longer recommended in Alpine geology, but geological characteristics of encountered rocks are still useful. The series mainly includes gneiss, schistose gneiss, and schist with pegmatite dykes and layers of amphibolite, eclogite, and marble. A special feature of the ‘Koralpenserie’ is the ‘Stainzer Plattengneis’ that build up the core of the Koralpe and also appears at tunnel level. It is considerably layered, shows feldspar and quartz lenses and is pervaded by pegmatite. Since the division of the Alpine nappes is still subject to investigations, recent publications stated a classification differing from the one by TOLLMANN. According to SCHMID et al. (2004), the Koralpe – Wölz nappe system belongs to the lower plate of the Upper Austro Alpine and is situated below respectively south of the Eoalpine plate boundary. The Koralpe-Wölz nappe system is of major importance for understanding the Alpine orogeny, since the occurrence of high-pressure rocks like eclogite mark the suture of the subduction zone between the Adriatic and the European plate. However, the tectonic context is not emphasized in this thesis.

The schematic longitudinal profile (Fig. 41) made during the preliminary investigation of the tunnel project sums up the geology into five major geological members: neogenic sediments in the east and west, and schistose gneisses / mica schists, fine / coarse-grained gneisses, and platy gneisses in the core of the Koralpe (ÖBB-INFRA 2009b). The study site of this dissertation is mainly situated in schistose gneisses and mica schist, but also cutting the unit of fine and coarse-grained gneisses. Both series are described in detail below. The main striking orientation of schistosity is documented at an acute angle to the tunnel axis dipping flat to moderate against tunnel advance. Due to small scale internal folding, the orientation may vary to a certain degree.

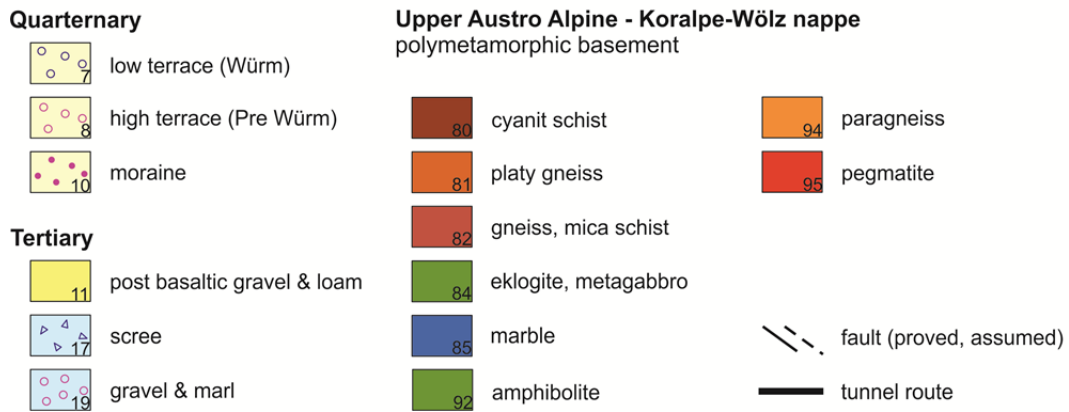
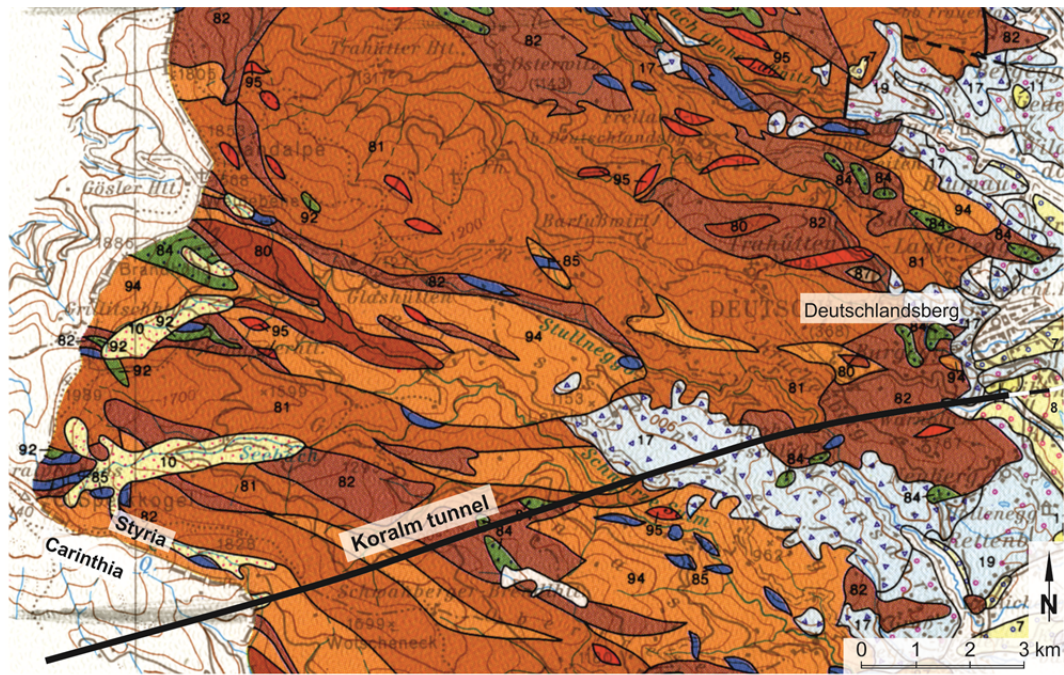


Fig. 40: Geological overview of the Styrian part of the project area with planned tunnel route in black (mod. from FLÜGEL & NEUBAUER 1984, BECK-MANNAGETTA et al. 1991).

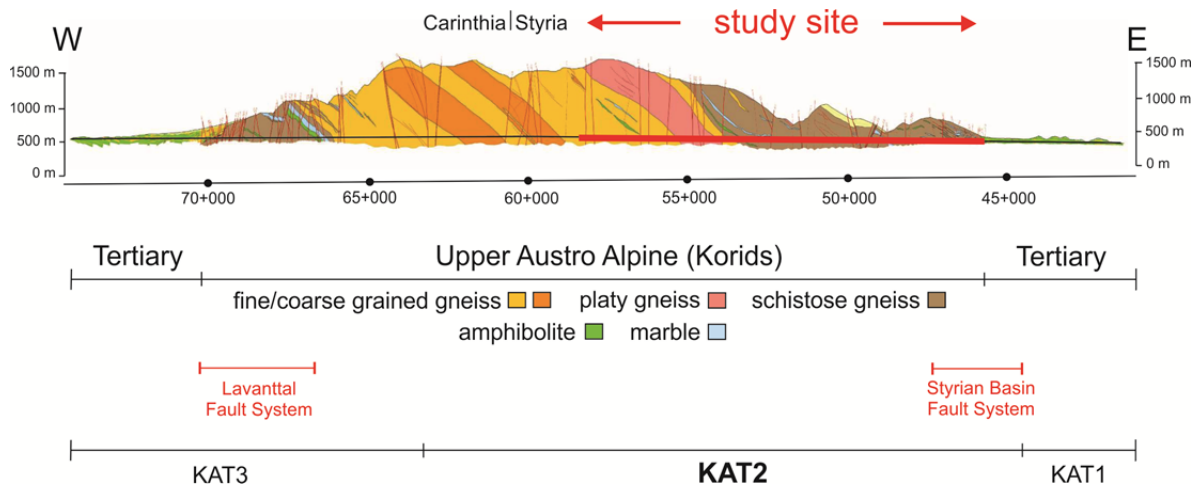


Fig. 41: Schematic geological longitudinal section through the Koralpe tunnel showing the construction lots KAT 1-3 and the major geological elements (mod. from MORITZ et al. 2011: 306).

Schistose gneiss series / mica schist

This member is an alternation of mica schists, schistose gneisses and gneisses. The transition between the different rock types is induced by a continuous increase of feldspar minerals leading from mica schist to schistose gneiss to gneiss. In this case, the transition is smooth which makes a strict distinction complicated. Thin sections reveal that mainly mica schist occurred in this series which has a high degree of anisotropy due to the layering of quartz and mica (Fig. 42). Some samples also show garnet or carbonate layers. Subordinated quartzite, pegmatite dykes and marble / amphibolite layers appear (ÖBB-INFRA 2009b). For a detailed petrographic description, see chapter 5.1.1.2.

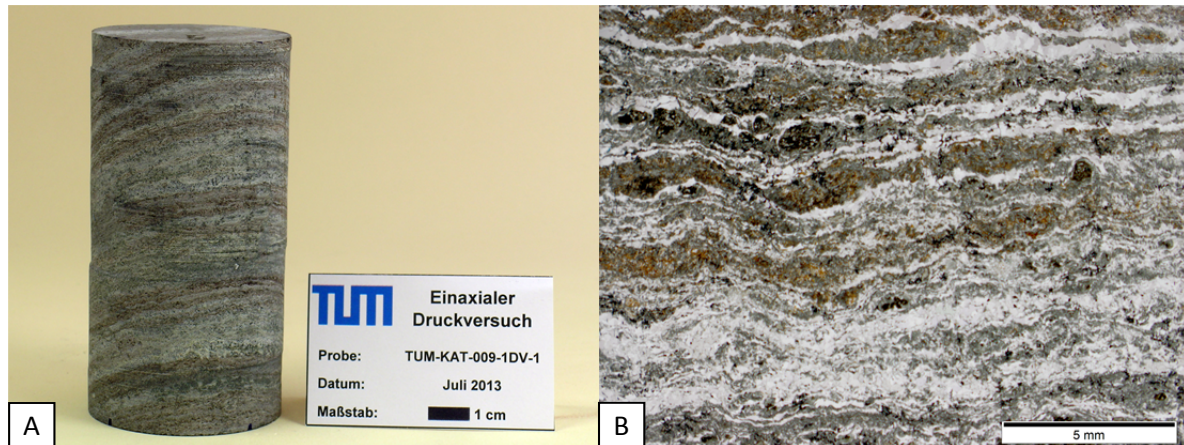


Fig. 42: Mica schist KAT2: specimen for uniaxial compression testing (A) and thin section analysis under plane polarized light (B). Schistosity is clearly visible due to layering of quartz (white) and biotite (brown).

Fine / coarse-grained gneiss series

In this series, gneiss with distinct schistosity occurs. Partially they show a high percentage of quartz (Fig. 43). In some samples, the mineral aggregates of quartz and feldspar reach sizes from several centimeters leading to augen gneiss with a porphyroblastic texture. This variety is assigned as coarse-grained gneiss series where the schistosity declines due to the porphyroblastic texture. The transition between fine- and coarse-grained gneiss is again smooth and difficult to distinguish in the field. Subordinated quartzite, pegmatite dykes, and marble / amphibolite layers appear (ÖBB-INFRA 2009b). For a detailed petrographic description, see chapter 5.1.1.2.

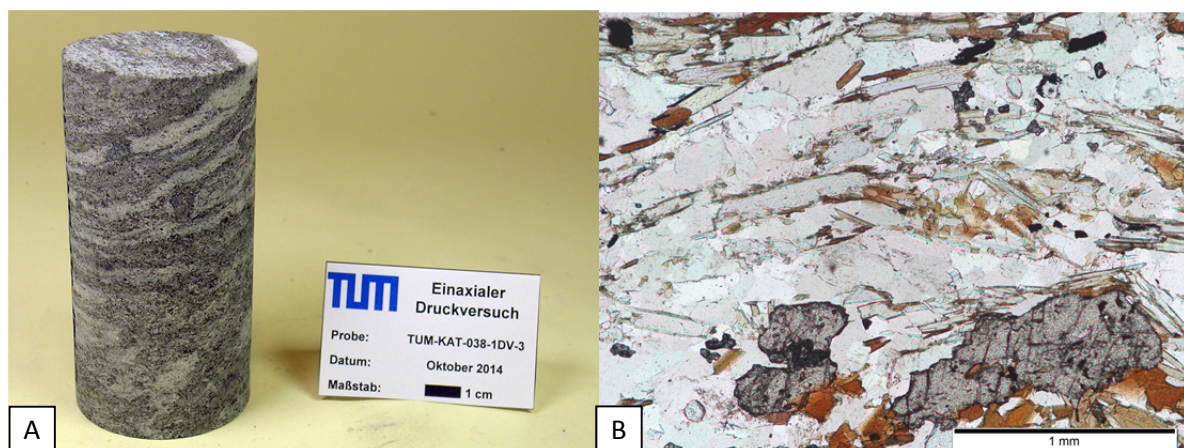


Fig. 43: Fine-grained gneiss KAT2: specimen for uniaxial compression testing (A) and thin section analysis under plane polarized light (B). Layering is vaguely visible due to alignment of biotite and muscovite. Furthermore, quartz and feldspar are detected.

3.2 Røssåga tunnel project

The Røssåga hydropower project is a milestone in Norwegian tunneling history since it marks the return of TBMs to Norway after 22 years of absence. It is situated in Nordland County (north Norway) near the city Mo i Rana (Fig. 44). The river Røssåga has been used since 1958 for hydropower production by the **Nedre Røssåga** power plant and has been extended few years later by the Øvre Røssåga power plant. Produced energy is mainly used for the iron and aluminum industry in surrounding municipalities (www-04). The actual tunnel project is enhancing the Nedre Røssåga by a new power plant with one unit to increase the capacity from 250 MW to 350 MW (www-05).

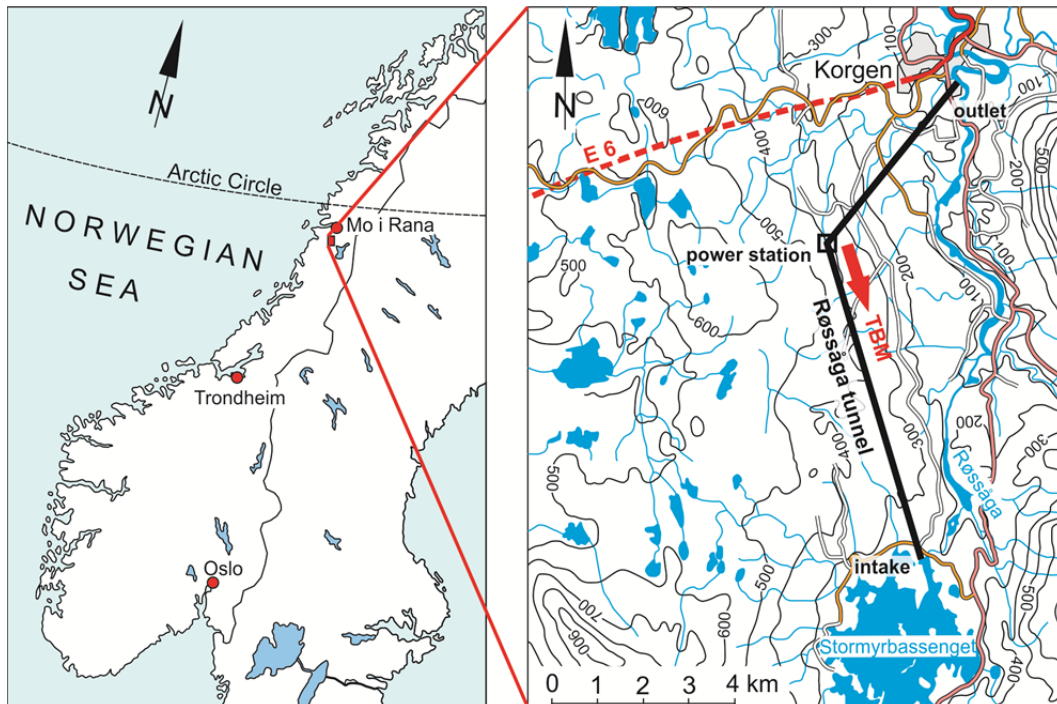


Fig. 44: Geographic location of the Røssåga hydropower project in Nordland County, Norway.

The project consists of a 7.4 km long headrace tunnel (orange line) and a 450 m long access tunnel (red line) (Fig. 44). Originally, the whole project was tendered as drill and blast tunneling, but the construction company LNS convinced the project owner to use a TBM by bringing to mind the benefits of this construction method in Norwegian hard rocks. In addition, the risk to damage the existing parallel headrace tunnel is reduced by using a TBM in contrast to drill and blast.

Consequently, the headrace and access tunnel are constructed by an open gripper TBM, and depending on the rock quality, a tailrace tunnel at the Øvre Røssåga power plant is also to be excavated by the TBM (www-06). The access tunnel (1:9 decline) leads to the power station with a 500 m curve radius from where the TBM excavates the rock in south eastern direction with a slight uphill gradient of 0.02 % (NORWEGIAN TUNNELLING SOCIETY 2014: 170). Key information of the New Nedre Røssåga hydropower project is summarized in Tab. 10. The research focus of this dissertation is geological back-mapping and analysis of eight penetration tests within the first 2,500 m.

Tab. 10: Short key information for the New Nedre Røssåga hydropower plant.

New Nedre Røssåga hydropower plant	
length	7.4 km headrace tunnel
diameter	7.2 m
excavation profile	41 m ²
gradient	0.02 % uphill
max. overburden	200-300 m
construction time	2014 – exp. 2016
client	Statkraft Energi AS
contractor	LNS (Leonhard Nilsen & Sønner)

3.2.1 Machine design Røssåga



Fig. 45: Robbins open gripper TBM used at Røssåga tunnel (www-06).

The TBM used at the Røssåga hydropower project is a refurbished main-beam gripper TBM by Robbins with a diameter of 7.2 m (Fig. 45). The machine is equipped with 19'' (483 mm) cutters and mean cutter tip widths of $\frac{3}{4}$ '' (19 mm). Since LNS encountered problems with ring chipping due to the hard rock with quartz lenses, the cutter tip width is in some cases extended to 1''. Calculating the force per disc cutter, the total number of cutters is reduced from 46 to 45 since gauge cutters only contribute to a small percentage of the penetration of the tunnel face (s. chapter 3.1.1). For 19'' cutters, GIRMSCHIED set the maximum force at 300 kN (2013: 452), but Robbins stated 311 kN. Key information of the Robbins TBM used at Røssåga hydropower project is summarized in Tab. 11.

Tab. 11: Short key information on the machine design of Robbins open gripper TBM used at Røssåga tunnel.

Machine design Røssåga tunnel	
cutterhead diameter	7.2 m
max. thrust force	14 325 kN
max. revolution per minute	8.7 rpm
stroke length	1.9 m
no. of cutters	46
cutter diameter	19'' (483 mm)
cutter spacing	78.6 mm
cutter tip width (mean)	$\frac{3}{4}$ '' (19 mm) (partly 1'' (25 mm))
max. force per cutter	311 kN

3.2.2 Project geology Røssåga

The tunnel project is geologically located in metamorphic and magmatic rocks of the Caledonian orogeny. Main deformation took place in Silurian and Devonian where large nappes were thrust onto the Precambrian rock of the Fennoscandian shield. Based on different transportation distances, a classification of the Caledonian nappes into Lower / Middle / Upper and Uppermost Allochthon is performed. The Lower Allochthon shows small transportation distance, whereas the rocks of the Upper and Uppermost Allochthon have been transported over distances from about 300-400 km (RAMBERG et al. 2008: 200).

The study site is part of the Uppermost Allochthon that suffered only low degree of metamorphism and consists mainly of mica schists and mica gneisses, partly with calcareous percentage (Fig. 46). The rocks are pervaded by quartzite, marble and metasandstone layers and also by magmatic rocks such as granite or granodiorite that intruded around 400 Myr ago. No rock stress problems are to be expected since the maximum overburden is 200 – 300 m.

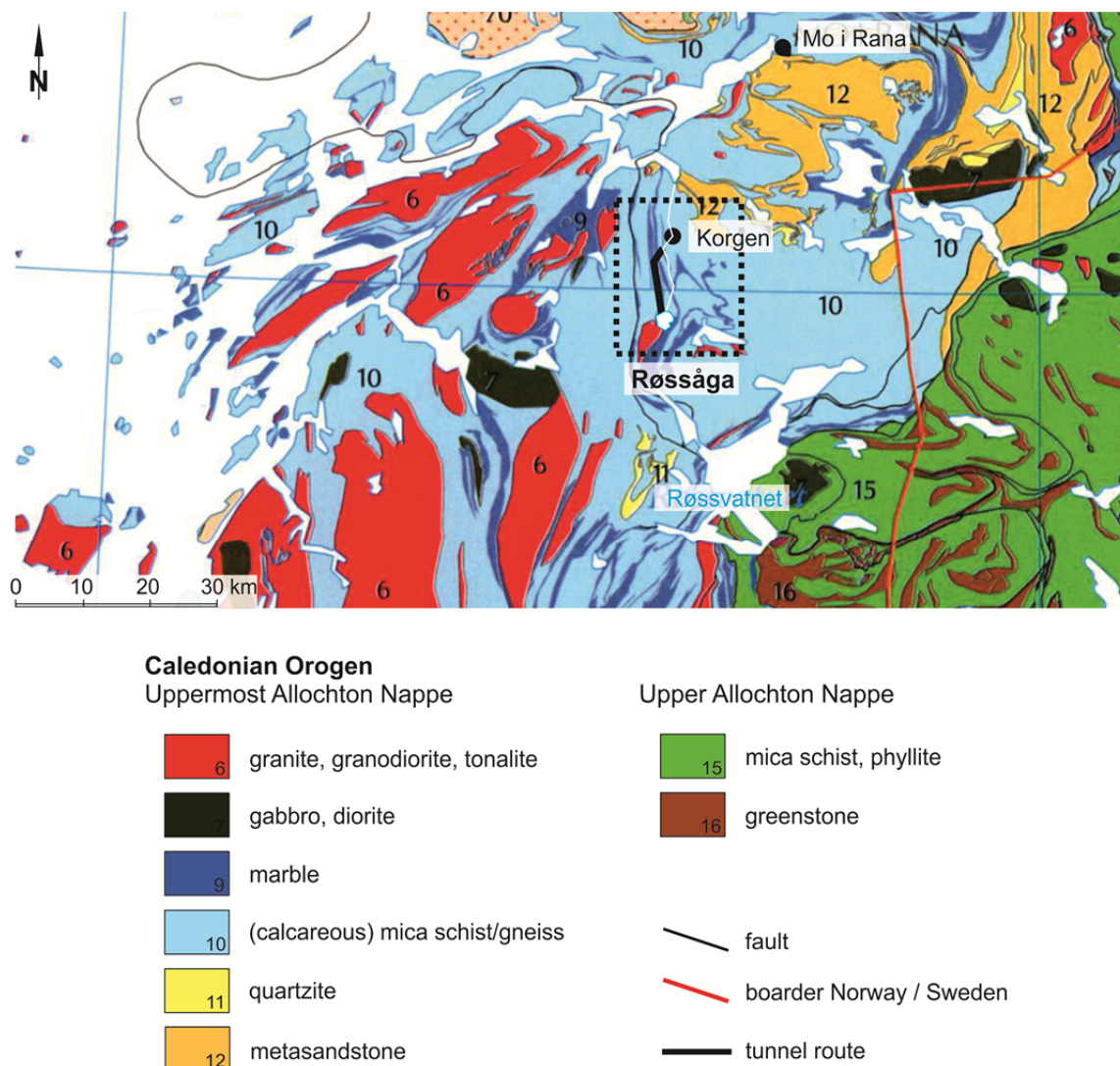


Fig. 46: Geological overview of the Røssåga tunnel project with planned tunnel route in rose (mod. from SOLLI & NORDGULEN 2006).

East of the project site the Upper Allochthon crops out with great variation in composition, deformation and degree of metamorphosis. Main rock types are greenstones, phyllites and mica schists.

Three main rock types could be observed at the analyzed 2,500 m tunnel length:

- (calcareous) mica schist
- granite
- quartzite

(Calcareous) mica schist

Main minerals of the dark grey mica schist are quartz and mica containing garnet as accessories. Schistosity is clearly visible due to the alternating layering of mica and quartz minerals causing an anisotropic fabric and a certain cleavage. Mica schist crops out at first 1,100 m of the TBM excavation. Same rock type appears again at about 2,200 m with the difference that the lime content raised significantly (calcareous mica schist) (Fig. 47). Some rock samples show an increasing percentage of feldspar minerals (mainly potassium feldspar) and can be classified as mica gneiss. For a detailed petrographic description, see chapter 5.1.1.2.

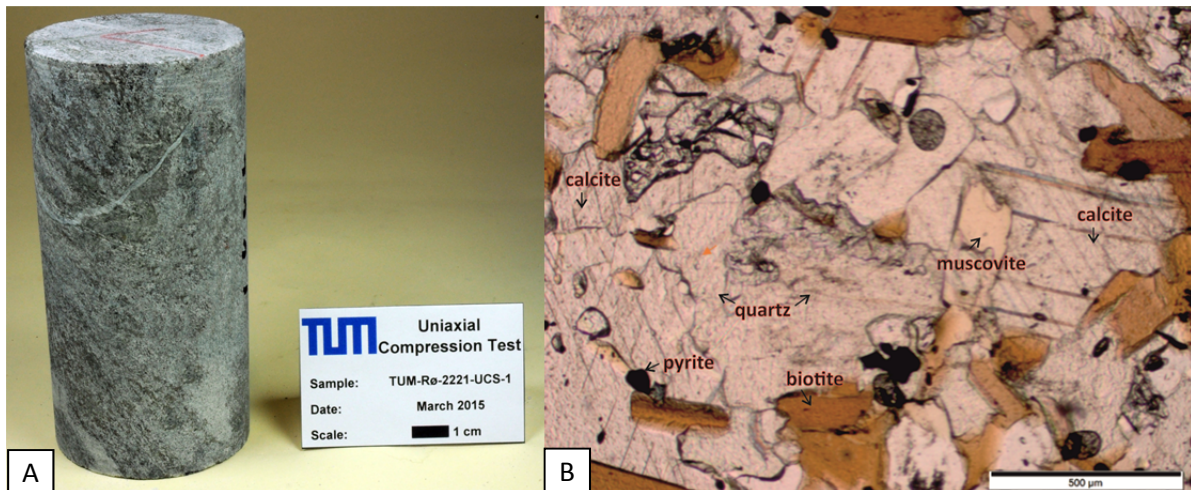


Fig. 47: Calcareous mica schist: specimen for uniaxial compression testing (A) and thin section analysis under plane polarized light (B). Detected minerals are quartz, calcite, muscovite and biotite.

Granite

This rock type mainly consists of xenomorphic quartz, feldspar and mica with a homogenous structure. In this area, the granite is developed as a fine-grained variety with a disorientated fabric. As feldspar members, more plagioclase than potassium feldspar can be observed. Mica content (mainly biotite) is thinly dispersed throughout the rock. This rock type did not appear in terms of geological back-mapping and is not explained further.

Quartzite

Light grey quartzite is mainly made up of xenomorphic quartz minerals that show no orientation. The rock is pervaded by spots of dark grey color that consist of mica, mainly biotite. Accessory feldspar (potassium feldspar and plagioclase) can be observed. Thin sections reveal that small grains of rutile are present as well (Fig. 48). The feldspar percentage and the type of feldspar vary to a certain degree. Quartzite with intersecting granite crops out at tunnel meter 1,100 – 2,000. For a detailed petrographic description, see chapter 5.1.1.2.

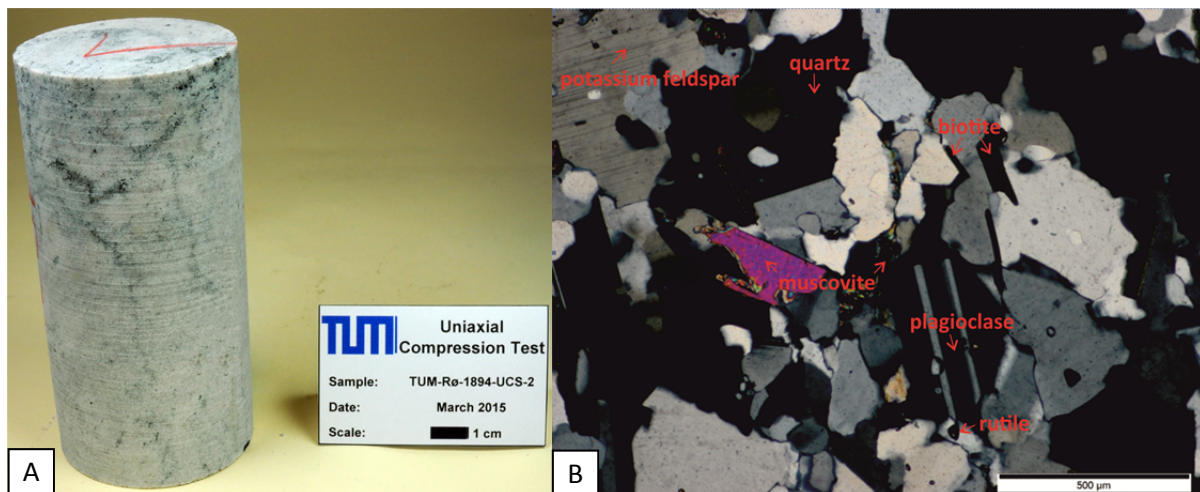


Fig. 48: Quartzite: specimen for uniaxial compression testing (A) and thin section analysis under crossed polarized light (B). Detected minerals are quartz, potassium feldspar, plagioclase, muscovite, biotite and rutile.

4 Methodology

To investigate the cuttability of rocks by tunnel boring machines, an extended laboratory program and field investigations have been performed. In a first step, the deformation behavior of rocks under load and thus rock toughness is analyzed by several laboratory testing methods described in chapter 4.1. The 25 tested rock types cover a wide area of existing rocks ranging from sedimentary to magmatic and metamorphic rocks. These measures serve as fundamental research with the aim of a consistent definition for rock toughness. The definition may be validated in a second step by field investigations in terms of penetration tests with tunnel boring machines. Furthermore, these tests are a useful tool to study general aspects of the interaction between the rock respectively rock mass and excavation tools such as disc cutters. The methodology of penetration tests is described in chapter 4.2. For proper analysis of conducted penetration tests, corresponding geotechnical parameters are obligatory. Therefore, the rock types encountered at tunnel projects where penetration tests are performed, are also investigated by following laboratory program. Investigations on the influence of discontinuity systems on the excavatability of rock mass in TBM tunneling are realized by detailed geological mapping of the tunnel face and side walls at chainages where penetration tests examine the relation between the applied thrust force and resulting penetration rates.

4.1 Laboratory testing

The laboratory testing program has been performed in the rock laboratories at the Chair of Engineering Geology at the Technical University of Munich. In total, 440 uniaxial compression tests, 340 Brazilian tensile tests, 350 point load tests, 100 Cerchar abrasivity tests, 100 LCPC abrasivity tests and 40 thin sections were performed and analyzed. Primarily, this provides a detailed data basis to study the deformation behavior of rocks under load and to correlate the deformation behavior with other geotechnical parameters that may characterize rock toughness. Furthermore, geotechnical parameters are inevitable to analyze conducted penetration tests at the Koralm and Rössåga tunnel and corresponding penetration prediction models properly. The following paragraphs explain the applied methods of each laboratory test.

4.1.1 Uniaxial Compression Test

Uniaxial compression tests were performed according to the German Recommendation No.1 for Uniaxial compression testing with free lateral expansion (DGGT 2004), following the suggested methods of ISRM (1979).

Cylindrical samples were cut to a length/diameter ratio of about 2:1 with minimum diameter of 5 cm to meet the recommendation that states diameter must be at least 10 times the largest grain. If the ratio is less, the resulting uniaxial compressive strength (UCS) was recalculated according to OBERT & DUVAL (1967) (s. Eq. 4-2). Since foliation (schistosity, layering etc.) of rocks shows a distinct correlation of the UCS with the angle between foliation and loading direction (THURO 1996: 110), the foliated samples were prepared with an angle of 90° between foliation and loading direction whenever possible.

The specimen ends were ground by a lapping machine to smooth the surface and to prepare coplanar and right-angled end planes.

Testing procedure

The tests were performed using the large loading frame (2,000 kN nominal load) of the servo-controlled hydraulic press (*ToniNorm*) which is shown in Fig. 49. The machine fits the accuracy requirements of class 1 in the German standard DIN 51220 and DIN EN ISO 7500-1. Before starting the test, the specimen dimensions were measured. This included the length in two perpendicular planes and the diameter at both end planes and in the center, each measured in two perpendicular directions. The samples were loaded with a constant deformation rate depending on the length and diameter of the specimen (DGGT 2004) until total failure of the rock occurred. One testing series was conducted with loading rates deviant from the DGGT recommendation to investigate the influence on the uniaxial compressive strength and the deformation behavior of the samples (s. chapter 5.1.3). During the test, axial, as well as lateral deformation of the sample could be measured using three digital inductive displacement transducers (HBM W5TK, www-07) and a strain measurement chain with a lateral displacement transducer (RDP Group D6, www-08) connected parallel to record the stress-strain curves.

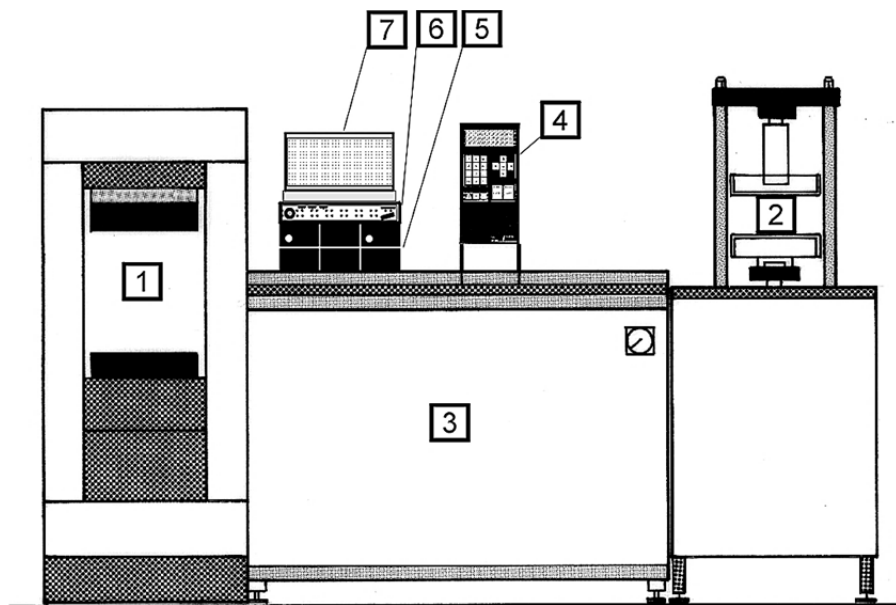


Fig. 49: Front view of "ToniNorm" Compression Testing Machine at the Chair of Engineering Geology (PLINNINGER 2002: 128).

- | | |
|--|---|
| ① Loading frame 1 (2000 kN nominal load) | ② Loading frame 2 (200 kN nominal load) |
| ③ „Powerbox“ (hydraulic unit) | ④ „ToniTrol“ control unit |
| ⑤ + ⑥ Measurement amplifiers for deformation recording | ⑦ Desktop PC with software „TestXpert“ |

Test analysis and classification

During the test, the failure load of the sample and the corresponding strain measurements were recorded with the help of the software *TestXpert*. In a second step, the uniaxial compressive strength (σ_u) was calculated as follows (Eq. 4-1).

$$\sigma_u = \frac{F_{\max}}{A} \quad \text{Eq. 4-1}$$

σ_u	uniaxial compressive strength [MPa]
F_{\max}	failure load of the sample [kN]
A	cross-section area of the sample [mm ²]

If the sample length-to-diameter ratio is less than 2, the UCS was adjusted using the Eq. 4-2 by OBERT & DUVAL (1967).

$$\sigma_{u(2)} = \frac{8 \cdot \sigma_u}{7 + 2 \cdot \frac{d}{l}} \quad \text{Eq. 4-2}$$

$\sigma_{u(2)}$	revised uniaxial compressive strength [MPa]
d	sample diameter [mm]
l	sample length [mm]

To describe the deformation behavior of the samples, the Young's modulus (E modulus in English, V modulus in German) was calculated in the linear-elastic, pre-failure part of the stress-strain curve since the ratio of the axial stress change to the axial strain change between around 40 and 60 % of maximum strength. According to the ISRM (1979), this modulus is called tangent Young's modulus E_t , which is generally measured at 50% of uniaxial compressive strength. The same procedure was also applied to describe the non-linear plastic part of the stress-strain curve. This modulus calculates the gradient between 40 and 100% of σ_u and is called E_{pl} modulus (V_{pl} in German) in this thesis (Fig. 50). This method, used to implement the plastic deformation range, is easy to determine and offers a simple application. Even if no lateral strain measurements are available to set the exact threshold from elastic to plastic determination (s. Fig. 54), the E_{pl} modulus can be applied. However, it must be noted that it is only an approximate determination.

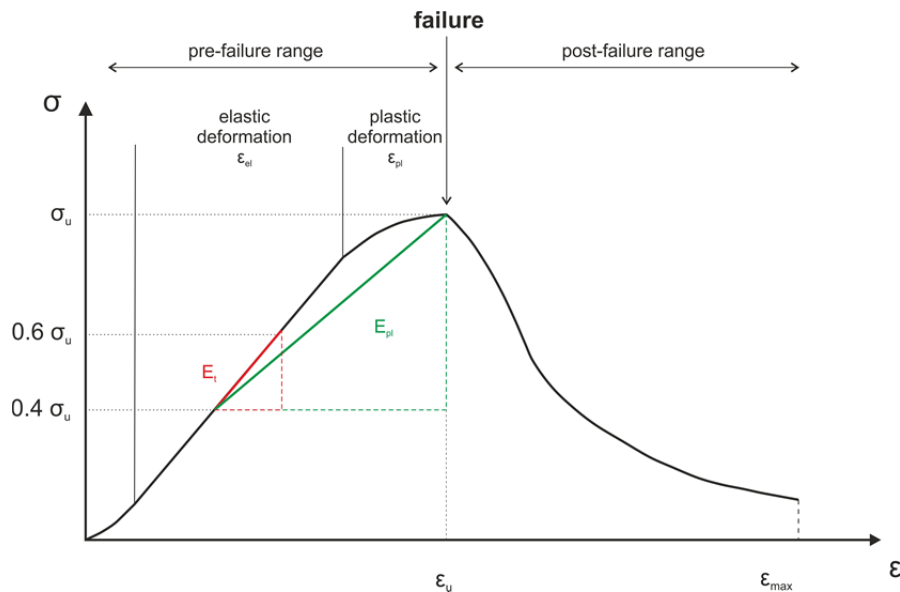


Fig. 50: Schematic stress-strain curve showing the determination of the Young's modulus (E_t) and the Young's modulus including plastic deformation range (E_{pl}).

$$E = \frac{\Delta \sigma}{\Delta \varepsilon} \quad \text{Eq. 4-3}$$

E	Young's modulus [GPa]
$\Delta \sigma$	axial stress change [MPa]
$\Delta \varepsilon$	axial strain change [mm]

Another aspect to describe the deformation behavior of rocks is captured in HUGHES (1972), GEHRING (1995) and THURO (1996) by taking the aspect of energy assumption during uniaxial compression into account. HUGHES and GEHRING focus on the energy in the pre-failure range (**failure energy**), while THURO characterizes the energy including the post-failure range (**destruction work**). These approaches were considered by calculating the work based on integration (Eq. 4-4, Eq. 4-5), whereby the areas beneath the stress-strain curve were described (Fig. 51). A specific description of these parameters is given in chapter 2.4.

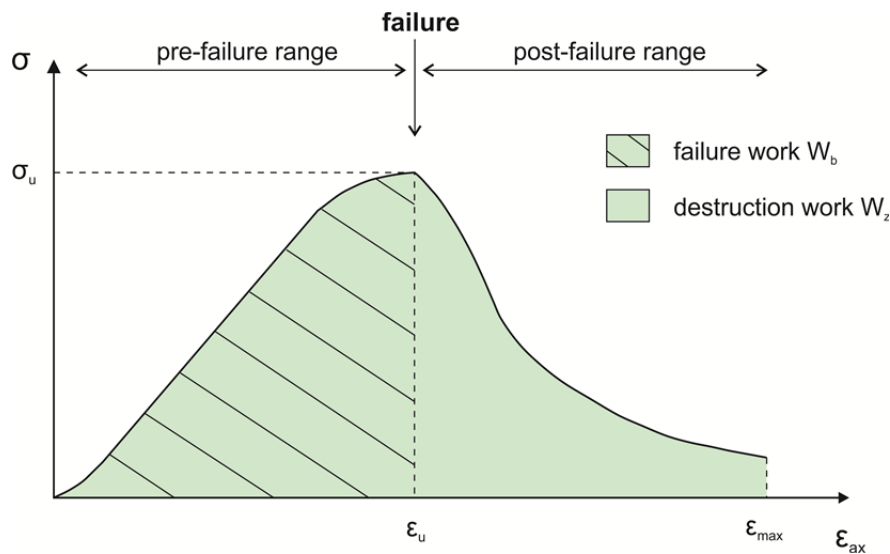


Fig. 51: Schematic stress-strain curve including the parameters of failure work W_b and destruction work W_z .

$$W_b = \int_0^{\varepsilon_u} \sigma \, d\varepsilon \quad \text{Eq. 4-4}$$

W_b	failure work [kJ/m ³]
ε_u	axial strain at UCS [mm/mm]
ε	axial strain [mm/mm]
σ	stress [MPa]

$$W_z = \int_0^{\varepsilon_{max}} \sigma \, d\varepsilon \quad \text{Eq. 4-5}$$

W_z	destruction work [kJ/m ³]
ε_{max}	maximum axial strain [mm/mm]
ε	axial strain [mm/mm]
σ	stress [MPa]

After analyzing the test, each sample was classified by its strength according to the ISRM (1979: 348) suggested method for quantitative description of discontinuities (Fig. 52) and by its destruction work according to THURO (2000) (Tab. 12).

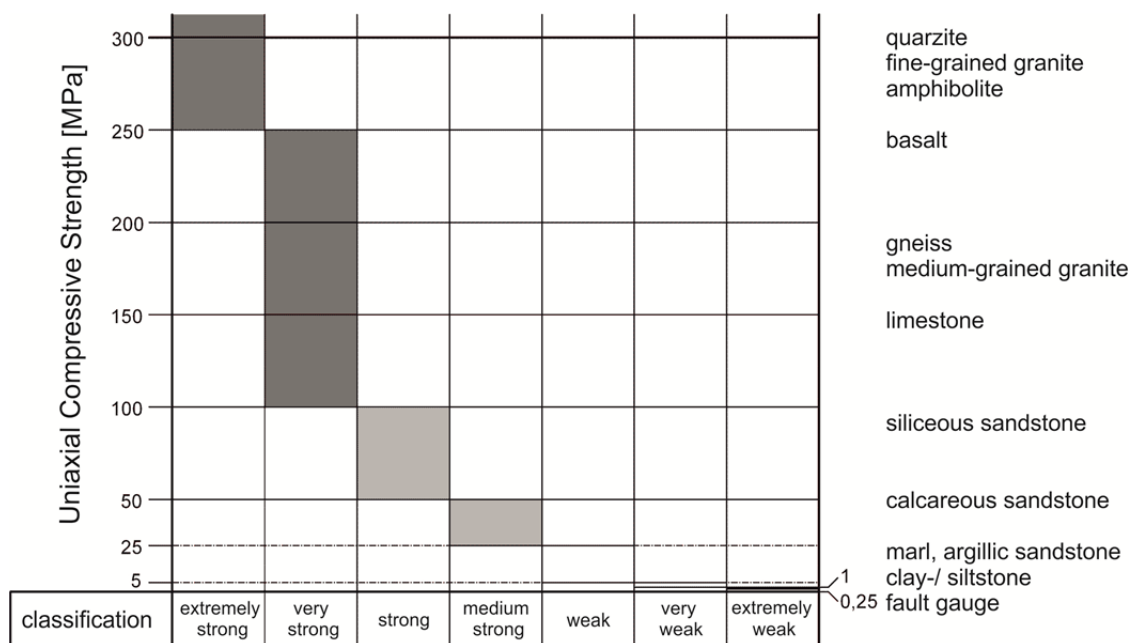


Fig. 52: Classification of the uniaxial compressive strength of hard rocks adapted from to the ISRM suggested method (1978: 348) with chosen rock type examples by THURO (1996: 55).

Tab. 12: Classification of destruction work according to THURO (2000).

Destruction Work W_z [kJ/m ³]	Classification
< 25 kJ/m ³	very low destruction work
25 – 50 kJ/m ³	low destruction work
50 – 100 kJ/m ³	moderate destruction work
100 - 250 kJ/m ³	high destruction work
250 – 500 kJ/m ³	very high destruction work
> 500 kJ/m ³	extremely high destruction work

Furthermore, the different modes of failure (Fig. 53) such as simple or multiple shear, i.e., simple or multiple extension, were recorded (SZWEDZICKI 2007: 99).

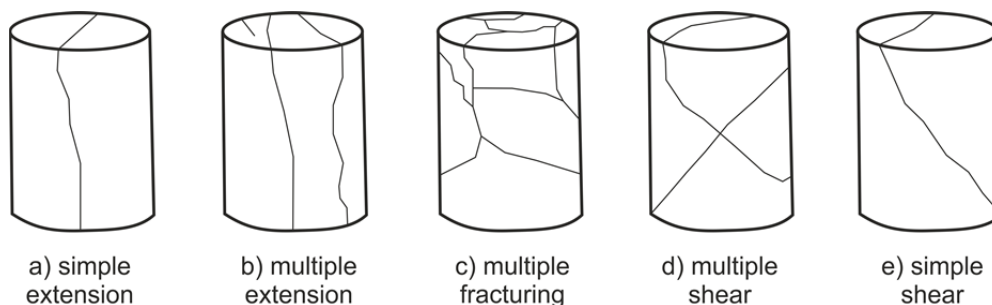


Fig. 53: Failure modes of tested rock samples after uniaxial compression (mod. from SZWEDZICKI 2007: 99).

The detailed description of existing deformation stages of rocks under uniaxial compression is described in detail in chapter 2.4.3. Axial and lateral strain values were measured during the test. In a second step, the volumetric strain was calculated according to PAULDING (1966) using Eq. 4-6.

$$\varepsilon_{\text{vol}} = \varepsilon_{\text{ax}} + 2 \varepsilon_{\text{lat}} \quad \text{Eq. 4-6}$$

ε_{vol}	volumetric strain [%]
ε_{ax}	axial strain [%]
ε_{lat}	lateral strain [%]

The following paragraphs will explain the evaluation procedures used to determine existing thresholds which depend on axial, lateral and volumetric strain (Fig. 54).

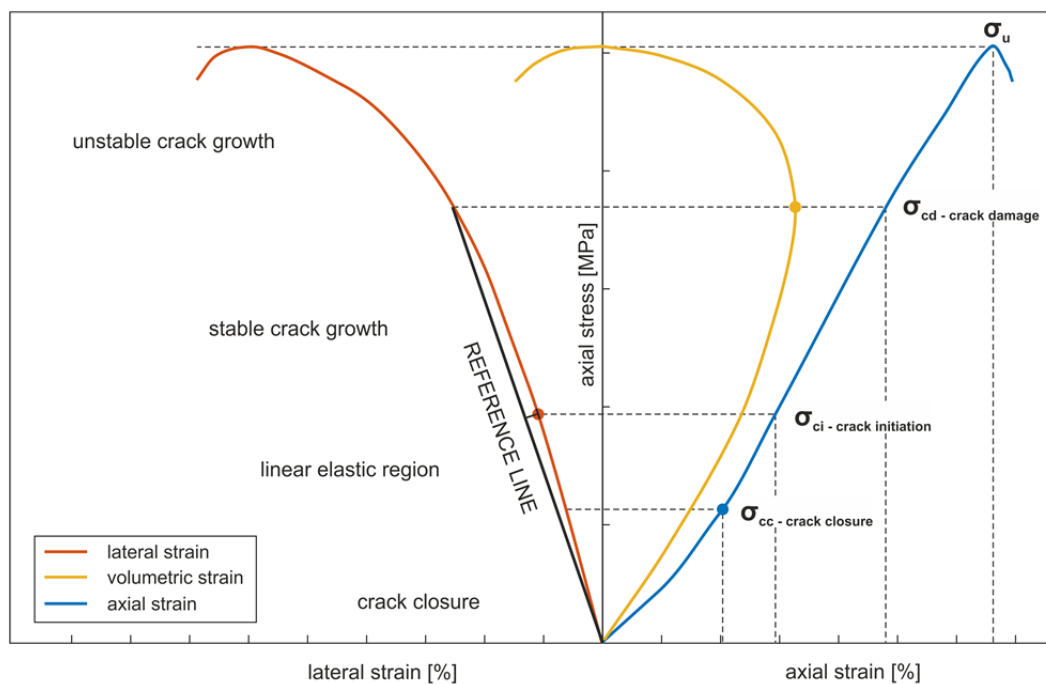


Fig. 54: Stress-strain diagram showing lateral, volumetric and axial strain and corresponding thresholds for crack closure, crack initiation and crack damage (mod. from MARTIN 1993: 77). In addition, the deformation stages acc. to BIENIAWSKI (1967) are plotted.

Crack closure threshold σ_{cc}

Crack closure point is characterized by the **axial strain** curve. It describes the starting point of linearity and therefore elastic deformation of the sample (BRACE 1964, BIENIAWSKI 1967). Since truly linear behavior is never reached, the determination of this threshold entails an element of uncertainty. Moving point regression of the axial stress-strain curve might be one possibility to set the threshold. Since changes in the slope of the curve have to be detected, the first derivative is suitable (EBERHARDT et al. 1998). Best results may be achieved by simultaneous acoustic emission measurements. The threshold is marked by a distinct decrease of acoustic events as existing cracks are closed and no new cracks are formed in the elastic region. However, crack closure threshold is not discussed in this thesis since it does not provide important information concerning the deformation behavior of rocks. For further information, see also WIESER (in prep.).

Crack initiation threshold σ_{ci}

Crack initiation is characterized by the **lateral strain** curve. It describes the point where lateral strain departs from linearity (LAJTAI 1974). In this thesis, the inflection point has been calculated using the lateral strain response method by NICKSIAR & MARTIN (2012: 612). Here, a linear reference line from zero stress to the onset of unstable crack growth (σ_{cd}) was drawn (Fig. 54). In a second step the deviation between lateral strain and reference line was determined. The point of maximum deviation marks the inflection point and was set as crack initiation point σ_{ci} .

Crack damage threshold σ_{cd}

Crack damage is characterized by the **volumetric strain** curve. It marks the point of maximum volumetric strain (BRACE 1964, BIENIAWSKI 1967). Exceeding the threshold of crack damage leads to unstable crack growth, explosive increase of crack formation, and irreversible damage of the specimen. This threshold can be clearly determined and is the most important factor in the investigation of rock toughness. During unstable crack growth, sliding along mineral cleavage cracks, flaws or grain boundaries is initiated leading to plastic deformation which is decisive for tough failure behavior.

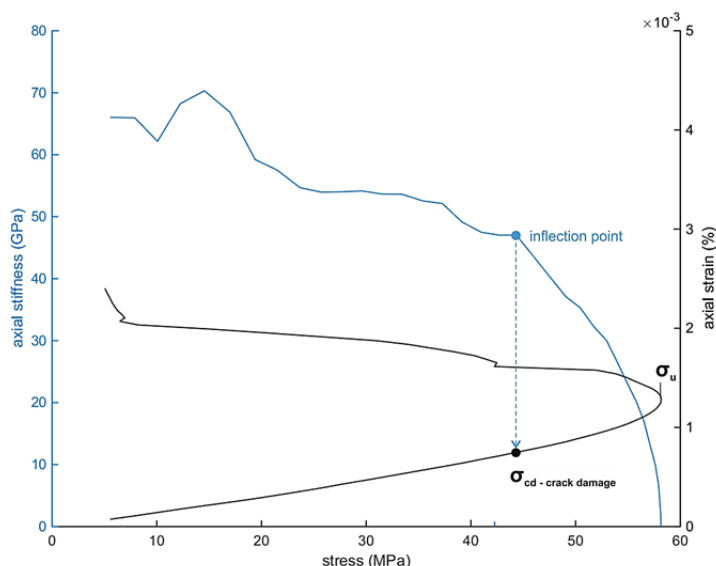


Fig. 55: Axial stiffness curve calculated by first derivation of axial stress-strain curve using moving point regression. Crack damage threshold is set by the inflection point in axial stiffness.

If no lateral strain measurements were possible, second method could be used to determine the crack damage threshold. The point does not only mark the maximum volumetric strain, but also the inflection point in the axial stress-strain curve. Passing this threshold results in a nonlinear relation between axial stress and axial strain (MARTIN 1993: 90). The inflection point could be determined by calculating the first derivation of the stress-strain curve to make changes in the slope obvious (Fig. 55). The first derivation is synonymous to the term of axial stiffness (EBERHARDT et al. 1998: 225). By using a moving point regression, the function of axial stiffness could be smoothed to simplify the determination of the inflection point.

The abovementioned thresholds were determined using a MATLAB[®] script programmed by Carola Wieser in terms of her doctoral thesis (WIESER in prep.). Summarized results of all tests are shown in Appendix A.

4.1.2 Brazilian Tensile Test

Brazilian tensile tests were performed according to the German Recommendation No.10 for indirect tensile test (DGGT 2008) following the suggested methods of ISRM (1979). This testing procedure was used as an indirect method to determine the Brazilian tensile strength (BTS) of rock samples.

The rock samples were cut with a water-cooled diamond saw into cylindrical samples with a length-to-diameter ratio of 0.5.

Testing procedure

The small loading frame of the servo-controlled hydraulic press with a nominal load of 200 kN was used for loading and measurement of the failure load. First of all, the specimen dimensions were measured including the length and diameter, each in two perpendicular planes. The loading frame is equipped with a BTS frame yoke that keeps the specimen in the right position during the test (Fig. 56). The samples were loaded until failure and the maximum load is recorded using the software *TestXpert*.

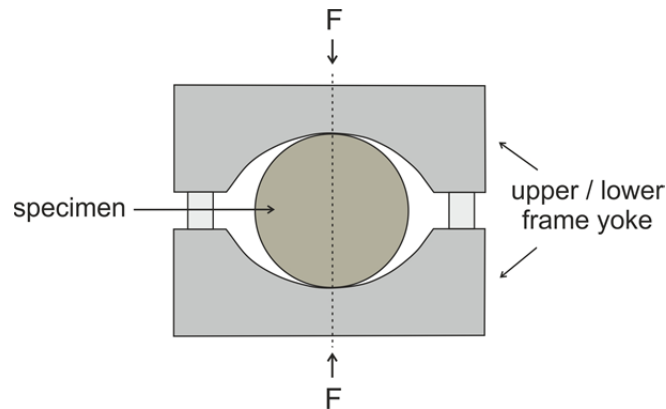


Fig. 56: Experimental setup of Brazilian tensile test with loading direction F .

Test analysis

The Brazilian tensile strength was derived from the failure load and the area of the failure surface using Eq. 4-7.

$$\sigma_t = \frac{2 \cdot F_B}{\pi \cdot d \cdot l} \quad \text{Eq. 4-7}$$

σ_t	Brazilian tensile strength [MPa]
F_B	failure load [N]
d	sample diameter [mm]
l	sample length [mm]

Summarized results of all tests are shown in Appendix A.

4.1.3 Point Load Test

The Point Load Test was performed according to the testing recommendation of the ISRM (1985) and DGGT (2010). Hereby the **point load index (I_p)** was calculated which can be used as an indirect method to determine the uniaxial compressive strength of rocks. Rock samples were cut into cubic samples with a standardized edge length of 50 mm whenever possible.

Testing procedure

Point Load Tests were conducted by two different testing procedures – servo-controlled hydraulic press and hydraulic hand pump.

At the beginning of the testing procedure, the small loading frame of the servo-controlled hydraulic press with a nominal load of 200 kN was used for loading, and for the measurement of the failure load (Fig. 49). First, the loading frame was equipped with point load testing pins and the specimen dimensions were measured. The samples were loaded with a constant loading rate of 3 kN/sec until failure of the specimen occurred. The maximum loading rate was recorded using the software *TestXpert*.

Second, the testing was performed by a hydraulic hand pump by *Wille Geotechnik*. It is equipped with a small loading frame, point load testing pins and an electronic manometer. The cubic sample was loaded by slowly pressing the hydraulic hand pump till maximum loading was reached and the failure occurred. This means the sample was loaded with a non-constant loading rate. The maximum force can be directly read from the manometer.

After the test, the geometry of the failure surface of the specimen was determined with a sliding caliper by two perpendicular measurements. Whenever possible, 10 rock cubes were tested for one sample number to calculate a mean value of I_s .

Test analysis

The point load index I_s was derived from the failure load and the failure surface of the block specimens (Eq. 4-8). It must be noted that the calculation of the failure surface area does not meet the ISRM recommendation from 1985, since it implies diametric testing on cylindrical specimens.

$$I_s = \frac{F_B}{A} = \frac{F_B}{h \cdot l} \quad \text{Eq. 4-8}$$

I_s	point load index [MPa]
F_B	failure load [N]
A	area of failure surface [mm ²]
h	sample height [mm]
l	sample length [mm]

Since the point load index is significantly influenced by sample size, the scale effect has to be considered when using block specimens with other than 50 mm edge length. Therefore, BROOK (1993) suggested the following correction factor to convert I_s to a standard sample dimension of 50 mm length:

$$I_{s(50)} = \left(\frac{A}{2500} \right)^{0.225} \cdot I_s \quad \text{Eq. 4-9}$$

$I_{s(50)}$	point load index for 50 mm edge length [MPa]
A	area of failure surface [mm ²]
I_s	point load index [MPa]

From $I_{s(50)}$, the uniaxial compressive strength σ^* was derived using the correction factor c (Eq. 4-10). The correction factor is an empirically determined constant which is set at $c \sim 20$ up to now, on the

basis of results from different studies. Since values for c can vary, the derived uniaxial compressive strength should only be considered as an approximation and is not used in this thesis.

$$\sigma^* = c \cdot I_{S(50)} \quad \text{Eq. 4-10}$$

σ^*	derived uniaxial compressive strength [MPa]
c	correction factor ~ 20 [-]
$I_{S(50)}$	point load index for 50 mm edge length [MPa]

Summarized results of all tests are shown in Appendix A.

4.1.4 Cerchar Abrasivity Test

The Cerchar Abrasivity Test was performed according to the testing recommendation of the Centre d'Etudes de Charbonnages de France (CERCHAR 1986) and ISRM (2014). A new draft of the German Society for Geotechnics with recommendations regarding the Cerchar abrasivity testing is in preparation at this time (DGGT in prep.). Hereby, the **Cerchar abrasivity index (CAI)**, which is an indicator for the abrasiveness of rocks causing wear on excavation tools, was determined. In this particular case, a steel pin with a standardized hardness (Rockwell HRC 54-56) is tested.

In most cases, rock samples with a rough surface, which was produced by fracturing the rock, were used for the Cerchar Abrasivity Test. In few countries, e.g. Austria, the CAI is usually determined on samples with a saw cut surface. Some tests were performed under these conditions, in which case, it is stated in the laboratory form. In ISRM (2014), a correlation and conversion for rough and saw cut surfaces are presented resulting in Eq. 4-11.

$$CAI_{\text{rough}} = CAI_{\text{saw cut}} \cdot 1.14 \quad \text{Eq. 4-11}$$

Testing of anisotropic or inhomogeneous rocks was carried out with foliation perpendicular to testing direction whenever possible.

Testing procedure

The testing device (Fig. 57) used in the laboratory is the modified Cerchar device according to WEST (1989). During the test, a steel pin was scratched over 10 mm of a sample surface under a static load of 7 kg. For each sample this procedure was repeated at least five times. In a second step, the resulting wear of the steel pins were determined with an accuracy of 0.02 mm using a reflected-light binocular microscope with a measuring scale. Each pin was measured in four perpendicular directions. The results were averaged afterwards.

Test analysis and classification

The Cerchar abrasivity index (CAI) was calculated using Eq. 4-12. A classification of the abrasiveness of each sample was done according to the classification table (Tab. 13).

$$CAI = d \cdot 10 \quad \text{Eq. 4-12}$$

CAI	Cerchar abrasivity index [-]
d	average wear of pin [mm]

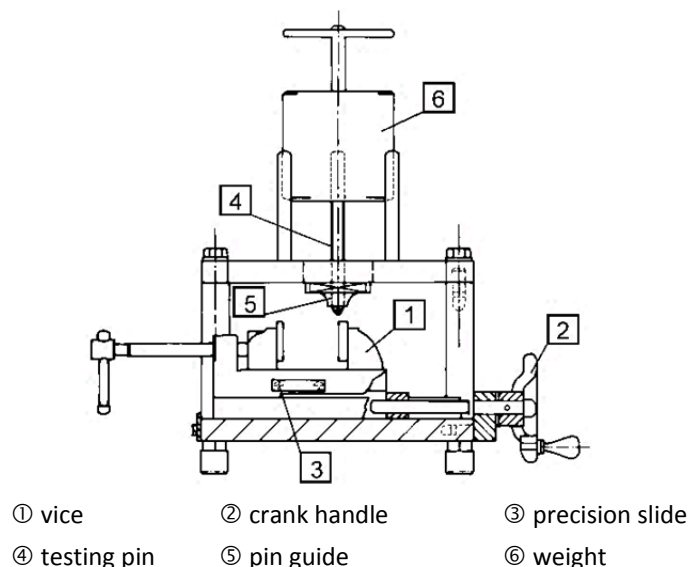


Fig. 57: Cerchar device for the determination of the Cerchar abrasivity index (mod. from WEST 1989).

Tab. 13: Abrasiveness classification using the Cerchar Abrasivity Test (acc. to CERCHAR 1986: 7).

CAI [-]	Classification
0.3 – 0.5	not very abrasive
0.5 – 1.0	slightly abrasive
1.0 – 2.0	medium abrasive
2.0 – 4.0	very abrasive
4.0 – 6.0	extremely abrasive

Summarized results of all tests are shown in Appendix A.

4.1.5 LCPC Abrasivity Test

LCPC Abrasivity Tests were performed according to the French Standard P 18-579 (AFNOR 1990). The *Laboratoire Central des Ponts et des Chaussées* (LCPC) developed this test for the determination of the abrasiveness (LCPC abrasivity coefficient - LAC) and breakability (LCPC breakability coefficient - LBC) of hard rock.

Testing procedure

The tests were performed using an abrasivity testing device (Fig. 58) according to the French Standard P 18-579 (AFNOR 1990). For LCPC abrasivity testing, $500 \text{ g} \pm 2 \text{ g}$ air-dried sample material of the fraction 4 – 6.3 mm is needed. Therefore, rock samples were crushed and sieved until sufficient sample material of the stated fraction was produced. The material was filled into the sample container through the funnel tube. Before filling, a rectangular metal impeller with a standardized quality (Rockwell B60-75) and dimension was weighted and mounted. After starting the test, the impeller rotated for five minutes with a speed of 4,500 rpm in the sample container. The weight of the impeller after testing was recorded and the mass loss was calculated for the characterization of the sample

abrasiveness (LAC). By sieving the tested sample material and determining the fraction below 1.6 mm, conclusions on the breakability (LBC) or brittleness of the sample material can be drawn (Eq. 4-14).

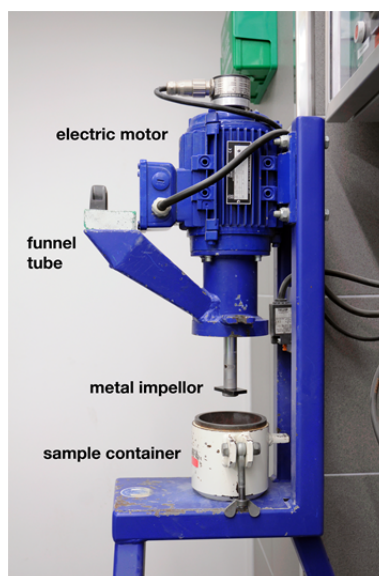


Fig. 58: LCPC testing device at the Chair of Engineering Geology with a 700 W electric motor.

Test analysis

For the determination of the LCPC abrasivity coefficient (LAC) and the LCPC breakability coefficient (LBC), Eq. 4-13 and Eq. 4-14 were used.

$$\text{LAC} = \frac{m_{F0} - m_F}{M} \quad \text{Eq. 4-13}$$

LAC	LCPC abrasivity coefficient [g/t]
m_{F0}	mass of metal impeller prior test [g]
m_F	mass of metal impeller after test [g]
M	sample mass [t]

$$\text{LBC} = \frac{100 - M_{1.6}}{M} \quad \text{Eq. 4-14}$$

LBC	LCPC breakability coefficient [%]
$M_{1.6}$	mass of sample material < 1.6 mm after test [g]
M	sample mass [g]

The LAC of soft and hard rocks normally ranges between 0 and 2,000 g/t. This range is divided into six abrasivity classes shown in Tab. 14. The classification can also be correlated with the Cerchar abrasivity index (CAI), which nearly shows a linear correlation to the LAC (THURO et al. 2006, THURO & KÄSLING 2009).

Tab. 14: Classification of the LCPC abrasivity coefficient LAC in accordance to the Cerchar abrasivity index CAI with chosen rock type examples (mod. from THURO et al. 2006: 40).

LAC [g/t]	CAI [-]	Classification	Rock type examples
0 – 50	0.0 – 0.3	not abrasive	wood, turf
50 – 100	0.3 – 0.5	not very abrasive	clay-silt stone, marl
100 – 250	0.5 – 1.0	slightly abrasive	schist, sandstone (fine grained, argillaceous cement), limestone (pure), marble (pure)
250 – 500	1.0 – 2.0	medium abrasive	limestone (sandy), marble (containing quartz) sandstone (calcareous cement)
500 – 1250	2.0 – 4.0	very abrasive	sandstone (siliceous cement), porphyry, andesite, basalt, phyllite, mica schist, some amphibolites
1250 – 2000	4.0 – 6.0	extremely abrasive	(vein-) quartz, granite, quartzite, eclogite, gneiss, some amphibolites

Summarized results of all tests are shown in Appendix A.

4.1.6 Thin section

An overview of the petrography of tested rock samples was obtained primarily by macroscopic analysis. In a second step, thin sections were prepared from each rock type for a detailed petrographic description by means of transmitted light microscopy. In total, 40 thin sections were evaluated.

Testing procedure

Thin sections were analyzed, using the microscope equipment by *Leica (DMLM)* with a 25 to 500-times magnification. Pictures of the thin sections were recorded with a 5-megapixel digital camera by *Olympus (DP25)*.

Test analysis

The minerals were identified during the qualitative analysis by their optical characters. As testing method, polarized light microscopy was used with two different filters (polarizer and analyzer). The two filters have their polarizing planes orientated perpendicular to one another. Therefore, analysis under plane and crossed polarized light could be performed. By means of this method, each mineral was described by its inherent color and interference color. Also an appraisal of the structural fabric and the degree of weathering and alteration was done. Exemplary analysis of calcareous mica schist under plane and crossed polarized light is shown in Fig. 59.

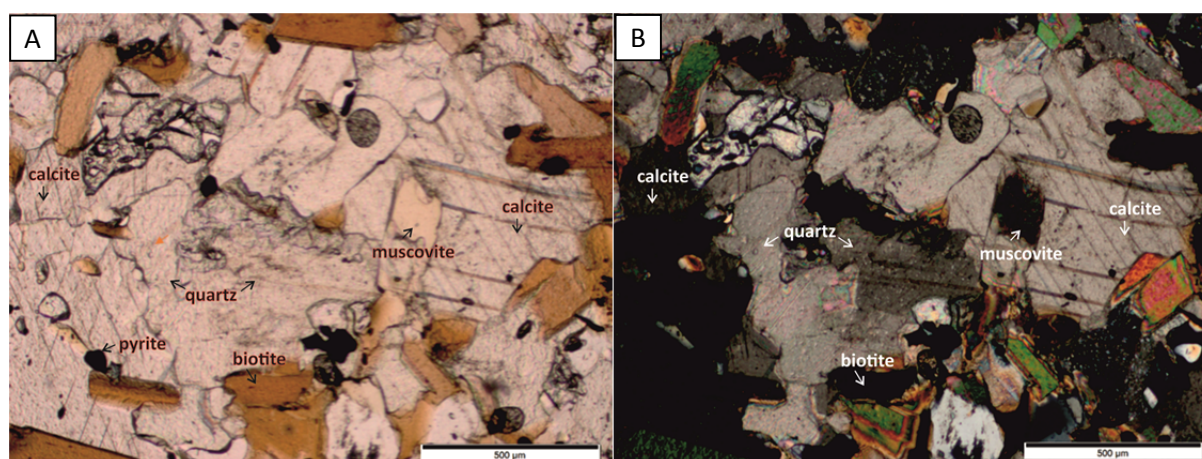


Fig. 59: Thin section analysis of calcareous mica schist under plane (A) and crossed (B) polarized light.

Results of thin section analysis are incorporated in the petrographic descriptions in chapter 5.1.1.

4.2 Field investigation

In combination with the laboratory testing program, field investigations were performed. A large part of the field work focused on the two considered tunnel projects (s. chapter 3). Schematic geological mapping was done as well at each quarry where material for laboratory testing has been taken.

4.2.1 Penetration test

The basic knowledge about penetration prediction and the theoretical background about the excavation process with a tunnel boring machine (TBM) have already been described in chapter 2. To validate the results of penetration prediction models, penetration tests were performed on-site. During the last years, more than 30 tests were conducted and analyzed at the Koralm tunnel and the Rössåga hydro-power project. In this thesis, the basic testing procedure (start-stop test) is taken by FRENZEL et al. (2012) and adapted in certain points. Before performing the test, it should be ensured that the tunnel face is stable and disc cutters are in good condition so that the cutter tip width of mounted cutters is not varying too much. These requirements are often met after daily cutterhead inspections. Another advantage is the possibility to enter the cutterhead during maintenance for a geological documentation of the tunnel face in the area of the penetration test. To validate the geological documentation, geotechnical parameters are necessary. For that purpose, rock cores were taken from the area surrounding of the test location for a laboratory program (s. chapter 4.1). Whenever possible, the penetration tests were performed after cutterhead inspection.

Testing procedure

During a penetration test, the TBM was operated under normalized conditions for a defined time interval which allowed the comparison between different test sites. The testing procedure is divided into four main phases.

First step is the determination of the friction via **friction stroke** (free stroke) right before the penetration test in order to gain information about the interaction between rock mass and the shield of the machine. Since different tunnel routes (straight line or curve), geology and machine types cause different friction values, this parameter has to be taken into account to ensure comparability. Therefore, the cutterhead was retracted from the tunnel face by approximately 40 cm and then pushed again forward with the average rotation speed and advance rate of the previous strokes. If the thrust was reasonably constant over a distance of 10 cm, the friction stroke could be finished and the cutterhead could be pushed forward close to the tunnel face without touching it (FRENZEL et al. 2012).

The main part of the penetration test is the **start-up** and **slow-down** phase. Before this step, the TBM should perform active excavation for few minutes to eliminate side effects such as preconditioned tunnel face. In this thesis, the suggested method by FRENZEL et al., explained in chapter 2.2, is adapted in some points. The advance rate (and so resulting thrust) was slowly increased to the maximum possible level at steps not exceeding 2,000 kN per 60 seconds with the average rotation speed of previous strokes. The maximum level was either given by maximum torque, thrust or penetration rate at a given geological environment and machine setup. When achieving the maximum level, the thrust should be kept constant for a short time to gain a detailed data set at this point. Afterwards, the advance rate was decreased slowly to zero thrust force respectively zero penetration by the same procedure as the start-

up process. The slow-down process should provide a validation of the start-up phase, since at the beginning of the test no pre-conditioning of the rock mass is given.

The last part of a penetration test was a **variation of the cutterhead rotational speed** to investigate whether decreasing cutterhead speed causes increasing penetration rates. If so, this can be a viable option to reduce wear at the cutters. To determine the coherence between rotational speed and penetration, the cutterhead rotational speed was set to the maximum possible given by geological conditions (FRENZEL et al. 2012). According to FRENZEL et al., the advance rate should be decreased until 50 % of maximum thrust is reached. However, first tests showed that a decrease of 50 % led to penetration rates lower 1 mm/rev. Consequently, the tests were conducted with 80 – 90 % of maximum thrust. Then, the rotational speed was reduced in steps from 1 rpm keeping the rotational speed constant for at least 3 minutes at each step. The test was finished when maximum torque or penetration was reached. During this procedure, the advance rate should remain unchanged.

Test analysis

The main result of a penetration test is the relationship between force and resulting penetration (Fig. 60 left). A detailed analysis is only possible if the following TBM parameters are recorded in 10 sec steps during the test: date and time, advance rate, rotation speed of the cutterhead, cutterhead torque, thrust force and resulting penetration rate. The friction force, the number and geometry of disc cutters, as well as the design of the cutterhead should be noted to calculate and plot the normal force per cutter (Fig. 60 right). First analysis has been done taking 100 % of measured friction into account. In a second step, results have been investigated for friction values of 50 % to account for the benefit of cutterhead vibration during the active boring process.

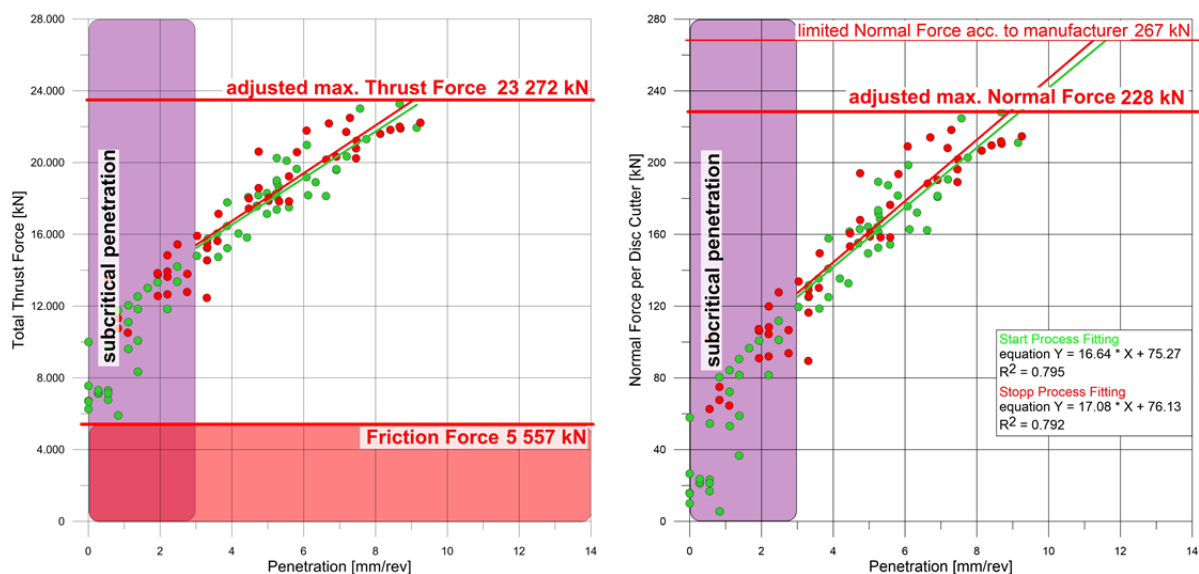


Fig. 60: Thrust-penetration curve including measured friction derived from a penetration test (left) and corresponding plot with normal force per disc cutter (right).

At penetration rates lower 3 mm/rev, data points spread wider and the slope of the regression line is steep. After passing the range of the subcritical penetration, data points generate a regression line with flatter slope and less fluctuation in measured data.

The validation of penetration prediction was carried out by using the Colorado School of Mines (CSM) model and the Gehring model. For a detailed description, see chapter 2.3. Both prediction

models need certain basic input parameters that are composed of geologic-geotechnical factors and machine-specific parameters. These include uniaxial compressive strength, Brazilian tensile strength, cutter ring diameter, cutter tip width, and cutter spacing.

4.2.2 Geological mapping and sample acquisition

For proper analysis of penetration tests, a detailed geological mapping is mandatory. The realization of mapping proved to be difficult depending on the machine type that excavates the tunnel. The Koralm tunnel project uses a double shield TBM, whereas the Røssåga hydropower project utilizes an open gripper TBM. Therefore, two different methods of mapping have been applied.

At the Koralm tunnel, **geological face mapping** was the sole possibility to take a look at the excavated rock mass since the side walls were covered with concrete segments. However, this could only be achieved to a limited extent via small inspection openings in the cutterhead and in the shield. The mapping was restricted to small areas and did not give a full overview of surrounding rock mass and discontinuity pattern. For this reason, it was extremely important to ensure geological face documentation as close as possible to the performed penetration test. Otherwise, the discontinuity pattern might have change significantly which leads to falsified results. To disrupt the construction schedule as little as possible, penetration tests were performed directly after the maintenance and corresponding geological face documentation. The geological mapping documented rock, as well as rock mass properties. A special focus was on the orientation and spacing of existing discontinuities, and potentially detached block at the face (Fig. 61). Furthermore, schematic geological cross sections, considering face documentation before and after the test, were drawn to gain a principal overview of the rock mass.

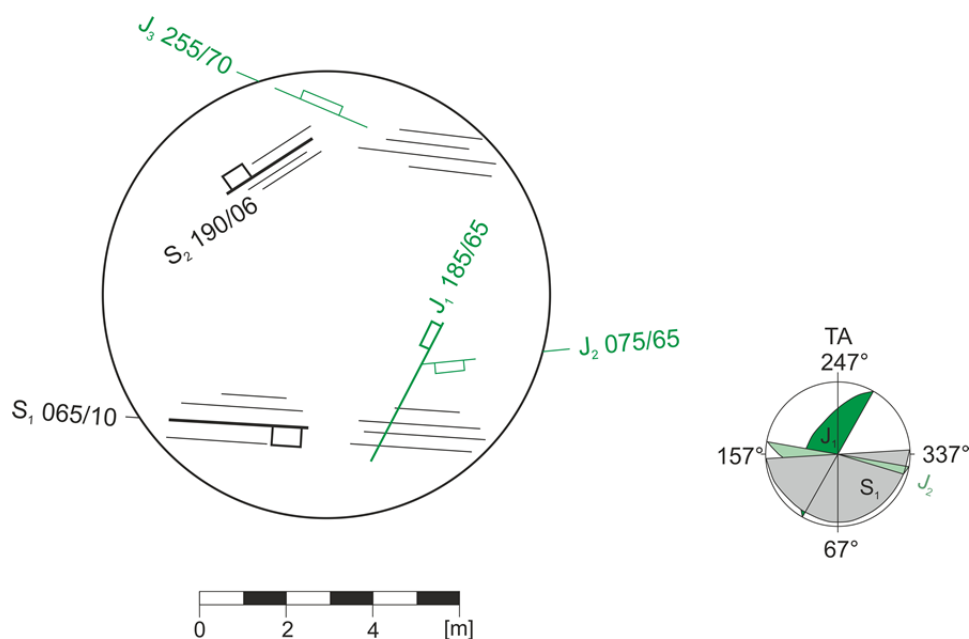


Fig. 61: Geological face documentation and structure model at the Koralm tunnel with mapped discontinuity systems (S = schistosity, J = joint).

Geological mapping at the Røssåga hydropower project was much easier since the excavated tunnel lining was not covered by concrete. Here, geological back-mapping of about 2,500 m tunnel length were performed in collaboration with researchers from the *Norwegian University of Science and Technology* (NTNU). By using this method, detailed mapping of schistosity, joints, fissures, and faults was possible (Fig. 62).

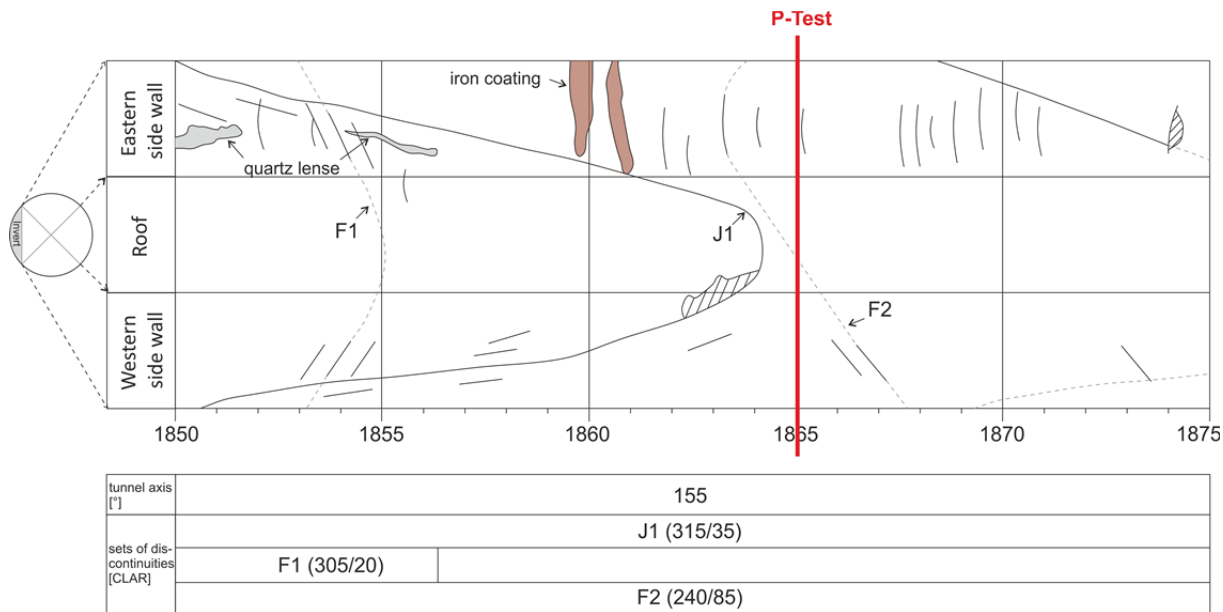


Fig. 62: Penetration test at chainage 1865 in quartzite at Røssåga hydropower project with mapped discontinuity systems (J = joint, F = fissure).

Sample acquisition for laboratory testing is inevitable. At the Koralm tunnel project, sampling was a difficult task. Concrete segments and the double shield TBM hindered the easy access to the tunnel side walls or tunnel face and the possibility to drill rock cores. Therefore, the decision was to perform penetration tests every 500 m close to cross passages. This facilitated the rock sampling to determine geotechnical parameters since cross passages were excavated by drill and blast and rock cobbles could be collected without much effort. Samples could then be prepared in the laboratory to gain high quality specimens. This guarantees that specimens fulfilling testing recommendations, were free of discontinuities and schistosity was perpendicular to the loading rate. Additionally, the standstill of the machine for penetration testing was reduced to the minimum.

At the Røssåga hydropower project, cores taken from the side walls directly at the chainage where the penetration test has been performed. This enabled a high correlation of determined rock properties and conducted testing, but might lead to poor specimen quality since one cannot influence the orientation of discontinuities at drilled rock cores. This aspect is most important with regard to metamorphic or sedimentary rocks with distinct schistosity or lamination.

5 Results and discussion of laboratory testing with a focus on rock toughness

5.1 Results

An extensive laboratory program has been performed on a number of different rock samples from 25 locations to primarily investigate the deformation behavior of rocks under load in terms of rock toughness. The methodology of each laboratory test has been described in chapter 4.1 (page 66). In addition, laboratory tests have been conducted at studied project sites to gain detailed geotechnical input parameters for the improvement of penetration prediction. The basic idea was to develop a conclusive and easily applicable method to determine rock toughness via standard laboratory tests. In a second step, the findings should have been transferred and validated in the field. Due to the lack of rock variability at actual tunnel projects, it was only possible to test several rock types in the laboratory and the influence of rock toughness on the penetration of a TBM could not be proved at the construction site. Nevertheless, the results that were obtained provide a good overview of how rocks deform under load. This chapter will summarize the results from laboratory analysis, including a short petrographic description of tested rock samples. A discussion of acquired results follows in chapter 5.2. Part of the laboratory testing has been performed in collaboration with C. Wieser and P. Ellecosta within the scope of their doctoral theses at the Technical University of Munich. Furthermore, several bachelor and master theses contributed to the results of the testing program under my supervision (ZAEGER 2012, LEISCH 2013, WEIGERT 2013, GRUBER 2015, HORNUNG 2015).

5.1.1 Petrographic analysis of tested samples

A wide range of the following petrographic descriptions are rock types that were encountered at several tunnel projects. In addition, typical rock types that may occur during tunneling works in Alpine regions were analyzed to get a broad variation of different rock types and to obtain profound information about their deformation behavior. Therefore, a total of 25 rock types from different locations which have been tested and are subsequently categorized into three major classes – magmatic, metamorphic, and sedimentary rocks. This classification is also used throughout the next chapters. The petrographic description provides the basis for investigations on the deformation behavior of rocks under load since the mineral content is a decisive parameter.

5.1.1.1 Magmatic rocks

FLB – Granite Flossenbürg

Flossenbürg granite is a felsic plutonic rock of yellowish to grey color that can be classified as two-mica granite. Rock samples were collected in quarries near the town of Flossenbürg in Upper Palatinate (Bavaria) and are of Upper Carboniferous age about 320 Myr ago (FREUDENBERGER & SCHWERD 1996). The density of the rock is determined at about 2.65 g/cm³. It is medium to coarse grained.

The maximum grain size may reach 6 mm. The rock is of heterogranular texture and homogeneous structure. Main constituents are quartz, potassium feldspar and plagioclase. As medium constituents, biotite, muscovite and chlorite could be determined in thin sections. Slight weathering of mica minerals results in the formation of ferric oxide (limonite) causing a yellowing of the rock. Mean uniaxial compressive strength is determined at 90.6 MPa.



Fig. 63: Flossenbürg: granite under reflected-light microscope.

TIT – Granite Tittling

Tittling granite is of light gray color and must actually be classified as granodiorite. Samples were taken from quarries in the surrounding area of the municipality of Fürstenstein / Tittling in the Bavarian Forest (Lower Bavaria). Intrusion of granitic magma took place in Upper Carboniferous about 320 Myr ago (LEHRBERGER 2007). The density of the rock is determined at about 2.67 g/cm³. It is medium grained, of equigranular texture and has a homogeneous structure. No specific mineral orientation could be observed. Main constituents are quartz (gray) and plagioclase (white). Potassium feldspar appears subordinated compared to plagioclase which is why the rock is classified as granodiorite. Mainly biotite as thinly dispersed dark mineral has been noted whereas muscovite appears as accessory. Furthermore, small amount of chlorite, hornblende and zircon may occur. Rock samples show no indication of weathering or preexisting cracks. Mean uniaxial compressive strength is determined at 180.4 MPa.

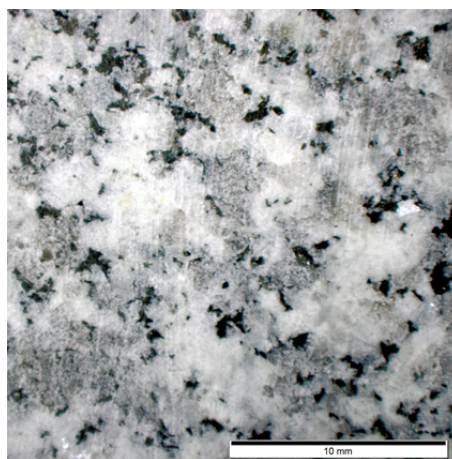


Fig. 64: Tittling: granite under reflected-light microscope.

BX – Granite Brixen

Brixen granite, a felsic plutonic rock of light gray to greenish color, must actually be classified as granodiorite. Rock samples were collected from the disposal site of excavated material from the Brenner Base tunnel near Mauls in South Tyrol. The intrusive was formed in Permian about 280 Myr ago. The density of the rock is determined at about 2.68 g/cm³. It is medium to coarse grained with a maximum grain size of 4 mm. The rock is of equigranular texture and homogeneous structure. Principal constituents are quartz and plagioclase. Biotite appears in a considerably amount. At grain boundaries biotite is partly weathered and altered to chlorite which is responsible for greenish color. Beginning weathering can also be observed by a cloudy surface of feldspar minerals. Accessory pyrite appears. A special attribute is zircon included in biotite minerals. Due to the radioactive decay of zircon, pleochroic halos are identified in thin sections. Mean uniaxial compressive strength is determined at 166.3 MPa.

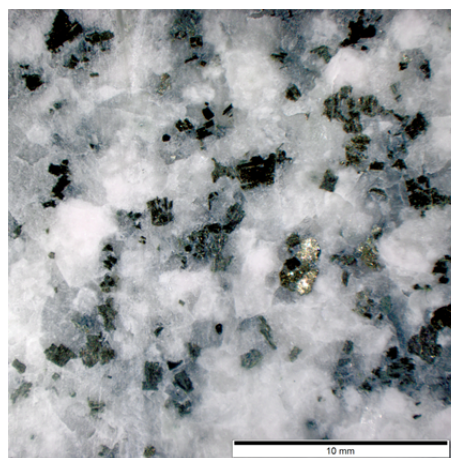


Fig. 65: Brixen: granite under reflected-light microscope.

MET – Granite Metten

Metten granite is of gray color and can be classified as two-mica granite. Samples were taken from a quarry in the surrounding area of the municipality of Metten in the Bavarian Forest (Lower Bavaria). Intrusion of granitic magma took place in Upper Carboniferous about 320 Myr ago (LEHRBERGER 2007). The density of the rock is determined at about 2.61 g/cm³. It is medium grained, of equigranular texture and possess homogeneous structure. Some varieties show porphyroblastic texture with grain sizes up to 14 mm. No specific mineral alignment could be observed. The main constituents are quartz, potassium feldspar and plagioclase. As medium constituents, biotite and muscovite could be determined in thin sections. Zircon included in biotite minerals and pleochroic halos are identified in thin sections. The rock is slightly to moderately weathered which is highlighted by the cloudy surface of feldspar minerals that are partly colored yellow.

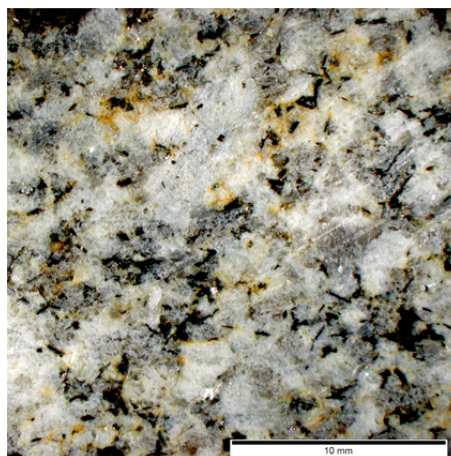


Fig. 66: Metten: granite under reflected-light microscope.

The rock is slightly to moderately weathered which is highlighted by the cloudy surface of feldspar minerals that are partly colored yellow. Mean uniaxial compressive strength is determined at 75.9 MPa.

NIT – Diorite Nittenau

Nittenau diorite is of a dark gray color and is classified as intermediate plutonic rock. Rock samples were collected in a quarry near Nittenau in the Upper Palatinate (Bavaria). Rock formation is part of the Regensburger Forest and by isotopic age determination the time of intrusion is detected at about 330 Myr ago (FREUDENBERGER & SCHWERD 1996). The density of the rock is determined at about 2.68 g/cm³. The rock is medium grained, partly quartz grains up to 20 mm are observed. Therefore, it can be described as heterogranular in texture, but homogenous in structure. No specific alignment of minerals could be observed. Mineral composition is built mainly by plagioclase, clearly identifiable by its oscillatory twin under the microscope. Principal mafic minerals are amphibole and biotite. As accessory constituents, quartz, pyroxene and pyrite could be determined in thin sections. Rock samples show a very low degree of weathering, with only some biotite minerals revealing beginning alteration to chlorite. Mean uniaxial compressive strength is determined at 211.1 MPa.

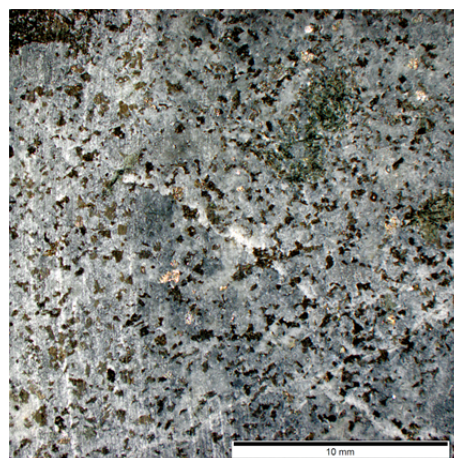


Fig. 67: Nittenau: diorite under reflected-light microscope.

PB – Basalt Pechbrunn

Pechbrunn basalt is of a dark black color and belongs to the group of mafic volcanic rock. The samples originate from a quarry near Pechbrunn in the Upper Palatinate (Bavaria). Here basalt from tertiary volcanism is mined at an age of about 21.4 Myr (STRUNZ et al. 1966). The density of the rock is determined at about 3.15 g/cm³. It is extremely fine grained and individual minerals are not visible to the naked eye. Partly olivine nodule appears with sizes up to several centimeters. Therefore, the rock is classified as porphyroblastic with a homogenous structure. Main constituents are pyroxene (titanaugite) and foid (nepheline) that built up the fine grained matrix. In addition, plagioclase, olivine and magnetite are detected in thin sections. Collected rock cobbles may display a weathered ochre-colored crust due to exposure on earth's surface. In contrast, tested rock specimens are only marginally weathered which is visible in olivine minerals under the microscope. Mean uniaxial compressive strength is determined at 421.4 MPa.

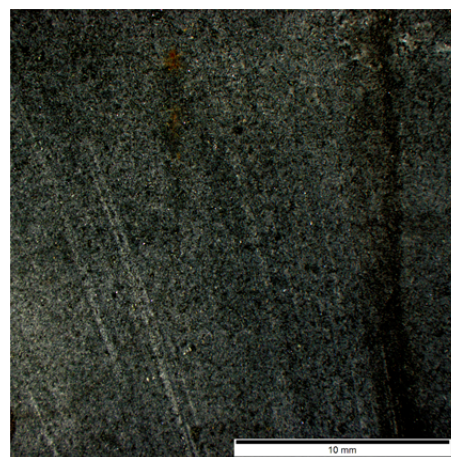


Fig. 68: Pechbrunn: basalt under reflected-light microscope.

5.1.1.2 Metamorphic rocks

KAT-SG – Schistose gneiss series Koralm tunnel

Rocks from the schistose gneiss series are of dark grey color and show a smooth transition between mica schist and schistose gneiss. Samples originate from the railway project Koralm tunnel and were taken mainly from rock cobbles of drill and blast excavation of cross passages between tunnel meter 1,000 and 8,500. The formation has mainly been formed during Variscan orogeny and suffered a second metamorphosis during the formation of the Alps. The density of the rock is determined at about 2.85 g/cm³. It is fine to medium grained with clotted quartz minerals of up to 1 cm. The rock is of heterogranular, partly porphyroblastic, texture and inhomogeneous structure. Minerals are aligned in the orientation of schistosity which is clearly visible due to changing color. Sometimes lamination also comes along with a change in grain size. The main constituents are quartz and mica whereby biotite predominates in contrast to muscovite. As a medium constituent, plagioclase could be observed under the microscope. Accessory pyroxene, garnet, chlorite and opaque minerals (presumably iron) are noted in thin sections. Some joints may be sealed by subsidiary new formed minerals such as pyrite. Samples reveal beginning weathering which is noted by means of biotite alteration to chlorite and microcracks with pyroxene minerals. Mean uniaxial compressive strength is determined at 86.2 MPa.

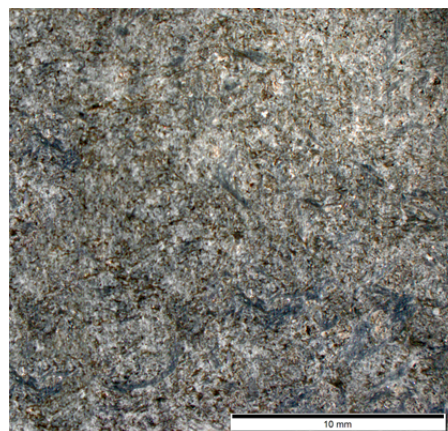


Fig. 69: Koralm tunnel: schistose gneiss under reflected-light microscope.

KAT-G – Gneiss series Koralm tunnel

Rocks from the gneiss series result from a smooth transition of schistose gneisses to fine grained gneisses with intercalary layers of platy gneiss. These rocks are of light gray to brownish color and were collected from cross passages of tunnel meter 8,500 to 11,500. The density of the rock is determined at about 2.78 g/cm³. Rock fabric is similar to that of schistose gneisses. The only difference is the increase of feldspar and quartz minerals that corresponds to a decreasing amount of mica. Furthermore, pyrite minerals are noted. Samples are fresh to slightly weathered and the mean uniaxial compressive strength is determined at 164.9 MPa.

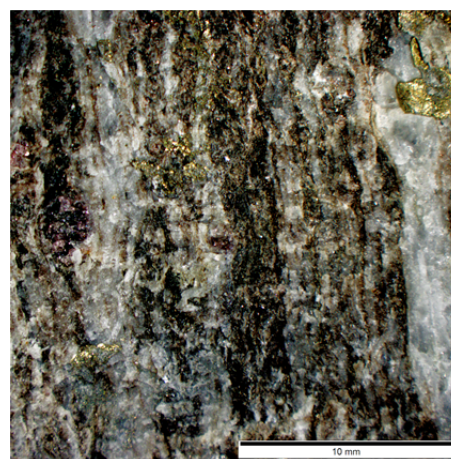


Fig. 70: Koralm tunnel: gneiss under reflected-light microscope.

AG – Augen gneiss Malta Valley

The metamorphic rock is of light gray color and can be classified as orthogneiss. Samples originate from a quarry in the Malta Valley (Carinthia) and were provided by the *Montanuniversität Leoben, Chair for Subsurface Engineering*. The density of the rock is determined at about 2.64 g/cm^3 . It is medium to coarse grained with clotted feldspar minerals called augen that are large eye-shaped mineral aggregates of centimeter size. The texture of the rock is porphyric and the structure is inhomogeneous with obviously visible cleavage planes. Main constituents are feldspar and quartz. As a medium constituent, mica has been noted under the microscope whereby mainly biotite and subordinated muscovite appear. Accessory chlorite has been detected due to the alternation of biotite. Rock samples are fresh to slightly weathered and no preexisting cracks are noted. Mean uniaxial compressive strength is determined at 213.5 MPa.

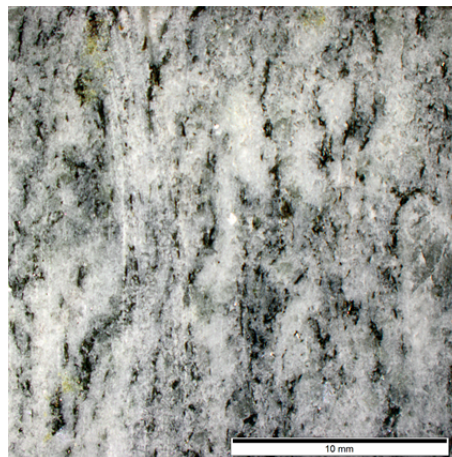


Fig. 71: Malta Valley: Augen gneiss under reflected-light microscope.

GG – Granitic Gneiss Humpelgraben

Granitic gneiss from Humpelgraben is a metamorphic orthogneiss of light gray color. Samples originate from a disused quarry in the Gleinalpe massif (Styria) of the Upper Austro Alpine and were provided by the *Montanuniversität Leoben, Chair for Subsurface Engineering*. The density of the rock is determined at about 2.66 g/cm^3 . Rock samples are mainly medium grained with a maximum grain size of 3 mm. Feldspar minerals may reach a size of up to 1 cm. The rock is classified as heterogranular in texture and inhomogeneous in structure. An alignment of mica minerals is existent, causing an indistinct schistosity. Mineral composition is built mainly by quartz and feldspar. Accessory constituents are biotite, muscovite, chlorite and zoisite. Rock samples are fresh to slightly weathered and nor preexisting cracks are noted. Mean uniaxial compressive strength is determined at 177.1 MPa.

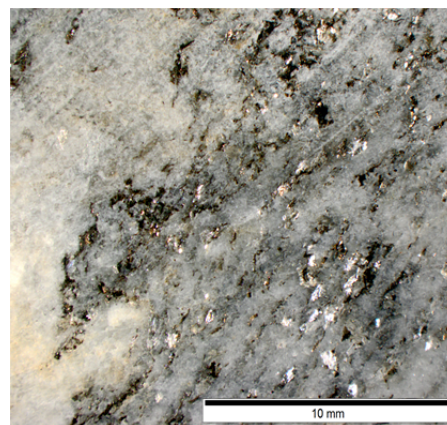


Fig. 72: Humpelgraben: granitic gneiss under reflected-light microscope.

PFT – Greenschist Pfunderer Valley

This rock type is of green to grayish color and has been formed by metamorphism of mudstones and must be actually classified as chlorite schist. Rock samples were collected in a quarry near Pfunders in South Tyrol. Metamorphic rocks from the Penninic (Mesozoic age) that appear in the Tauern window are mined in this quarry. The density of the rock is determined at about 2.99 g/cm³. It is mainly fine grained, and individual minerals of rock matrix are not visible to the naked eye. The texture of the rock is equigranular and its structure is homogenous. Due to the alignment of phyllosilicates, the rock indicates a clear schistosity. Main constituents are chlorite (phyllosilicate) and actinolite (green hornblende) which cause the green color of the rock. Accessory quartz and feldspar were detected in thin sections. The rock shows no sign of weathering. Mean uniaxial compressive strength is determined at 239.4 MPa.

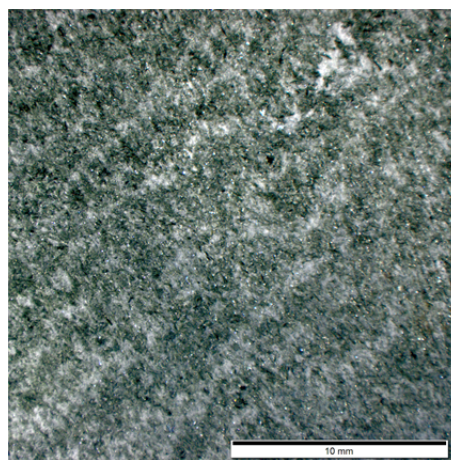


Fig. 73: Pfunderer Valley: greenschist under reflected-light microscope.

KGS – Calcareous Mica Schist Limberg hydropower plant

Calcareous mica schist is of light gray color and has been formed by metamorphism of sedimentary rocks. It belongs to the schist shell of the Penninic and is of Mesozoic age. Samples originate from the hydropower plant Limberg II (Salzburg) and were provided by the *Montanuniversität Leoben, Chair for Subsurface Engineering*. The density of the rock is determined at about 2.71 g/cm³. It is fine to medium grained, of heterogranular texture and inhomogeneous structure. The alignment of mica minerals causes a clearly visible schistosity. The main constituent is calcite with more than 70 Vol. %. It is also decisive because of larger grain sizes and clotted mineral aggregates. Medium constituents are quartz and muscovite. Accessory pyrite minerals were noted in thin sections due to its opaque character. Rock samples are fresh to slightly weathered and no preexisting cracks are noted. Mean uniaxial compressive strength is determined at 95.0 MPa.

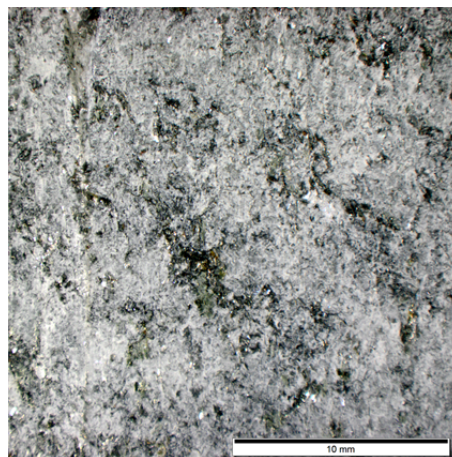


Fig. 74: Limberg hydropower plant: calcareous mica schist under reflected-light microscope.

RØ-2221 – Calcareous Mica Schist Røssåga hydropower plant

The metamorphic rock is of a grey, slightly greenish color and belongs to the Caledonian orogeny in Norway that was formed around 400 Myr ago (Silurian age). Samples were taken at chainage 2221 of the Røssåga hydropower plant near the city of Mo i Rana in Nordland County (Norway). The density of the rock is determined at about 2.80 g/cm³. The matrix is fine to medium grained with quartz lenses up to one centimeter in size with quartz veinlets irregularly dispersed throughout the rock. The texture can be described as heterogranular and the structure is classified as inhomogeneous and anisotropic. Schistosity is clearly visible due to the alternating layering of pale and dark minerals. Main constituents are quartz, calcite and biotite. Subordinated muscovite appears in thin sections. Accessory garnet minerals were detected due to its opaque optical character under the microscope. No signs of weathering are observed, but quartz sealed joints are noted at several specimens. Mean uniaxial compressive strength is determined at 100.8 MPa.

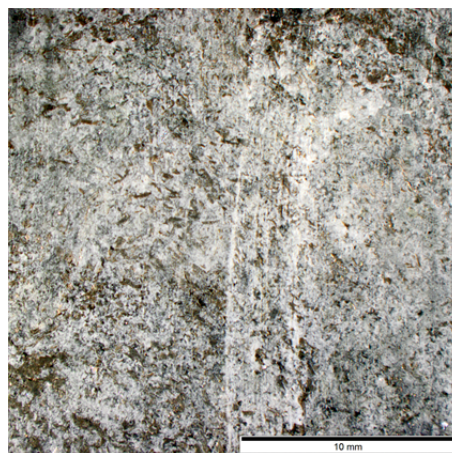


Fig. 75: Røssåga hydropower plant: calcareous mica schist under reflected-light microscope.

OBM – Amphibolite Oberbaumühle

Oberbaumühle amphibolite is a dark gray to green rock type that is formed by the metamorphosis of basalt. The samples originate from a quarry near Windischeschenbach in Upper Palatinate (Bavaria). The quarry is situated in the Bohemian Massif where basalt eruption took place about 485 Myr ago (STRUNZ et al. 1966). The density of the rock is determined at about 2.95 g/cm³. It is fine to medium grained with quartz lenses up to one centimeter in size with quartz veinlets irregularly dispersed throughout the rock. The texture of the rock is heterogranular and the structure can be described as inhomogeneous. If an alignment of minerals is visible, amphibole minerals are responsible for this, which are also main constituents of the rock. Primarily green hornblende (actinolite) has been determined, subordinated brown hornblende appears. In addition, quartz and plagioclase are existent that built up light gray layers within the rock. Accessory, biotite, chlorite and epidote are detected in thin sections due to the alteration of hornblende. Furthermore, opaque minerals are noted to a small amount (most likely garnet). Rock samples are slightly weathered, as several plagioclase minerals reveal beginning saussuritization, and hornblende minerals are marginally altered. Mean uniaxial compressive strength is determined at 254.9 MPa.

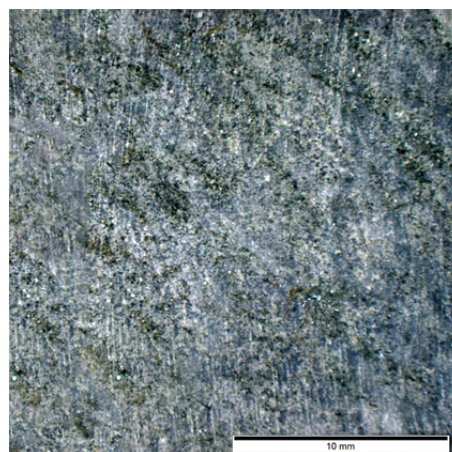


Fig. 76: Oberbaumühle: amphibolite under reflected-light microscope.

HUM – Amphibolite Humpelgraben

Amphibolite from Humpelgraben is of gray to green color and is formed by the metamorphosis of mafic rocks. Samples were collected from a disused quarry in the Gleinalpe massif (Styria) belonging to the Upper Austro Alpine nappe, i. e. to the basement layers of the Silvretta-Seckau nappe system. The density of the rock is determined at about 2.88 g/cm³. It is fine grained, of equigranular texture and homogeneous in structure. Schistosity is clearly visible due to the narrow spaced alternation of pale and dark mineral layers. Mineral composition is built up of quartz and amphibole. Accessory, opaque minerals (presumable pyrite) and garnets are scattered throughout the sample. Amphibole minerals are marginally weathered and altered to chlorite. Mean uniaxial compressive strength is determined at 230.0 MPa.

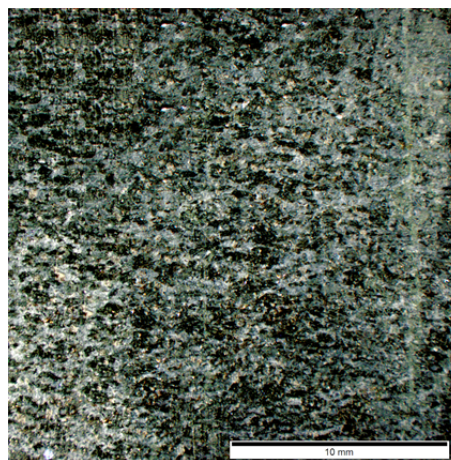


Fig. 77: Humpelgraben: amphibolite under reflected-light microscope.

GLT – Amphibolite Gleinalm tunnel

Amphibolite from the Gleinalpe Massif is of green to gray color and originates from the Gleinalm tunnel project in Styria. The rock belongs to the metamorphic core zone of the massif and to the basement layers of the Silvretta-Seckau nappe system. The density of the rock is determined at about 2.91 g/cm³. It is fine grained, of equigranular texture and inhomogeneous in structure, as the thickness of amphibole layers may vary significantly reaching up to 1 cm. Schistosity is clearly evident due to the layering of pale and dark minerals. Main constituents are plagioclase and amphibole (green hornblende) that represent about 50 Vol. %. Medium constituents are quartz, chlorite and biotite whereby its content may vary within the samples. Accessory epidote and opaque minerals are observed in thin sections. Several rock samples show plagioclase or quartz sealed fractures that are dispersed irregularly throughout the rock, causing planes of weakness in terms of rock strength. Samples are classified as slightly weathered as amphibole minerals are partly altered to chlorite and plagioclase minerals show cloudy surface character. Mean uniaxial compressive strength is determined at 130.8 MPa.

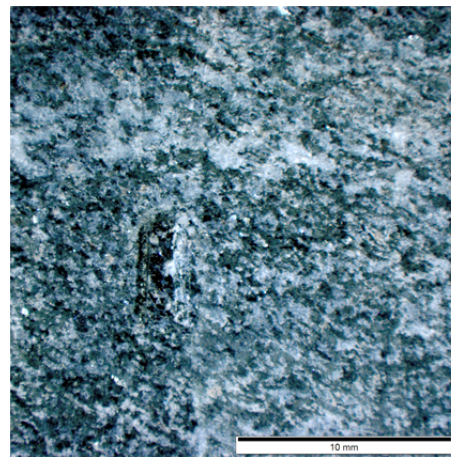


Fig. 78: Gleinalm tunnel: amphibolite under reflected-light microscope.

Rø-1294, 1894 – Quartzite Røssåga hydropower plant

The metamorphic rock is of light grey color and is formed by the metamorphosis of sandstone during the Caledonian orogeny around 400 Myr ago (Silurian age). Samples were taken at chainage 1294 and 1894 of the Røssåga hydropower plant near the city of Mo i Rana in Nordland County (Norway). The density of the rock is determined at about 2.66 g/cm³. It is fine grained, of equigranular texture and homogenous in structure. An alignment of minerals is not visible. Main constituent are xenomorphic quartz minerals. Accessory mica (mainly biotite) and feldspar (mainly potassium feldspar) were determined in thin sections. Biotite minerals are irregularly and thinly scattered throughout the rock. Feldspar content may vary depending on the specimen. Partly rutile grains appear as inclusion in quartz minerals. No evidence of weathering is found. Mean uniaxial compressive strength is determined at 257.6 MPa.

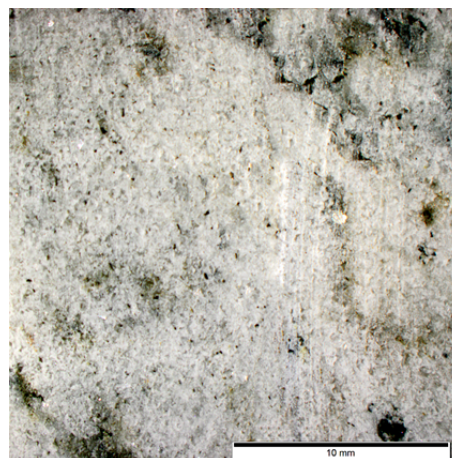


Fig. 79: Røssåga hydropower plant: quartzite under reflected-light microscope.

LAM – Marble Laas

The marble is of pure white color and originates from a quarry near the town Laas in South Tyrol. Marble formation of Laas is the basis of Ortler-Campo-Crystalline and has been formed during the Variscan orogeny about 400 Myr ago where Penninic gneiss layers with overlying sedimentary rocks were subject to metamorphosis (NOCKER 2007). The density of the rock is determined at about 2.72 g/cm³. The rock is medium grained with a maximum grain size of about 1.5 mm. The texture can be described as equigranular with an homogenous structure. An alignment of minerals is not obvious. It is a monogenic rock that is built of calcite with about 95 Vol. %. Calcite minerals show a distinct twinning characteristic under the microscope. Accessory quartz and mica minerals can be observed in thin sections. No evidence of weathering is found. Mean uniaxial compressive strength is determined at 87.9 MPa.

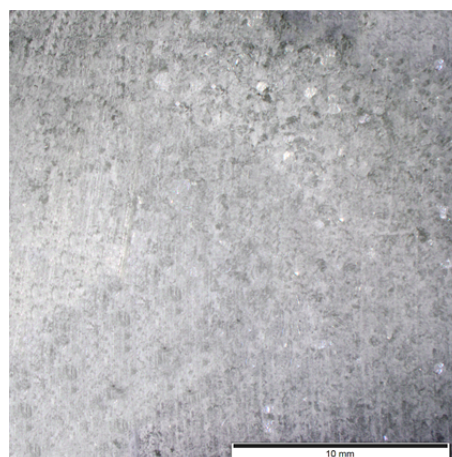


Fig. 80: Laas marble under reflected-light microscope.

KAT-M – Marble Koralm tunnel

Marble from the Koralm tunnel is of a white to partly greenish color. In most cases, it must actually be classified as siliceous marble. It originates from different cross passages where marble bands occur. These bands were formed during Variscan orogeny about 400 Myr ago. The density of the rock is determined at about 2.75 g/cm³. The rock is medium to coarse grained with a maximum grain size of about 6 mm. The fabric on the rock depends on mineral content as two different varieties of marble are observed. One shows a regular layering of quartz and mafic minerals within carbonate matrix, whereas the other one shows irregular single veins of quartz and mafic minerals with a considerable thickness of 1 cm. The main texture is equigranular, whereas the structure can be described as homogenous. An alignment of minerals is indicated by the presence of mica minerals. Samples mainly consist of calcite, but also few specimens with main constituent of dolomite are noted. Accessory mica, quartz, pyroxene (orthopyroxene), amphibole (tremolite) and opaque minerals were detected in thin sections causing lamination within the rock. The quartz and pyroxene content may vary to a certain degree leading to high variation of rock strength. Beginning weathering process can be observed due to microcracks within pyroxene minerals. Mean uniaxial compressive strength is determined at 94.2 MPa where the quartz and pyroxene rich variety results in 112 MPa and the carbonate dominated variety results in 63 MPa.

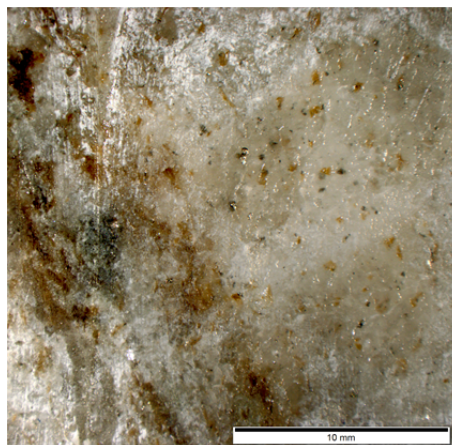


Fig. 81: Koralm tunnel: marble under reflected-light microscope.

5.1.1.3 Sedimentary rocks

RTF – Sandstone Rothenfels

The sandstone originates from a project near Würzburg in Lower Franconia (Bavaria) and is of red to beige color. Rock samples belong to the ‘Germanic Buntsandstein’ formation, are of Triassic age and are classified as clastic sediment (arenite). The density of the rock is determined at about 2.39 g/cm³. The average grain size is fine to medium with a maximum grain size of 1.5 mm. Grains are mainly rounded and equigranular. A subordinated angular grain shape was also observed. The main constituent is quartz, partly with hematite coating. Accessory feldspar and mica were detected in thin sections. One sample shows clay lenses of up to 5 mm in diameter. The majority of tested samples reveal siliceous grain bonding whereas only one sample is bonded by clay minerals. Thin section analysis show that the porosity is relatively low. Macroscopic rock description may give the impression of certain layering due to color changes from red to beige. The microscopic analysis proved this statement to be false, as it is only a matter of hematite coating and samples are of homogeneous structure. Rothenfels sandstone is classified as slightly weathered with a mean uniaxial compressive strength of 60.8 MPa.

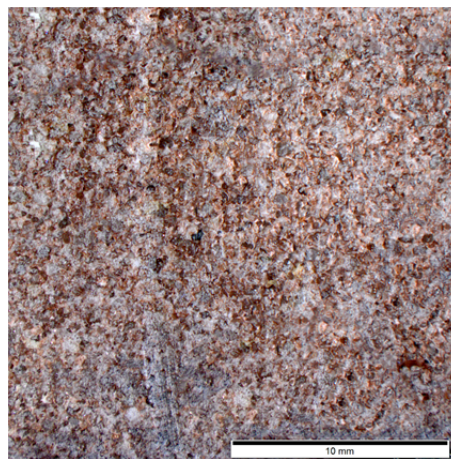


Fig. 82: Rothenfels: sandstone under reflected-light microscope.

POS – Sandstone Posta

Posta sandstone is of beige to yellowish color and can be classified as clastic sediment (arenite). Samples were taken from a quarry near Posta (Saxony). It is situated in the Elbe Sandstone Mountains. The age of the rocks is determined with Cretaceous age about 90 Myr ago. The density of the rock is determined at about 2.08 g/cm^3 . It is fine to medium grained partly a maximum grain size of 4 mm may be reached. Grains are mainly rounded and equigranular, and subordinated angular grain shape was also observed. Mineral composition is built mainly of quartz minerals with a significant amount of iron ore (limonite). Siliceous grain bonding and moderately high porosity could be observed in thin sections. Single grains can easily be removed by the finger. Limonitization causes foliation within the rock that is underlined by the color change. The formation of limonite is an evidence for beginning weathering process and has been noted for the majority of tested samples. Mean uniaxial compressive strength is determined at 61.3 MPa.

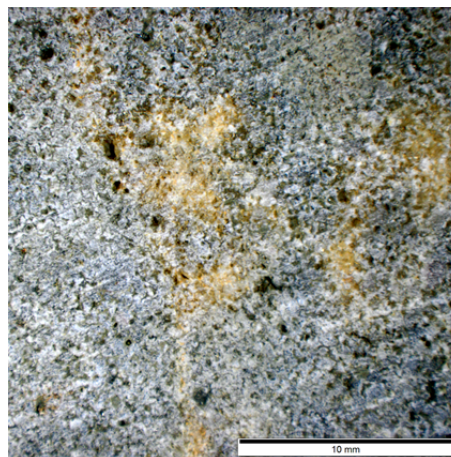


Fig. 83: Posta: sandstone under reflected-light microscope.

ABC – Sandstone Abtswind Castell

Castell sandstone is a yellow to greenish sandstone and is a variety of Abtswind sandstone that is classified as clastic sediment. Samples originate from a quarry near Abtswind in Lower Franconia (Bavaria). The quarry is situated in the 'Schilfsandstein' rock formation which is of Triassic age (Keuper). The density of the rock is determined at about 2.08 g/cm^3 . The rock is fine grained with a maximum grain size of 1 mm. Grains are mainly rounded and equigranular. Main constituent is quartz, whereas accessory feldspar and chlorite appear which is responsible for the greenish color. Bonding of the sandstone is argillaceous. Lamination could not be observed by macroscopic and microscopic analysis and the structure is classified as homogeneous. Partly clay lenses up to 5 mm in diameter exist as well. Castell sandstone can be classified as slightly weathered with a mean uniaxial compressive strength of 28.4 MPa.

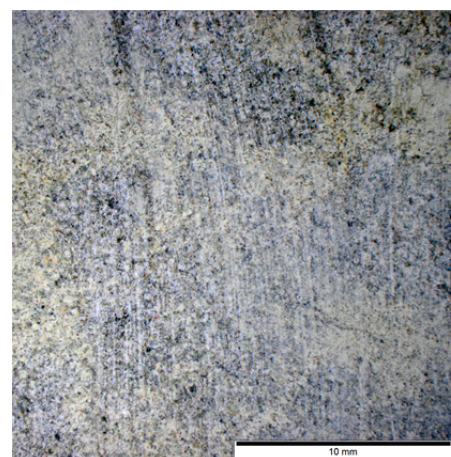


Fig. 84: Abtswind Castell: sandstone under reflected-light microscope.

WIE – Limestone Wiesenhofen

Wiesenhofen limestone is of a grey color and belongs to the group of organic sediments (carbonate rock). It is a layered limestone, intersected by thin marl layers. Samples were collected in a quarry near Wiesenhofen in Upper Bavaria. Rock formation is part of the Franconian Alp during the Jurassic ages (Malm). The density of the monogenic rock is determined at about 2.61 g/cm^3 . It is extremely fine grained. Single minerals cannot be detected by the naked eye. The matrix can be described as dense and micritic and the structure is homogenous with no distinct lamination. Calcite minerals are main constituent of the rock. Accessory clay and pyrite minerals appear. Tested rock samples show little fossil content, but ammonites and belemnites are to be expected in Jurassic limestones. No evidence of weathering could be observed for Wiesenhofen limestone. Mean uniaxial compressive strength is determined at 229.2 MPa.

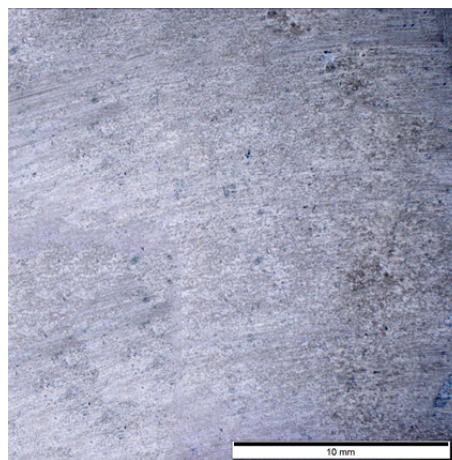


Fig. 85: Wiesenhofen: limestone under reflected-light microscope.

DK – Limestone Dietfurt

Rock samples are gray to brownish dolomitic limestone that belongs to the group of organic sediments (carbonate rock). Samples originate from a quarry near Dietfurt in Middle Franconia (Bavaria) which is part of the Franconian Alp with rocks from the Jurassic ages (Malm). The density of the rock is determined at about 2.58 g/cm^3 . The monogenic rock is extremely fine grained with a micritic matrix. Some samples show up to 4 mm large intraclasts and can be classified as intramicrite. No lamination can be observed. Main constituent is calcite and dolomite. Furthermore, bioclasts from fossils like bivalve are noted. The weathering of these fossil fragments leads to pore space that causes higher porosity. This can be found by a small number of tested samples which is why the rock is classified as slightly weathered. Mean uniaxial compressive strength is determined at 156.5 MPa.

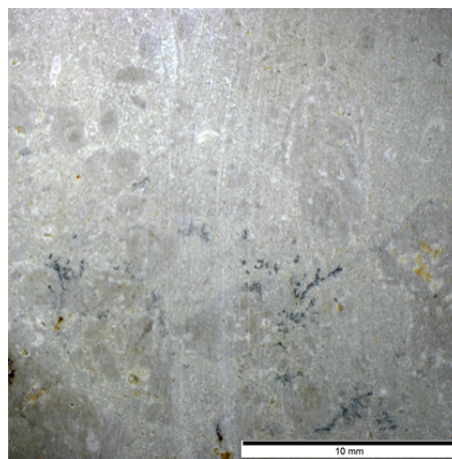


Fig. 86: Dietfurt: limestone under reflected-light microscope.

MO – Anhydrite Moosegg

Moosegg anhydrite is of white to light gray color and is numbered among the group of chemical sedimentary rocks. Samples were taken from a quarry near Golling in Salzburg. It is situated in evaporite deposits of the ‘Haselgebirge’ that consist mainly of gypsum, anhydrite and salt of Permian age. The density of the monogenic rock is determined at about 2.97 g/cm^3 . It is fine to medium grained with a maximum grain size of about 2 mm. The texture can be described as equigranular with a homogeneous structure. Slight lamination is indicated by irregularly changing color that is not a result of changes in mineral composition. The main constituent is anhydrite with about 90 Vol. %. Accessory gypsum and clay minerals may appear. In addition, very small veins of calcite are dispersed throughout the rock. Thin sections reveal that the rock is of low porosity and no evidence of weathering is found. Mean uniaxial compressive strength is determined at 86.0 MPa.

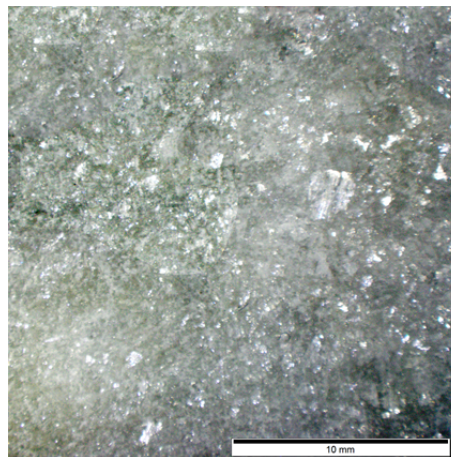


Fig. 87: Moosegg: anhydrite under reflected-light microscope.

5.1.2 Standard laboratory testing

This chapter summarizes the basic laboratory results from Uniaxial Compression Tests, Brazilian Tensile Tests, Point Load Tests, Cerchar Abrasivity Tests and LCPC Abrasivity Tests. Tab. 15 lists the number of performed tests depending on the rock type, whereas Tab. 16 shows the mean value of resulting laboratory parameters. It must be noted that the results presented in Tab. 16 are, for the sake of clarity, an arithmetic average for rocks with the same sample ID originating from the same location. Sample acquisition is mostly done by collecting cobbles of rock at quarries or construction sites. As rock is a natural product and not perfectly homogenous, this implies that cobbles deriving from the same source may obviously vary in their geotechnical parameters. For the detailed analysis of the deformation behavior of rocks under uniaxial compression, each block is considered individually to achieve the maximum possible precision (s. chapter 5.1.3, Tab. 17).

The abovementioned classification into magmatic, metamorphic and sedimentary rock types is continued in this chapter. In the following tables and figures, red color marks magmatic rocks, green indicates metamorphic rocks and blue marks sedimentary rocks.

Tab. 15: Number of performed laboratory tests depending on different rock types (magmatic = red, metamorphic = green, sedimentary = blue).

	Thin section	Uniaxial compression test incl. lateral strain		Brazilian tensile test	Point load test	Cerchar test	LCPC test
Granite							
Flossenbürg (FLB)	1 ²⁾	4	3	3	10	-	-
Tittling (TIT)	1	15	15	3	12	-	-
Brixen (BX)	1	30	-	33	16	1	2
Metten (MET)	1	6	1	4	10	2 ³⁾	2 ³⁾
Diorite							
Nittenau (NIT)	1	18	3	20	14	1	4
Basalt							
Pechbrunn (PB)	1	12	5	14	10	3	4
Gneiss							
Schistose gneiss (KAT-SG)	5	80	10	87	76	49	34
Gneiss (KAT-G)	5	27	27	31	40	5	8
Augen gneiss (AG)	1	14	14	6	2	1	2
Granitic gneiss (GG)	1	5	5	5	15	1	1
Greenschist							
Pfunderer Valley (PFT)	1	21	-	26	10	1	2
Calcareous mica schist							
Limberg hydr. (KGS)	1	7	1	6	-	1	2
Røssåga hydr. (Rø-2221)	1	8	2	6	-	2	-
Amphibolite							
Oberbaumühle (OBM)	1	20	3	9	7	3	6
Humpelgraben (HUM)	1	16	-	8	-	1	2
Gleinalm tunnel (GLT) ¹⁾	12	12	-	12	6	12	12
Quartzite							
Røssåga hydropower (Rø-1294, Rø-1894)	2	5	1	4	-	1	-
Marble							
Laas (LAM)	1	7	7	6	20 ¹⁾	3	2
Koralm tunnel (KAT-M)	2	12	-	10	9	4	2
Sandstone							
Rothenfels (RTF) ¹⁾	6	12	-	12	30	6	-
Posta (POS)	3 ²⁾	8	3	3	10	2 ³⁾	2 ³⁾
Abtswind Castell (ABC)	1	26	26	8 ³⁾	10 ¹⁾	2 ³⁾	1 ³⁾
Limestone							
Wiesenhofen (WIE)	1	4	4	3	7	2	2
Dietfurt (DK)	1 ²⁾	20	20	3	13	2	3
Anhydrite							
Moosegg (MO)	1	42	23	14	13	3	8

¹⁾ Project data base chair of engineering geology, TUM

²⁾ dissertation C. Wieser (TUM), in prep.

³⁾ dissertation P. Ellecosta (TUM), in prep.

Tab. 16: Summary of basic laboratory results: uniaxial compressive strength (UCS), Brazilian tensile strength (BTS), point load index (I_s), Cerchar abrasivity index (CAI), LCPC abrasivity coefficient (LAC) and LCPC breakability coefficient (LBC).

	UCS [MPa]	BTS [MPa]	I_s [MPa]	CAI [-]	LAC [g/t]	LBC [%]
Granite						
Flossenbürg (FLB)	87.8	5.4	4.5	-	-	-
Tittling (TIT)	180.4	12.7	10.7	-	-	-
Brixen (BX)	166.3	8.5	6.8	4.6	1210	55
Metten (MET)	75.9	7.0	5.1	4.2	1140	77
Diorite						
Nittenau (NIT)	211.1	13.6	8.9	3.7	1270	30
Basalt						
Pechbrunn (PB)	421.4	18.0	13.0	2.6	923	19
Gneiss						
Schistose gneiss (KAT-SG)	86.2	9.7	4.5	2.8	860	60
Gneiss (KAT-G)	164.9	13.1	9.0	4.0	1050	49
Augen gneiss (AG)	213.5	14.5	10.7	4.6	1120	46
Granitic gneiss (GG)	177.1	13.7	7.6	4.7	1160	48
Greenschist						
Pfunderer Valley (PFT)	239.4	13.2	8.3	3.4	380	80
Calcareous mica schist						
Limberg hydr. (KGS)	95.0	7.7	-	2.1	590	60
Røssåga hydr. (Rø-2221)	100.8	7.2	-	2.8	-	-
Amphibolite						
Oberbaumühle (OBM)	254.9	16.2	17.7	3.4	830	24
Humpelgraben (HUM)	230.0	9.1	-	4.5	820	39
Gleinalm tunnel (GLT)	130.8	11.5	7.8	4.2	1018	44
Quartzite						
Røssåga hydropower (Rø-1294, Rø-1894)	257.6	12.4	11.1	5.4	-	-
Marble						
Laas (LAM)	87.9	6.3	4.8	1.0	10	89
Koralm tunnel (KAT-M)	94.2	6.8	4.5	1.8	220	96
Sandstone						
Rothenfels (RTF)	60.8	3.2	3.4	2.1	-	-
Posta (POS)	61.3	4.3	3.2	2.3	140	99
Abtswind Castell (ABC)	28.4	2.2	2.1	0.5	120	99
Limestone						
Wiesenhofen (WIE)	229.2	11.9	5.9	0.9	10	36
Dietfurt (DK)	156.5	8.9	6.2	1.0	26.7	34
Anhydrite						
Moosegg (MO)	86.0	7.6	2.8	0.9	20	58

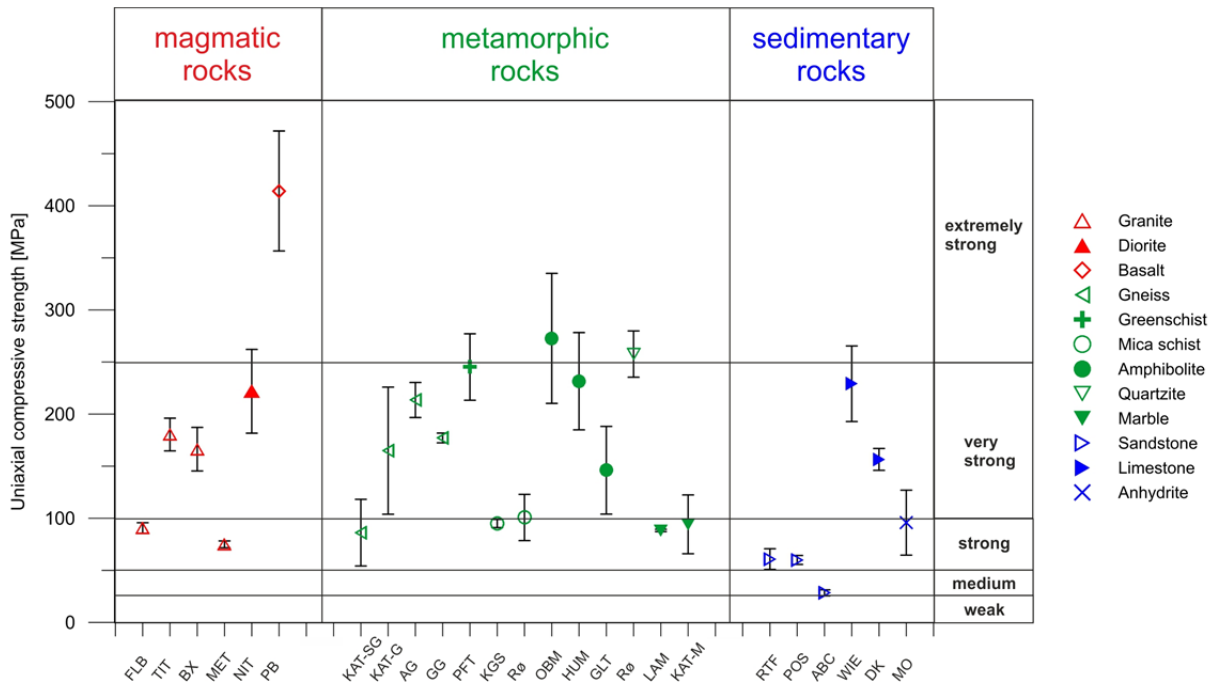


Fig. 88: Uniaxial compressive strength of tested rock types with strength classification acc. to ISRM (1978).

Fig. 88 indicates that the chosen rock samples cover more or less the whole field of rock strength classification ranging from weak / medium (argillaceous sandstone ABC) to extremely strong (fine grained basalt PB). When several rock blocks are tested for the same sample ID, the uniaxial compressive strength often varies to a higher degree. This is indicated by larger error bars, for example basalt (PB), gneiss (KAT-SG/-G), amphibolite (OBM, HUM, GLT) and anhydrite (MO). Apart from weathering and other exogenous processes, strength variations within one sample ID may have different reasons. A major influence on the strength of metamorphic rocks shows the schistosity that leads to a high degree of anisotropy and an inhomogeneous texture. All amphibolite samples reveal varying mineral content and often lenses of amphibolite and plagioclase could be observed. Furthermore, pre-existing cracks were noted for some specimens that may decrease measured UCS values. Inhomogeneous texture in magmatic rock types is caused by inclusions. In this case, olivine inclusions in tested basalt specimens reduce rock strength and cause high standard deviation for otherwise very homogeneous rock samples. Strength variation for sedimentary rock types may derive from bedding and lamination planes, as well as from mineral impurity and grain size distribution. Five different cobbles of anhydrite have been tested and within these, three varieties could be distinguished. This is due to the variation of clay content and particle size leading to UCS values of 55 MPa, 90 MPa and 115 MPa. This fact demonstrates, that for a detailed interpretation of uniaxial compression tests, each block should be considered individually (s. Tab. 17).

5.1.3 Uniaxial Compression Tests: detailed analysis

For a detailed analysis of the deformation behavior of rocks under uniaxial compression, 29 different rock samples have been tested. For some samples, the specimens were prepared from different blocks which are marked by ascending numbers (Tab. 17). As important parameters, the uniaxial compressive strength σ_u , tangent Young's modulus E_t , deformation modulus - including plastic deformation E_{pl} , total axial strain ϵ_u , failure W_b and destruction work W_z are listed. Simultaneous lateral strain

measurements allow the determination of the strength at crack damage point σ_{cd} and corresponding strain rate ϵ_{cd} . ϵ_{cd} marks the beginning of plastic deformation that is used to characterize rock toughness. The following table summarizes the obtained results. Detailed analysis in terms of deformation behavior, respectively rock toughness, is presented in chapter 5.2.

Classification of rock samples displaying the uniaxial compressive strength has already been shown in previous chapter (Fig. 88). DEERE & MILLER (1966: 139) published a classification system that characterizes the deformation behavior of rock depending on the uniaxial compressive strength and tangent Young’s modulus. In Fig. 89, mean values of each sample block are plotted showing that the majority of tested samples can be classified by average modulus ratio. Only basalt results in low modulus ratio and anhydrite in high modulus ratio. These rock types are representative of either brittle (basalt), or tough (anhydrite) failure under load. Therefore, the classification might give a first indication of how rocks react to the applied stress. However, the classification does not seem to be accurate enough, since all other test results illustrate average modulus ratio although different failure behaviors under load were observed.

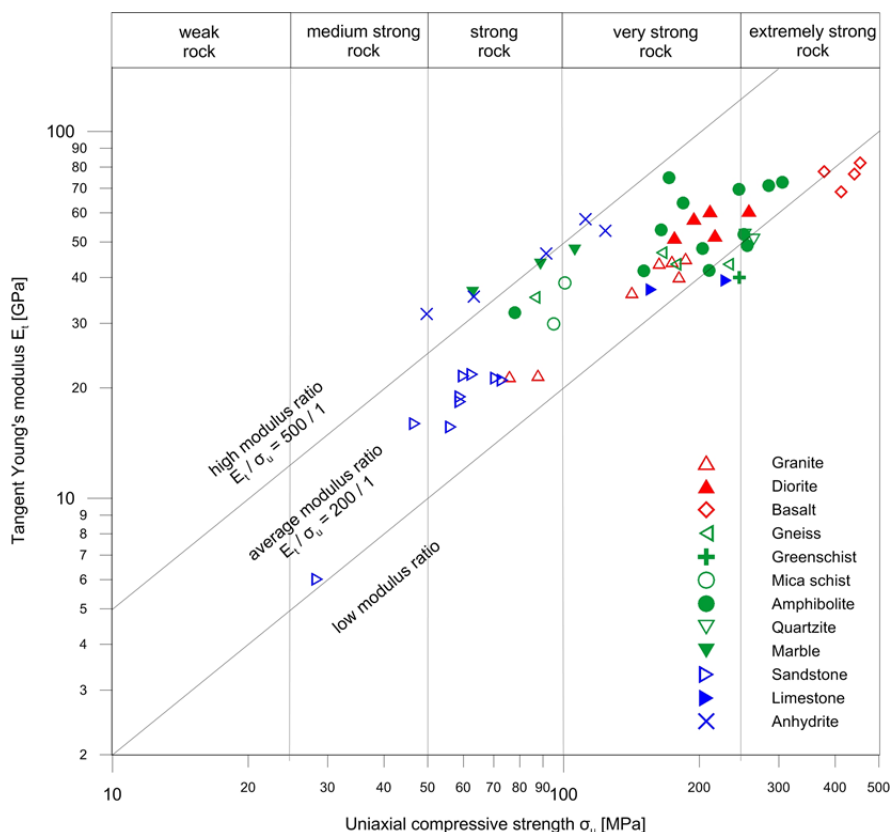


Fig. 89: Uniaxial compressive strength σ_u plotted against tangent Young’s modulus E_t of tested samples. In addition, the classification system of DEERE & MILLER (1966: 139) into high, average and low modulus ratio is illustrated.

Tab. 17a: Summary of laboratory results from Uniaxial Compression Tests in detail.

	σ_u	E_t	E_{pl}	W_b	W_z	σ_{cd}	ϵ_{cd}	ϵ_u
	[MPa]	[GPa]	[GPa]	[kJ/m ³]	[kJ/m ³]	[%]	[%]	[%]
Granite								
FLB-1	87.8	21.7	16.6	253.6	312.7	77.7	0.4254	0.5161
TIT-5	180.4	40.2	37.5	509.7	549.6	91.4	0.4550	0.5117
BX-1	141.8	38.3	38.2	435.2	495.4	88.8	0.3404	0.3622
BX-3	163.0	43.7	40.7	447.6	499.6	87.8	0.3714	0.4411
BX-4	174.0	43.8	42.8	525.7	577.2	84.4	0.3493	0.4141
BX-5	186.5	43.9	44.4	554.8	597.7	84.1	0.3377	0.4695
MET-4	75.9	24.4	17.8	175.5	220.4	48.0	0.2957	0.5271
Diorite								
NIT-1	194.5	59.7	51.3	378.8	416.4	-	-	0.3414
NIT-2	211.2	60.7	56.3	523.5	558.7	-	-	0.2902
NIT-3	257.7	60.9	53.9	632.8	721.1	-	-	0.4672
NIT-8	216.4	52.1	50.3	484.8	502.0	-	-	0.392
NIT-18	175.9	51.5	49.0	344.4	389.9	96.9	0.3587	0.3787
Basalt								
PB-1	454.3	78.5	75.1	1338.1	1378.5	-	-	0.6491
PB-2	377.7	74.7	70.1	1018.8	1057.5	-	-	0.5730
PB-3	412.6	68.4	69.3	1303.6	1327.2	99.1	0.6299	0.6252
PB-4	440.9	76.6	75.9	1376.6	1423.1	-	-	0.6389
Gneiss								
KAT-SG	86.2	35.3	24.2	184.2	218.7	85.3	0.2810	0.3140
KAT-G	164.9	46.7	38.2	-	-	78.3	0.3212	0.4250
AG-1	231.5	43.4	42.4	-	-	97.7	0.6286	0.6349
GG-1	174.6	43.4	40.6	-	-	80.1	0.4813	0.4897
Greenschist								
PFT-1	239.4	39.3	34.9	942.6	1010.5	91.7	0.7602	0.8190
Calcareous mica schist								
KGS-1	95.0	33.9	28.9	181.7	194.4	79.7	0.2908	0.3684
R ϕ -2221	100.8	38.6	30.1	-	-	87.6	0.2285	0.2881
Amphibolite								
OBM-1	284.8	71.2	69.4	666.1	709.0	-	-	0.5720
OBM-2	184.3	63.8	62.5	290.6	310.7	-	-	0.2183
OBM-3	305.5	72.7	67.9	719.0	750.6	99.2	0.4939	0.4621
OBM-4	244.9	69.6	66.4	564.1	597.9	-	-	0.2041
HUM-1	255.4	49.1	48.5	830.7	872.8	97.3	0.6808	0.7004
HUM-2	203.4	47.9	41.0	544.9	567.8	94.6	0.5390	0.5922
HUM-3	210.4	43.6	44.1	635.4	673.2	98.5	0.5390	0.5396
HUM-4	250.8	53.7	54.1	826.6	878.3	97.5	0.5391	0.5464
GLT-3	77.9	32.1	28.1	150.1	204.4	91.3	0.2370	0.2685
GLT-6	171.4	74.8	69.5	231.2	249.4	-	-	0.2539
GLT-7	123.0	54.0	54.0	191.0	200.1	-	-	0.2188
GLT-10	150.7	41.7	37.8	341.0	363.9	92.9	0.0515	0.4095
Quartzite								
R ϕ -1294	252.7	52.4	48.6	-	-	98.9	0.6005	0.6005
R ϕ -1894	264.0	50.8	48.6	-	-	99.2	0.6794	0.6794
Marble								
LAM-2	87.4	42.9	32.0	-	-	78.5	0.1841	0.2771
LAM-5	88.9	43.5	31.3	143.1	209.6	92.6	0.2223	0.2693
KAT-29	105.9	47.5	40.8	172.9	215.2	-	-	0.2795
KAT-31	62.8	36.4	20.9	-	-	-	-	0.2742

Tab. 17b: Summary of laboratory results from Uniaxial Compression Tests in detail.

	σ_u	E_t	E_{pl}	W_b	W_z	σ_{cd}	ϵ_{cd}	ϵ_u
	[MPa]	[GPa]	[GPa]	[kJ/m ³]	[kJ/m ³]	[%]	[%]	[%]
Sandstone								
RTF-1	73.2	21.0	15.3	-	-	80.3	0.3205	0.4466
RTF-2	59.0	18.9	13.5	-	-	83.8	0.2737	0.3608
RTF-3	70.8	21.3	-	-	-	-	-	0.4088
RTF-4	59.1	18.3	-	-	-	-	-	0.4295
RTF-5	56.3	15.6	-	-	-	-	-	0.4661
RTF-6	46.8	16.0	-	-	-	-	-	0.4294
POS-2	60.0	21.5	17.6	148.6	162.9	92.4	0.2717	0.3185
ABC-1	28.4	6.0	4.8	-	-	74.3	0.3710	0.5255
Limestone								
WIE-2	229.2	39.3	35.9	805.9	824.2	90.8	0.6311	0.7020
DK-2	156.5	37.1	36.3	-	-	99.9	0.4582	0.4534
Anhydrite								
MO-1	119.3	54.9	42.2	225.1	321.7	74.4	0.1829	0.2740
MO-2	57.4	30.6	27.2	122.1	199.9	76.5	0.1071	0.1701
MO-3	49.7	31.8	19.0	102.8	147.2	85.7	0.1340	0.2084
MO-5	91.5	46.5	37.1	176.7	314.6	86.8	0.1902	0.2388
MO-6	111.9	57.6	46.8	208.0	312.5	85.8	0.1891	0.2273

Variation of loading rate at Uniaxial Compression Test

The loading rate of uniaxial compression tests has been varied between 1/3- and 20-fold of the recommended rate according to DGGT. The recommended strain rate for samples with a diameter of 5 cm is 0.06 mm/min. Tests have been performed with representatives of magmatic, metamorphic and sedimentary rocks. For each loading rate level, a minimum of three tests were conducted to diminish measuring errors. Toughness defining parameters such as deformation moduli (E_t , E_{pl}), failure and destruction work (W_b , W_z) were measured. Simultaneous to axial strain measurements, lateral strain was also recorded to obtain information about the crack damage point σ_{cd} and corresponding portion of plastic deformation ($\epsilon_u - \epsilon_{cd}$). Tab. 18 summarizes the obtained results of loading rate variation.

Tab. 18: Summary of laboratory results from Uniaxial Compression Tests with varying loading rate.

	loading rate	σ_u	E_t	E_{pl}	W_b	W_z	σ_{cd}	ϵ_{cd}	ϵ_u
	[x-fold from standard]	[MPa]	[GPa]	[GPa]	[kJ/m ³]	[kJ/m ³]	[%]	[%]	[%]
Granite									
TIT-5	1/3 x	160.2	38.2	34.5	510.3	548.4	89.1	0.3951	0.4664
TIT-5	1 x	180.4	40.2	37.5	509.7	549.6	91.4	0.4550	0.5117
TIT-5	2 x	191.6	40.4	38.1	561.9	617.2	97.6	0.5169	0.5387
TIT-5	4 x	169.4	38.4	34.5	509.2	555.9	89.4	0.4435	0.5073
TIT-5	10 x	169.2	38.1	33.4	562.8	619.0	87.8	0.4270	0.5177
Augengneiss									
AG-1	1 x	200.3	43.9	43.2	517.2	560.8	97.1	0.5837	0.5963
AG-1	4 x	213.0	45.7	44.9	557.7	619.4	92.4	0.5719	0.6103
AG-1	10 x	214.1	46.2	45.1	554.3	558.4	96.2	0.5903	0.6139
AG-1	20 x	226.7	47.5	45.8	614.3	641.8	90.0	0.6146	0.6389
Sandstone									
ABC-1	1/3 x	32.8	6.5	5.1	117.2	144.7	80.2	0.4646	0.6316
ABC-1	1 x	33.1	7.8	6.1	117.8	141.4	86.7	0.4322	0.5262
ABC-1	2 x	32.0	6.4	5.1	125.5	160.9	77.2	0.4053	0.5877
ABC-1	4 x	33.8	7.3	5.8	105.1	124.4	72.1	0.3921	0.5879
ABC-1	10 x	33.2	7.3	5.8	102.0	124.2	70.7	0.3823	0.5774
ABC-1	20 x	34.4	7.3	5.7	120.5	157.9	81.4	0.4322	0.5819
Limestone									
DK-1	1/3 x	160.6	40.1	38.6	413.5	448.8	99.0	0.4363	0.4374
DK-1	1 x	156.5	43.1	42.1	361.8	406.9	99.9	0.3749	0.3981
DK-1	2 x	166.6	37.7	37.0	421.4	431.5	99.9	0.4766	0.4766
DK-1	4 x	153.5	35.7	34.0	383.4	443.3	92.3	0.4320	0.4700
DK-1	10 x	172.6	38.9	37.1	434.7	454.8	99.7	0.4949	0.4949
DK-1	20 x	170.2	43.5	40.2	432.1	451.3	99.1	0.4386	0.4441
Anhydrite									
MO-5-11	1/3 x	107.0	49.6	39.6	156.3	272.1	92.9	0.2372	0.2791
MO-5-9	1 x	91.5	46.5	37.1	176.7	314.6	86.8	0.1902	0.2388
MO-5-10	2 x	84.3	37.3	35.4	106.2	218.0	97.5	0.2370	0.2495
MO-5-12	17 x	120.8	49.2	42.0	188.2	258.8	-	-	0.2847
MO-6	1/3 x	105.5	49.3	37.9	173.6	322.8	84.8	0.1949	0.2611
MO-6	1 x	111.9	57.6	46.8	208.0	312.5	85.8	0.1891	0.2273
MO-6	2 x	118.8	50.2	40.2	225.3	419.7	93.8	0.2426	0.2864
MO-6	4 x	121.6	58.8	47.0	256.6	448.5	91.9	0.2005	0.2455
MO-6	10 x	119.1	50.6	39.5	237.8	459.8	88.1	0.2126	0.2805

Former research proved that higher loading rates result in higher uniaxial compressive strength (s. chapter 2.4.1). This trend can be confirmed for certain rock types (gneiss, limestone, anhydrite), but others reveal nearly no change (sandstone). Sandstone samples show only insignificantly small changes in all determined parameters for different loading rates. Fig. 90 illustrates the influence of loading rate on the stress-strain curve of tested granite and anhydrite. For the sake of clarity, the stress-strain curves of maximum values at each loading rate level were plotted in the graphs. Granite samples differ from the trend of increasing uniaxial compressive strength since the maximum strength was reached at 2-fold loading rate. This may be caused by inhomogeneity in the specimens. If this result is considered as a discordant value, measured curves of granite and anhydrite agree in magnitude and trend with the theoretical assumption of OKUBO et al. (1990). With higher loading rates, the uniaxial compressive strength increases and the stress-strain curve tends to shift to the right in direction of the post-failure part. However, the deformation behavior in the pre-failure part does not change significantly, meaning that no changes in the Young's modulus could be observed.

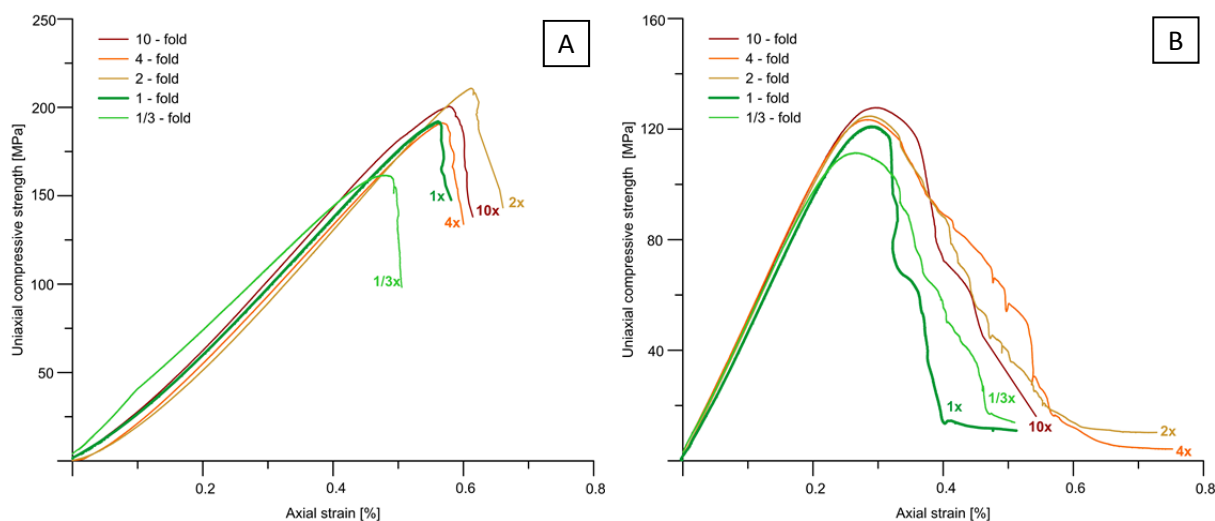


Fig. 90: Variations in stress-strain curves of tested granite TIT-5 (A) and anhydrite MO-6 (B) at five different loading rates from $\frac{1}{3}$ - to 10-fold of recommended rate acc. to DGGT (2004).

A detailed discussion on the influence of loading rate variations on toughness defining parameters is given in chapter 5.2.1. However, it must be noted that measured values at higher loading rates reveal certain fluctuation and higher standard deviation, since the machine may not record data with the same accuracy as at the standard loading rate.

5.2 Discussion

The following chapters discuss existing definitions to classify rock toughness referring to mentioned approaches in chapter 2.4. These are namely, the strain and energy approach, the strength approach and the special test approach. Furthermore, new characterization possibilities are presented and analyzed. The strategy follows the basic idea of plotting obtained laboratory results into existing definition systems. In a second step, resulting classification is compared with the actual behavior of tested rock types under uniaxial compression. Therefore, criteria are necessary to distinguish whether a rock behaves tough or brittle under compression. Theoretical background of how tough rocks fail under load has already been described in chapter 2.4. Fig. 91 - Fig. 93 show, how the theory can be

transferred to practice. To differentiate tough rocks from brittle ones, the existence of plastic deformation and a post-failure range are the main parameters. Laboratory results reveal that three different types of tough failure under uniaxial compression occur:

1. **High plastic deformation and no post-failure range** (Fig. 91A)
2. **Minor plastic deformation and major post-failure range** (Fig. 91B)
3. Combination of both: **high plastic deformation and major post-failure range** (Fig. 91C)

Calcareous mica schist (KGS) is a typical example for tough failure with high plastic deformation and nearly no post-failure range (Fig. 91A). The behavior might be explained by its mineral content. High plastic deformation is caused by minerals with existing cleavage planes and a tendency to glide along these. Calcite and mica are typical representatives of these minerals and built up a significant percentage of calcareous mica schist. After linear cutting tests with a disc cutter, KGS shows cracks mainly following mica layers, as well as cleavage planes of calcite and feldspar (LASSNIG 2012: 108). In contrast, damage zones produced in quartz follow grain boundaries and no intra-granular cracks are observed. The absence of a post-failure range may have its origin in the portion of quartz minerals in the sample that tend to fail with extremely brittle behavior, especially for unweathered conditions.

The **Anhydrite** (MO) specimen failed by showing minor plastic deformation and a distinct post-failure range (Fig. 91B). The crack damage point of the samples is at about 85 % of maximum strength resulting in plastic deformation of 15 % from total deformation. The late start of plastic deformation may be explained by the grain size and fabric of anhydrite. Large anhydrite minerals may hinder the coalescence of different microcracks so that unstable crack growth starts quite close to actual failure. The distinct post-failure range is an indicator for continuous internal cracking even after maximum strength is reached. This ongoing process requires a certain amount of energy to cause complete rupture of the rock structure.

Weathered Metten granite (MET) failed by combining both decisive parameters – high plastic deformation and a distinct post-failure range (Fig. 91C). This failure behavior is explained on the one hand by high feldspar and mica content. The minerals tend to glide along the dominant cleavage planes. The weathering process is the second factor and shows first impact at feldspar minerals. It causes cloudy surfaces and an alteration of feldspar minerals to clay minerals. Under the microscope, saussuritization of plagioclase minerals is also visible, leading to a mineral assemblage of chlorite, amphibole, carbonate and zoisite. All these minerals reveal a high tendency to glide and may explain the tough failure behavior of Metten granite. MARTIN (1993: 83) proved for granite samples that the first formation of cracks is located within the feldspar minerals along cleavage planes. High feldspar content may, therefore, favor the formation of microcracks accompanied by plastic deformation.

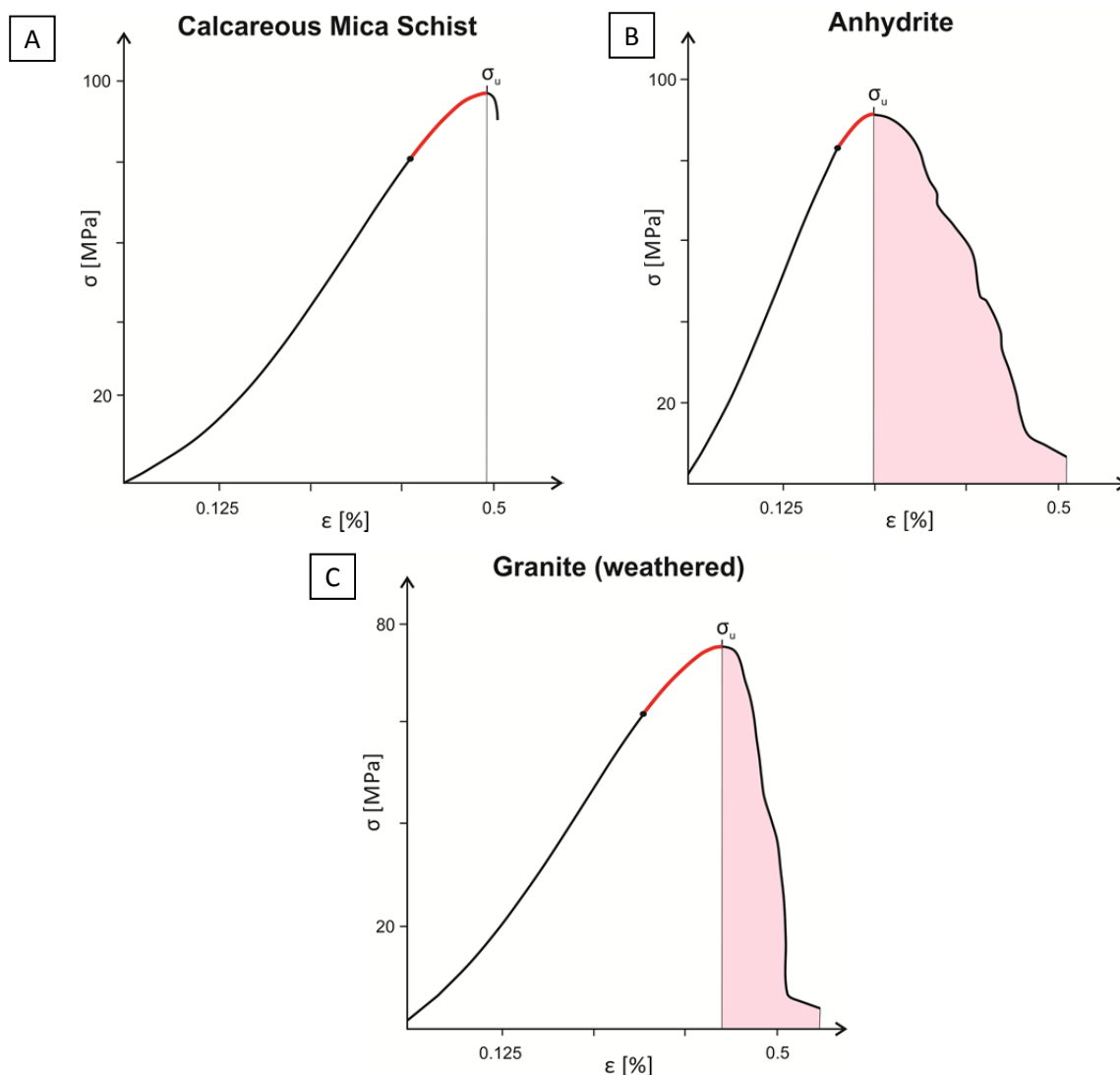


Fig. 91: Exemplary stress-strain curves of three different types of tough failure behavior. **A)** High plastic deformation & no post-failure range. **B)** Minor plastic deformation & major post-failure range. **C)** High plastic deformation & major post-failure range.

As special feature, the stress-strain curve of **quartzitic sandstone** (RTF) is plotted in Fig. 92A. The maximum deformation is extremely high compared to resulting strength. This is caused by the porosity of the tested samples. The pores may be open, or filled by cementing material like silicate. However, the pore structure can be compressed which leads to high deformation rates and a distinct post-failure range. Another feature is the stress-strain curve of tested **marble** (LAM, Fig. 92B). The twin gliding of calcite minerals is the dominant factor influencing the behavior of marble under load. This process leads to high plastic deformation, and although distinctive damage occurs within the rock sample, certain strength and cohesion is maintained even after maximum strength is reached. By acoustic emission testing simultaneously to uniaxial compression tests, it has been proven that real crack formation first started in the post-failure range and plastic deformation in the pre-failure range is only reducible to twin gliding along cleavage planes (WIESER in prep.). The influence of cleavable minerals such as calcite is even more obvious at higher loading rates. HAWKES & MELLOR (1970: 205) showed that doubling the loading rate leads to 50 % change in the slope of the stress-strain curve for marble and rock salt indicating that these rocks creep quite readily.

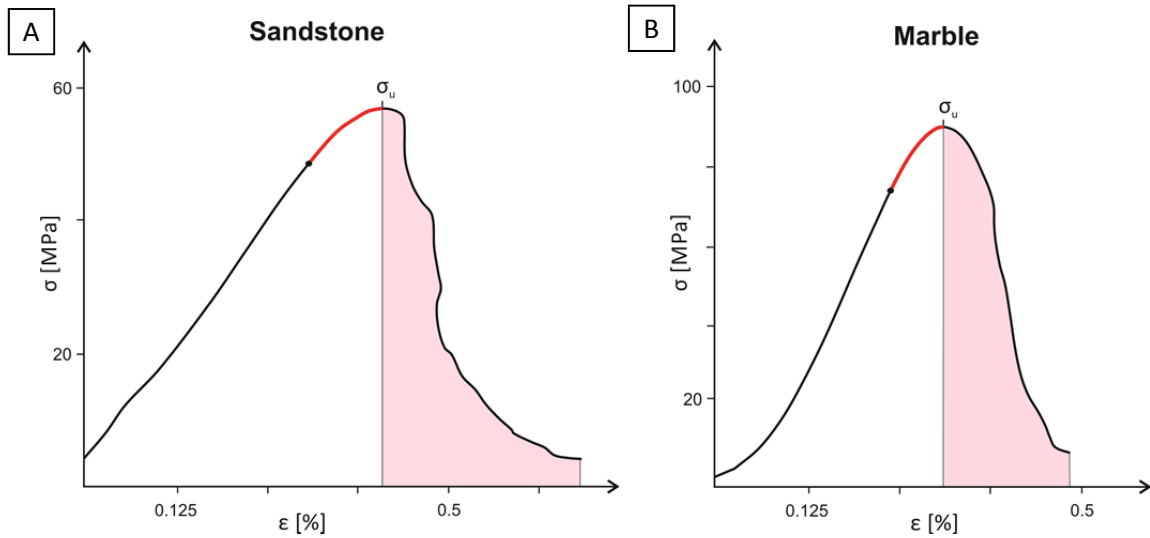


Fig. 92: Special stress-strain curves of tough failure behavior. **A)** Sandstone reveals extremely high deformation relative to its strength due to existing porosity. **B)** Marble shows major post-failure behavior and plastic deformation due to twin gliding.

The opposite of rock toughness is shown in Fig. 93. **Basalt** and **augen gneiss** are typical representatives for brittle failure behavior with infinitesimal plastic deformation and nearly no post-failure range. The rocks tend to be highly elastic until maximum strength and fail in an explosive manner when formed microcracks coalesce to macrocracks. The behavior has also been verified by punch penetration tests, where tested augen gneiss failed by coalescing cracks which abruptly formed large chips (ERBEN 2013: 63).

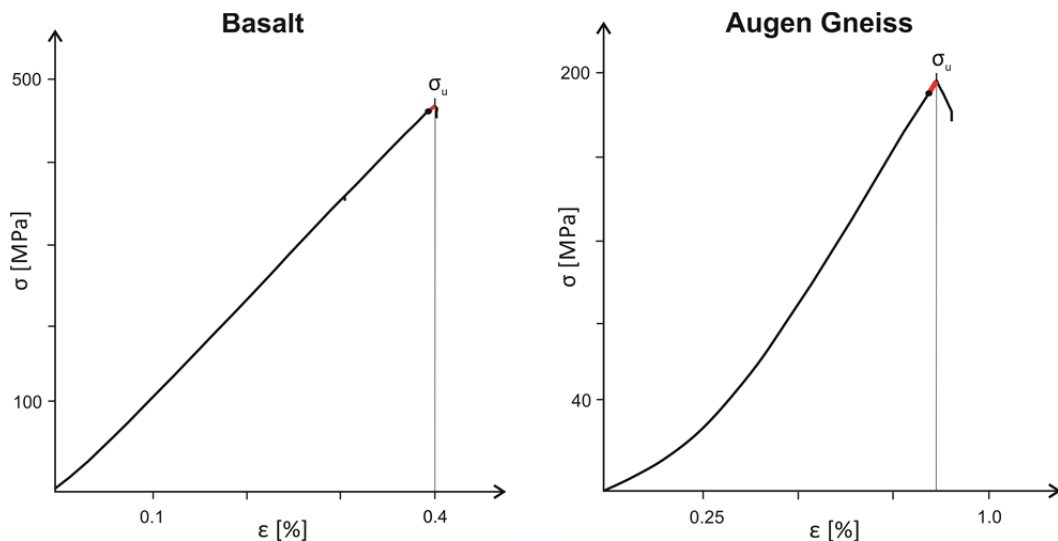


Fig. 93: Exemplary stress-strain curves of basalt and augen gneiss with brittle failure behavior showing minimal plastic deformation and no post-failure range.

Tab. 19 summarizes the results of tested rock samples in terms of several definition indices that may classify rock toughness. If corresponding classification systems are already existent, results are categorized into suggested classes. A detailed analysis of each mentioned index follows in the next chapters.

Tab. 19: Results of toughness defining indices of tested rock samples. If corresponding classification system is available, the background is highlighted (tough = light blue; brittle = light yellow).

Rock type	Failure behavior under compression	Existing classification system			No existing classification system			
		$T_z = \sigma_u / \sigma_t$	$T_{PLT} = \sigma_u / I_s$	T_{PPT}	E_t / E_{pl}	$\epsilon_u / \epsilon_{el}$	W_z / W_b	LBC / σ_t
Granite								
Flossenbürg (FLB)	tough	16.8	20.1	4.8	1.31	1.21	1.23	–
Tittling (TIT)	unspecific	14.2	16.9	6.7	1.07	1.12	1.08	–
Brixen (BX)	unspecific	19.6	24.5	13.1	1.03	1.2	1.11	6.41
Metten (MET)	tough	10.7	14.7	-1.8	1.21	1.78	1.25	11.00
Diorite Nittenau (NIT)	brittle	16.3	24.9	13.0	1.09	1.06	1.10	2.21
Basalt Pechbrunn (PB)	brittle	23.0	31.9	41.9	1.03	1.00	1.03	1.03
Gneiss								
Schistose gneiss (KAT-SG)	tough	8.9	19.2	-5.2	1.55	1.12	1.19	6.14
Gneiss (KAT-G)	tough	12.6	18.3	2.9	1.17	1.32	–	3.74
Augen gneiss (AG)	brittle	14.7	20.0	9.4	1.02	1.01	–	3.17
Granitic gneiss (GG)	brittle	13.0	23.3	4.0	1.05	1.09	–	3.52
Greenschist Pfunderer Valley (PFT)	brittle	18.5	29.2	18.7	1.04	1.08	1.06	–
Calcareous mica schist								
Limberg hydr. (KGS)	tough	12.3	16.7	0.7	1.23	1.30	1.07	7.77
Røssåga hydr. (Rø-2221)	tough	14.1	–	3.1	1.29	1.26	–	–
Amphibolite								
Oberbaumühle (OBM)	brittle	16.8	15.4	17.7	1.06	1.01	1.03	1.48
Humpelgraben (HUM)	brittle	25.4	–	24.8	1.05	1.04	1.05	4.22
Gleinalm tunnel (GLT)	unspecific	12.7	18.7	2.8	1.08	1.14	1.10	3.79
Quartzite (Rø-1294. Rø-1894)	brittle	20.7	23.2	22.6	1.06	1.0	–	–
Marble								
Laas (LAM)	tough	14.0	18.4	2.5	1.36	1.34	1.65	14.05
Koralmtunnel (KAT-M)	tough	13.9	21.1	2.6	1.46	–	1.25	14.12
Sandstone								
Rothenfels (RTF)	tough	19.0	17.9	3.5	1.34	1.36	–	–
Posta (POS)	tough	14.0	18.8	0.6	1.23	1.17	1.10	23.02
Abtswind Castell (ABC)	tough	12.9	13.5	-1.1	1.26	1.43	–	45.00
Limestone								
Wiesenhofen (WIE)	brittle	19.3	39.5	18.1	1.09	1.11	1.02	2.98
Dietfurt (DK)	brittle	17.6	24.3	10.2	1.02	1.00	–	3.87
Anhydrite Moosegg (MO)	tough	12.6	17.7	1.4	1.37	1.39	1.55	7.63

5.2.1 Toughness definition – strain and energy based approach

Fig. 94 shows the results of a strain and energy based approach characterizing rock toughness. In the left graphs (A-C), three ratios that may perhaps describe toughness are illustrated (s. chapter 2.4.3). In the right graphs (D-F), resulting indices are plotted against to tested rock types. For the sake of clarity in graphs D-F, mean values of each sample ID are used wherever specimens were drilled from different block numbers.

The first ratio is the **tangent Young's modulus** E_t divided by the **deformation modulus** E_{pl} which includes the plastic deformation part of the stress strain curve. If rocks reveal a high percentage of plastic deformation, this ratio should be significantly greater than 1.0 since the E_{pl} modulus is defined by a flatter slope due to the inflection of the stress-strain curve. Fig. 94A reveals that this ratio reflects the actual failure behavior of tested samples under load with good accuracy. A separation of tough (blue cross) and brittle (red cross) failure is clearly obvious. Therefore, the ratio of tangent Young's modulus E_t and the deformation modulus E_{pl} (**DI = deformation modulus index**) might be suitable for toughness classification. Fig. 94D emphasizes that indices greater than $DI = 1.1$, result in tough failure, whereas $DI = 1.0 - 1.1$ reveal brittle failure. The deformation modulus index DI also offers the advantage of a quick and easy determination method, since it can be calculated from results of standard uniaxial compression test.

The second relation is shown in Fig. 94B by the **axial strain at failure** ϵ_u and the **axial strain at crack damage point** ϵ_{cd} which marks the inflection point of the stress-strain curve. The ratio also characterizes the percentage of plastic deformation and can be determined by lateral strain measurements simultaneously to uniaxial compression tests (s. chapter 2.4.3). A classification of tough and brittle failure is not clearly evident. This might be caused by the fact that the measurement and data analysis is challenging (s. chapter 4.1.1). Furthermore, slight uncertainties lead to varying results for the determination of the crack damage point and corresponding axial strain. Uncertainties are diminished when using mean values (Fig. 94E), but measuring methods and data analysis are time consuming and only few laboratories use lateral strain measurements as standard. Therefore, toughness classification based on the **strain index** $SI = \epsilon_u / \epsilon_{cd}$ is not recommended although a threshold of $SI = 1.1$ is indicated.

Third possibility describes the energy based approach and consists of the ratio of **destruction work** W_z to **failure work** W_b (s. chapter 2.4.3.2). Ratios significantly greater than 1.0 indicate the existence of a post-failure range and therefore a tough failure behavior. Since the magnitude of destruction and failure work highly depends on the uniaxial compressive strength, normalized values are plotted in Fig. 94C for illustrative purposes. It is obvious that tough and brittle rocks can be well defined and a threshold of 1.1 becomes apparent. The **work index** $WI = W_z / W_b$ reveals good accordance with actual failure behavior of rocks under load, but bears some weaknesses. The accuracy of recording the post-failure range is highly dependent on the stiffness and setting of the testing machine and there is no standardized testing recommendation, concerning the post-failure range, available. Therefore, this method is not suitable for defining rock toughness. However, it may give a first impression of how each rock type behaves under compression.

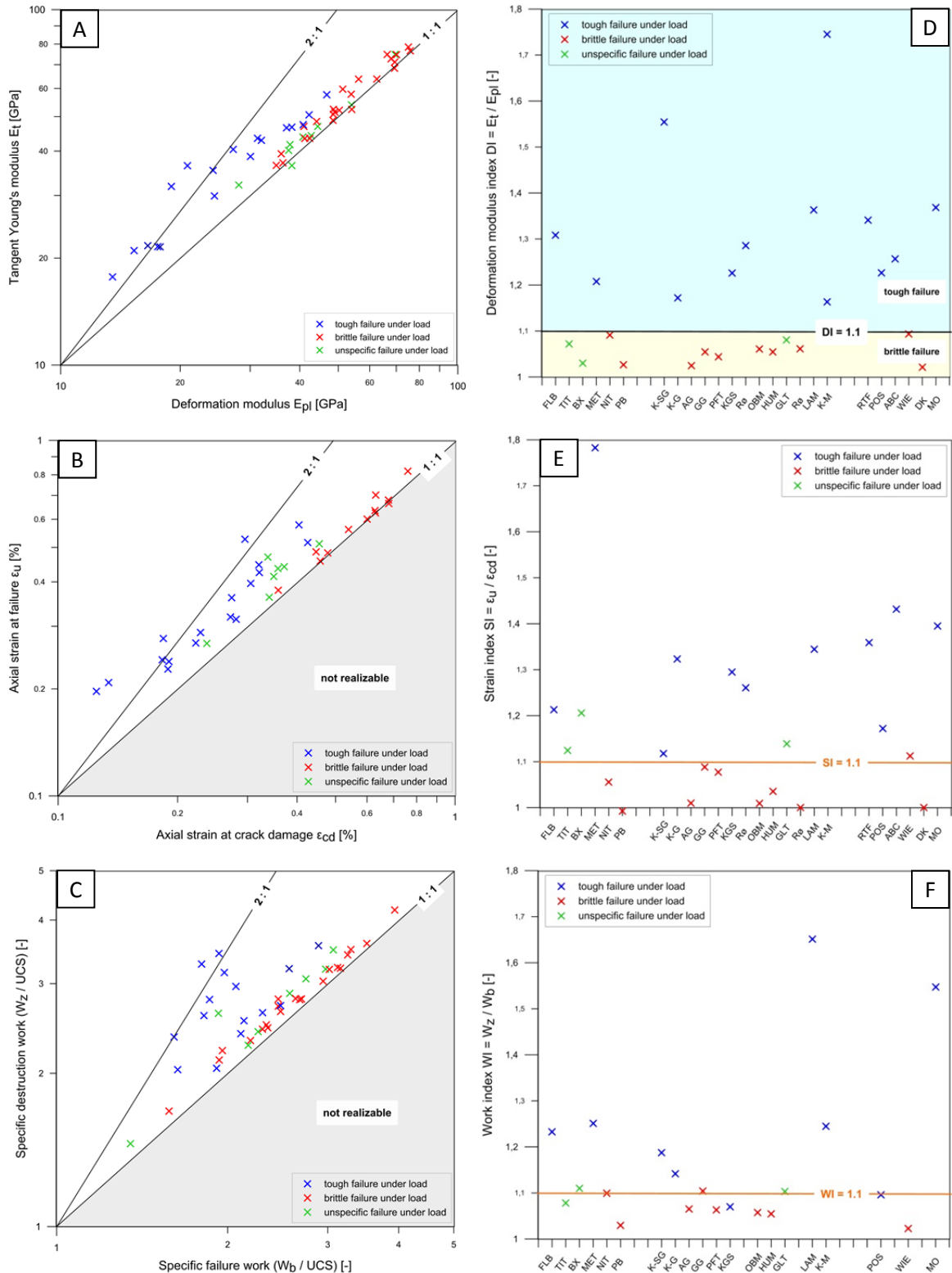


Fig. 94: **Strain based approach:** Tangent Young's modulus E_t is plotted against deformation modulus E_{pl} (A) resp. strain at failure ϵ_u is plotted against strain at crack damage ϵ_{cd} (B) of all sample blocks. **Energy based approach:** Relation of specific destruction work W_z is plotted against specific failure work W_b (C) of all sample blocks. Assignment of index values to corresponding sample IDs is shown in D – F, where a mean value of specimens from different blocks is illustrated.

Concluding, all three classification methods of the strain and energy based approach are in good agreement with each other and the actual observed failure behavior. The analysis leads to index thresholds of 1.1. Within the different testing methods, the strain approach via deformation moduli and resulting deformation modulus index DI reveals best results, especially with regard to the applicability. However, it must be noted that the method is only an approximation to characterize the portion of plastic deformation during compression and is not applicable to determine an exact value.

Influence of loading rate on deformation behavior

Loading rate variations have been performed for five rock types. The loading rate has been varied from $\frac{1}{3}$ up to 20-fold of testing recommendation acc. to DGGT (2004). The recommended strain rate for samples with 5 cm diameter is 0.06 mm/min. Samples with 8 cm diameter are to be loaded by 0.1 mm/min for standard testing. In this research, uniaxial compression tests with a maximum loading rate of 1.2 mm/min were performed. It seems to be close to the maximum recordable testing speed for used sample size since some tests at this level last only 20 s. Tests with higher loading rate may result in very high inaccuracies at measured parameters since the testing equipment is unable to record properly. Significant inaccuracies already occur at loading rates of more than 10-fold. Fig. 95 shows the relation between loading rate and uniaxial compressive strength. It is evident, that measured values vary to distinct degrees, indicated by error bars. Regression coefficients of plotted curves are low and the increase in strength between minimum and maximum loading rate of each rock type is often smaller than the variation within one loading rate level.

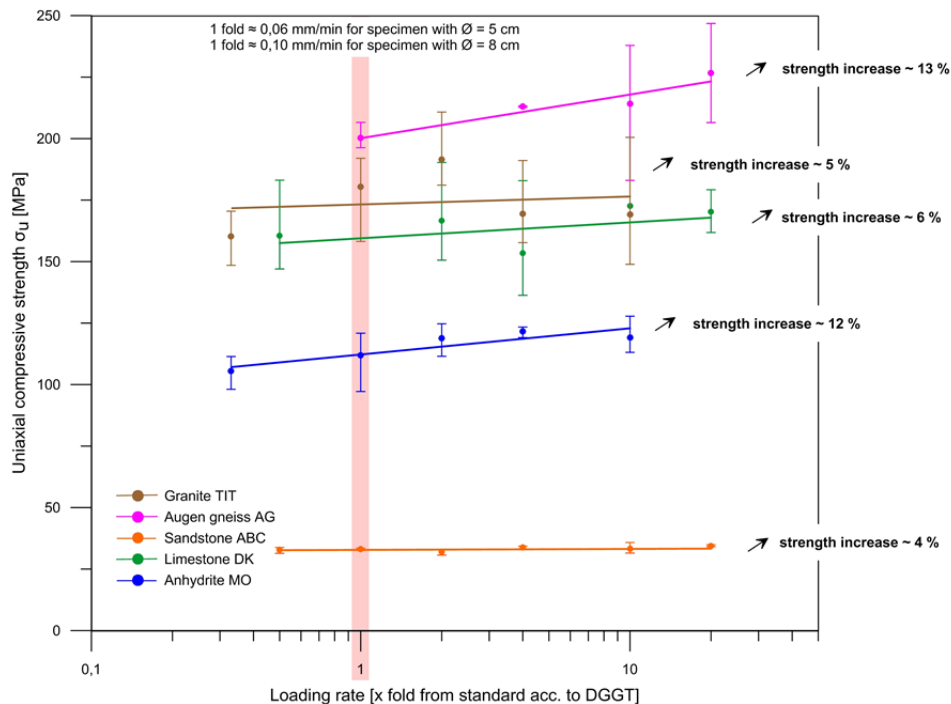


Fig. 95: Influence of loading rate on the uniaxial compressive strength of five rock types. Slight upward trend is noted since with increasing loading rate, also the uniaxial compressive strength increases. The increase in strength is calculated by using the average value of minimum and maximum loading rate.

The result of tested limestone is exemplarily explained (green line). Here, the increase in strength values for minimum to maximum loading rate is determined with about 6 %, meaning that the trend

line has a very shallow slope. However, the variance within one loading rate level, for example 4-fold, is $\pm 15\%$. This fact shows quite clearly that the increase in strength for higher loading rates is inferior to the variances that occur even within one loading rate level. Therefore, colored lines should only be considered as trend curves. Basically a certain trend is visible which indicates that the uniaxial compressive strength increases with increasing loading rate. Sandstone reveals no change in strength for all loading rate levels, which can be explained by the structure of the rock. Due to higher porosity, samples can transfer introduced energy to existing pores. This process takes place very fast so that higher loading rates do not change the strength significantly. KOBAYASHI (1971) observed that high porosity results in a low effect of loading rate variations. The author stated that much higher loading rates (minimum 1,000-fold) are necessary to record a certain influence on porous rocks.

According to HAWKES & MELLOR, low loading rates should result in a higher significance of the non-linear part of the stress-strain curve and thus higher plastic deformation. The general slope, expressed by the Young's modulus, should also decrease. This may be caused by thermal processes that favor lattice dilatancies and gliding along mineral grains (HAWKES & MELLOR 1970: 198). Results from performed tests reveal that Young's modulus changes infinitesimally and the effect of loading rate variation can be neglected (Fig. 96A). The strength at crack damage threshold is plotted in Fig. 96B. This parameter characterizes the beginning of the non-linear part of the stress-strain curve and value significantly lower than 100% indicate distinct plastic deformation. A slight trend is obvious that at an increasing loading rate, the crack damage strength decreases and correspondingly plastic deformation increases. This is precisely contradictory to former research. However, it is not noted for all rock types since anhydrite shows contrary results. Again measured results exhibit quite high fluctuation and colored lines are to be considered as trend line and not as regression. The influence of loading rate on failure and destruction work is marginal. However, a slight upward trend for increasing the loading rate has been observed, but again, standard deviation is quite high. It appears that the testing equipment used was not able to record the investigated parameters properly and with the accuracy to allow a detailed analysis of deformation behavior.

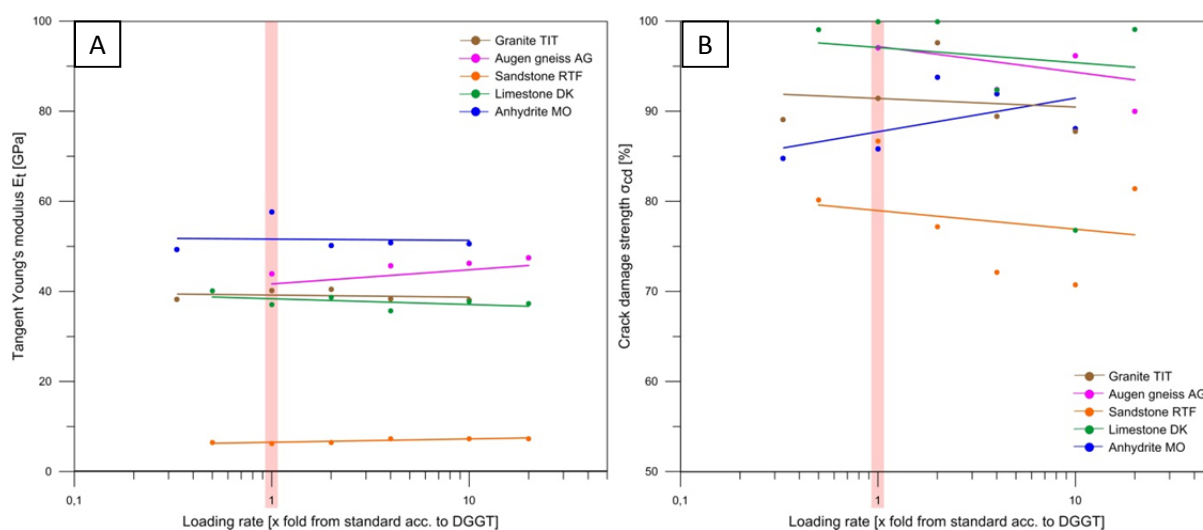


Fig. 96: Influence of loading rate variations on the Young's modulus (A) and the crack damage strength (B) at tested rock samples.

Furthermore, it must be kept in mind that the loading rate rocks are exposed during excavation by a TBM is about 1,000-times as high as usual loading rate at uniaxial compression testing (GEHRING 1997). This fact hampers the transfer of laboratory findings to the actual processes occurring at the tunnel face since higher loading rates correspond to the production of heat that favors thermal effects such as lattice deformation. These effects are hard to investigate by means of laboratory testing and are not yet fully understood.

Conclusively, tests confirmed existing research that with increasing loading rate also the uniaxial compressive strength increases. Nevertheless, the effect is not very pronounced and measurement results highly depend on the setting and accuracy of the testing machine. Young's modulus, failure and destruction work seems to be unaffected from loading rate variations.

5.2.2 Toughness definition – strength based approach

Ratio of uniaxial compressive strength to Brazilian tensile strength

First, the analysis considers the commonly used ratio of uniaxial compressive strength and Brazilian tensile strength. It is called toughness coefficient T_z which corresponds to the brittleness index B_1 (s. chapter 2.4.4). According to SCHIMAZEK & KNATZ (1976), the threshold between tough and brittle failure is at $T_z = 10$. THURO (1996) extended the classification by ranges for very tough ($T_z < 5$) and very brittle ($T_z > 20$). Fig. 97A shows that from over 400 individual tests only the mean value of one sample ID (mica gneiss) is classified as tough. This leads to the assumption that the existing threshold of $T_z = 10$ is not suitable. The link of the T_z coefficient to the failure behavior of tested samples under uniaxial compression is shown in Fig. 97B. Rocks that reveal tough failure behavior are marked with blue crosses, whereas brittle failure is illustrated in red. Green crosses represent rocks which failure behavior cannot clearly be attributed to tough, or brittle. It is also highlighted, that rocks with the same T_z coefficient (~ 19) may fail in entirely different ways, as shown by a blue, red, and green cross that follow the same line (brown triangle). Consequently, the existing definition of rock toughness by the ratio of uniaxial compressive strength to Brazilian tensile strength reveals poor results and has to be revised. It must be noted that a number of researchers found evidence that B_1 index correlates well with penetration rates in TBM tunneling (GONG & ZHAO 2007, KAHRAMAN 2002). Due to this fact, it seems likely that the failure mechanisms occurring in rock during excavation do not directly correspond to the failure behavior observed under uniaxial compression. This means, rocks that are hard respectively tough to drill, must not necessarily fail by tough behavior under uniaxial compression.

HUCKA & DAS (1974) and ALTINDAG (2003) proposed two additional indices ($B_2 = T_d$, $B_3 = T_e$) to determine the brittleness considering compressive and tensile strength of rocks (s. chapter 2.4.4). Both indices have been validated by the acquired data set, resulting in Fig. 98. It has been proven that T_e illustrates quite a strict separation of tough or brittle failure, whereas T_d reveals poor correlation. Therefore, the index T_e might be suitable for a new classification system to describe rock toughness. Fig. 98B shows that rocks with values $T_e < 1,000$ fail by tough behavior, whereas rocks with $T_e > 1,000$ show brittle failure under load. This index is very properly illustrated, since it shows that besides failure behavior under uniaxial compression, it also seems to reflect the behavior of rocks during excavation. This is the fact as it considers both parameters - uniaxial compressive strength and Brazilian tensile strength - that influence the formation of rock chips.

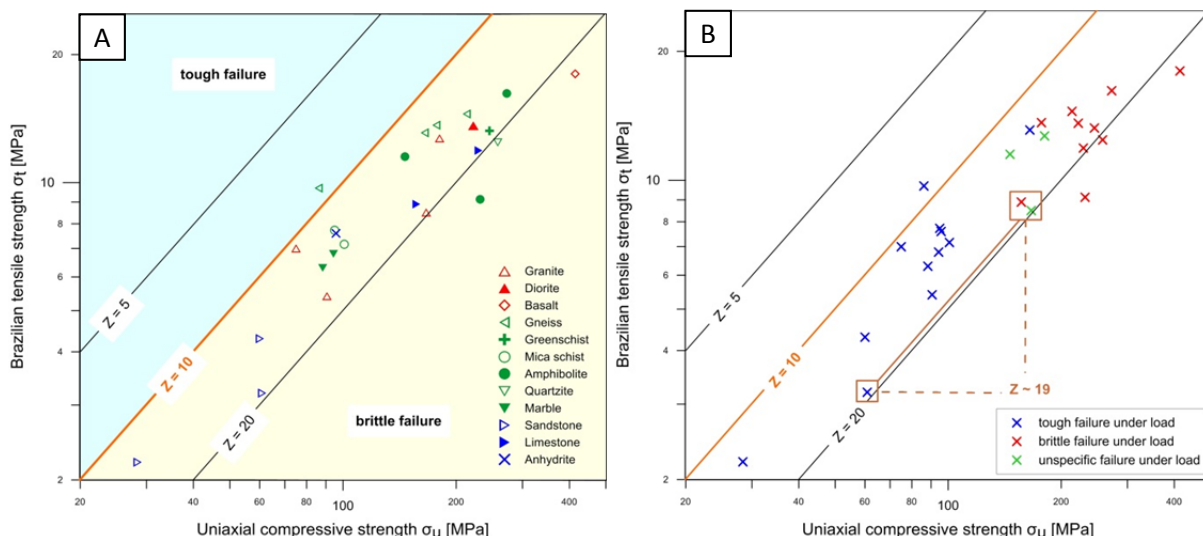


Fig. 97: **(A)** Toughness coefficient T_z , Uniaxial compressive strength vs. Brazilian tensile strength with the existing classification of SCHIMAZEK & KNATZ (1976) and THURO (1996). **(B)** In addition, failure behavior of tested rock samples under uniaxial compression is considered, which reveals that same T_z value results in either tough or brittle failure (brown triangle).

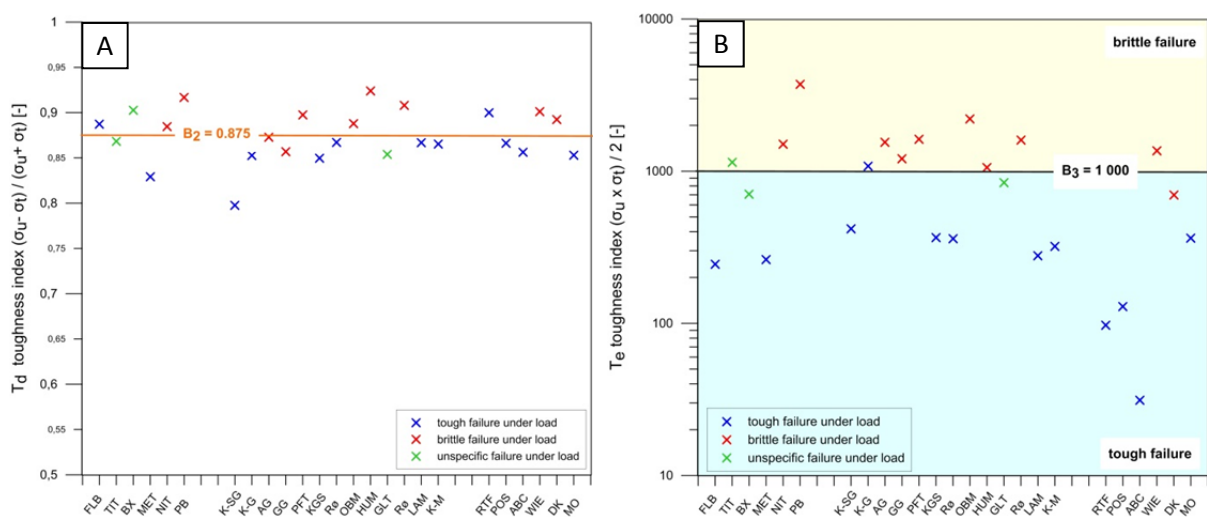


Fig. 98: Calculation of toughness indices T_d **(A)** and T_e **(B)** depending on the rock type. The failure behavior of tested rock samples under uniaxial compression is considered by colored crosses. In addition, possible classification for tough or brittle failure behavior based on T_e is plotted.

In conclusion, it can be stated that from three approaches to characterize toughness via uniaxial compressive strength and Brazilian tensile strength, only one method reveals satisfying results. This is the probably least known factor $T_e = B_3$ that is based on the idea of specific energy (ALTINDAG 2003: 165). A threshold of $T_e = 1,000$ seems suitable for a classification of rock toughness respectively brittleness.

Ratio of uniaxial compressive strength to point load index

The second approach to define toughness is the ratio of uniaxial compressive strength and point load index I_s leading to the correction factor c and **toughness index** T_{PLT} (s. chapter 2.4.4). KLEIN et al. (1995) and BARTON (2000) found that ratios lower than the threshold of $c \sim 20$ result in low TBM penetration rates. The authors explained this coherence by rock toughness and stated that rocks with

low ‘c factors’ behave tough and show a higher resistance against the boring process. From the rock mechanical point of view, both parameters somehow characterize similar failure processes. However, the point load index might also include aspects of tensile strength. The conical indenter simulates the fragmentation process under a disc cutter quite well and the uniaxial compressive strength is responsible for the formation of a crushed zone, whereas tensile strength is the decisive parameter for the crack formation causing the collapse of the cubic rock sample. Fig. 99A illustrates that a number of samples such as anhydrite, sandstone and mica gneiss are classified as tough. Considering the failure mode of plotted data points, shows that the suggested toughness classification by KLEIN et al. (1995) and BARTON (2000) meets the observed failure behavior under uniaxial compression, more or less. Since the ratio of UCS and I_s is used - and I_s combines compressive and tensile strengths - it might be an indicator that the tensile strength seems to be the decisive parameter in terms of rock toughness.

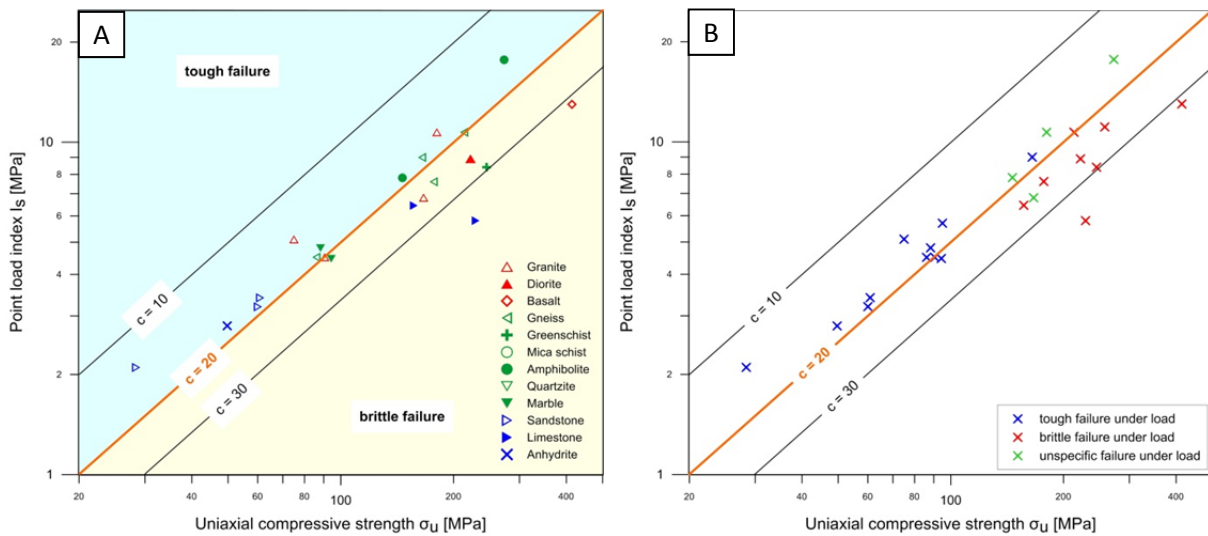


Fig. 99: (A) Toughness index T_{PLT} . Uniaxial compressive strength σ_u vs. point load index I_s . Threshold for tough failure behavior are adopted from KLEIN et al. (1995) and BARTON (2000). (B) Failure behavior of tested rock samples under uniaxial compression is considered. It reveals that suggested toughness classification approximately meets observed failure behavior under load.

Since the accuracy of abovementioned ratios depend on the reliability of measured geotechnical parameters, the correlation between BTS and I_s has been analyzed to cross-check the plausibility of laboratory results. By means of this it could be proved, that the point load index is 0.73 times the Brazilian tensile strength. This value is in good agreement with the suggested factor of 0.8 by the ISRM (1985) and verifies the plausibility of obtained parameters.

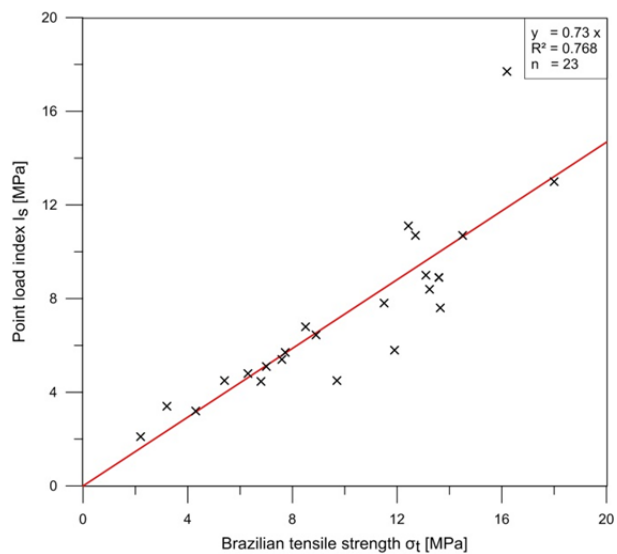


Fig. 100: Brazilian tensile strength σ_t vs. point load index I_s of tested rock samples. I_s is approximately 0.73 times σ_t .

Conclusively, the ratio of uniaxial compressive strength to point load index might be an appropriate tool to describe rock toughness and is suitable for further development and subsequent implementation into a penetration prediction model. Since the point load index somehow combines compressive and tensile strength, the good fitting of the ratio of UCS and I_p indicates that tensile strength might be the decisive parameter in terms of rock toughness. The approach is discussed in chapter 6.2.2.

5.2.3 Toughness definition – special test based approach

For further investigations on the special test approach, one representative is chosen for each testing method of impact tests and rotary tests.

Impact test (punch penetration index)

The punch penetration test reflects the resistance of rocks against indentation (s. chapter 2.4.5). On the American continent, this test is often used, also to characterize rock brittleness and toughness. Since the determination of the brittleness index is based on results from the punch penetration test, it is commonly not used in Europe. The conversion formula of YAGIZ (2009: 72) allows the determination via standard laboratory tests such as uniaxial compression test and Brazilian tensile test ($BI_p = T_{PPT}$, Eq. 2-29). Results are plotted in Fig. 101. It reveals that the existing classification system does not fit to the failure behavior of rocks under uniaxial compression. This leads to the assumption that a new threshold for tough to brittle transition might be set at $T_{PPT} = 10$ instead of 20. Furthermore, T_{PPT} can result in negative value which is caused by the proposed formula. If the uniaxial compressive strength is low in relation to the Brazilian tensile strength, the calculated index decreases below zero.

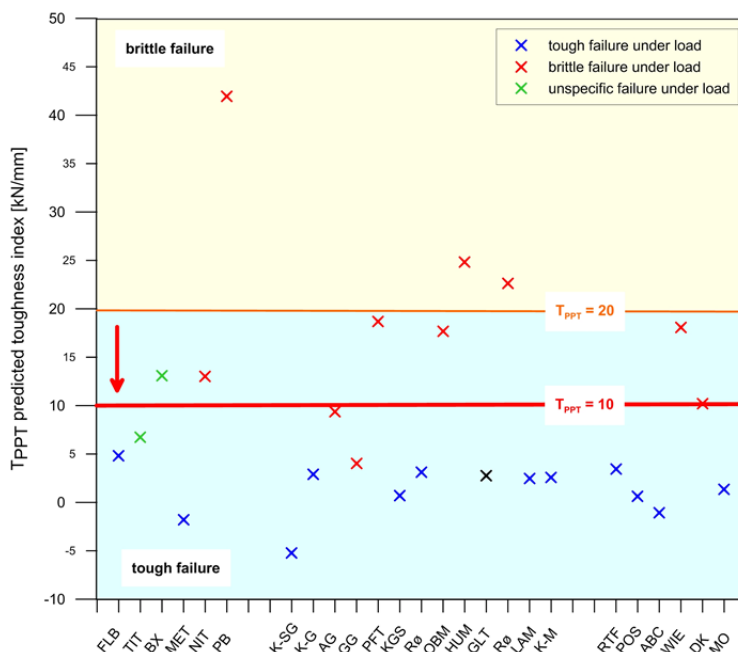


Fig. 101: Calculation of the punch penetration toughness index T_{PPT} depending on the rock type. Failure behavior of tested rock samples under uniaxial compression is considered by colored crosses. In addition, existing classification for tough / brittle failure behavior with the threshold of $T_{PPT} = 20$ is plotted (YAGIZ 2009). New threshold of $T_{PPT} = 10$ seems more reasonable.

Furthermore, clear correlation between failure behavior under uniaxial compression and data by ERBEN (2013) concerning punch penetration has been found. Augen gneiss (AG) as brittle rock reveals a highly fluctuating force – penetration graph which corresponds to brittle failure. Conversely, calcareous mica schist (KGS) shows smooth force – penetration curve which corresponds to tough failure (Fig. 102). These findings coincide with the observed failure behavior during the uniaxial compression test. Further, tough rocks do not fail suddenly and no large rock chips are formed under punch penetration. Analysis of the rock surface after the test reveals that no rock pieces are missing and the material was simply pushed aside by the indenter where it procrastinated. The crushed zone is shallow, but wide. Conversely brittle rocks tend to form large, wedge shaped chips with deeper crushed zone (ERBEN 2013).

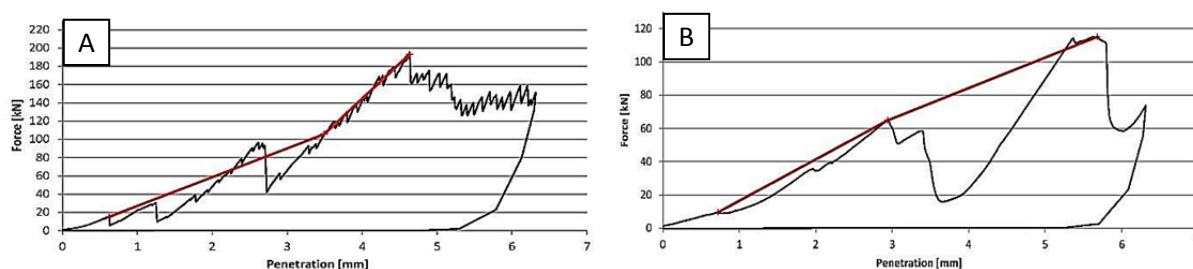


Fig. 102: Force – penetration graphs as results of punch penetration test. **A)** shows augen gneiss (AG) as brittle rock with highly fluctuating curve and **B)** calcareous mica schist (KGS) as tough rock with smooth curve (ERBEN 2013: 53).

Conclusively, the determination of toughness index T_{PPT} via the conversion formula of YAGIZ yields good results. However, the existing classification has to be revised. On the basis of obtained data set, a new threshold of $T_{PPT} = 10$ seems to be more suitable.

Rotary tests (LCPC breakability coefficient)

Another parameter that has to be investigated when talking about rock toughness is the **LCPC breakability coefficient LBC**. Tough rocks seem to show a greater resistance against indentation by disc cutters and therefore lower penetration rates. Since the penetration highly depends on the efficiency of fracture propagation, the toughness of rocks might also be described by the breakability coefficient (s. chapter 4.1.5). High LBC values correspond to good breakability, whereas low LBC values describe rocks that are hard to crush. Combining this idea with results from the uniaxial compression tests leads to the hypotheses that rocks with a tough failure behavior under load should result in low breakability coefficients. Results reveal that a sole consideration of LBC does not fit to this hypothesis, since very brittle rocks such as basalt yield low LBC. In contrast, marble as tough rock results in very high LBC values (s. Tab. 16, page 101). This fact may be explained by correlating rock strength parameters such as UCS, BTS, and I_s with the breakability coefficient LBC. Fig. 103 illustrates that a distinct trend between rock strength parameters and LBC is obvious resulting in regression coefficients between 0.74 and 0.81. Low strength values cause higher breakability coefficients, meaning that the rock is easier to crush since the forces that keep grains together are lower. This fact is not remarkable and can be observed for uniaxial compression strength, as well as for point load index by logarithmic regression (Fig. 103A, B). The trend is even clearer at the correlation of LBC and Brazilian tensile strength where the linear relationship reveals a regression coefficient of 0.75 (Fig. 103C). Low tensile strength allows easy formation and propagation of cracks, since the grain bonding is lower

which leads to higher LBC values. These findings have been proven by acoustic emission testing to analyze the amount of newly formed cracks. Here, Basalt shows only few acoustic emissions, meaning that few cracks have been formed. This correlates with low breakability coefficient. Conversely marble, sandstone, and anhydrite reveal a number of events which corresponds to many newly formed cracks and a high breakability (WIESER in prep.).

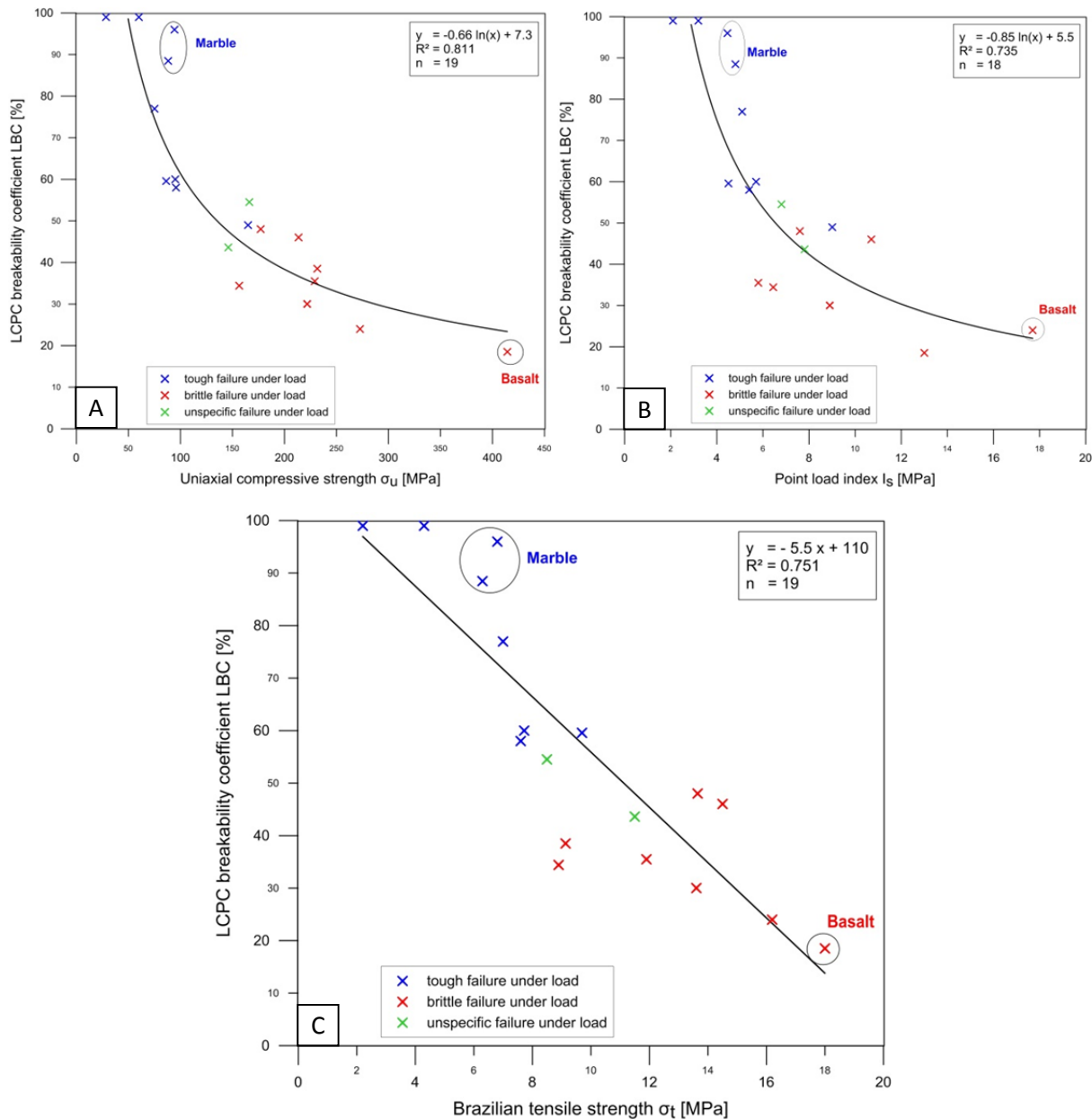


Fig. 103: Uniaxial compressive strength (A), point load index (B) and Brazilian tensile strength (C) of tested rock samples plotted against LCPC breakability coefficient.

The link of these correlations with the deformation behavior of samples under load, results in some interesting findings. Fig. 104 shows the same graphs as Fig. 103, but rock samples are classified according to their failure behavior under uniaxial compression (tough = blue, brittle = red). By this, a clear distinction into two ranges is obvious. Upper left part cumulates rock samples that fail under tough deformation, whereas in the lower right part samples with brittle failure are plotted. Thresholds for $LBC / \sigma_u = 1/3$ and $LBC / I_s = 8$ seems to be reasonable (Fig. 104A, B). The best correlation is

achieved by the ratio of LBC to Brazilian tensile strength BTS. Here, a threshold of 5 reveals high accuracy (Fig. 104C). This new index is named T_{LBC} since it defines rock toughness by the ratio of LBC and BTS.

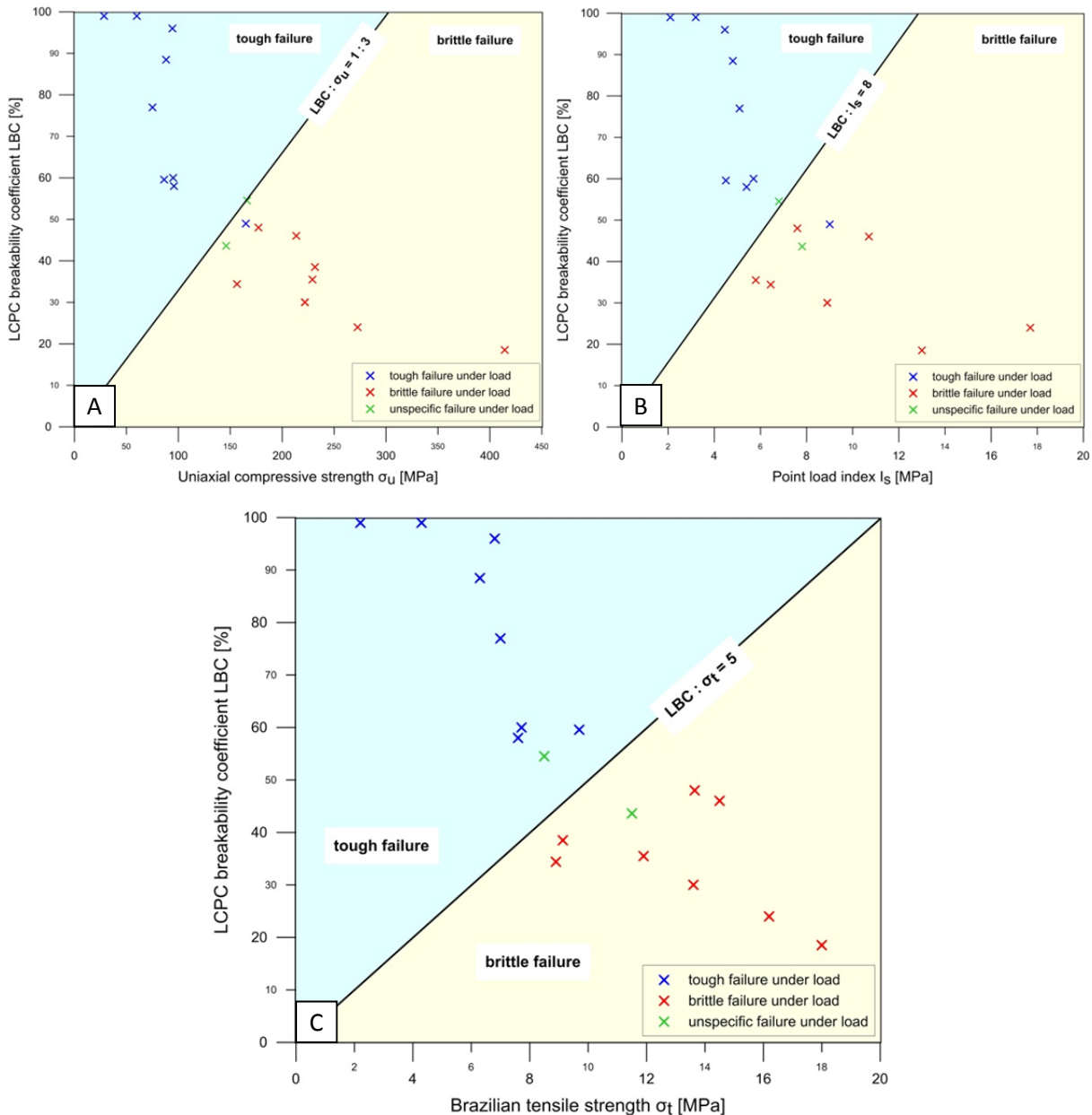


Fig. 104: Uniaxial compressive strength (A), point load index (B) and Brazilian tensile strength (C) plotted against LCPC breakability coefficient. Rock samples that behave tough under uniaxial compression are plotted in blue, brittle failure is plotted in red. Suggested thresholds for tough (bluish) resp. brittle (yellowish) failure is marked with colored background.

However, it must be noted that this trend is contradicting to the research opinion where tough rocks show higher resistance against boring, since rocks that fail under tough behavior result in high breakability and also low tensile strength in this research. This would mean that the binding forces are generally smaller for tough rocks than for brittle ones. It might be explained by the fact that several rocks that are classified as tough in presented graphs contain certain mica and calcite percentage or exhibits

distinctive porosity. These observations are responsible for pronounced plastic deformation under load, but also result in lower strength values. Therefore, it is recommended to extend obtained results by several more rock types.

To briefly summarize, the correlation of Brazilian tensile strength and LCPC breakability coefficient (Fig. 104C) is named T_{LBC} and results in a suggested threshold of $LBC / \sigma_t = 5$. Ratios higher than five are related to tough rocks, whereas lower ratios correspond to brittle rocks. However, it must be noted that this trend is contradicting to the research opinion that tough rocks show higher resistance against boring. Further analysis is discussed in chapter 6.2.2.

The abovementioned results analyzed the existing possibilities to characterize rock toughness in the laboratory. Further step is the investigation on how a tough failure behavior influences the performance and particularly the penetration of a TBM. Tough failure behavior is accompanied with a significant amount of plastic deformation and a distinct post-failure range. Since both processes are associated with high energy consumption, it is suggested that tough rocks are harder to excavate than brittle ones. Furthermore, the formation of a crushed zone beneath the disc cutter and the propagation of major cracks are hampered (GONG & ZHAO 2007, BRULAND 2000b) (s. chapter 2.4, page 25). These facts must lead to lower penetration rates for tough than for brittle rocks. The correlation of the abovementioned, suitable toughness definitions with penetration rates measured at two tunnel projects is presented in chapter 6.2.2.

6 Results and discussion of field investigations with a focus on discontinuity pattern

Field investigations have been performed on two tunnel projects as described in chapter 3. The emphasis is on conducting penetration tests at construction sites to analyze the interaction of tunnel boring machines and excavated rock mass, as well as the influence of discontinuities on the performance and penetration rate of hard rock TBMs. In total, 28 penetration tests have been performed. In addition to the actual test, a detailed geological mapping and sample acquisition has been done at each chainage where penetration tests have been conducted. This is obligatory for further analysis on the discontinuity pattern and validation of existing penetration prediction models.

6.1 Results

Due to the large number of existing penetration prediction models, two representatives from different approaches have been chosen for detailed analysis (s. chapter 2.3). These are namely the commonly used Colorado School of Mines (CSM) model - as theoretical approach - and the Gehring model - as an empirical approach (ROSTAMI 1997, GEHRING 1995). The chosen approach is to compare estimated parameters of both prediction models with actual penetration test results. In a first step, only basic formulas without correction factors for geological or geotechnical parameters are analyzed. In a second step, the influence of discontinuity pattern is validated by implementing suggested correction factors into the prediction models and comparing predicted values with measured data.

Initially, results from the laboratory program in terms of rock toughness should be compared with data acquired in the field. This should have result in a correction factor suggestion for rock toughness that could have been implemented into the prediction model. However, the rock variability at actual tunnel projects is limited, and the influence of rock toughness on penetration rates can only be investigated at four rock types. These were encountered at the Koralm tunnel and the Rössåga hydropower project: schistose gneiss, mica gneiss, calcareous mica schist and quartzite. Unfortunately, this covers only the range of metamorphic rocks and no investigation could be made on magmatic or sedimentary rock types.

This chapter summarizes representative results of the penetration tests. Besides test evaluation, CSM and Gehring model are plotted in their basic version without correction factors for rock toughness or discontinuity patterns. A discussion on the influence of discontinuity systems, as well as on rock toughness, follows in chapter 6.2. Detailed geological mapping is the basis for proper interpretation of obtained data and has been conducted at all penetration tests (s. chapter 4.2.2). For the sake of brevity, only a chosen number of geological tunnel mappings are presented in this thesis.

Part of the field investigation has been performed in collaboration with P. Ellecosta within the scope of his doctoral theses at the TUM (ELLECOSTA in prep.) and several master theses (LEISCH 2013, WEIGERT 2013, RAUCH 2016).

6.1.1 Influence of discontinuities on TBM penetration

To investigate the influence of discontinuities on the overall TBM performance, several more aspects have to be taken into account concerning the construction process such as time for mucking, rock support and the adapted controlling of the machine as a reaction on weaker rock mass conditions.

However, the aim of this work is to examine the effect of planes of weakness on the parameter ‘penetration rate’. In case of favorable orientation and spacing, discontinuities reduce the required thrust at the same penetration rates. In contrast, unfavorable discontinuity systems can cause blocky faces, and lead to worse performance than predicted.

At studied project site, the Koralm tunnel provides better opportunities to study the effect of fractured rock mass since the Koralm crystalline basement is highly fractured in some parts due to Alpine orogeny. Conversely, the Røssåga hydropower project is situated in mostly unfractured rock mass of the Caledonian orogeny.

Fig. 105 illustrates TBM data analysis of the **Røssåga hydropower project**. The mean penetration is plotted against 1,000 m of tunnel length and the result is compared with predicted values from the basic CSM and Gehring model. Altogether, prediction agrees quite well in trend and magnitude with actual measured penetration rates. Both models are used in its basic version and no correction for discontinuity systems is incorporated. Nevertheless, the result is satisfying which is only possible since the tunnel is located in almost unfractured rock mass. The divergence of – 30 % at chainage 1,600 might be caused by inaccuracies within the input parameters since rock samples for uniaxial compression testing have been taken only 300 m before and after this chainage. However, the rock type does not change significantly. This suggests that here, the influence of discontinuities affects the prediction to a significant extent. The same fact can be observed at the other peaks, where the actual penetration rate is clearly higher than predicted one. Conclusively, both models show good accuracy for massive, almost unfractured rock mass and certain variances for fractured rock mass.

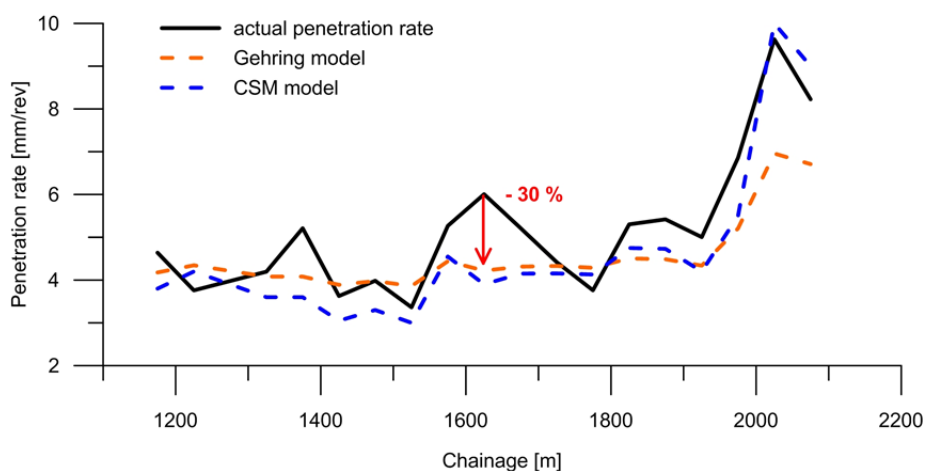


Fig. 105: TBM data analysis at the Røssåga hydropower project. Mean penetration rate is plotted against 1,000 m tunnel length. Additionally, predicted values from the basic CSM (blue) and basic Gehring (orange) model are displayed. Both models reveal reasonable accordance with actual measured data. The divergence of up to -30 % is caused by inaccuracies in input data and higher fracturing degree.

The opposite is shown in Fig. 106 where TBM data of about 500 m tunnel length at the **Koralm tunnel** is analyzed. Analyzed section is subdivided into three section – rock type 1 to rock type 3 – whereas the term of ‘rock type’ describes the whole rock mass in this context, including rock inhomogeneities and petrographic variations, as well as discontinuity patterns. The data preparation has been done by LEISCH in terms of his master thesis (LEISCH 2013). To investigate the accuracy of the penetration prediction models, geotechnical input parameter are taken from the report of ÖBB-INFRA 2009b for the rock mass of schistose gneiss that occurs up to chainage 4,000. However, this rock mass

strength appears to be inappropriate for the first rock type section, since prediction models calculate way too high forces, although geological mapping shows no significant fracturing degree. Laboratory test results reveals that there are two varieties of schistose gneiss, one with a uniaxial compressive strength of around 70 MPa and the other with around 120 MPa. The rock type that appears in the area of rock type 1 is more likely a schistose gneiss with only 70 MPa UCS, since the divergence cannot be explained by other influencing factors such as discontinuities. The implementation of the lower strength value into the models results in good accuracy with the actual data.

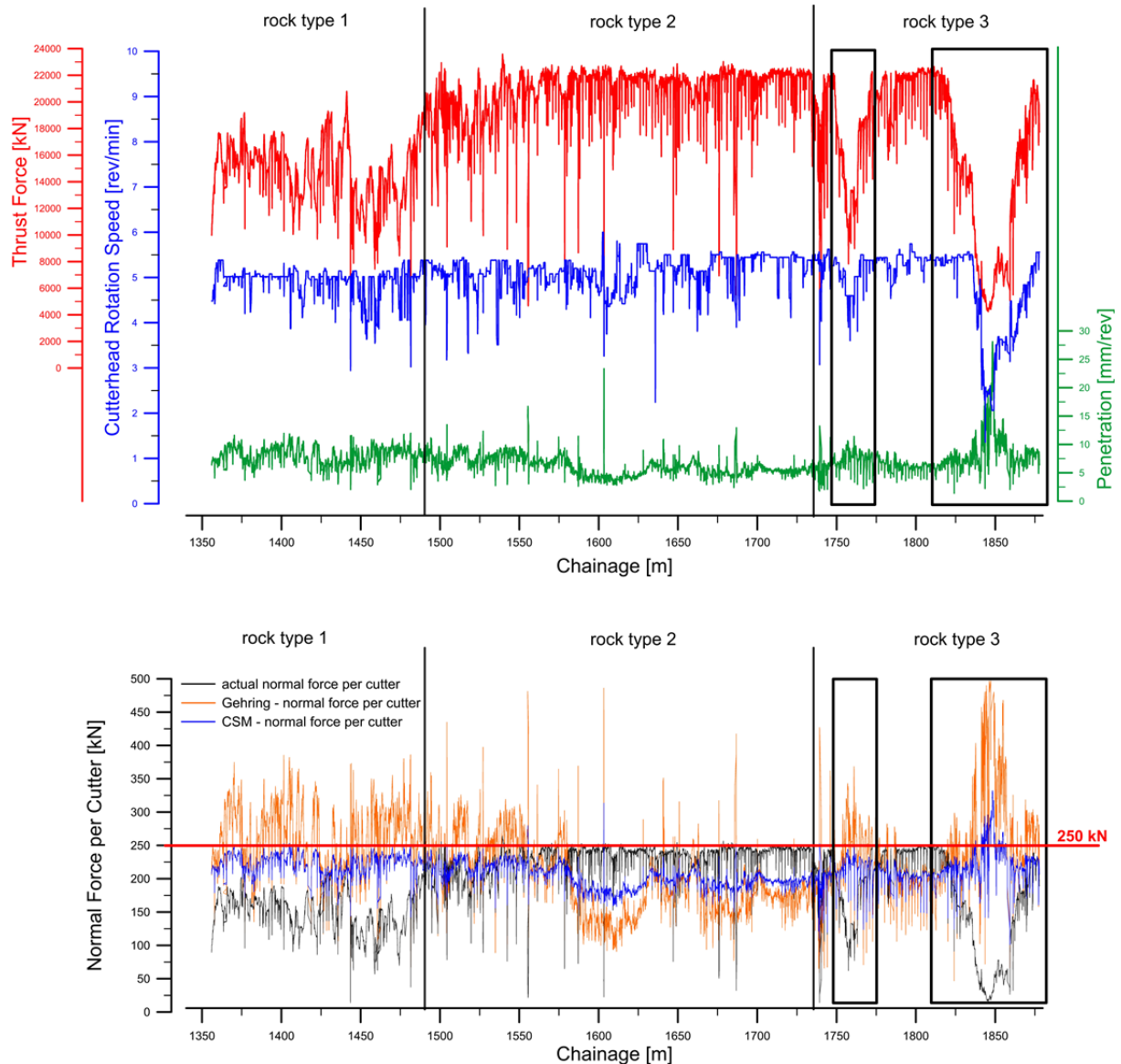


Fig. 106: TBM data analysis at the Koralm tunnel. Marked force drop is accompanied with an increase in penetration rate (black rectangles). In addition, calculated forces from the CSM (blue) and Gehring (orange) model are displayed. Both models reveal extreme deviation from actual measured normal force in the section of rock type 3.

In the area of rock type 2, the TBM reaches approximately the maximum possible thrust force. However, in this range, the penetration rate reveals the lowest results of the total analyzed section. The rock mass in area 2 is built up by schistose gneiss with siliceous marble layers and only a low fracturing degree with minor fissures is noted. Individual variations in this section may be caused by the

orientation and surface characteristics of schistosity layers, since these parameters define whether a plane of weakness can be activated to facilitate the cutting process. In this case, both prediction models meet approximately the measured forces. In rock type 3, the discrepancy between predicted and measured values can be noticed intensively although the rock type (schistose gneiss) does not change within the area. Here, one section is emphasized with a black rectangle. The force, as well as the cutterhead's rotational speed decrease significantly. In contrast, the penetration rate increases to the same extent. Similar trends can be noted at chainage 1,760. Geological documentation reveals that the rock mass is moderately to strongly fractured. Several numbers of slickensided planes of weakness, joints, fissures, and detached blocks at the tunnel face were detected. Large blocks have been observed around the caliper of the cutterhead.

Geological conditions lead to falsified predicted penetration rates which are around three times lower than actual achieved penetration (7.9 mm/rev) at the Gehring model (3.0 mm/rev) and even less at the CSM model (0.8 mm/rev) (LEISCH 2013). Back-calculating the strength with both models by actual required force, results in a rock mass strength of 55 MPa for the Gehring model and 42 MPa for the CSM model. Actual strength of this rock mass is set at 130 MPa according to the report by ÖBB-INFRA (2009b). It can be assumed that the reduction of 60 % in rock mass strength may be caused to a significant extent by the high fracturing degree of the rock mass. This observation highlights the effect of discontinuities on the strength of the rock mass and resulting penetration rates which is discussed in detail in chapter 6.2.3. Analysis of TBM data from the exploratory tunnel Aicha at the Brenner base tunnel results in the same findings and so detected weakness zones should be transferred to main tunnel tubes (WEGSCHEIDER 2012).

6.1.2 Penetration test

The basic result of a penetration test is the relation between penetration rate and total thrust force (s. chapter 4.2.1, Fig. 60). During the penetration test, the machine is conducted under normalized conditions for a defined time interval. For detail testing procedure, see chapter 4.2.1 (page 82). To enable the comparison of penetration tests at different tunnel projects or different chainage of one tunnel project, these graphs are converted from total thrust force to normal force per cutter. Therefore, 100 % of the measured friction is subtracted from the total thrust before dividing it through the number of disc cutters. Analysis has also been done with friction values of 50 %, which is discussed later (s. Fig. 114 and Fig. 115).

Tab. 20 summarizes the results of conducted penetration tests at the Koralm tunnel and the Røssåga hydropower project. Predicted penetration rate of the Gehring and CSM model for maximum normal force per cutter is also listed. Force and corresponding stress under the disc cutter at the point of subcritical penetration (3 mm/rev penetration) are presented since these parameters are significant for investigations on the relation between force and penetration (s. chapter 6.2.1). Besides TBM data, geotechnical parameters acquired from laboratory tests are presented. Since most of the presented penetration test results were performed in gneiss, the term of anisotropy is shortly mentioned. The determination of all geotechnical parameters was done with attaching importance to proper sample preparation. This means, that all samples were tested with their schistosity perpendicular to the loading rate. This fact eliminates the influence of anisotropies as much as possible resulting in the maximum achievable strength value. The incorporation of the maximum strength value seems to be reasonable,

since the schistosity mostly did not act as active discontinuity during the penetration test. If no samples were available, these parameters were taken from the geotechnical report whenever applicable.

Tab. 20: Summarized results of performed penetration tests and corresponding laboratory program.

F_{Dmax} = max. force per disc cutter; P_{max} = max. penetration; $P_{Gehring/CSM}$ = predicted penetration at F_{Dmax} ; F_{D3mm} = force at 3 mm penetration; σ_{D3mm} = stress under cutter at 3 mm penetration; σ_u = uniaxial compressive strength; σ_t = Brazilian tensile strength; I_s = point load index, LBC = LCPC breakability coefficient.

Test ID	F_{Dmax} [kN]	P_{max} [mm/rev]	$P_{Gehring}$ [mm/rev]	P_{CSM} [mm/rev]	F_{D3mm} [kN]	σ_{D3mm} [MPa]	σ_u [MPa]	σ_t [MPa]	I_s [MPa]	LBC [%]
Koralm tunnel										
No. 12	229	12.5	10.2	8.9	120	151.4	68.6	9.7		70.5
No. 13	242	13.0	14.5	19.0	120	151.4	96.3	11.0	5.6	65.0
No. 14	165	10.5	13.5	16.0	85	107.2	70.3	7.4	4.9	78.0
No. 15	228	9.0	12.0	14.0	124	156.4	105.9	8.3	5.4	38.5
No. 17	118	14.0	9.3	4.0	70	88.3	62.8	4.7	3.4	96.0
No. 18	228	12.3	10.5	11.0	120	151.4	122.4	8.9	7.4	50.0
No. 19	203	9.4	12.1	11.0	114	143.8	92.8	10.6	4.8	45.0
No. 20	176	13.1	8.5	5.0	78	98.4	118.0	9.5	6.4	44.5
No. 21	181	12.5	18.0	10.0	100	126.2	73.0	12.1	3.1	-
No. 22	221	10.0	15.5	24.0	122	153.9	79.0	7.8	3.4	49.0
No. 23	225	7.0	19.5	35.0	162	204.4	63.0	7.7	3.5	32.0
No. 24	104	14.5	9.5	3.2	22	27.8	104.0	11.7	7.5	66.0
No. 25	153	11.8	11.8	7.2	59	74.4	75.0*	8.8*	-	-
No. 26	154	10.5	5.2	1.3	70	88.3	108.2*	11.0*	-	-
No. 29	156	10.5	6.1	2.1	70	88.3	146.2	11.8	10.1	41.5
No. 30	233	9.2	9.0	6.8	140	176.6	141.3	12.3	6.1	42.5
No. 32	227	6.1	11.0	10.0	180	227.1	116.6*	10.7*	-	-
No. 34	232	4.8	12.0	14.0	175	220.8	108.2*	11.0*	-	-
No. 36	119	11.0	6.2	1.7	70	88.3	108.2*	11.0*	-	-
No. 37	161	7.8	8.5	2.8	104	131.2	108.2*	11.0*	-	-
Rössåga tunnel										
No. 1 (1865)	300	7.2	4.1	3.8	210	290.2	-	-	-	-
No. 2 (1895)	295	7.5	4.0	3.4	225	310.9	264.0	13.0	-	-
No. 3 (1967)	303	8.2	4.1	3.6	230	317.8	-	-	-	-
No. 4 (2201)	280	6.0	10.0	26.0	210	290.2	-	-	-	-
No. 5 (2246)	293	6.9	10.5	20.0	220	304.0	101.0	7.2	-	-
No. 6 (2480)	292	7.2	10.5	20.0	220	304.0	-	-	-	-

* value taken from geotechnical report

6.1.2.1 Field penetration index FPI

Field penetration index FPI of performed penetration tests is shown in Fig. 107. The index is calculated by the ratio of normal force per cutter and resulting penetration. The calculation is based on the assumption that the relation between both parameters is linear intersecting at zero. However, penetration test results showed that this might not reflect reality (s. chapter 6.1.2.2). Thus, the index is useful to provide a first impression of the cuttability of rock mass. The results of performed penetration tests

range from rock mass that is easy (No. 24) up to very hard to bore (No. 34). All tests from the Røssåga project (pink cross) are situated in a narrow field of poor boreability. This fact is quite surprisingly, since the tests comprise rocks with completely different geotechnical properties such as calcareous mica schist with about 100 MPa UCS and quartzite with 265 MPa UCS. In this case, other influencing parameters must be of more importance. However, nearly no discontinuities were mapped at the Røssåga project. The most influencing parameter at the Røssåga tests appears to be the way of operating the TBM. Since it is the first time in 20 years that a TBM is used in Norway, the personnel has few experience and needs certain time to gain required know-how on how to run the TBM properly. This teaching phase is also visible in the penetration test results. The varying results from the Koralm tunnel are attributed to rock and rock mass properties such as strength values, fracturing degree, and state of stress. However, it has been noted that tests at rocks with similar geotechnical parameters may result in completely different FPI. Geological mapping of cross passages that reveal poor boreability (No. 23, 32, 34) noted no discontinuity systems or only one minor fissure. In contrast, cross passage No. 24 shows extremely good boreability and the tunnel face was pervaded by five joint systems. Another rock mass property that affects the FPI may have its origin in the encountered primary stress field. At cross passage No. 36, high stresses were observed during the face mapping leading to spalling potential and increasing boreability. Tests that reveal fair boreability are illustrated by greyish colored background (Fig. 107). Here, the geological face mapping noted mainly moderate fracturing degree like one existing plane of weakness (No. 18). However, it must be mentioned, that the number of fractures mapped at the tunnel face may vary significantly from zero to four. This emphasizes that a single analysis of the number of fractures per tunnel face is not an adequate method to characterize the effect of fractures on the penetration.

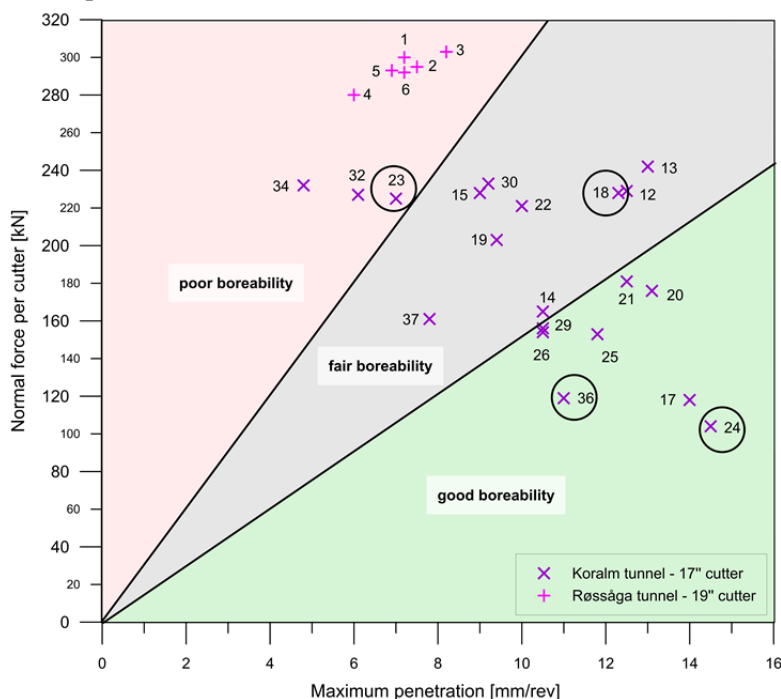


Fig. 107: Field penetration index FPI of penetration tests at the Koralm tunnel and Røssåga hydropower project. Numbers mark the cross passage resp. sample ID at which the tests have been performed. Suggested classification into good, fair and poor boreability classes are highlighted by colored background.

The orientation, spacing, surface roughness, and the type of fracture are even more important which is why correction factors for prediction models are based on it. Detailed discussion on these parameters follows in chapter 6.2.

6.1.2.2 Penetration prediction models (Gehring & CSM)

To validate penetration estimations of the CSM and Gehring model, several machine input parameters are obligatory. Input parameters such as cutter spacing, number of disc cutters, mean cutter tip width, and cutter radius can be assumed constant for each tunnel project (Tab. 21). Geological and geotechnical parameters are adapted at each penetration test on the basis of laboratory results and geological mapping.

Tab. 21: Machine input parameters at the Koralm and Røssåga tunnel project for penetration prediction models.

Machine parameter	Koralm tunnel	Røssåga tunnel
No. of cutters	78	45
cutter radius	216 mm	241.5 mm
cutter tip width (mean)	22 mm	19 mm
cutter spacing	65 mm	78.6 mm

The **Gehring model**, as an empirical approach, was developed for machine types with 17'' cutters and a cutter spacing of 80 mm. Since this machine setting is not met at analyzed tunnel projects, correction factors for varying cutter radius and cutter spacing (s. chapter 2.3.8) are used in all presented results that follow in this chapter. Correction factor k_4 accounts for cutter diameter unequal to 17'' (432 mm). Since the machine at Røssåga hydropower project was equipped with 19'' cutters, a correction factor of $k_4 = 0.89$ is incorporated into the test analysis of this project (s. Eq. 2-20, page 23). Correction factor k_5 considers cutter spacing unequal to 80 mm. The cutterhead at the Koralm tunnel project was designed with a cutter spacing of 65 mm - resulting in a correction factor $k_5 = 1.4$ (s. Fig. 9, page 24). In terms of cutterhead and cutter geometry, the **CSM model** allows for high flexibility since it was developed by linear cutting tests where different cutter types were investigated. Therefore, actual values at each tunnel project can simply be implemented into the model.

Basic validation of prediction models is given by comparing measured penetration rates of performed tests to predicted values from the basic version of both models (Fig. 108). First finding is that predicted penetration varies significantly and the results are not satisfying. The CSM model shows even higher discrepancies from actual penetration rates than the Gehring model, leading to prediction that is even five times higher than measured value. The high variance clearly shows the necessity of an improvement and update of the existing models. For detailed analysis, four representative tests of the Koralm tunnel are chosen, each of them standing for special test results and different geological factors of influence. Detailed force – penetration graphs of these examples are discussed in the following figures (Fig. 110 - Fig. 113). Test No. 18 is one of the rare cases where prediction reveals high accuracy. No. 23 is an extreme example on overestimating possible penetration rates, whereas No. 24 and No. 36 underestimate achievable penetration. The location of the abovementioned cross passages is illustrated in the schematic profile in Fig. 109.

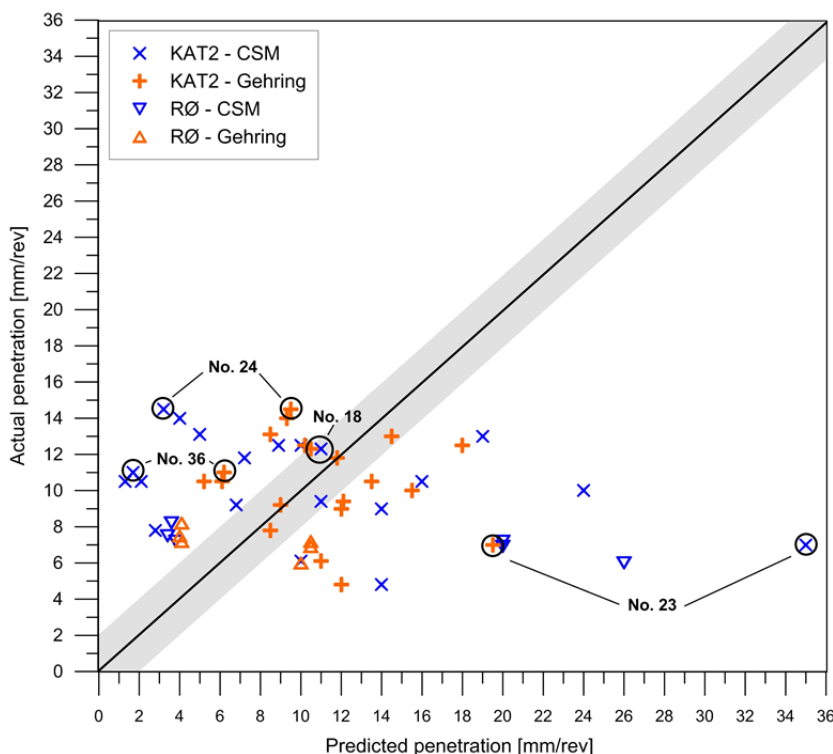


Fig. 108: Actual measured penetration rate plotted against predicted penetration rate of the basic CSM (blue) and Gehring (orange) model of performed penetration tests at Koralm and Røssåga tunnel. Highlighted are four tests, each of them represents special testing result.

In the following figures, the term of subcritical penetration describes the range where relatively high force causes a crushing of rock material and no chipping takes place (s. chapter 2). The overcoming of a certain threshold results in an effective cutting of rock since tension cracks can develop and rock chips are thus formed. Analysis of all penetration tests reveal that chipping occurs if penetration rates around 3 mm/rev are exceeded - which is set as critical threshold in this work.

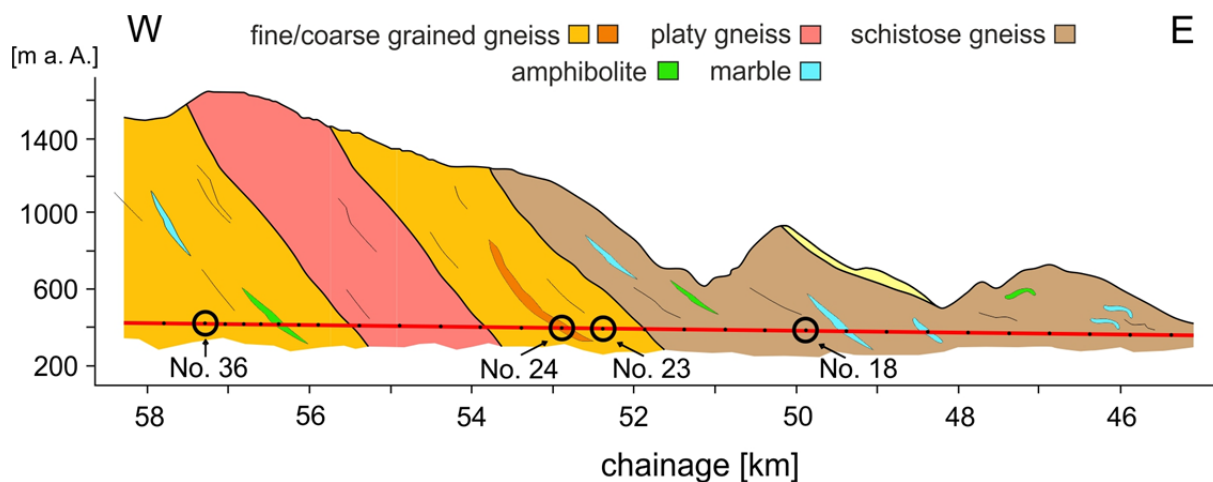


Fig. 109: Schematic profile of the studied tunnel section at the Koralm tunnel with actual encountered formation boundaries. Highlighted are four penetration tests at different cross passages that are of special interest for further research since they represent different geological factors of influence.

Penetration test – type 1 (represented by cross passage No. 18)

Fig. 110 shows the results of a penetration test, from which the predicted values agree quite well with the measured data. The maximum achieved normal force is about 228 kN which is close to the specified maximum force, according to manufacturer for 17'' cutters (267 kN). Since the regression lines of the start / stop test are identical, a pre-conditioning and relaxation of the rock mass due to the standstill of the TBM before the test, could not be observed. Results of the CSM and the Gehring model reveal that prediction models show more or less appropriate fitting, especially in the maximum penetration range of about 10 mm/rev where all regression curves intersect.

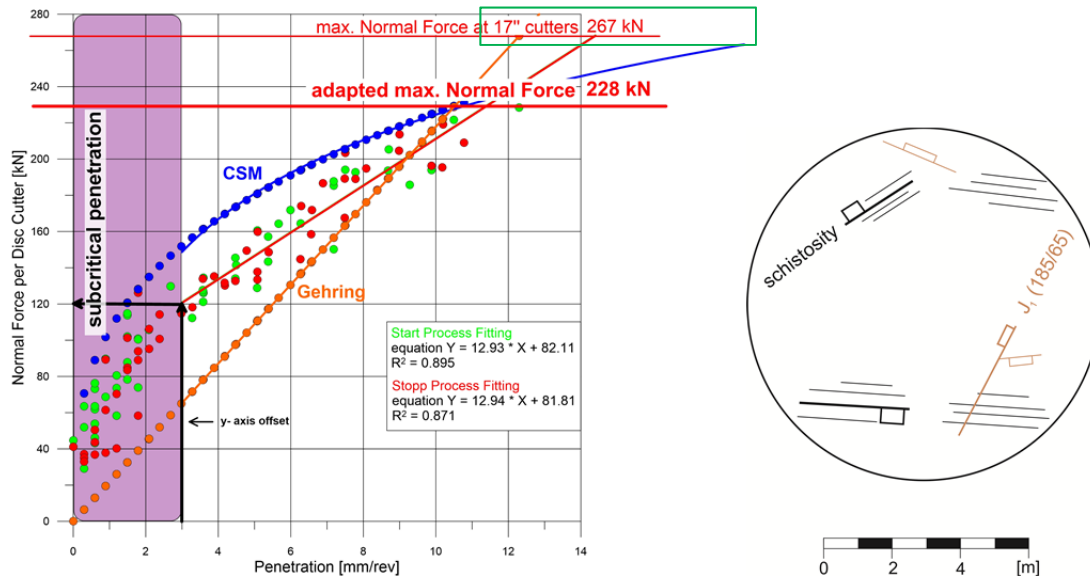


Fig. 110: **Penetration test type 1**– **Left**: Normal force per cutter is plotted against resulting penetration rates of start (green) and stop (red) test. In addition, CSM (blue) and Gehring (orange) models are displayed. Specific geotechnical input parameters are: UCS = 122 MPa; BTS = 8.9 MPa; Shield friction = 3,523 kN. **Right**: Corresponding schematic geological documentation of the tunnel face.

Detailed analysis on the behavior of the **CSM** curve reveals that this model calculates normal forces that are slightly higher (+ 30 kN) than measured data. This trend decreases at penetration rates greater than 7 mm/rev and at maximum penetration rate of 10 mm/rev, the CSM model subtends the red regression line. The **Gehring** model calculates slightly lower normal forces (- 50 kN) than measured data. This trend decreases at higher penetration rates and at 9 mm/rev predicted values meet actual data. However, the graph demonstrates interesting findings on the principal relation between force and penetration. Both prediction models deviate from actual measured data which is due to the mathematical function each model is based on. Scientific background of the CSM model is a power function, whereas the Gehring model relies on linear function through the origin. Nevertheless, analyses of all penetration tests reveal that the majority shows neither a power nor a linear function through the origin. It appears that the relation of force to resulting penetration can be described best by a linear function with a certain y-axis offset depending on the subcritical penetration (Fig. 110, black line). On which parameters the amount of the y-axis offset may be dependent upon, is discussed in chapter 6.2.1. At present, it is worth mentioning that both models are constructed according to an inappropriate mathematical equation. The fact might also be highlighted by taking a closer look at the maximum normal force at 17'' cutters that is set by manufacturers at 267 kN (Fig. 110 left, green rectangle).

For estimating the future penetration rate at tunnel projects, this value is usually set as input parameter. In this case, the CSM model results in unrealistic high penetration of about 18 mm/rev - due to its power function. Conversely, Gehring calculated 12 mm/rev which is slightly lower than the interpolation of the measured penetration rate.

The test has been performed in unweathered, schistose gneisses and geological face documentation illustrating that rock mass is pervaded only by one major (J_1) and two minor joints that are closed and mechanically of minor effect. At the intersection of these discontinuities, small rock fragments are detached from the tunnel face. However, the tunnel face is mostly smooth and the tracks of disc cutters are continuously visible. No fine-grained material has been noted on the tunnel face or the cutterhead. The schistosity dips shallow nearly horizontal or shallow towards the right tunnel wall, and does not appear as active discontinuity. The rock mass can be described as massive to slightly fractured with discontinuity spacing of about 200 cm. A detailed petrographic description has already been presented in chapter 5.1.1.2 (page 90). Mean uniaxial compressive strength of taken rock samples at cross-passage No 18 is determined to be 122 MPa. For further geotechnical parameters see also Tab. 17 (page 104) and Tab. 20 (page 128). Summarizing, this test proves that in massive rock mass, penetration prediction agrees quite well with measured data.

Penetration test – type 2 (represented by cross passage No. 24)

Fig. 111 reveals a penetration test result, for which both prediction models do not fit to the measured data. Due to a given geological conditions, normal force per cutter is limited to 104 kN which is only 40% of the maximum possible force. Nevertheless, measured forces are enough to cause penetration rates up to 14 mm/rev. Data points from the start-stop-test hardly vary with the result that the accuracy of the start regression line (green) is about 83 % and the fitting of the stop regression line (red) is at 94 %. An influence of pre-conditioned rock mass due the standstill previous to the start-test is slightly visible. Both models predict way too high forces to gain certain penetration. At a maximum penetration rate of 14 mm/rev, the difference between the estimated and measured force is about 150 kN.

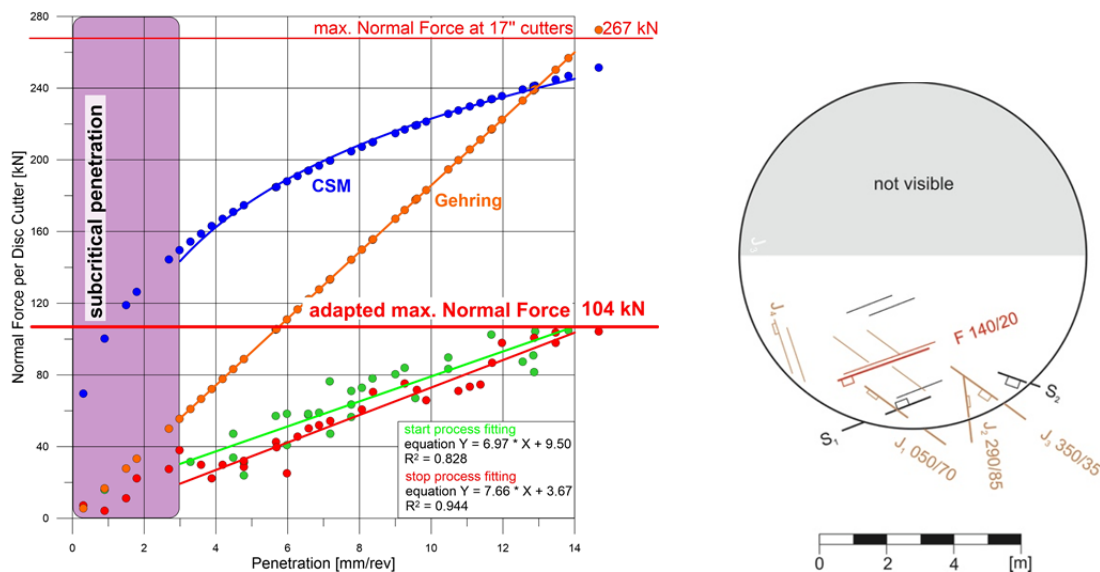


Fig. 111: **Penetration test type 2**– **Left**: Normal force per cutter is plotted against resulting penetration rates of start (green) and stop (red) test. In addition, CSM (blue) and Gehring (orange) models are displayed. Specific geotechnical input parameters are: UCS = 104 MPa; BTS = 11.7 MPa; Shield friction = 5,070 kN. **Right**: Corresponding schematic geological documentation of the tunnel face.

The test has been performed in unweathered, coarse grained gneisses with indistinct schistosity dipping shallow in direction of the left tunnel wall. Geological face documentation illustrates that the rock mass is moderately to highly disintegrated by three distinctive joint sets (J_1 , J_2 , J_3) and a 0.1 m thick zone (F) with coarse grained fault material. The distance between planes of weakness is estimated between 60 and 200 cm and some joints reveal certain aperture. Schistosity does not appear as active discontinuity. Unfortunately, only the bench was accessible for documentation. However, it has been noted that the heading tunnel face was smooth leading to the assumption that the fracturing degree decreases towards the roof. A detailed petrographic description of encountered rock type has already been presented in chapter 5.1.1.2. High shield friction of about 5,000 kN verifies the fractured character of the rock mass. Mean uniaxial compressive strength is determined to be 104 MPa. For further geotechnical parameters also see Tab. 20 (page 128).

The test reveals that for fractured rock mass, no prediction model in its basic version (without correction factors in terms of rock mass fabric) is applicable. It could be argued that the difference between estimated and measured values has no negative effect on the calculation of construction cost and time since the rock mass is “easier” to excavate and lower forces are required. But one should bear in mind that fractured rock mass might lead to instabilities and detached blocks at the tunnel face. Furthermore, the thrust force has to be reduced since the conveyor belt acts as limiting factor in terms of removing muck. All these parameters are of minor importance for unfractured rock mass and corresponding higher forces. Results of the prediction models might thus pretend better rock quality which consequently leads to falsified estimations of construction time and cost. Thus, it is very important that predicted penetration reflects, as closely as possible, the actual rock mass conditions.

Penetration test – type 3 (represented by cross passage No. 36)

Fig. 112 shows the result of a penetration test, for which both prediction models do not fit to the measured data. Estimated forces are about 200 % of measured forces resulting in a deviation of 100 kN. Data points from the start-stop-test spread to a certain extent. Consequently, the accuracy of the start regression line (green) is about 70 % and the fitting of the stop regression line (red) is at 60 %. An influence of pre-conditioned rock mass, due the standstill previous to the start-test is not obvious.

The test has been performed in unweathered, fine grained gneisses with the main schistosity dipping shallow in direction of the left tunnel side. Small scale folding of the layering is noted, though the schistosity does not appear as active discontinuity. Geological face documentation illustrates that only one major joint (J_1) is observed that dips steeply against tunnel advance. A detailed petrographic description of encountered rock types has already been presented in chapter 5.1.1.2 (page 89). Mean uniaxial compressive strength is taken from the report by ÖBB-INFRA (2009a) for fine grained gneiss, since up to now no rock cobbles for laboratory testing are available (s. Tab. 20, page 128).

However, a small part with highly fractured rock mass (20-40 cm spacing) and blocky rock conditions is mapped in the left center of the tunnel face. The rock fragments are of prismatic and platy shape and the fractures are mainly open. The character of this small area suggests that fractures might not be formed by tectonic activity since cracks are observed only to very limited scale. It may more likely be formed by high primary stresses in the rock mass that cause small, but highly disintegrated areas leading to detached blocks (volume > 10 dm³) at the tunnel face and side walls. The idea is assured by the

fact that during face mapping, stress induced microcracking can be heard and platy rock fragments are noted in the reamer of the TBM. These facts lead to unstable tunnel face conditions and the tracks of the disc cutter are rarely visible.

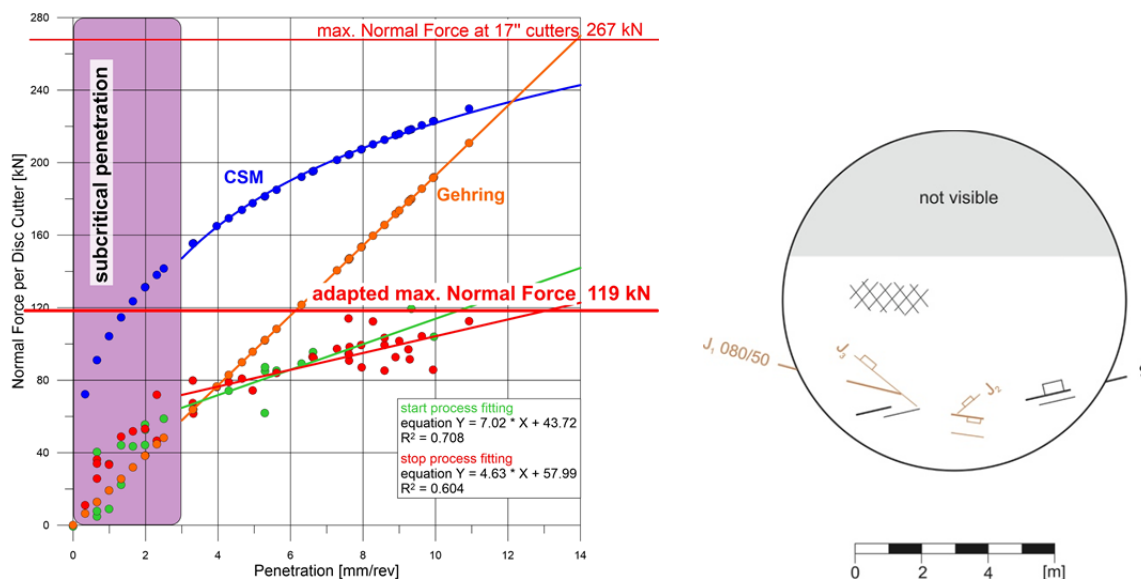


Fig. 112: **Penetration test type 3** – **Left:** Normal force per cutter is plotted against resulting penetration rates of start (green) and stop (red) test. In addition, CSM (blue) and Gehring (orange) models are displayed. Specific geotechnical input parameters are: UCS = 108 MPa; BTS = 11.0 MPa; Shield friction = 4,390 kN. **Right:** Corresponding schematic geological documentation of the tunnel face.

The relaxation of the rock mass and instabilities at the tunnel face and side walls lead to a reduced normal force that is 45 % of maximum possible. Conclusively, prediction models without a correction factor for the state of stress are not able to simulate penetration rates in rock mass with high stresses. The content of this thesis, the influence of the state of stress on the penetration rate and corresponding implementation of a correction factor is not discussed in detail, but has to be investigated in future.

Penetration test – type 4 (represented by cross passage No. 23)

Fig. 113 reveals a penetration test result, for which both prediction models do not fit to the measured data. This time, the trend is reverse, since estimated values are much lower than actually required normal forces. The test has been conducted with maximum normal force of 225 kN. This value is equal to the normal forces at penetration test type 1 (Fig. 110) where a maximum penetration of 12 mm/rev is reached. In contrast, only 7 mm/rev can be achieved here. It may perhaps be the consequence of stable rock mass behavior with very high uniaxial compressive strength. However, the results of laboratory testing reveal the opposite. Uniaxial compressive strength of the fine grained gneiss is determined at 63 MPa (mean value of six tests from two block IDs). The value is confirmed by point load testing, which results in derived UCS of 70 MPa with the standard c-coefficient of $c = 20$.

The UCS estimated at the tunnel face was stated in the geological documentation with about 150 MPa. However, no damage or pre-existing cracks due to drill and blast excavation has been noted at tested samples. The cross passage, where rock cobbles for laboratory testing were collected is only 10 m away from the chainage where the test was conducted. This significant change in rock strength at such short distance seems unlikely, but might still be possible due to small-scale variations in the rock mass. Penetration prediction has been performed at 63 MPa since laboratory tests reveal higher

accuracy as the inaccurate estimation by a hammer stroke. Therefore, both prediction models deviate extremely from measured data and 2.5 times higher forces are required to cause certain penetration. Notwithstanding the fact whether 63 MPa or 150 MPa are the actual strength of the rock, one important observation has to be noted. The normal force which is needed to cause chipping (penetration rates > 3 mm/rev) is about 160 kN. In comparison, this value is 1.5 times higher than the maximum normal force at penetration test type 2 (104 kN) where we gain penetration rates of about 14 mm/rev. This finding might be explained by rock toughness. If rocks behave tough under load, more energy is required to induce chipping and complete failure of a rock. The high value of 160 kN coincides with numerical results by GONG & ZHAO (2007) where the authors showed, that the formation of a crushed zone is harder for tough rocks than for brittle rocks.

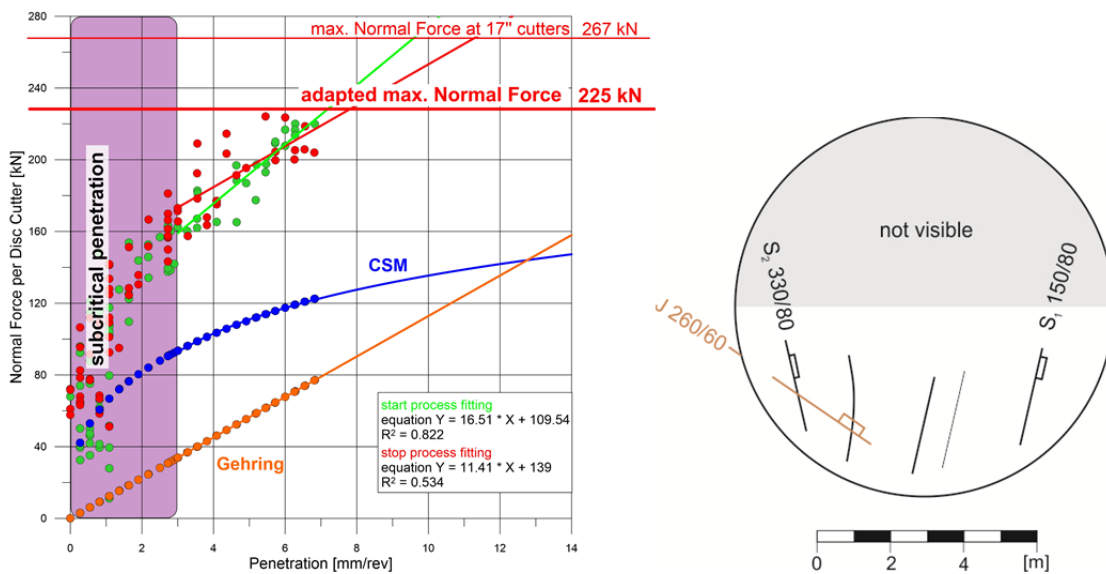


Fig. 113: Penetration test type 4 – Left: Normal force per cutter is plotted against resulting penetration rates of start (green) and stop (red) test. In addition, CSM (blue) and Gehring (orange) models are displayed. Specific geotechnical input parameters are: UCS = 63 MPa; BTS = 7.7 MPa; Shield friction = 4,700 kN. **Right:** Corresponding schematic geological documentation of the tunnel face.

Furthermore, the geological documentation underlines that very high amount of fine grained material and debris could be observed in the cutterhead. Tracks of the disc cutters are clearly visible due to white crushed material that stayed in the tracks and the tunnel face is smooth. The cutterhead and disc cutters are also partly covered with fine-grained rock powder. Analysis of laboratory tests reveals that tested specimens from this chainage obviously show tough failure behavior with high plastic deformation and very present post-failure range. Since geological face documentation illustrates, that the rock mass is not weathered and massive with only one minor joint (J) and spacing of the discontinuity is classified > 200 cm, the influence of discontinuities can be excluded. Furthermore, the joint are closed or sealed with calcite in most cases and the effect on the penetration can be neglected. Thus, this test might show the influence of rock toughness on the penetration rate of TBMs. This aspect is discussed in more detail chapter 6.2.2.

Friction force

For the calculation of normal force per cutter, the parameter of **friction force** is of essential importance, since this value is subtracted from the total thrust before dividing it by the number of disc cutters. According to the manufacturer's specification, the shield friction at the Koralm tunnel is assumed to be 3,000 kN. However, there is still no agreement within the community as to what percentage the determined friction value has to be taken into account for penetration prediction.

Values range from 50 – 100%. Presented results in Fig. 110 - Fig. 113 are based on a consideration of 100 % friction. Furthermore, test analysis has been done for 50 % friction to illustrate the variation in testing results.

Fig. 114 illustrates the results for total friction value of 5,500 kN obtained by a friction stroke previous to a penetration test. If measured friction is considered with 50 % instead of 100 %, resulting normal forces per cutter are about 15 % higher (Fig. 114A). The deviations between resulting forces decrease with decreasing total friction. This is presented in Fig. 115 where the result of a penetration test with 3,500 kN total friction is shown. If determined total friction is considered with 50 %, resulting normal forces per cutter are only 10 % higher (Fig. 115A). Both tests are chosen since they were performed in unfractured rock mass and influencing parameters are minimized as much as possible. However, it is notable that such different friction values were determined for similar test conditions in unfractured rock mass and the same lithology. The value of 3,500 kN seems reasonable for unfractured rock mass. In contrast, the value of 5,500 kN corresponds rather to a rock mass that is moderately to highly fractured since the friction increases due to clogging of the annular gap by crushed rock material. It might be explained by the rock mass conditions that were encountered before the test was conducted. If the fracturing degree was significantly higher than at the chainage of the test, the rock material might still be trapped in the annular gap since the material can only be transported outwards passively by advance of the machine. This process may cause higher friction values than actually expected.

Furthermore, estimated parameters of the basic CSM and Gehring model are displayed. Tests were conducted in schistose gneisses with a maximum uniaxial compressive strength around 100 MPa. For unfractured rock mass, both prediction models should result in good agreement with actual measured data as it is the case in Fig. 114B and Fig. 115B. This leads to the assumption, that taking 50 % friction force into account might underestimate the forces that act on the machine during active excavation. This is why further research is performed by considering 100 % of measured friction, although the magnitude of forces acting on the machine are not clearly understood yet.

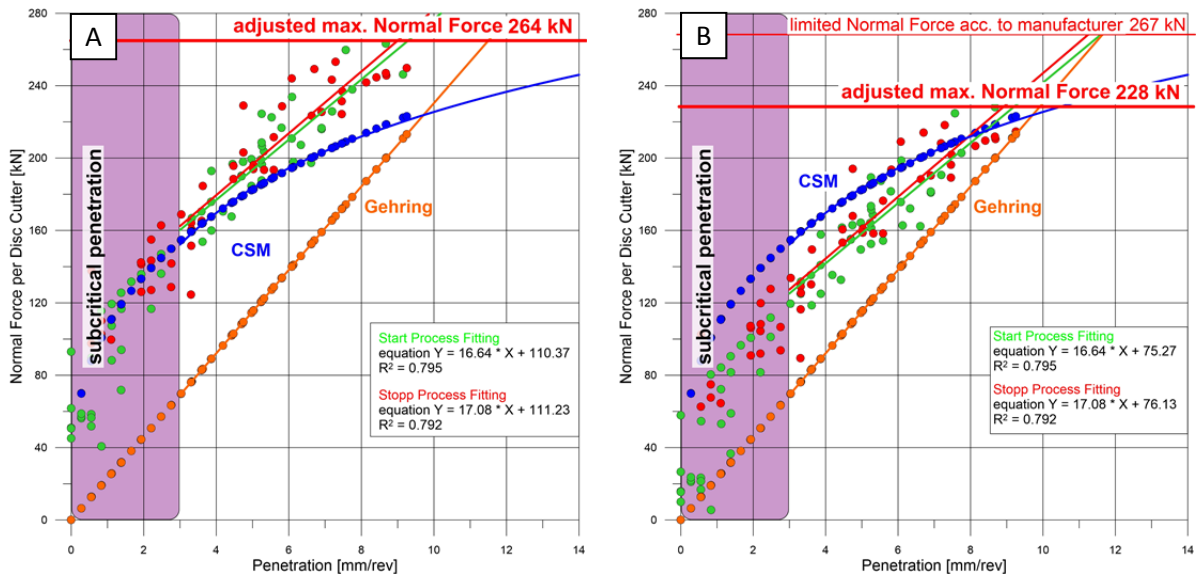


Fig. 114: **Friction 5,500 kN**: Force – penetration graphs of start / stop test including CSM (blue) and Gehring (orange) models. Specific geotechnical input parameters are taken from laboratory tests. Friction force is considered by 50 % (A) and 100 % (B) of measured value leading to divergence in force per cutter of about 15 %.

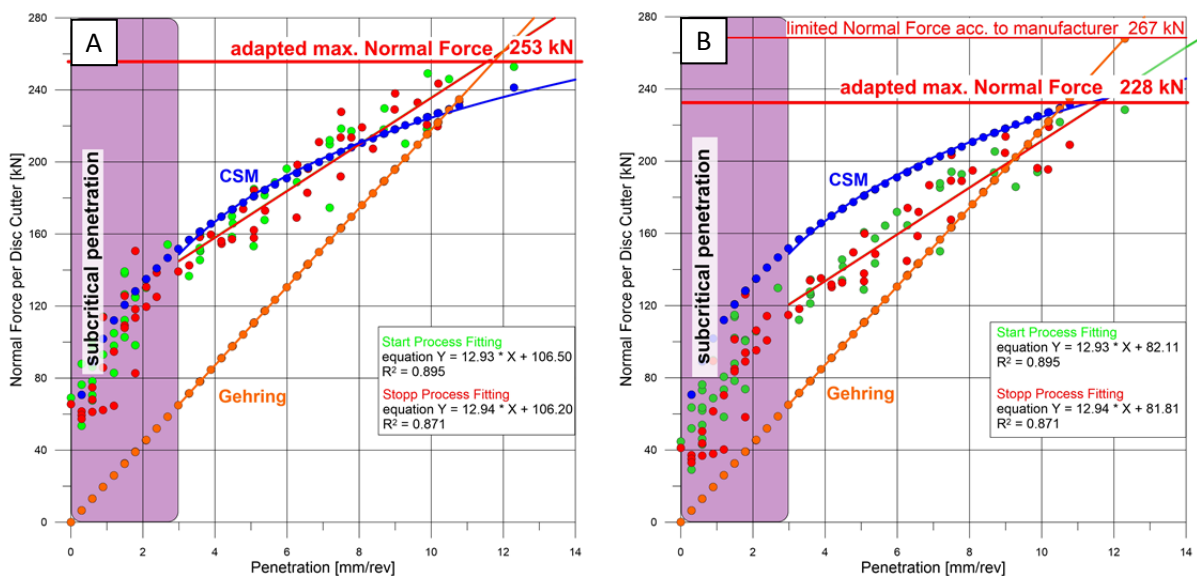


Fig. 115: **Friction 3,500 kN**: Force – penetration graphs of start / stop test including CSM (blue) and Gehring (orange) models. Specific geotechnical input parameters are taken from laboratory tests. Friction force is considered by 50 % (A) and 100 % (B) of measured value leading to divergence in force per cutter of about 10 %.

6.1.2.3 Variation of cutterhead rotational speed

The decrease of cutterhead rotational speed should result in higher penetration rates, since the force on one single spot of the rock can act for longer time. If so, the reduction of cutterhead speed can be a viable option to decrease cutter wear and cutter consumption. Testing procedure has already been described in chapter 4.2.1. Results of cutterhead speed tests at the Koralm tunnel are shown in

Fig. 116. For the sake of clarity, mean values of each speed level are plotted. It appears that there is no clear trend detectable. Some of the tests reveal the expected tendency of increasing penetration corresponding to a reduction of cutterhead speed. However, nearly 50 % of the performed tests show the opposite trend, since the penetration rate decreases by decreasing rotational speed. All tests have been performed in the same way, so the difference has to be caused by external influences. The rock type appears to be not decisive since tests in schistose gneiss result in either type A or type B behavior. Analysis of the graph suggests that the deviation may have its origin in the fracturing degree of the rock mass. Six from seven tests in Fig. 116B were conducted in fractured rock mass where geological mapping of the tunnel face reveals at least three discontinuity systems. Conversely, tests in Fig. 116A were mainly performed in rock mass with low fracturing degree. However, this assumption cannot be generalized. The test at cross passage No. 24 (Fig. 116A, light blue line) reveals extremely high penetration rates of 18 mm/rev for low cutterhead speed thus the rock mass is highly fractured. Similar observations are noted for cross passage No. 17 (Fig. 116A, brown line), where the fracturing degree at the test start was very low, but increases significantly during the test. It suggests that due to the fracturing degree, the excavation process may not be described as cutting, but rather as ripping loose rock fragments from the tunnel face. Nevertheless, a slight tendency can be noted that expected increase in penetration rates can only be achieved in rock mass with low fracturing degree. Until now, it is not clearly understood which other factors may influence the relation between cutterhead rotational speed and penetration rate of a TBM. The link to the deformation behavior of rocks under different loading rates (s. chapter 5.2.1, page 112) might give an indication. The higher the rotational speed, the higher is the loading rate rocks are exposed under the cutter. This means that the apparent uniaxial compressive strength of the rock might also increase, which explains lower penetration rate for higher cutterhead rotational speed. However, this has to be subject to further research.

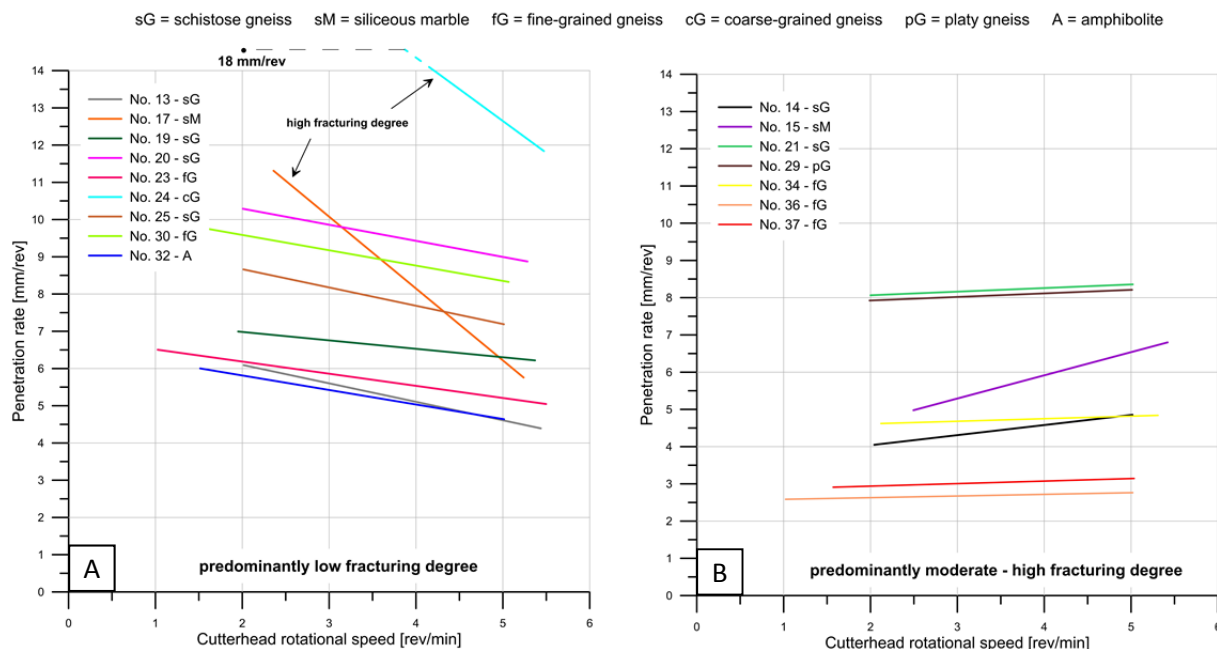


Fig. 116: Variation of cutterhead rotational speed at the Koralm tunnel. **(A)** Penetration rate increases with decreasing cutterhead speed in predominantly massive or slightly fractured rock mass. **(B)** Penetration rate decreases with decreasing cutterhead speed in rock mass with distinctive discontinuity pattern and medium fracturing degree.

6.2 Discussion

6.2.1 General investigations on force – penetration graphs

Penetration tests provide useful information on the excavation behavior of rocks by tunnel boring machines. Resulting force-penetration graphs show that the relation between both parameters might best be described by a linear function with certain y-axis offset which is set by the threshold of subcritical penetration. This chapter summarizes investigations on influencing factors that may define this offset which helps to improve existing prediction models. The following analyses are based on the statement that the subcritical penetration is set at 3 mm/rev. This threshold has been set on the basis of performed penetration test. However, the findings can also be transferred to a threshold of 2 mm/rev which are stated in literature (FRENZEL et al. 2012).

A useful tool to give a first impression of the excavatability of rocks is the field penetration index (FPI). The results of penetration tests - according this index - have already been presented in chapter 6.1.2.1. However, it must be noted that the relation between the normal force and resulting penetration is not a linear function with the point of intersection at zero. Therefore, the original FPI is transferred to the point, at which the relation becomes linear. This is the fact at the threshold of subcritical penetration, which is set at 3 mm/rev in this thesis. The modified FPI_{3mm} is calculated by the force that is needed to cause a penetration rate of 3 mm/rev (Eq. 6-1). By applying this method, inaccuracies due to the mathematical function are eliminated best possible.

$$\text{FPI}_{3\text{mm}} = \frac{F_{N\ 3\text{mm}}}{3\ \text{mm/rev}} \quad \text{Eq. 6-1}$$

$\text{FPI}_{3\text{mm}}$	modified field penetration index [kN/mm/rev]
$F_{N\ 3\text{mm}}$	normal force per cutter at $p = 3\ \text{mm/rev}$ [kN]

The modified FPI is correlated with several geotechnical parameters to find out, which factor might control the y-intercept. To diminish side effects that influence the results of penetration tests, only a particular selection has been used for this analysis. These were data from penetration tests that have been performed in unfractured rock mass and no other rock mass properties such as high primary stress were obvious. Furthermore, all corresponding geotechnical parameters must be available. However, this approach excludes performed penetration tests at the Rössåga hydropower project since only small amount of sample material was available, resulting in limited laboratory data. Therefore, the procedure reduces the number of suitable tests to a small portion. Nevertheless, the selection is necessary to ensure proper analysis since the fracturing degree or the in-situ stress falsifies the excavation behavior and cannot be used as reference test for fundamental research on the relation between the applied force and penetration, but correlations should be understood as trend lines only. Furthermore, one must be aware that for such a small data set, one additional data point might change the trend significantly. Fig. 117 summarizes the results of FPI_{3mm} correlated with uniaxial compressive strength (UCS), Brazilian tensile strength (BTS) and LCPC breakability coefficient (LBC). Additionally, the classification of boreability into poor, fair, and good according to KLEIN et al. (1995) is plotted. The graphs emphasize that uniaxial compressive strength appears to have no influence on the field penetration index. High UCS values result in similar FPI_{3mm} and the regression line is more or less horizontal. The same trend has been observed for failure, as well as for destruction work. This fact provides

interesting information, since UCS is said to be responsible for the formation of the crushed zone, but not for the process of chipping (s. chapter 2). Obtained results underline this assumption as UCS affects the force-penetration relation within the crushed zone, but not at the transition to effective rock cutting where cracks propagate and rock chips are formed. Also the point load index results in extremely low regression coefficient and does not affect the FPI_{3mm} .

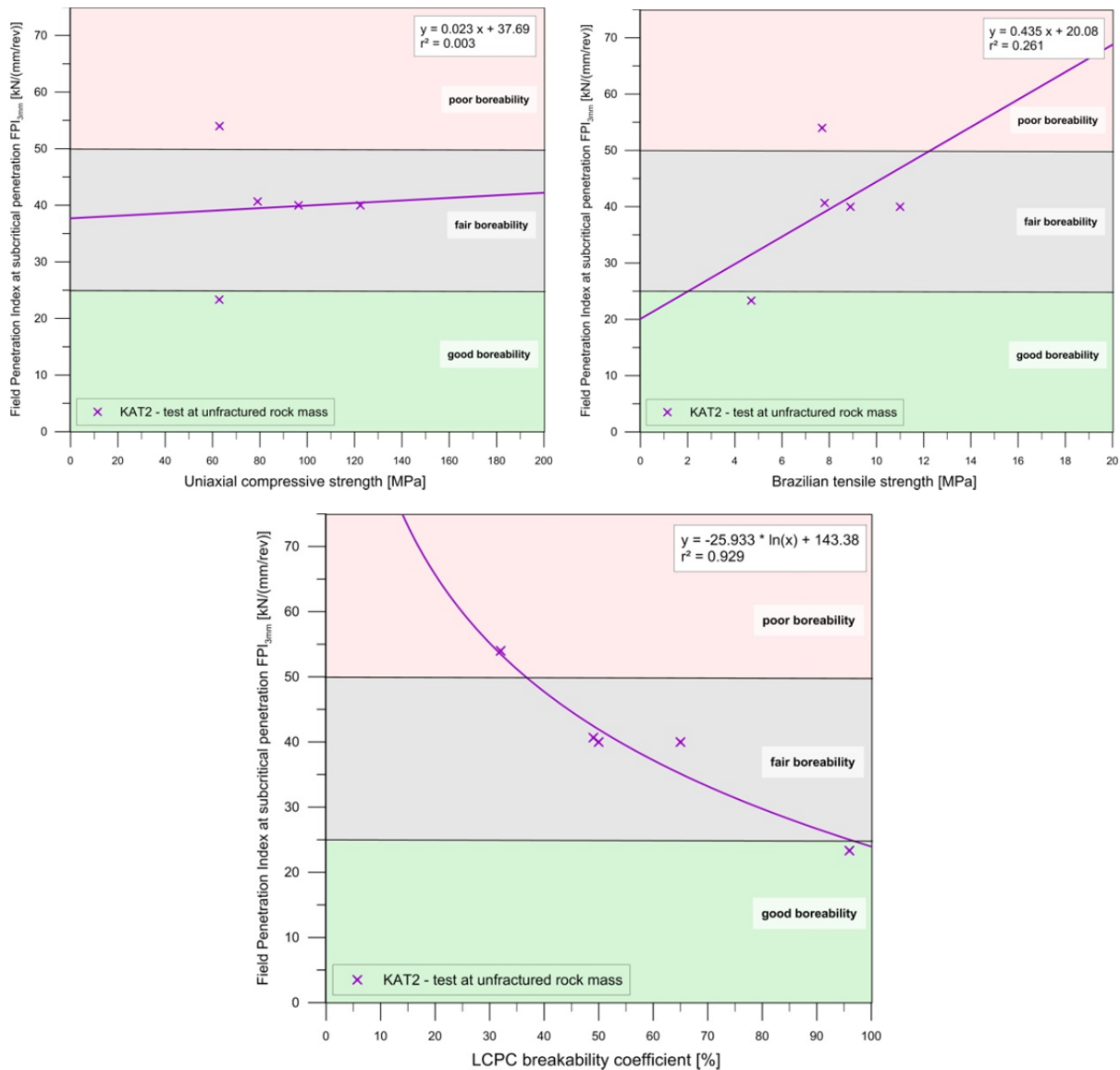


Fig. 117: Field penetration index at subcritical penetration FPI_{3mm} plotted against chosen geotechnical parameters. Classification system acc. to KLEIN et al. (1995) is shown by colored background.

Uniaxial compressive strength appears to have no influence. Brazilian tensile strength resp. LCPC breakability coefficient results in moderately resp. significant correlation.

In contrast, Brazilian tensile strength shows the trend that with increasing strength, the boreability decreases. This observation confirms the theory of rock cutting, since BTS seems to be the parameter that influences the propagation of cracks and causes formation of rock chips. If the tensile strength of rocks increases, higher normal forces have to be applied to overcome the cohesive force that keeps mineral grains together. This results in lower boreability. Therefore, test results in Fig. 117 agree with the theoretical approach of characterizing the cutting process by disc cutters and corresponding crack

propagation in rocks. However, it must be noted that the correlation coefficient is quite low. In case of performed penetration tests at the Koralm tunnel, best correlation has been achieved by the parameter of LCPC breakability coefficient. The relation between FPI_{3mm} and LBC can be defined by a logarithmic regression curve with regression coefficient of 0.93. It has been shown that an increase in breakability coefficient leads to lower FPI values which correspond to higher boreability. This finding is consistent in terms of rock mechanics since the LBC characterizes the resistance of rocks against destruction and therefore toughness. High LBC values correspond to rock types that are easy to destroy and thus classified as 'well boreable'. Besides the actual breakability coefficient, the parameter of LBC somehow reflects the strength of a material. Rocks with high tensile strength should result in low LBC, since crack propagation is difficult. This coherence is validated as LBC and BTS are the only geotechnical parameters that reveal certain influence on the force that is needed to cause effective rock cutting, whereas UCS is of minor importance for this threshold. However, one must bear in mind that these observations rely only on a small data basis and have to be improved by further research at different tunnel projects.

For accurate penetration prediction, it is inevitable to define the y-axis offset of the linear force-penetration function at subcritical penetration. Thus, the transfer of abovementioned findings to a definition of the y-axis offset requires further steps. The results of penetration tests provide an idea of the offset in terms of required force to cause a penetration rate of 3 mm/rev. To enable proper comparison between the applied force at 3 mm/rev penetration and geotechnical parameters such as uniaxial compressive strength, Brazilian tensile strength and point load index, measured force is converted to the stress occurring under the disc cutter during the cutting process.

The calculation follows the concept of the CSM model. In a first step, the angle of the contact area between rock and cutter is determined for certain penetration rates (s. chapter 2.3.7, Eq. 2-11). In a second step, the contact area between cutter and rock is calculated by using the cutter tip width and the length of the contact area. The length is computed by particular percentage, set by the angle of contact, of total perimeter of the cutter (Fig. 118). The average cutter tip width has been calculated for each penetration test on the basis of the cutter records of maintenance. Then, the applied stress at any penetration rate can be determined by the ratio of the applied normal force and contact area. This calculation is of sufficient accuracy for this analysis. However, it must be noted, that the actual area of loading is smaller than the calculated area by the angle of the arc of contact (ROSTAMI 1997: 189ff.). This effect is even more obvious for rocks with high uniaxial compressive strength such as basalt and granite. Here, the actual loading area is only 40 % of calculated contact area. For softer rocks like limestone, the value is about 70 %.

As a first step, this method has been applied at each penetration test for all force-penetration pairs of value. In a second step, special focus is on the applied stress at the subcritical threshold of $p = 3 \text{ mm/rev}$.

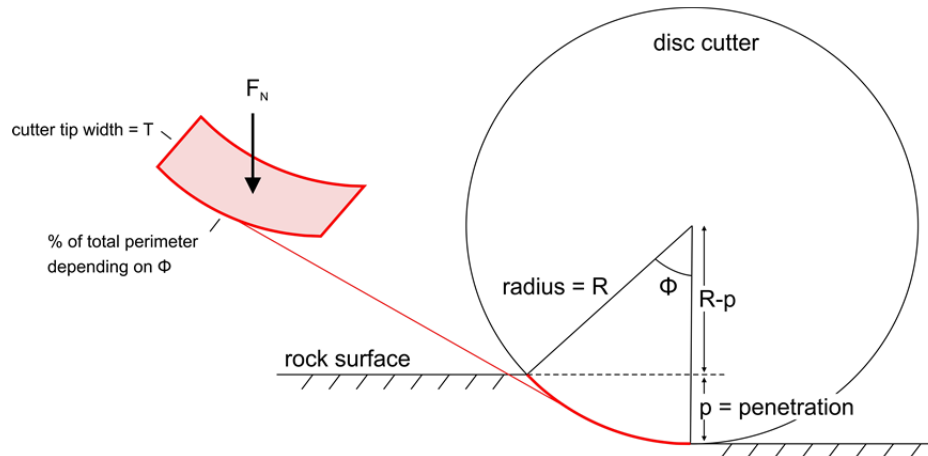


Fig. 118: Schematic figure of the contact area between disc cutter and rock. The contact area can be calculated by the cutter tip width T (determined on the basis of the cutter records during maintenance) and a certain percentage of the total perimeter depending on the angle of contact Φ (on the basis of ROSTAMI 1997).

Analysis reveals that there are three different trends of how the stress under the disc cutter develops during the penetration test. First trend is shown in Fig. 119. The stress-penetration graph is more or less horizontal in the range of effective rock cutting which means that the stress under the disc cutter is constant and independent from the penetration rate (purple line). The result can be explained by the fact that with higher penetration rate, also the contact area increases. Higher penetration rates are caused by an increase in the applied force which is shown by the steeper slope of the force-penetration graph (gray line). If the increase in force is proportional to the increase in contact area, the stress that is calculated by the ratio of force to contact area remains constant as it is the case in Fig. 119. This observation suggests that the trend of the stress under the disc cutter is dependent on parameters such as intact rock or rock mass properties.

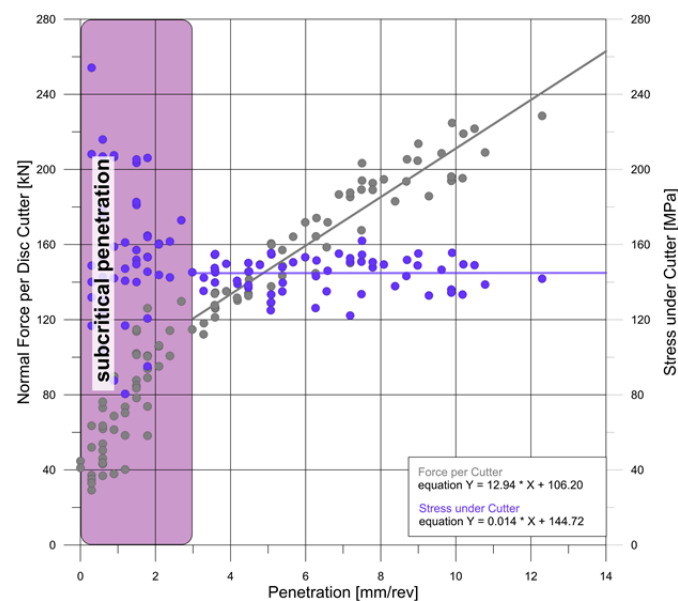


Fig. 119: Result of a penetration test at cross passage No. 18 at the Koralm tunnel. Besides force-penetration graph (gray), also the applied stress under the cutter is plotted (purple). Stress under the disc cutter is independent from the penetration rate in the range of effective rock cutting.

Nevertheless, two types of divergence from the abovementioned behavior have been noted. There are penetration tests at which the stress-penetration graph shows either positive or negative slope characteristics. Two extreme examples are presented in Fig. 120 and shortly discussed. Both test results derive from two following cross passages at which high primary stress were to be expected. In Fig. 120A, maximum penetration is very low and the stress-penetration regression line results in a positive gradient. The increase in forces is not proportionally with respect to resulting penetration and corresponding contact area. This means that crack propagation and increasing penetration only takes places when a relatively high amount of force is induced into the rock mass. The behavior can be explained by the state of stress at the cross passage. Significant in-situ stress within the rock mass is observed, thus, it is not high enough that cracks propagate without additional force input. The tunnel face is free of discontinuities and no detached blocks are noted. The gap between tunnel side walls and the machine shows no clogging as well. However, the annular gap in the top is blocked by rock cobbles that were expelled from the roof. This is a first indication for a certain in-situ stress, but the stress level in the rock mass seems to be not sufficient to facilitate the excavation process and to cause self-propagating cracks. In contrast, the stress field in Fig. 120B is high enough to cause a negative slope of the stress-penetration graph. This means that the stress under the cutter decreases, although the penetration rate increases. Nevertheless it must be mentioned that the trend is not as clearly as shown in Fig. 120B since measured data are plotted in a quite narrow field and the trend of the regression lines is only an interpolation with a regression coefficient $r^2 \sim 0.2$. This leads to an enhanced impact and a steep negative slope. The principal excavation behavior at Fig. 120B can be explained by cracks that are somehow self-propagating since minimal force has to be induced to increase penetration. Clogging of the annular gap at the roof and detached blocks of one-meter depth at the tunnel face is noted. These are phenomena caused by very high in-situ stresses around the tunnel opening. Hence, the primary stress field in the rock mass influences also the stress under the cutter to a significant degree. These findings emphasize the need of further investigations on the effect of the state of stress on the performance of a TBM. Though, it also states clearly that the calculation of the stress under the disc cutter provides an important tool for this analysis.

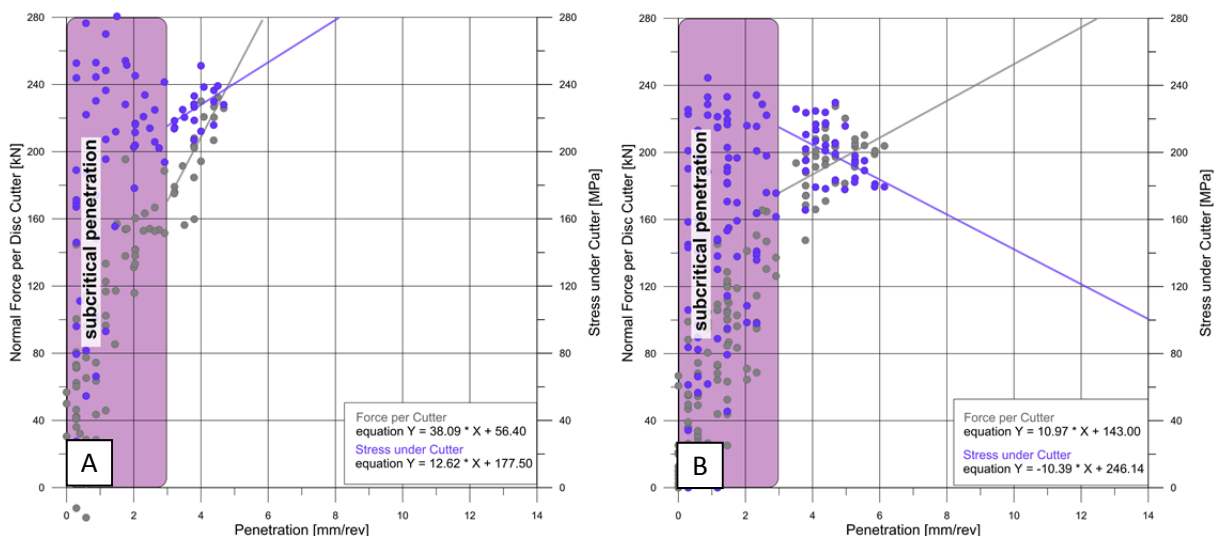


Fig. 120: Results of penetration tests at Koralm tunnel. Besides force-penetration graphs (gray), also the applied stress under the cutter is plotted (purple). Stress under cutter depends on penetration rate, resulting in either positive (A) or negative (B) slope in the range of effective rock cutting.

Analysis of all performed penetration tests at the Koralm tunnel shows that the trend of the stress-penetration graphs appear to depend on rock mass and not on intact rock properties (Fig. 121). Tests performed in the same lithology with similar material properties, such as uniaxial compressive strength and Brazilian tensile strength, result in either positive, negative or no gradient. Furthermore, tests in different rock types with varying geotechnical parameters result in the same stress-penetration trend. However, horizontal stress values were observed at tests where the rock mass is not or slightly fractured and no high in-situ stresses are noted (black lines). Conversely, divergence of the horizontal regression line is caused by either high fracturing degree or high in-situ stresses (blue or red lines). Based on the available data set, no trend, positive or negative, could be assigned to certain rock mass property since both types occur in rock mass with high fracturing degree or high in-situ stresses. Nevertheless, these findings are quite important since it has been shown that the **slope** of the **stress-penetration curve** depends rather on **rock mass properties** than on intact rock properties. Geotechnical parameters of the rock might define the point of intersection of the stress-penetration graph at subcritical penetration and can be used to characterize the critical y-axis offset. However, one must bear in mind that these findings rely only on one tunnel project with very narrow range of rock types (schistose gneiss, fine-/coarse grained gneiss, siliceous marble). Further investigation with several more rock types such as limestone with sedimentary layering, homogeneous granite, etc. is inevitable.

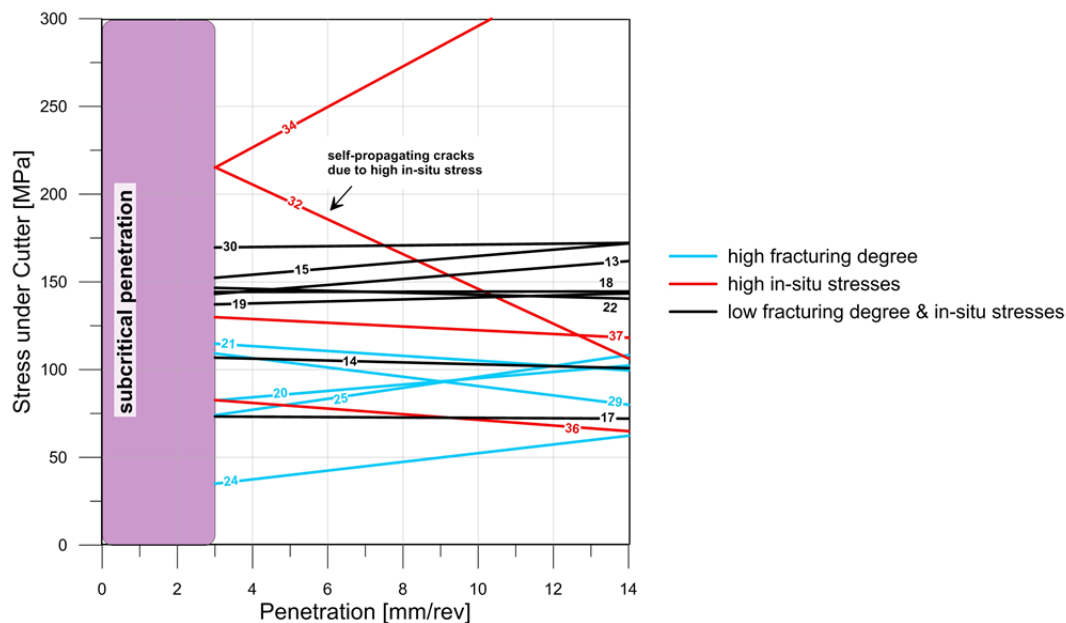


Fig. 121: Investigations on the correlation between the stress under disc cutters and corresponding penetration for penetration tests at the Koralm tunnel. Numbers mark the cross passages. The gradient of regression lines seems to be affected by rock mass properties such as fracturing degree or in-situ stress.

To characterize the y-intercept, the stress under the disc cutter at 3 mm/rev penetration rate (hereafter called **critical stress**) is correlated with corresponding geotechnical parameters (Fig. 122). To diminish side effects that influence the results of penetration tests, only the tests at unfractured rock masses and without high primary stresses are used, reducing the available data set significantly. Furthermore, one must be aware that for such a small data set, one additional data point might change the trend significantly. The stress-penetration graphs reveal similar results than the comparison of FPI_{3mm} and same geotechnical parameters (s. Fig. 117, page 141).

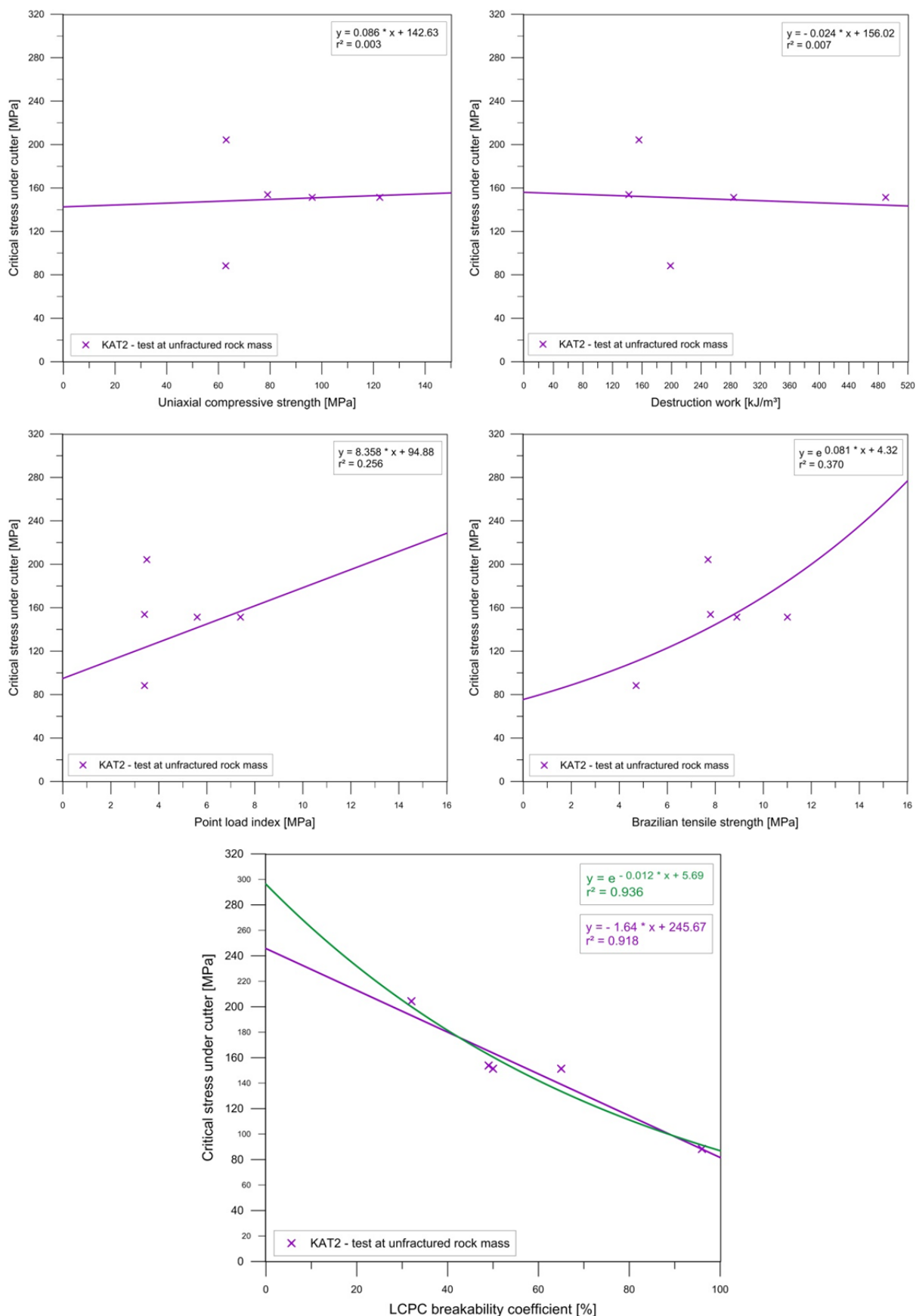


Fig. 122: Stress under disc cutter at subcritical penetration plotted against uniaxial compressive strength, destruction work, point load index, Brazilian tensile strength and LCPC breakability coefficient. Only the LCPC breakability reveals high correlation.

Uniaxial compressive strength, destruction work and also failure work (no graph shown here) have no influence on the critical stress under the cutter. This fact underlines the abovementioned results and the assumption that UCS is responsible for the formation of the crushed zone, but not for effective rock cutting in terms of crack propagation and chipping. The point load index shows certain trend with low correlation accuracy. If an average value is determined for the data points with point load indices around three, it appears that the trend also tends to be horizontal. Therefore, more data points are inevitable for further statement. The two geotechnical rock properties that seem to affect the critical stress are the Brazilian tensile strength and most, the LCPC breakability coefficient. Regression analysis suggests that the critical stress and BTS correlate by exponential function and with increasing tensile strength, also the critical stress level increases. However, the regression coefficient of BTS is quite low and one might better call it trend line than regression line. Nevertheless, the result underlines the theory that tensile strength is the determining factor for crack propagation and the process of chipping, but further data acquisition is highly recommended. Though, the LCPC breakability coefficient appears to be much more accurate for the determination of the y-axis offset in terms of critical stress under the cutter ($\sim 90\%$ fitting). A regression analysis reveals that the relation of stress and penetration can be described either by exponential (Fig. 122, green line) or linear function (Fig. 122, purple line). Since both regressions result in similar coefficients, the linear function is preferable for the sake of simplicity. Although LBC shows very high correlation, the parameter bears one weakness. The test is not used as a standard laboratory test during pre-investigations of tunnel projects up to now. This fact changes slowly due to newly published guidelines for construction contract procedures for earthworks. Summarizing, the Brazilian tensile strength is a commonly determined geotechnical parameter, but reveals low correlation coefficient with regard to the available data set. Conversely, the LCPC breakability results in a very high correlation coefficient, but the applicability might be constraint by the testing apparatus. Therefore, detailed analysis of the y-axis offset in the following paragraph is performed with the parameter of Brazilian tensile strength and LCPC breakability coefficient to enable practical applicability, thus keeping in mind the respective strengths and weaknesses of each parameter.

To allow further analysis on the y-intercept in terms of penetration prediction models, the abovementioned regression functions are back-transformed to the normal force per cutter. Since the Brazilian tensile strength and the LCPC breakability result in moderate and significant correlation, the y-intercept at subcritical penetration is determined for both parameters, resulting in Eq. 6-2 and Eq. 6-3. This fact allows higher flexibility for further development of the prediction models. However, it must be kept in mind that the regression coefficient of the Brazilian tensile strength is only $r^2 = 0.37$.

$$b_{\text{BTS } 3\text{mm}} = e^{0.08 \cdot \sigma_t + 4.1} = y - \text{intercept}_{\text{BTS } 3\text{mm}} \quad \text{Eq. 6-2}$$

$b_{\text{BTS } 3\text{mm}}$	y-intercept BTS approach at penetration 3 mm/rev [-]
σ_t	Brazilian tensile strength [MPa]

$$b_{\text{LBC } 3\text{mm}} = -1.3 \cdot \text{LBC} + 194.7 = y - \text{intercept}_{\text{LBC } 3\text{mm}} \quad \text{Eq. 6-3}$$

$b_{\text{LBC } 3\text{mm}}$	y-intercept LBC approach at penetration 3 mm/rev [-]
LBC	LCPC breakability coefficient [%]

The incorporation of suggested y-intercepts into the Gehring model is achieved by transforming the linear function. Since the parameter is based on the threshold of subcritical penetration, the value of 3 mm/rev penetration rate must be accounted for in the new prediction model and results in a basic linear equation depending on the **slope a** and the **y-intercept b** (Eq. 6-4).

$$F_N = a \cdot (p - 3) + b \quad \text{Eq. 6-4}$$

F_N	normal force per cutter [kN]
p	penetration rate [mm/rev]
a	slope of the line [-]
b	y-intercept of the line [-]

The y-intercept has been defined above by two possibilities. The slope of the force-penetration graph appears to depend on rock mass parameters such as discontinuities and in-situ stress (s. Fig. 121). These parameters are already included in the Gehring model by correction factors that reduce the slope of the basic Gehring function. Therefore, the approach can be directly transferred to a **modified Gehring model** or '**Alpine Model**' (Eq. 6-5). However, it must be noted, that the correction factor for the state of stress is not yet defined. This is why it is of major importance, that the basic penetration factor k_0 and correction factor for discontinuity pattern k_2 is implemented into the modified model, despite other correction factors k_i , to prevent too steep gradients. Otherwise the modified function results in even lower correlation than the basic model as the y-intercept amplifies the discrepancy.

'Alpine Model' (modified Gehring model)	$p = \frac{F_N - b_{\text{BTS/LBC}}}{\sigma_u} \cdot k_0 \cdot k_2 \cdot k_i + 3$	Eq. 6-5
p	penetration rate [mm/rev]	
F_N	normal force per cutter [kN]	
$b_{\text{BTS/LBC}}$	y-intercept BTS or LBC approach [-]	
k_0	basic penetration factor = 4.0 [-]	
k_2	correction factor for discontinuity pattern [-]	
$k_i =$	further correction factors for geotechnical / machine parameters [-]	

The '**Alpine model**' strongly improves the existing version of 1995 by GEHRING, since the y-intercept is of major importance to reflect the actual relation between the applied force and resulting penetration. However, it must be made quite clear that investigations are based on only one tunnel project and must be validated by further data. But the approach shows promising results for future research. Furthermore, the incorporation of correction factor k_2 is inevitable for the 'Alpine model'. This finding bears some problems since the factor is not sufficiently developed yet (s. chapter 6.2.3).

To briefly summarize, the relation between force and resulting penetration is characterized by linear behavior with y-axis offset which is defined by the point of subcritical penetration. Detailed investigation on this critical threshold has been done using the stress level under the cutter since it allows proper correlation with geotechnical parameters. It has been shown that the magnitude of the y-axis offset is highly influenced by the LCPC breakability coefficient and the Brazilian tensile strength, whereas uniaxial compressive strength,

destruction work and point load index reveal no significance. In contrast, the slope of the stress-penetration graph seems to be characterized by rock mass properties such as fracturing degree and primary stresses. By means of these findings, a modified Gehring model is proposed – the ‘*Alpine model*’ (Eq. 6-5) that reveals promising results. However, one must bear in mind that investigations are only based on one tunnel project with a narrow range of rock types. Therefore, further validation at various tunnel projects is highly recommended.

6.2.2 Parameter - rock toughness

Originally, laboratory investigations on rock toughness should be transferred and validated in the field. Due to the lack of rock variation at actual tunnel projects incorporated in this thesis, several rock types have only been analyzed in the laboratory. However, some of these rock types were tested at a linear cutting machine by researchers from *Montanuniversität Leoben* who are participating in the ABROCK research group (MORI 2012, LASSNIG 2012). It has been shown, that augen gneiss (AG) as brittle rock type results in lower normal forces for given penetration than the tough calcareous mica schist (KGS), although the uniaxial compressive strength of augen gneiss is twice as high. This indicates the influence of toughness on the cutting process which is, in this case, significant. The same trend has also been detected for Brixen granite and granitic gneiss which reveal higher strength values than KGS, but also lower or similar normal forces for certain penetration. Analysis of the fracture pattern showed, that crack propagation in mica schist and schistose gneiss (KAT-SG) follows existing mica layers and nearly no cracks have been observed in quartz. Calcareous mica schist additionally reveals cracks along cleavage planes of calcite. The same rock types have been tested by punch penetration test though investigations show different trends (ERBEN 2013). Calcareous mica schist results in much lower normal forces than augen gneiss, Brixen granite, or granitic gneiss. It can be explained by the fact that the punch penetration test is only an impact test which does not consider the formation of tensile cracks. However, this process seems to be essentially for effective rock cutting and has to be taken into account to reflect reality.

Following, the influence of toughness is investigated by comparing results from penetration tests with corresponding laboratory results of encountered rocks from the Koralm tunnel. At the Rössåga hydro-power project, only a small amount of sample material was available resulting in limited laboratory data. Therefore, these values are excluded from further analysis. As a first step, the existing correction factor k_1 by GEHRING was planned to be analyzed (Eq. 2-18, page 21). However, this factor bears insuperable obstacles, since the determination of the geotechnical parameter specific failure energy (w_f), proposed by Gehring, is not transparent. One parameter, which is necessary, is the volume of the rock specimens tested by GEHRING. Unfortunately, this information is not provided in the published papers. Anyhow, the specific failure energy cannot be equated to the term of failure work used in this thesis. Therefore, the correction factor k_1 cannot be evaluated properly in terms of this work, which is why other definition possibilities for rock toughness are analyzed.

The applicability of existing rock toughness definitions on obtained data from the laboratory program have already been described in chapter 5.2 (page 107). This chapter transfers the findings from laboratory investigation to field investigation and validates the results by analyzing penetration tests in terms of rock toughness. The influence of rock toughness on the penetration can be best described by using the **field penetration index FPI_{3mm}** at the point of subcritical penetration since this value includes the applied force at 3 mm /rev penetration. Analysis on the correlation of geotechnical parameters with

FPI_{3mm} has proven that the only geotechnical parameters that appear to have certain effect are the Brazilian tensile strength and the LCPC breakability coefficient (s. Fig. 117). These parameters are also in focus of research since they are a suitable tool to characterize rock toughness.

Therefore, the suggested index T_{LBC} is analyzed as it combines both parameters by the ratio of LBC and BTS. For illustration purpose, the inverse index $T_{LBC}^{-1} = BTS / LBC$ is used. The correlation of T_{LBC}^{-1} with resulting FPI_{3mm} is presented in Fig. 123A. Only tests at unfractured rock mass are plotted to eliminate the effect of rock mass properties as good as possible. A distinct trend is obvious since with an increase in T_{LBC}^{-1} , the boreability decreases. An increase in T_{LBC}^{-1} can be either caused by high BTS values or low LBC values. Both facts lead to lower boreability since high tensile strength or resistance against destruction has to be overcome. So the determined trend seems to be reasonable and suitable for an implantation into penetration prediction models. However, this observation is contradicting to presented classification for rock toughness by the coefficient T_{LBC} in chapter 5.2.3. High T_{LBC}^{-1} values correspond to brittle failure. Though, according to the graph in Fig. 123A, these rock types result in low boreability. Unfortunately, the same observation has been made when comparing the field penetration index to other toughness describing indices such as $T_{PLT} (UCS / I_s)$ and $T_e (UCS * BTS / 2)$. The correlation of FPI_{3mm} to toughness coefficient $T_z (UCS / BTS)$ is in strong contrast. The validation is shown in Fig. 123B and reveals that with increasing brittleness, the boreability increases. This result agrees with the common opinion that tough rocks are harder to excavate than brittle ones. However, the toughness coefficient T_z was one of those definition possibilities that show very low coincidence in the laboratory part of this thesis. This means, that by the factor T_z , the actual failure behavior of rocks under load is not described properly. Nevertheless, it appears that this coefficient reflects the cuttability of rock in practice.

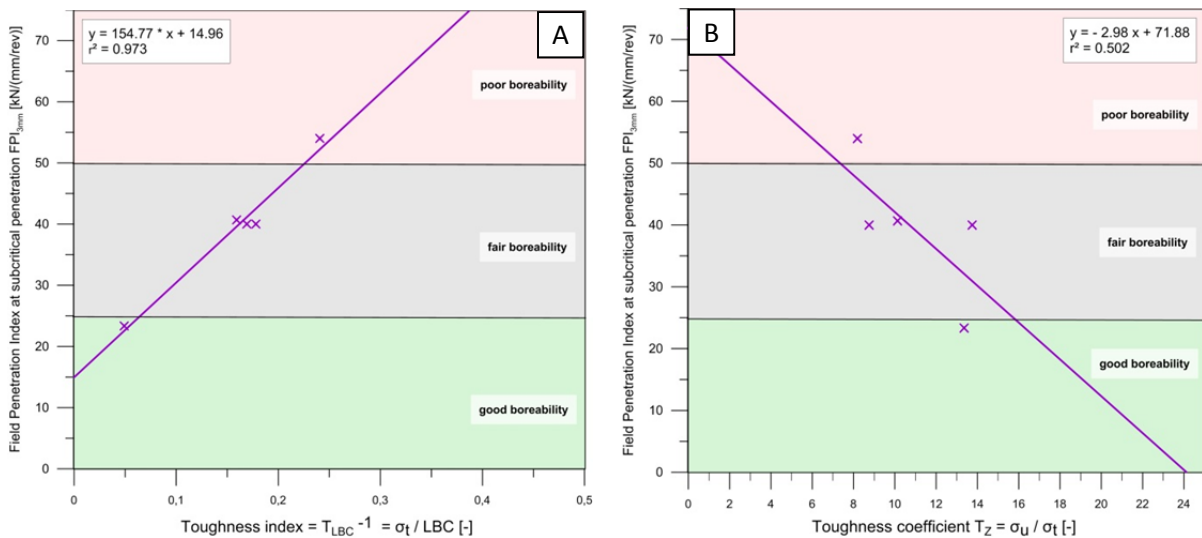


Fig. 123: Field penetration index at subcritical penetration FPI_{3mm} is plotted against the toughness coefficient T_{LBC}^{-1} (A) and T_z (B). Only tests at unfractured rock mass are presented to eliminate the influence of rock mass properties.

In terms of penetration prediction, presented indices by using the ratio of LBC and BTS respectively UCS and BTS seem to be suitable for incorporation as correction factor. Nevertheless, this correction factor might rather be described by the term of excavation index than by the term of rock toughness. These findings suggest that the deformation behavior of rocks under uniaxial compression in the

laboratory does not reflect the actual ‘cuttability’ in TBM tunneling since the rock is subject to a triaxial state of stress. Although plastic deformation and post-failure range determine rock toughness in terms of rock mechanical aspect, they seem to be not decisive to describe the excavatability of rocks by TBMs. Here, the parameters of breakability, compressive and tensile strength are of major importance and reflect the cuttability of rocks in practice. This fact leads to the conclusion, that abovementioned toughness indices are suitable in principle, but suggested classification systems into tough or brittle are not applicable to describe the excavatability in tunneling since they are based on the idea that toughness is characterized by high plastic deformation and distinct post failure range.

However, this fact cannot be generalized since the results rely only on one tunnel project where rocks with distinct mica content were encountered which may falsify the analysis. A proposal of precise values for the correction factor could not be achieved in the course of this thesis due to the lack of rock variability at analyzed tunnel projects. Thus, investigations at more tunnel projects with different rock types are recommended.

Conclusively, the field penetration index FPI_{3mm} seems to be highly affected by two rock properties, namely the Brazilian tensile strength BTS and the LCPC breakability coefficient LBC. An increase of BTS or a decrease of LBC results in low cuttability. The ratio of both parameters also characterizes rock toughness. Distinct correlation of the toughness coefficient with the excavatability has been found. However, the correlation shows contrary trend to proposed classification systems stated in the laboratory part. This leads to the assumption, that the toughness of rocks, determined in the laboratory under uniaxial compression, cannot be equated to the resistance of rock against cutting by tunnel boring machines since the rock is subject to a triaxial stress field.

6.2.3 Parameter - discontinuity pattern in rock mass

To analyze the influence of discontinuities on the penetration rate, existing correction factors for the Gehring and CSM model are investigated. GEHRING implemented the **correction factor k_2** that can be determined by proposed table (Tab. 5, page 23), whereas the CSM model incorporates the **rock fracture index RFI** that is calculated by a correlation formula (Eq. 2-30, page 56). Both approaches are based on the spacing of discontinuities and the smallest angle α between tunnel axis and planes of weakness. Analysis has been done for all penetration test results. In the following, the test No. 24 is picked as example for rock mass that is highly fractured by three distinctive joint sets and a 0.1 m thick zone with coarse grained fault material (s. Fig. 111). On the basis of this test, analysis on the Gehring model is done by two different approaches. First, suggested factor k_2 by GEHRING (1995) is implemented and then compared to the total fracturing factor k_{s-tot} by BRULAND (2000b).

Gehring factor results in $k_2 = 1.3$ since only the major plane of weakness can be considered. Despite this fact, other joint systems measure spacing more than 50 cm and are never accounted for. The observed fault zone is also not included in the consideration since it is a single marked discontinuity. Fig. 124A illustrates that k_2 by GEHRING leads to an improvement, but still, estimated values vary from measured data in high degree. This is due to the fact that only the major discontinuity set is implemented and the increasing impact of intersecting systems on the penetration is neglected. Furthermore, faults cannot be considered as single marked discontinuities show no spacing < 50 cm. Both aspects are weightily weaknesses of the proposed Gehring factor k_2 . An improvement might be achieved by extending the table to distances between planes of weakness up to 160 cm, since

GEHRING noted distinct effect for greater spacing already in 1997, but without further implementation (GEHRING 1997). Since k_2 is based on observations by BRULAND, k_2 is directly substituted by k_{s-tot} (BRULAND 2000b). The total fracturing factor results in much higher value of $k_{s-tot} = 3.3$ as it considers spacing up to 160 cm, the interaction of different discontinuity sets among each other and single marked joints like faults. Fig. 124B shows that the implementation of k_{s-tot} into the Gehring model results in good representation of reality in this example.

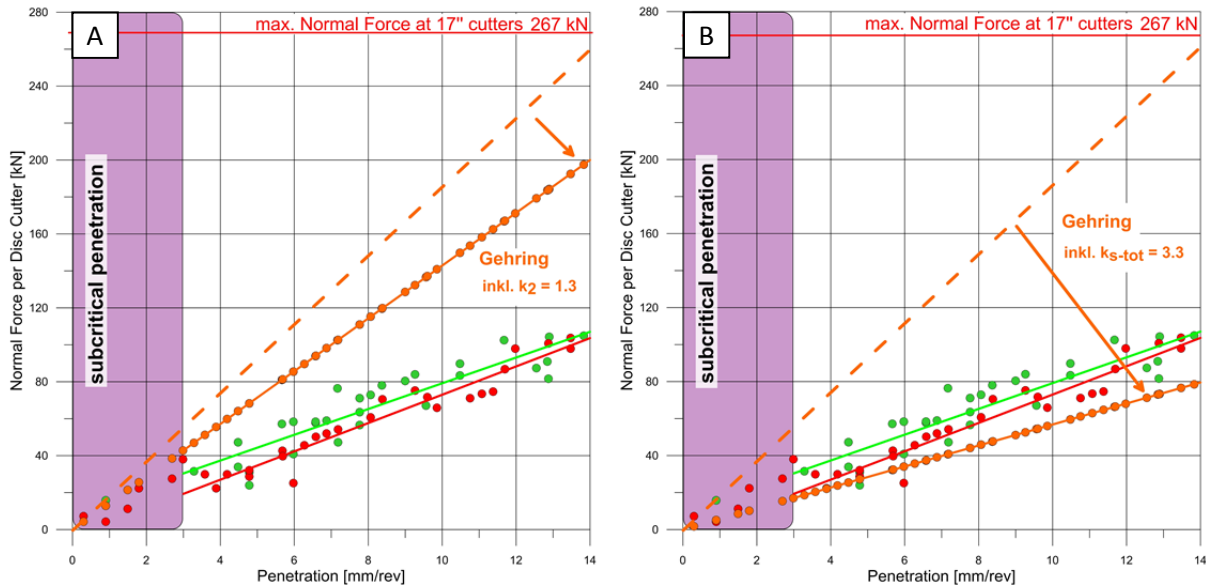


Fig. 124: Corrected Gehring model including correction factors for rock mass fabric compared to basic Gehring model (dashed line) of penetration test No. 24. **(A)** $k_2 = 1.3$ acc. to proposed factors by Gehring (Tab. 5). **(B)** $k_{s-tot} = 3.3$ based on suggested NTNU total fracturing factor.

In a second step, the suggested correction factors by GEHRING and BRULAND are compared with the actual deviation between predicted Gehring values and actually measured values (Fig. 125). The input data of this figure is summarized in Tab. 22. It has been proven that the total fracturing factor overestimates the influence of discontinuity systems in most cases (Fig. 125, upper left). If the rock mass is only low to moderately fractured, this factor results in too optimistic prediction of penetration rates (e.g. Tab. 22, No. 14). Nevertheless, the approach that the factor may also drop below one appears to be reasonable at rock mass that is free of discontinuities or only slightly fractured (lower left part). Examples for this statement are the tests at cross passage number 12, 13, 14, 17, 18, 19, 22, and 23 listed in Tab. 22. Here, the actual correction factor must be less than one to meet the data recorded during the penetration test. These entire tests have in common that none or only one set of discontinuities was mapped. This fact is considered better by the total fracturing factor and is one of the facts that has to be improved for the correction factor k_2 by GEHRING. The observation has shown, that the minimal correction factor might not be described by the index 1, since unfractured rock mass is harder to cut than the basic version of the Gehring model is predicting.

Conversely, if the rock mass is moderately to highly fractured, the Gehring correction factor usually underestimates the impact of planes of weakness since only one system is considered and the critical spacing of 50 cm seems not to be sufficient (Fig. 125, lower right). Examples are the test results at cross passage number 24 and 36 (Tab. 22).

Tab. 22: Summarized results of penetration tests at the Koralm tunnel concerning the correction factor for discontinuities for the Gehring model. Actual deviation of predicted to measured data (k_{act}) is compared with predicted correction factors by GEHRING (k_2) and the total fracturing factor by BRULAND (k_{s-tot}). In addition, the number and the type (J = joint, F = fault, S = slickenside) of discontinuity sets are listed.

Test ID	Rock type	No. of sets	Type of sets	k_{act}	k_2	k_{s-tot}
No. 12	schistose gneiss	1	J	0.55	1.00	0.90
No. 13	schistose gneiss	0	-	0.62	-	-
No. 14	schistose gneiss	1	J / S	0.70	1.40	2.20
No. 15	schistose gneiss with siliceous marble	2	S	0.60	1.00	2.48
No. 17	schistose gneiss with siliceous marble	0	-	0.95	-	-
No. 18	schistose gneiss	1	J	0.83	1.00	0.80
No. 19	schistose gneiss	1	J	0.61	1.00	0.80
No. 20	schistose gneiss	2	J / S	1.46	1.40	2.14
No. 21	schistose gneiss	3	J / S	0.54	1.28	2.80
No. 22	schistose gneiss	1	J	0.55	1.00	0.70
No. 23	fine-grained gneiss	1	J	0.30	1.00	0.90
No. 24	coarse-grained gneiss	4	J / F	2.48	1.30	3.30
No. 25	schistose gneiss	1	F	0.97	1.00	1.20
No. 26	platy gneiss	1	S	1.53	1.00	1.00
No. 29	platy gneiss	4	J / S / F	1.53	1.45	3.72
No. 30	fine-grained gneiss	3	J / S	0.78	1.00	2.38
No. 32	amphibolite	0	-	0.60	-	-
No. 34	fine-grained gneiss	0	-	0.50	-	-
No. 36	fine-grained gneiss	3	J	1.67	1.00	1.80
No. 37	fine-grained gneiss	4	J	0.75	1.50	1.40

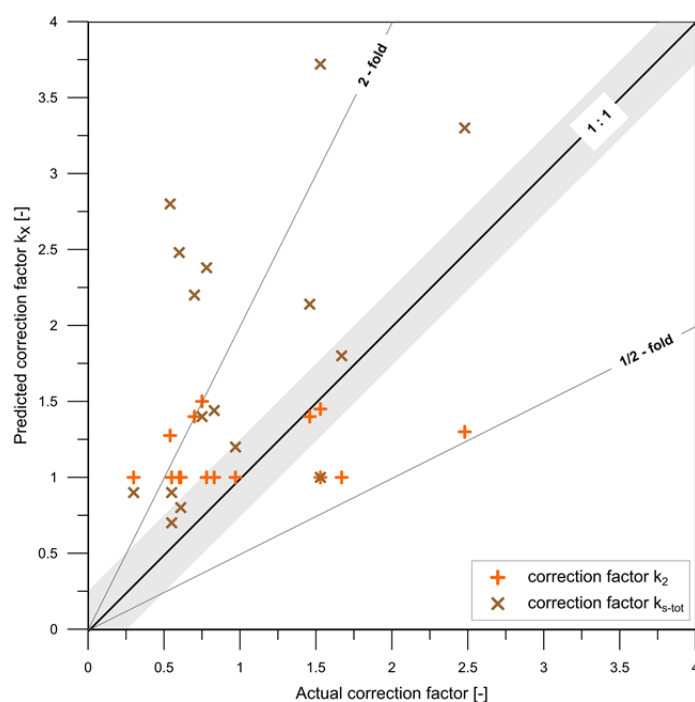


Fig. 125: Predicted correction factors k_2 and k_{s-tot} for the Gehring model compared with actual deviation of predicted to measured data determined by penetration tests at the Koralm tunnel.

Summarizing, the Gehring correction factor k_2 reveals appropriate results for ‘common’ conditions, meaning that the rock mass is not free of discontinuities, but also not highly fractured. The correction factor results in high inaccuracy, once rock mass properties deviate from this ‘common’ behavior. An improvement can be possibly achieved by combining the strengths of the total fracturing factor into the determination table by GEHRING. Unfortunately, collected data is not sufficient to define new correction factors, since results from other tunnel projects with different rock types are required for proper investigations. Furthermore, the geological face mapping must be of more detail including an exact recording of the spacing of each discontinuity set and possible block sizes. Without this profound information, no systematization for a correction factor for discontinuity pattern is possible.

The influence of rock mass properties for the **CSM model** is considered by the modified CSM (MCSM) version developed by YAGIZ (2014: 174) (s. chapter 2.5.4). The MCSM is based on regression analysis and results in an equation where each parameter is added to or subtracted from the basic CSM penetration rate (Eq. 2-32). Therefore, the formula can only be applied when all included factors are available. These are the rock fracture index, which is based on spacing and orientation of the main discontinuity system, and the brittleness index, which is based on results from the punch penetration test. If the punch penetration test is not performed, conversion formula is proposed that includes strength values and density of the sample (s. chapter 2.4.5).

The approach has been applied at chosen penetration test results with only partial success. Test No. 24 is exemplarily shown in Fig. 126. The MCSM moves closer to the actual measured TBM data; however, discrepancies are still significant which may have several reasons. First, the procedure bears a number of uncertainties starting with the conversion formula of the punch penetration result up to the consideration of only one discontinuity set. However, the main problem is the applicability. The calculation of penetration rates at the CSM model is complex since the model is designed to predict normal forces and not the penetration rate itself. Additionally, the MCSM cannot be used if one parameter is not available due to the linear relation with sums and differences. The model appears quite inflexible and all these facts make the application for users impractical and complicated. Furthermore, the modified equation is based on only one tunnel project and needs to be improved and validated at several tunnel projects. Consequently, the approach was not subject to further research in this thesis.

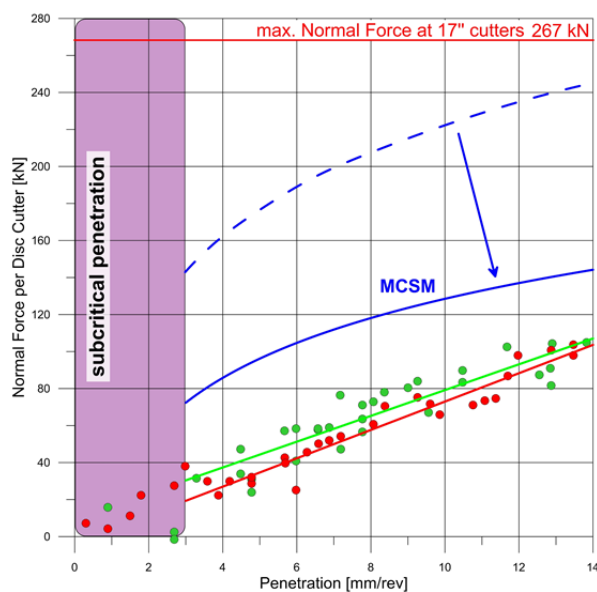


Fig. 126: Modified CSM model including correction factors for rock mass fabric and rock brittleness compared to basic CSM model (dashed line) of penetration test No.24.

In summary, the influence of planes of weakness on the penetration rate is not sufficiently described by existing correction factors. Analyses have proven that the Gehring model allows high flexibility regarding the implementation of correction factors for rock mass fabric. However, proposed factor k_2 by GEHRING results in low fitting if no 'common rock mass, such as rock mass that is free of discontinuities or highly fractured, is encountered. The combination with the total fracturing factor by BRULAND may rectify this weakness leading to an extended determination table for k_2 . The modified CSM model could only be applied with moderate success and fails with regard to the applicability. Unfortunately, collected data is not sufficient to define new correction factors, since the geological face mapping must be of more detail including an exact recording of the spacing of each discontinuity set and possible block sizes. Without the profound information, no systematization for a correction factor for discontinuity pattern is reasonable.

7 Conclusions

In this work, investigations on the cuttability of rocks by hard rock tunnel boring machines have been presented. A special focus was laid on improving existing penetration prediction models by performing an extensive laboratory program, as well as field studies. These efforts aimed to explain the principal relation between the rock respectively rock mass and the excavation tool. Furthermore, the parameters of rock toughness and rock mass discontinuity pattern have been analyzed in a profound way since both influence penetration rate significantly. The initial aim of incorporating new correction coefficients for these factors of influence into penetration prediction models was only partially achieved. This is due to the fact that obtained results have to be validated by several more tunnel projects to allow proper development and a general applicability of new correction factors. Nevertheless, this thesis resulted in important findings that must be subject to of further research.

Outcomes of laboratory investigations

The term of rock toughness is contrary to rock brittleness and describes the deformation behavior at which the rock responds to the applied load by high plastic deformation and distinct post-failure range. Existing definition possibilities of rock toughness have been analyzed to investigate if these approaches reflect the actual deformation behavior of rocks under load. Furthermore, new characterization methods have been suggested. The outcomes are shown in Tab. 23, whereby presented final suitability includes the accuracy of laboratory results, as well as the applicability of the testing method.

Tab. 23: Final outcomes of the existing and newly developed characterization possibilities for rock toughness concerning the accordance of laboratory results and the applicability of the testing method. Further explanations, see text.

Designation	Calculation approach	Suitability
T_z	σ_u / σ_t	not suitable
SI	$\epsilon_u / \epsilon_{cd}$	not – moderately suitable
WI	W_z / W_b	not – moderately suitable
DI	E_t / E_{pl}	moderately suitable
T_{PPT}	$0.0198 \sigma_u - 2.174 \sigma_t + 0.913 \rho - 3.807$	moderately suitable
T_{LBC}	LBC / σ_t	highly suitable
T_e	$(\sigma_u \cdot \sigma_t) / 2$	highly suitable
T_{PLT}	σ_u / I_s	highly suitable

The most commonly used T_z coefficient surprisingly resulted in very low accuracy and was no indicator if a rock reveals high plastic deformation or post-failure range. Thus, this factor does not correspond to the term of rock toughness with regard to rock mechanics, but might reflect the cuttability of rocks by disc cutters (s. next paragraph). The newly developed strain and energy based approaches (strain index SI, work index WI, deformation index DI) showed reasonable accordance to distinguish tough rocks from brittle ones. However, especially SI and WI slid down the ranking due to

the disadvantages in terms of applicability. The **strain index SI** can only be determined by using lateral strain measurements and corresponding time-consuming test analyses. Moreover, the determination of the decisive parameter ‘crack damage threshold’ involves distinct uncertainties. The **work index WI** is basically a good approach since it includes the aspect of energy consumption, but the measurement is the limiting factor. The parameter ‘destruction work’ is highly dependent on the testing machine and the procedure is not set as standard. The **deformation index DI** was attributed to a moderate rating since it is a quick and approximating method to characterize rock toughness. If only the uniaxial compression test is available for analysis, the deformation index DI is recommended. The approach via punch penetration test (T_{PPT}) could be investigated only by proposed conversion formula as the test is commonly not used in Europe. The results revealed good fitting in terms of describing tough failure behavior, but the limited use of the testing apparatus led to a moderate ranking.

The strength based **approach T_e** relies on the same input parameters, uniaxial compressive strength and Brazilian tensile strength, like the T_z coefficient. However, it somehow considers the energy by incorporating the area under the correlation line of both strength values. This fact strongly increased the accuracy of the coefficient T_e leading to a good correlation of tough failure behavior under load. The best fitting had been achieved by the **coefficient T_{LBC}** that is based on the LCPC breakability and the Brazilian tensile strength. It has been shown that rocks with tough failure behavior under load were attributed to low tensile strength and consequently high breakability. However, this trend is contradicting to the opinion, that tough rocks reveal higher resistance against boring. The result is explained by the fact that several rocks that were classified as tough showed high mica and calcite content or significant porosity. These parameters were responsible for distinct plastic deformation under load, but also resulted in lower strength values. So far the LCPC test is rarely used, but this is slowly changing due to the new German construction contract procedures for earthworks (DIN 18300) and the Austrian guideline for geotechnical planning of subsurface constructions (ÖGG 2013). Thus, it might be a useful tool for future analysis. Another alternative for the T_z coefficient was presented by the **T_{PLT} coefficient** which is based on the uniaxial compressive strength and the point load index. The method is straightforward since the point load test is a simple tool that can be used at the construction site itself. Besides the advantage in terms of applicability, the coefficient T_{PLT} provided high accuracy to characterize rock toughness and is thus recommended for practical use. In addition, the link to the cuttability of rocks by TBM, as well as the scientific aspect is covered by the coefficient, since input parameters are somehow responsible for the formation of a crushed zone (uniaxial compressive strength) and following crack propagation (tensile strength).

Analysis revealed that three different approaches are characterizing tough failure behavior respectively high plastic deformation and distinct post-failure range with high accuracy. The remarkable fact is that each one is based on different input parameters covering the whole range of laboratory testing (uniaxial compressive strength, Brazilian tensile strength, LCPC breakability coefficient, point load index). These findings allow high flexibility since the coefficients can be applied depending on the available input parameters.

Outcomes of field investigations

Field investigations were performed by means of penetration tests with the TBM directly at the construction site. It has been shown that these tests are a suitable tool to analyze the interaction between the rock and the machine in terms of force-penetration graphs. However, broader rock variability would have been desirable which is why further tests at different tunnel projects are recommended.

One of the major findings of this thesis was the fact that analyzed penetration prediction models (CSM model, Gehring model) are based on an inappropriate mathematical equation. The actual relation between the applied force and resulting penetration can be described by a **linear function** with certain **y-intercept** specified by the threshold of subcritical penetration. The magnitude of the offset highly depends on the LCPC breakability and subordinated on the Brazilian tensile strength, whereas uniaxial compressive strength, failure and destruction work and point load strength revealed no significance. To enable proper correlation, investigations had been done by analyzing the stress under the disc cutter. Therewith, it had been proven that the slope of resulting stress-penetration graphs is rather dependent on rock mass properties such as discontinuity systems or the state of in-situ stress, than on intact rock properties. At ‘average’ rock mass conditions, meaning low fracturing degree and low in-situ stresses, the slope can be described as nearly horizontal. By means of these findings, a newly developed modified Gehring model, so-called ‘Alpine Model’, is proposed that includes the important parameter of y-intercept. However, it must be clarified that investigations are only based on one tunnel project with a narrow range of rock types and must be validated by further data. Nevertheless, the approach shows promising results for future research.

‘Alpine Model’ (modified Gehring model)		$p = \frac{F_N - b_{BTS/LBC}}{\sigma_u} \cdot k_0 \cdot k_2 \cdot k_i + 3$	
$p =$	penetration rate [mm/rev]	$k_0 =$	basic penetration factor = 4.0 [-]
$F_N =$	normal force per cutter [kN]	$k_2 =$	correction factor for discontinuity pattern [-]
$b_{BTS/LBC} =$	y-intercept BTS or LBC approach [-]	$k_i =$	further correction factors for geotechnical / machine parameters [-]
$\sigma_u =$	uniaxial compressive strength [MPa]		

Analysis on the influence of **rock toughness** showed a very strong correlation of T_{LBC} and corresponding excavatability of the rock. The toughness coefficients T_{PLT} and T_e also revealed significant correlation. However, the trend was contrary to suggested classifications resulting from laboratory research in this thesis. Rocks that were classified as tough according to laboratory investigations resulted in better boreability which is contradicting to common research opinion. Conversely, comparison of T_z and the field penetration index resulted in the expected trend that tough rocks were harder to excavate than brittle ones. Though, the toughness coefficient T_z was one of those definition possibilities that showed very low coincidence in the laboratory part of this thesis. These findings support the conclusion that the deformation behavior of rocks under uniaxial compression in the laboratory does not reflect the actual ‘cuttability’ in TBM tunneling since the rock is subject to a triaxial state of stress. Although plastic deformation and post-failure range determine rock toughness in terms of rock mechanics, they are not decisive to describe the excavatability of rocks by TBMs. Here, the parameters of compressive and tensile strength, as well as the breakability are of major importance and reflect the boreability of

rocks in practice. Therefore, toughness indices are suitable in principle, but suggested classification systems into tough or brittle rock are not applicable for characterizing the cuttability since they are based on the idea that toughness is described by high plastic deformation and distinct post failure range. Furthermore, it seems to be reasonable to use two different terms for the deformation behavior in the laboratory and the excavatability during tunnel construction. This aspect must be examined in greater detail which is why further tests and analysis at future tunnel projects regarding toughness coefficients T_{LBC} , T_{PLT} , T_z and T_e are highly recommended.

Analysis on the influence of the **discontinuity pattern** in the Gehring model showed that suggested correction factor k_2 only provided appropriate results at ‘common’ rock mass conditions. ‘Common’ means that the rock mass was not free of discontinuities, but also not highly fractured. If these conditions were not met, the corrections factor revealed high inaccuracies. If the rock mass is slightly fractured, a correction factor below one seems reasonable, which is not considered by the existing factor k_2 . Furthermore, the determination table must be extended by greater distances between the planes of weakness since a maximum of 50 cm proved not to reflect actual rock mass conditions. Major weakness is the missing possibility to account for intersecting discontinuity sets, as well as the incorporation of marked single planes like faults. These problems can be solved by combing k_2 with the total fracturing factor k_{s-tot} by BRULAND, since the factor includes all abovementioned weaknesses. Simple exchange of both parameters failed to have the desired effect as k_{s-tot} mostly overestimates the effect of joints and fractures on the penetration. This is caused by the fact that it has been developed for Scandinavian rock mass conditions where fracturing degree is often low compared to Alpine geology.

Regarding the CSM model, the rock fracturing factor and consequently the modified CSM model (MCSM) by YAGIZ has been applied, thus with only partial success. Still significant discrepancies between predicted and measured data were observed. Besides this fact, the MCSM failed in terms of applicability. Therefore, recommendations for future research are an extended determination table for proposed correction factors k_2 , which considers discontinuity spacing up to 160 cm, intersecting planes of weakness, single marked joints and unfractured rock mass conditions. Unfortunately, collected data is not sufficient to define new correction factors, since the geological face mapping must be of more detail, including an exact recording of the spacing of each discontinuity set and possible block sizes. Without this information, no systematization for a correction factor for discontinuity pattern is reasonable. Therefore, investigations on a larger number of tunnel projects are inevitable so that different machine designs and varying geological conditions are considered properly.

8 Bibliography

- AASEN, O. (1980): Influence of rock properties and jointing by disc cutting with a triple-boom tunnel boring machine. – *Fjellsprengningsteknikk - Bergmekanikk - Geoteknikk*, 27: 1–9.
- AFNOR - P18-579 (1990): Aggregates - abrasiveness and grindability test. – 9 pp.; Paris (afnor groupe).
- ALBER, M. (1996): Prediction of penetration and utilization for hard rock TBMs. – In: BARLA, G. (Ed.): *Proceedings of the EUROCK conference: 721–725*; Rotterdam (Balkema).
- ALBER, M. (2000): Advance rates of hard rock TBMs and their effects on projects economics. – *Tunnelling and Underground Space Technology*, 15 (1): 55–64.
- ALTINDAG, R. (2003): Correlation of specific energy with rock brittleness concepts on rock cutting. – *Journal of The South African Institute of Mining and Metallurgy*: 163–172.
- ALTINDAG, R. (2010): Assessment of some brittleness indexes in rock-drilling efficiency. – *Rock Mech. Rock Eng.*, 43: 361–370.
- AMANN, F., BUTTON, E., ALAN E., K.F., GISCHIG, V. & BLÜMEL, M. (2011): Experimental study of the brittle behavior of clay shale in rapid unconfined compression. – *Rock Mech. Rock Eng.*, 44 (4): 415–430.
- ANDREEV, G. (1995): Brittle failure of rock material. – 456 pp.; Rotterdam (Balkema).
- ASTM - E111-04 (2010): Standard test method for Young's modulus, tangent modulus and chord modulus. – 7 pp.; Cary (J & J Editorial).
- BARRON, K. (1971): Brittle fracture initiation in and ultimate failure of rocks. – *Int. J. Rock Mech. & Min. Sci.*, 8: 541–551.
- BARTON, N. (2000): TBM tunnelling in jointed and faulted rock. – 1, 173 pp.; Rotterdam (Balkema).
- BASU, A., MISHRA, D.A. & ROYCHOWDHURY, K. (2013): Rock failure modes under uniaxial compression, Brazilian, and point load tests. – *Bull. Eng. Geol. Environ.*, 72 (3-4): 457–475.
- BECK-MANNAGETTA, P. (1952a): Aufnahmen über das Lavanttal und die Koralpe (Kärnten, Steiermark). – *Verh. Geol. B. -A.*: 24-27.
- BECK-MANNAGETTA, P. (1952b): Zur Geologie und Paläontologie des Teriärs des unteren Lavanttals. – *Verh. Geol. B. -A.*, 95, 102 pp.; Wien (Geologische Bundesanstalt).
- BECK-MANNAGETTA, P. (1980): Geologische Karte der Republik Österreich 1:50 000 - Blatt 188 Wolfsberg. – Wien (Geologische Bundesanstalt).
- BECK-MANNAGETTA, P., EISENHUT, M., ERTL, V. & HOMANN, O. (1991): Geologische Karte der Republik Österreich 1 : 50 000 - Blatt 189 Deutschlandsberg. – Wien (Geologische Bundesanstalt).
- BENJUMEA, R. & SIKARSKIE, D. (1969): A note on the penetration of a rigid wedge into a non-isotropic brittle material. – *Int. J. Rock Mech. & Min. Sci.* (6): 343–352.
- BIENIAWSKI, Z. (1967): Mechanism of brittle fracture of rock. – *Int. J. Rock Mech. & Min. Sci.*, 4: 395–430.
- BIENIAWSKI, Z. (1989): *Engineering Rock Mass Classifications*. – 251 pp.; New York (Wiley & Sons).
- BIENIAWSKI, Z., TAMAMES, B., FERNÁNDEZ, J. & HERNÁNDEZ, M. (2006): Rock Mass Excavability (RME) Indicator: new way to selecting the optimum tunnel construction method. – *Tunnelling and Underground Space Technology*, 3-4 (21): 237–244.
- BOMBOLAKIS, E. (1973): Study of the brittle fracture process under uniaxial compression. – *Tectonophysics*, 18: 231–248.
- BRACE, W. (1961): Dependence of fracture strength of rocks on grain size. – *Bull. Penn. State Univ. Mineral Industries Experiment Station*, 76: 99–103.

- BRACE, W. (1964): Brittle fracture of rocks. – In: JUDD, W. (Ed.): State of stress in the earth's crust, 110–178; New York (American Elsevier Publishing Company).
- BROOK, N. (1993): The measurement and estimation of basic rock strength. – In: HUDSON, J. (Ed.): Comprehensive rock engineering. Principles, practice & projects, 41–81; Oxford (Pergamon).
- BRULAND, A. (2000a): Hard rock tunnel boring - Vol. 1 - Background and discussion. – Dissertation Thesis, Norwegian University of Science and Technology, 49 pp.; Trondheim.
- BRULAND, A. (2000b): Hard rock tunnel boring - Vol. 3 - Advance rate and cutter wear. – Dissertation Thesis, Norwegian University of Science and Technology, 54 pp.; Trondheim.
- BRULAND, A. (2000c): Hard rock tunnel boring - Vol. 6 - Performance data and back-mapping. – Dissertation Thesis, Norwegian University of Science and Technology, 95 pp.; Trondheim.
- BRULAND, A. (2000d): Hard rock tunnel boring - Vol. 8 - Drillability test methods. – Dissertation Thesis, Norwegian University of Science and Technology, 25 pp.; Trondheim.
- BÜCHI, E. (1984): Einfluss geologischer Parameter auf die Vortriebsleistung einer Tunnelbohrmaschine. – Dissertation Thesis, Philosophisch-naturwissenschaftliche Fakultät, Universität Bern, 136 pp.; Bern.
- CERCHAR (1986): The Cerchar Abrasiveness Index. – 12 pp.; Verneuil.
- CHEEMA, S. (1999): Development of a rock mass boreability index for the performance of tunnel boring machines. – Dissertation Thesis, Colorado School of Mines, 262 pp.; Golden.
- CRUDEN, D. (1974): The static fatigue of brittle rock under uniaxial compression. – Int. J. Rock Mech. Min. Sci. & Geomech. Abstr., 11: 67–73.
- DEERE, D. & MILLER, R. (1966): Engineering classification and index properties for intact rock. – 302 pp.; Urbana.
- DELISIO, A., ZHAO, J. & EINSTEIN, H. (2013): Analysis and prediction of TBM performance in blocky rock conditions at the Lötshberg Base Tunnel. – Tunnelling and Underground Space Technology, 33: 131–142.
- DGGT (2004): Neufassung der Empfehlung Nr.1 des Arbeitskreises "Versuchstechnik Fels" der Deutschen Gesellschaft für Geotechnik e.V. : Einaxial Druckversuche an zylindrischen Gesteinsprüfkörpern. – Bautechnik, 81: 825–834.
- DGGT (2008): Empfehlung Nr. 10 des Arbeitskreises "Versuchstechnik Fels" der Deutschen Gesellschaft für Geotechnik e.V.: Indirekter Zugversuch an Gesteinsproben – Spaltzugversuch. – Bautechnik, 85: 623–627.
- DGGT (2010): Empfehlung Nr.5 des Arbeitskreises "Versuchstechnik Fels" der Deutschen Gesellschaft für Geotechnik e.V.: Punktlastversuch an Gesteinsproben. – Bautechnik, 87: 322–330.
- DGGT (in prep.): Empfehlung Nr. 23 des Arbeitskreises "Versuchstechnik Fels" der Deutschen Gesellschaft für Geotechnik e.V.: Bestimmung der Abrasivität von Gesteinen mit dem Cerchar Versuch. – Geotechnik.
- DIN 51220 (2003): Werkstoffprüfmaschinen - Allgemeines zu Anforderungen an Werkstoffprüfmaschinen und zu deren Prüfung und Kalibrierung. – 9 pp.; Berlin (Beuth).
- DIN 18135 (2012): Baugrund, Untersuchung von Bodenproben. – 38 pp.; Berlin (Beuth).
- DIN 18300 (2015): VOB Vergabe- und Vertragsordnung für Bauleistungen. – 18 pp.; Berlin (Beuth).
- DIN EN ISO 7500-1 (2004): Metallische Werkstoffe - Prüfung von statischen einachsigen Prüfmaschinen - Teil 1: Zug- und Druckprüfmaschinen. – 20 pp.; Berlin (Beuth).
- DOLLINGER, G., HANDEWITH, H. & BREEDS, C. (1998): Use of the punch test for estimating TBM performance. – Tunnelling and Underground Space Technology, 13 (4): 403–408.
- EBERHARDT, E. (1998): Brittle rock fracture and progressive damage in uniaxial compression. – Dissertation Thesis, Department of Geological Sciences, University of Saskatchewan; Saskatchewan.

- EBERHARDT, E., STEAD, D., STIMPSON, B. & READ, R. (1998): Identifying crack initiation and propagation thresholds in brittle rock. – *Can. Geotech. J.*, 35: 222–233.
- ELLECOSTA, P. (in prep.): Determining abrasivity for mechanical excavation in hard rock. – Dissertation Thesis, Technische Universität München; München.
- ENTACHER, M. (2013): Measurement and interpretation of disc cutting forces in mechanized tunneling. – Dissertation Thesis, Subsurface Engineering, Montanuniversität Leoben, 153 pp.; Leoben.
- ERBEN, H. (2013): Punch penetration tests - Input parameter for TBM performance prediction. – unpubl. Diploma Thesis, Montanuniversität Leoben, 102 pp.; Leoben.
- EVANS, I. & POMEROY, C. (1966): The strength, fracture and workability of coal. – 277 pp.; Oxford (Pergamon).
- FARMER, I. & GLOSSOP, N. (1980): Mechanics of disc cutter penetration. – *Tunnels and Tunnelling Int.*, 12: 22–25.
- FARMER, I., HIGNETT H. & HUDSON J. (1979): The role of geotechnical factors in the cutting performance of TBM in rocks. – In: ISRM (Ed.): Proc. of the 4th Congress of the ISRM, 371–377.
- FLÜGEL, H. & NEUBAUER, F. (1984): Steiermark. – 127 pp.; Wien (Geologische Bundesanstalt).
- FOX, P. & SORTA-RUIZ, J. (1970): Fracture-induced thermal decomposition in brittle crystalline solids. – *Proc. R. Soc.*, 317: 79–90.
- FRENZEL, C., GALLER, R., KÄSLING, H. & VILLENEUVE, M. (2012): Penetration tests for TBMs and their practical application. – *Geomechanics and Tunnelling*, 5 (5): 557–566.
- FREUDENBERGER, W. & SCHWERD, K. (1996): Erläuterungen zur geologischen Karte von Bayern 1 : 500 000. – 329 pp.; München (Bayerisches Geologisches Landesamt).
- GEHRING, K. (1995): Leistungs- und Verschleißprognose im maschinellen Tunnelbau. – *Felsbau Magazin*, 13 (6): 493–448.
- GEHRING, K. (1997): Classification of drillability, cuttability, borability and abrasivity in tunnelling. – *Felsbau Magazin*, 15 (3): 183–189.
- GERSTNER, R., TENTSCHERT, E. & VIGL, A. (2001): Quantifizierung oder Qualifizierung geologischer Parameter für TBM-Vortriebe. – *Felsbau Magazin*, 19 (5): 107–113.
- GERTSCH, R. (2000): Rock toughness and disc cutting. – Dissertation Thesis, University of Missouri-Rolla, 255 pp.; Missouri.
- GIRMSCHIED, G. (2013): Bauprozesse und Bauverfahren des Tunnelbaus. – 3, 760 pp.; Berlin (Wilhelm Ernst & Sohn).
- GONG, Q. & ZHAO, J. (2007): Influence of rock brittleness on TBM penetration rate in Singapore granite. – *Tunnelling and Underground Space Technology*, 22 (3): 317–324.
- GONG, Q. & ZHAO, J. (2009): Development of a rock mass characteristics model for TBM penetration rate prediction. – *Int. J. Rock Mech. & Min. Sci.*, 46: 8–18.
- GONG, Q., JIAO, Y. & ZHAO, J. (2006): Numerical modelling of the effects of joint spacing on rock fragmentation by TBM cutters. – *Tunnelling and Underground Space Technology*, 21 (1): 46–55.
- GONG, Q., ZHAO, J. & JIANG, Y. (2007): In situ TBM penetration tests and rock mass boreability analysis in hard rock tunnels. – *Tunnelling and Underground Space Technology*, 22 (3): 303–316.
- GONG, Q., ZHAO, J. & JIAO, Y. (2005): Numerical modeling of the effects of joint orientation on rock fragmentation by TBM cutters. – *Tunnelling and Underground Space Technology*, 20 (2): 183–191.
- GRAHAM, P. (1976): Rock exploration for machine manufacturers. – Proc. of the Congress of Exploration for Rock Engineering: 173–180.
- GRIFFITH, A. (1921): The phenomena of rupture and flow in solids. – *Philosophical Transactions of the Royal Society of London*, 221: 163–198.

- GRUBER, J. (2015): Einfluss der Belastungsgeschwindigkeit beim einaxialen Druckversuch auf das Verformungsverhalten von Gesteinen. – unpubl. Bachelor's Thesis, Technische Universität München, 31 pp.; München.
- HALLBAUER, D., WAGNER, H. & COOK, N.G. (1973): Some observations concerning the microscopic and mechanical behaviour of quartzite specimens in stiff, triaxial compression tests. – *Int. J. Rock Mech. Min. Sci. & Geomech. Abstr.*, 10: 713–726.
- HANDIN, J. (1966): Strength and ductility. – In: CLARK, S. (Ed.): *Handbook of physical contacts*: 223–289; New York (Geol. Soc. Am.).
- HAWKES, I. & MELLOR, M. (1970): Uniaxial testing in rock mechanics laboratories. – *Engineering Geology*, 4 (3): 177–285.
- HEITFELD, M. (1989): Geotechnische Untersuchungen zum mechanischen und hydraulischen Verhalten von Dichtwandmassen bei hohen Beanspruchungen. – Dissertation Thesis, RWTH Aachen, 233 pp.; Aachen.
- HOEK, E. & BIENIAWSKI, Z. (1965): Brittle rock fracture propagation in rock under compression. – *International Journal of Fracture Mechanics*, 1: 137–155.
- HOEK, E. & BROWN, E.T. (1997): Practical estimates of rock mass strength. – *Int. J. Rock Mech. & Min. Sci.*, 34 (8): 1165–1186.
- HORNUNG, M. (2015): Untersuchungen zum Deformationsverhalten verschiedener Gesteinstypen mit Hilfe von Querdehnungsmessungen. – unpubl. Bachelor's Thesis, Technische Universität München, 34 pp.; München.
- HOWARTH, D. (1981): The effect of jointed and fissured rock on the performance of tunnel boring machines. – In: ISRM (Ed.): *Proceedings of the International Symposium on Weak Rock*, 1069–1074.
- HUCKA, V. & DAS, B. (1974): Brittleness determination of rocks by different methods. – *Int. J. Rock Mech. & Min. Sci.*, 11: 389–392.
- HUDSON, J., BROWN, E.T. & FAIRHURST, C. (1971): Optimising the control of rock failure in servo-controlled laboratory tests. – *Rock Mech. Rock Eng.*, 3 (4): 217–224.
- HUGHES, H.M. (1972): Some aspects of machining. – *Int. J. Rock Mech. & Min. Sci.*, 9: 205–211.
- ISRM (1978): Suggested methods for the quantitative description of discontinuities in rock masses. – *Int. J. Rock Mech. Min. Sci. & Geomech. Abstr.*, 15: 319–368.
- ISRM (1979): Suggested methods for determining the uniaxial compressive strength and deformability of rock Materials. – *Int. J. Rock Mech. Min. Sci. & Geomech. Abstr.*, 15: 137–140.
- ISRM (1985): Suggested method for determining point load strength. – *Int. J. Rock Mech. Min. Sci. & Geomech. Abstr.*, 22: 51–60.
- ISRM (2014): Suggested methods for determining the abrasivity of rock by the CERCHAR abrasivity test. – *Rock Mech. Rock Eng.*, 47 (1): 261–266.
- JAEGER, J. & COOK, N.G. (1979): *Fundamentals of rock mechanics*. – 1, 593 pp.; London (Chapman and Hall).
- KAHRAMAN, S. (2002): Correlation of TBM and drilling machine performances with rock brittleness. – *Engineering Geology*, 64: 269–283.
- KÄSLING, H. (2009): Bestimmung der Gesteinsabrasivität - Grundlagen, Anwendung und Einsatzgrenzen bei maschinellen Tunnelvortrieben. – Dissertation Thesis, Technische Universität München, 123 pp.; München.
- KLEIN, S., SCHMOLL, M. & AVREY, T. (1995): TBM performance at four hard tunnels in California. – In: WILLIAMSON, G. & GOWRING, I. (Eds.): *Proceedings of the Rapid Excavation and Tunnelling Conference*, 61–75; Littleton (Soc. for Mining, Metallurgy and Exploration Inc.).

- KOBAYASHI, S. (1971): Initiation and propagation of brittle fracture in rock like materials under compression. – *J. Soc. Mat. Sci.*, 20: 164–173.
- KOLYMBAS, D. (2011): *Geotechnik*. – 3, 595 pp.; Heidelberg (Springer).
- LAJTAI, E. (1974): Brittle fracture in compression. – *International Journal of Fracture Mechanics*, 10: 525–536.
- LASSNIG, K. (2012): *Verwendung von Tunnelausbruchmaterial*. – Dissertation Thesis, Montanuniversität Leoben, 158 pp.; Leoben.
- LEHRBERGER, G. (2007): Granit - das Höchste und das Tiefste. – In: HELM, W. (Ed.): *Granit*, 19–49; Hausenberg (Granitzentrum Nayerischer Wald).
- LEINS, W., THUM, W. & BECKER, J. (1973): *Ermittlung der Sprengfähigkeit von Gesteinen*. – 128 pp.; Wiesbaden (Verlag für Sozialwissenschaften).
- LEISCH, C. (2013): *Baugeologische Dokumentation und Auswertung von TBM-Maschinendaten am Koralmtunnel*. – unpubl. Master's Thesis, Technische Universität München, 59 pp.; München.
- LI, Y. & XIA, C. (2000): Time-dependent test on intact rocks in uniaxial compression. – *Int. J. Rock Mech. & Min. Sci.*, 37: 467–475.
- LINDQVIST, P.A. & LAI, H.H. (1983): Behaviour of the crushed zone in rock indentation. – *Rock Mech. Rock Eng.*, 16: 199–207.
- LINDQVIST, P.A., LAI, H.H. & ALM, O. (1984): Indentation fracture development in rock continuously observed with a scanning electron Microscope. – *Int. J. Rock Mech. Min. Sci. & Geomech. Abstr.*, 21 (4): 165–182.
- LISLERUD, A. (1997): *Principles of mechanical excavation*. – 186 pp.; Helsinki (Posiva).
- LISLERUD, A.; JOHANNESSEN, S.; BRULAND, A.; MOVINKEL, T. & JOHANNESSEN, O. (1983): *Hard rock tunnel boring report*. – 1-83, 159 pp.; Trondheim.
- LORENZ, S. (2013): *Entwicklung eines Modellversuchs zur Schneidbarkeitsermittlung von Hartgestein*. – unpubl. Master's Thesis, Montanuniversität Leoben, 83 pp.; Leoben.
- MACIAS, J., JAKOBSON, P. & BRULAND, A. (2014a): Rock mass variability and TBM prediction. – In: ISRM (Ed.): *Proc. of the EUROCK 2014*, 1–6.
- MACIAS, J., JAKOBSON, P., SEO, Y. & BRULAND, A. (2014b): Influence of rock mass fracturing on the net penetration rates of hard rock TBMs. – *Tunnelling and Underground Space Technology*, 44: 108–120.
- MARTIN, C.D. (1993): *The strength of Massive Lac du Bonnet granite around underground openings*. – Dissertation Thesis, University of Manitoba, 278 pp.; Winnipeg.
- MESECK, H. (1987): *Mechanische Eigenschaften von mineralischen Dichtwandmassen*. – Dissertation Thesis, Technische Universität Braunschweig, 176 pp.; Braunschweig.
- MISSBICHLER, H. (1997): *Untersuchung des Spannungsdehnungsverhaltens von Felsproben unter einaxialmen Belastungszustand*. – unpubl. Diploma Thesis, Technische Universität Graz, 61 pp.; Graz.
- MOKHNACHEV, M. & GROMOVA, N. (1969): Laws of variation of tensile strength indices and deformation properties of rocks with rate and duration of loading. – 4 pp.; New York.
- MORGENSTERN, N.R. & PHUKAN, A. (1966): Non-linear deformation of a sandstone. – *Proc. of the 1st Int. Congress of the ISRM*:543–548.
- MORI, L. (2012): *Results of linear cutting tests on different alpine lithologies*. – unpubl. Master's Thesis, Montanuniversität Leoben; Leoben.
- MORITZ, B., WAGNER, H.M., HANDKE, D. & HARER, G. (2011): Criteria for the selection of tunnelling method through the example of the Koralm Tunnel. – *Geomechanics and Tunnelling*, 4: 305–316.
- MORLEY, A. (1944): *Strength of materials*. – 35 pp.; London (Longmans Green).
- MOTT, N. (1948): Fracture of metals. – *Engineering Fracture Mechanics*, 165: 16–18.

- NATAU, O., MUTSCHLER, T. & LEMPP, C. (1991): Estimation of the cutting rate and bit wear of partial-face tunnelling machines. – In: ISRM (Ed.): Proceedings of the 7th Congress of the ISRM, 1591–1595.
- NICKSIAR, M. & MARTIN, C.D. (2012): Evaluation of methods for determining crack initiation in compression tests on low-porosity rocks. – *Rock Mech. Rock Eng.*, 45 (4): 607–617.
- NOCKER, C. (2007): Petrologie und Stukturgeologie des Ortler-Campo-Kristallin im Bereich Jennwand, Laas (Südtirol, Italien). – unpubl. Diploma Thesis, Institute for Mineralogy and Petrography, Universität Innsbruck; Innsbruck.
- NORWEGIAN TUNNELLING SOCIETY (2014): Norwegian tunnelling technology - Publication No. 23. – 216 pp.; Oslo.
- ÖBB-INFRASTRUKTUR AG (2009a): Koralmbahn Graz - Klagenfurt Baulos KAT2: Gutachten zur Geologie, Hydrogeologie und Geotechnik. – unpubl. project report, 171 pp.
- ÖBB-INFRASTRUKTUR AG (2009b): Koralmbahn Graz - Klagenfurt Baulos KAT2: Unterlagen zum Baugrund - Kontinuierliche Vortriebe. – unpubl. project report, 40 pp.
- ÖBB-INFRASTRUKTUR AG (2012): Bau-Information Koralmbahn Wettmannstätten - St. Andrä. – 7 pp.; Graz.
- OBERT, L. & DUVALL, W. (1967): Rock mechanics and the design of structures in rock. – 650 pp.; New York (John Wiley & Sons Inc.).
- ÖGG (2013): Richtlinie für die geotechnische Planung von Untertagebauten mit kontinuierlichem Vortrieb. – 49 pp.; Salzburg (Österreichische Gesellschaft für Geomechanik).
- OKUBO, S., NISHIMATSU, Y. & HE, C. (1990): Loading rate dependence of class II rock behaviour in uniaxial and triaxial compression tests - An application of a proposed new control method. – *Int. J. Rock Mech. Min. Sci. & Geomech. Abstr.*, 27 (6): 559–562.
- OROWAN, E. (1949): Fracture and strength of solids. – *Rep. Progr. Phys.*, 12: 185–232.
- OZDEMIR, L.; MILLER, R. & WANG, F. (1977): Mechanical tunnel boring prediction and machine design. – *Annual Report*; Washington.
- PALMSTRÖM, A. (1982): The volumetric joint count - a useful and simple measure of the degree of rock mass jointing. – *Proc. of the 4th Int. Congress of IAEG*, (5): 221–228.
- PAULDING, B. (1966): Techniques used in studying the fracture mechanics of rock. – *ASTM, Testing Techniques for Rock Mechanics*, 402: 73–86.
- PLINNINGER, R. (2002): Klassifizierung und Prognose von Werkzeugverschleiß bei konventionellen Gebirgs-lösungsverfahren im Festgestein. – 17, 146 pp.; München (Münchener Geologische Hefte).
- POISEL, R., TENTSCHERT, E., PREH, A., OSTERMANN, V., CHWATAL, W. & ZETTLER, A. (2010): The interaction of machine and rock mass analysed using TBM data and rock mass parameters. – *Geomechanics and Tunneling*, 3 (5): 510–519.
- PRANDTL, L. (1928): Ein Gedankenmodell zur kinetischen Theorie der festen Körper. – *Zeitschrift für angewandte Mathematik und Mechanik*, 8 (2): 85–106.
- RAMBERG, I., BRYHNI, I., NOTTVEDT, A. & RANGNES, K. (2008): The making of land - Geology of Norway. – 624 pp.; Trondheim (Norsk Geologisk Forening).
- RAUCH, R. (2016): Einfluss des Gebirges auf die Vortriebsleistung und den Diskenverschleiß beim tiefliegenden TBM-Vortrieb am Koralmtunnel (Österreich). – unpubl. Master's Thesis, Technische Universität München; München.
- RIBACCHI, R. & LEMBO FAZIO, A. (2005): Influence of rock mass parameters on the performance of a TBM in a gneissic formation (Varzo Tunnel). – *Rock Mech. Rock Eng.*, 38 (2): 105–127.

- ROSTAMI, J. (1997): Development of a force estimation model for rock fragmentation with disc cutters through theoretical modeling and physical measurement of crushed zone pressure. – Dissertation Thesis, Colorado School of Mines, 384 pp.; Golden.
- ROXBOROUGH, F. & PHILLIPS, H. (1975): Rock excavation by disc cutter. – *Int. J. Rock Mech. Min. Sci. & Geomech. Abstr.*, 12 (12): 361–366.
- SANGHA, C. & DHIR, R. (1972): Influence of time on the strength, deformation and fracture properties of a lower Devonian sandstone. – *Int. J. Rock Mech. Min. Sci. & Geomech. Abstr.*, 9 (3): 343–354.
- SANIO, H. (1983): Nettovortriebsprognose für Einsätze von Vollschnittmaschinen in anisotropen Gesteinen. – Dissertation Thesis, Ruhr-Universität Bochum, 147 pp.; Bochum.
- SANIO, H. (1985): Prediction of the performance of disc cutters in anisotropic rock. – *Int. J. Rock Mech. Min. Sci. & Geomech. Abstr.*, 22 (3): 153–161.
- SCHIMAZEK, J. & KNATZ, H. (1976): Die Beurteilungen von Gesteinen der Bearbeitbarkeit von Gesteinen durch Schneid- und Rollenbohrwerkzeuge. – *Erzmetall* (29): 113–119.
- SCHMID, S., FÜGENSCHUH, B., KISSLING, E. & SCHUSTER, R. (2004): Tectonic map and overall architecture of the Alpine and Pyrenean orogens with their foreland lithosphere. – *Eclogae geologicae Helveticae*, 97: 93–117.
- SCHNEIDER, E. & THURO, K. (2007): Prognose von Penetration und Verschleiß für TBM-Vortrieb im Festgestein. – *Felsbau Magazin*, 6: 44–46.
- SCHNEIDER, E., GEHRING, K. & TÜRTSCHER, M. (2011): Development of an improved prediction model for penetration - Alpine Model - ABROCK project report No. 1. – 29 pp.; Innsbruck.
- SCHOLZ, C. (1968): Microfracturing and the inelastic deformation of rock in compression. – *J. geophys. Res.*, 73: 1417–1432.
- SOLLI, A. & NORDGULEN, Ø. (2006): Bedrock map of Norway and the Caledonides in Sweden and Finland. – Trondheim (Norges geologiske undersøkelse).
- STRUNZ, H., PAULITSCH, P., SEELIGER, E. & TENNYSON, C. (1966): Die Mineralien im Basalt von Groschlattengrün in der Oberpfalz. – *Acta Albertina Ratisbonensia*, 26: 9–34.
- SZWEDZICKI, T. (2007): A hypothesis on modes of failure of rock samples tested in uniaxial compression. – *Rock Mech. Rock Eng.*, 40 (1): 97–104.
- TAYLOR, G. (1934): The mechanism of plastic deformation of crystals. – *Proceedings of the Royal Society of London*, 145: 362–387.
- TEALE, R. (1965): The concept of specific energy in rock drilling. – *Int. J. Rock Mech. & Min. Sci.*, 2: 57–73.
- TENTSCHERT, E., POISEL, R. & ZETTLER, A. (2005): Gefügeeinfluss auf TBM-Vortriebe. – *Felsbau Magazin*, 23 (5): 42–47.
- THURO, K. (1996): Bohrbarkeit beim konventionellen Sprengvortrieb. – *Münchener Geologische Hefte - Reihe B: Angewandte Geologie*, 1, 145 pp.; München (Verlag Dr. Friedrich Pfeil).
- THURO, K. (2002): Geologisch-felsmechanische Grundlagen der Gebirgslösung im Tunnelbau. – *Münchener Geologische Hefte - Reihe B: Angewandte Geologie*, 18, 160 pp.; München (Verlag Dr. Friedrich Pfeil).
- THURO, K. & KÄSLING, H. (2009): Abrasivity classification for rock and soil. – *Proceedings of the 17. Conference of Engineering Geology*: 1–5.
- THURO, K. & PLINNINGER, R. (2001): Scale effects in rock strength properties. – In: SÄRKKÄ, P. & ELORANTA, P. (Eds.): *Rock mechanics - A challenge for society*: 175–180; Lisse (Balkema).
- THURO, K., SINGER, J., KÄSLING, H. & BAUER, M. (2006): Soil abrasivity assessment using the LCPC testing device. – *Felsbau Magazin*, 24 (6): 37–45.
- TOLLMANN, A. (1977): *Geologie von Österreich - Die Zentralalpen*. – I, 766 pp.; Wien (Deuticke).

- TÜRTSCHER, M. (2012): Analyse von Penetration und Vortriebsgeschwindigkeit bei maschinellen Vortrieben in Festgestein. – Dissertation Thesis, Leopold-Franzens-Universität Innsbruck, 392 pp.; Innsbruck.
- VARDAR, M. (1977): Zeiteinfluß auf das Bruchverhalten des Gebirges in der Umgebung von Tunneln. – Dissertation Thesis, Universität Karlsruhe, 117 pp.; Karlsruhe.
- VILLENEUVE, M. (2008): Examination of geological influence on machine excavation of highly stressed tunnels in massive hard rock. – Dissertation Thesis, Queens University, 481 pp.; Kingston.
- VUTUKURI, V., LAMA, R. & SALUJA, S. (1974): Handbook on mechanical properties of rocks. – 1, 1, 280 pp.; Clausthal (Trans Tech Publ.).
- WANNER, H. & AEBERLI, U. (1978): On the influence of discontinuities at the application of tunnelling machines. – Proc. of the 3rd Int. Congress of IAEG, 3: 7–14.
- WANNER, H. & AEBERLI, U. (1979): Tunnelling machine performance in jointed rock. – In: ISRM (Ed.): Proc. of the 4th Congress of the ISRM: 1-8.
- WAWERSIK, W.R. & FAIRHURST, C. (1970): A study of brittle rock fracture in laboratory compression experiments. – Int. J. Rock Mech. & Min. Sci., 7: 561–575.
- WEGSCHEIDER, D. (2012): Einfluss des Trennflächengefüges auf die Penetration und Korrelation mit RMR am Beispiel des Erkundungsstollen Aicha-Mauls. – unpubl. Diploma Thesis, Leopold-Franzens-Universität Innsbruck, 75 pp.; Innsbruck.
- WEIGERT, F. (2013): Penetrationsversuche am Koralmtunnel im Bereich des Bauloses KAT2. – unpubl. Master's Thesis, Technische Universität München, 55 pp.; München.
- WEST, G. (1989): Rock abrasiveness testing for tunneling. – Int. J. Rock Mech. Min. Sci. & Geomech. Abstr., 6: 151–160.
- WIESER, C. (in prep.): Stress-induced microcracking and its influence on the deformation behavior of rocks. – Dissertation Thesis, Technische Universität München; München.
- YAGIZ, S. (2002): Development of rock fracture and brittleness indices to quantify the effects of rock mass features and toughness in the CSM model basic penetration for hard rock tunneling machines. – Dissertation Thesis, Colorado School of Mines, 128 pp.; Golden.
- YAGIZ, S. (2009): Assessment of brittleness using rock strength and density with punch penetration test. – Tunnelling and Underground Space Technology, 24: 66–74.
- YAGIZ, S. (2014): Modified CSM model for predicting TBM performance in rock mass. – 1, 235 pp.; Saarbrücken (LAP Lambert Academic Publishing).
- ZAEGER, T. (2012): Untersuchung der Zähigkeit ausgewählter Gesteine. – unpubl. Bachelor's Thesis, Technische Universität München, 49 pp.; München.
- ZHOU, Z., SU, B., WANG, Z., LI, Z., SHU, X. & ZHAO, L. (2013): Shear-compression failure behavior of PMMA at different loading rates. – Material Letters, 109: 151–153.

9 URL Resources

www-01: <http://www.uibk.ac.at/abrock/>; last access on February 15, 2016

www-02: <http://www.jaegerbau.com/untertagebau/verkehrstunnelbau/projekte-in-ausfuehrung/koralmtunnelkat2/>; last access on September 3, 2015

www-03: <http://forum.bauforum24.biz/forum/index.php?showtopic=57002>; last access on September 7, 2015

www-04: <http://www.statkraft.com/energy-sources/Power-plants/Norway/Ovre-Rossaga/>; last access on September 15, 2015

www-05: <http://www.statkraft.com/about-statkraft/Projects/norway/Nedre-Rossaga/>; last access on September 15, 2015

www-06: <http://www.therobbinscompany.com/en/news/rossaga/>; last access on September 15, 2015

www-07: <http://www.hbm.sh.cn/images/PDF/W1T3-D.pdf>; last access on March 3, 2015

www-08: <http://www.rdpe.com/uk/d5-d6.pdf>; last access on March 19, 2015

Appendix A – Summary of laboratory test results (project data excluded)

Summarizing table of laboratory test results : uniaxial compressive strength (σ_u), tangent Young's modulus (E_t), plastic deformation modulus (E_{pl}), failure work (W_b), destruction work (W_z), axial strain at uniaxial compressive strength (ϵ_u), axial strain at crack damage threshold (ϵ_{cd}), Brazilian tensile strength (σ_t), point load index (I_s), LCPC breakability coefficient (LBC), LCPC abrasivity coefficient (LAC) and Cerchar abrasivity index (CAI). Project results are excluded due to data protection.

Sample ID		σ_u [MPa]	E_t [GPa]	E_{pl} [GPa]	W_b [kJ/m ³]	W_z [kJ/m ³]	ϵ_u [%]	ϵ_{cd} [%]	σ_t [MPa]	I_s [MPa]	LBC [%]	LAC [g/t]	CAI [-]
FLB-1	No. of tests	4	4	4	4	4	4	3	3	10	-	-	-
	Min.	81.7	20.4	14.0	234.5	286.3	0.485	0.341	4.8	3.3	-	-	-
	Max.	96.1	23.0	20.8	270.8	320.9	0.551	0.552	6.2	5.4	-	-	-
	Mean	87.8	21.7	16.6	253.6	312.7	0.516	0.425	5.4	4.5	-	-	-
	STDEV	5.2	0.9	2.6	12.9	29.1	0.027	0.091	0.5	0.7	-	-	-
TIT-5	No. of tests	3	3	3	3	3	3	3	3	12	-	-	-
	Min.	158.0	37.9	34.4	490.2	517.7	0.463	0.389	12.7	8.5	-	-	-
	Max.	192.0	41.5	39.1	534.8	566.7	0.543	0.482	12.7	11.9	-	-	-
	Mean	180.4	40.2	37.5	509.7	549.6	0.512	0.455	12.7	10.7	-	-	-
	STDEV	15.7	1.6	2.2	18.6	22.6	0.035	0.047	0.0	0.9	-	-	-
BX-1	No. of tests	4	4	1	4	4	4	1	10	6	-	-	1
	Min.	132.5	35.1	-	402.6	441.2	0.362	-	7.4	5.0	-	-	-
	Max.	153.2	38.7	-	502.5	551.9	0.490	-	11.0	8.4	-	-	-
	Mean	141.8	38.3	38.2	435.2	495.4	0.362	0.340	8.5	6.5	-	-	4.6
	STDEV	7.6	1.4	-	37.5	39.2	0.050	-	1.1	1.3	-	-	-
BX-3	No. of tests	14	14	2	14	14	14	2	13	10	2	2	-
	Min.	123.8	39.5	40.7	339.1	398.2	0.267	0.351	5.2	3.7	54.0	1200.0	-
	Max.	188.3	49.5	40.9	524.5	615.9	0.477	0.392	12.3	9.2	55.0	1220.0	-
	Mean	163.0	43.8	40.8	447.6	499.6	0.413	0.371	8.0	7.1	54.5	1210.0	-
	STDEV	15.2	2.3	-	61.2	60.9	0.049	-	1.7	1.9	-	-	-
BX-4	No. of tests	7	7	1	7	7	7	1	6	-	-	-	-
	Min.	123.3	40.7	-	265.2	290.8	0.271	-	5.3	-	-	-	-
	Max.	188.3	47.5	-	669.3	708.4	0.475	-	8.9	-	-	-	-
	Mean	174.0	43.8	42.8	525.7	577.2	0.414	0.349	7.5	-	-	-	-
	STDEV	21.0	2.1	-	115.6	123.7	0.065	-	1.3	-	-	-	-
BX-5	No. of tests	5	5	1	5	5	5	1	4	-	-	-	-
	Min.	162.8	38.9	-	466.0	483.1	0.427	-	8.8	-	-	-	-
	Max.	212.4	51.3	-	612.8	717.1	0.509	-	10.7	-	-	-	-
	Mean	186.5	43.9	44.4	554.8	597.7	0.470	0.377	10.1	-	-	-	-
	STDEV	17.9	5.1	-	50.6	74.8	0.027	-	0.7	-	-	-	-
MET-4	No. of tests	8	8	1	8	8	8	2	4	10	2	2	4
	Min.	70.1	15.0	-	136.8	178.0	0.327	0.274	5.5	5.3	77.0	1140.0	4.2
	Max.	80.4	32.9	-	257.1	327.0	0.585	0.306	8.3	6.8	77.0	1140.0	4.2
	Mean	75.0	21.5	17.8	194.8	243.7	0.459	0.290	7.0	5.1	77.0	1140.0	4.2
	STDEV	3.3	5.2	-	45.1	53.2	0.084	-	1.0	0.5	-	-	-

Sample ID		σ_u [MPa]	E_t [GPa]	E_{pl} [GPa]	W_b [kJ/m ³]	W_z [kJ/m ³]	ϵ_u [%]	ϵ_{cd} [%]	σ_t [MPa]	I_s [MPa]	LBC [%]	LAC [g/t]	CAI [-]
NIT-1	No. of tests	3	3	1	3	3	3	1	-	-	-	-	-
	Min.	171.9	57.0	-	279.9	300.0	0.234	-	-	-	-	-	-
	Max.	213.1	59.7	-	460.7	498.8	0.441	-	-	-	-	-	-
	Mean	194.5	58.0	51.3	378.8	416.4	0.341	0.183	-	-	-	-	-
	STDEV	17.1	1.2	-	74.7	83.6	0.084	-	-	-	-	-	-
NIT-2	No. of tests	2	2	1	2	2	2	1	3	-	2	2	1
	Min.	195.3	57.7	-	522.4	246.2	0.274	-	8.4	-	29.0	1220.0	-
	Max.	227.1	63.7	-	524.6	571.2	0.306	-	12.2	-	30.0	1240.0	-
	Mean	211.2	60.7	56.3	523.5	558.7	0.290	0.184	10.4	-	29.5	1230.0	3.7
	STDEV	-	-	-	-	-	-	-	1.6	-	-	-	-
NIT-3	No. of tests	6	6	1	6	6	6	2	3	-	2	2	-
	Min.	226.9	55.3	-	521.5	587.6	0.409	0.320	10.5	-	30.0	1300.0	-
	Max.	315.9	69.9	-	803.8	870.3	0.505	0.330	13.9	-	31.0	1320.0	-
	Mean	257.7	60.9	53.9	632.8	721.1	0.467	0.325	12.2	-	30.5	1310.0	-
	STDEV	28.7	5.3	-	100.3	96.0	0.032	-	1.4	-	-	-	-
NIT-8	No. of tests	2	2	1	2	2	2	1	-	-	-	-	-
	Min.	214.9	51.2	-	456.9	498.8	0.330	-	-	-	-	-	-
	Max.	218.1	53.0	-	492.6	505.2	0.483	-	-	-	-	-	-
	Mean	216.4	52.1	50.3	484.8	502.0	0.392	0.236	-	-	-	-	-
	STDEV	-	-	-	-	-	-	-	-	-	-	-	-
NIT-18	No. of tests	3	3	3	3	3	3	3	4	5	-	-	-
	Min.	131.1	48.8	47.7	184.4	187.8	0.289	0.287	15.3	7.4	-	-	-
	Max.	207.3	55.1	50.9	448.6	491.9	0.430	0.423	16.6	11.0	-	-	-
	Mean	175.9	51.5	49.0	344.4	27808.0	0.379	0.359	15.8	8.9	-	-	-
	STDEV	32.5	2.6	1.4	114.8	142.9	0.063	0.056	0.5	1.2	-	-	-
PB-1	No. of tests	4	4	1	4	4	4	1	4	10	2	2	-
	Min.	364.7	70.6	-	1011.5	1030.5	0.552	-	15.8	10.7	20.0	940.0	-
	Max.	211.0	80.7	-	1565.1	1593.8	0.693	-	24.6	15.0	20.0	1000.0	-
	Mean	454.3	78.5	75.1	1338.1	1378.5	0.649	0.648	16.0	13.0	20.0	970.0	-
	STDEV	54.4	4.0	-	202.0	211.5	0.057	-	5.2	1.4	-	-	-
PB-2	No. of tests	3	3	1	3	3	3	1	3	-	2	2	-
	Min.	370.1	72.0	-	928.7	979.4	0.526	-	14.8	-	17.0	880.0	-
	Max.	385.8	78.7	-	1078.7	1144.1	0.609	-	16.6	-	17.0	920.0	-
	Mean	377.7	74.7	70.1	1018.8	1057.5	0.563	0.471	15.9	-	17.0	900.0	-
	STDEV	6.4	2.8	-	64.9	67.5	0.034	-	0.8	-	-	-	-
PB-3	No. of tests	3	3	3	3	3	3	3	3	-	-	-	1
	Min.	311.3	59.5	60.8	894.3	929.6	0.600	0.601	18.1	-	-	-	-
	Max.	496.7	81.7	76.5	4657.3	1639.1	0.641	0.652	26.1	-	-	-	-
	Mean	412.6	68.4	69.3	1303.6	1327.2	0.6252	0.6299	21.0	-	-	-	2.5
	STDEV	76.7	9.6	6.5	314.0	295.9	0.018	0.021	3.6	-	-	-	-

Sample ID		σ_u [MPa]	E_t [GPa]	E_{pl} [GPa]	W_b [kJ/m ³]	W_z [kJ/m ³]	ϵ_u [%]	ϵ_{cd} [%]	σ_t [MPa]	I_s [MPa]	LBC [%]	LAC [g/t]	CAI [-]
PB-4	No. of tests	2	2	2	2	2	2	1	4	-	-	-	2
	Min.	434.3	76.3	72.2	1280.9	1373.8	0.574	-	13.7	-	-	-	2.6
	Max.	447.4	80.9	79.6	1472.3	1472.3	0.639	-	25.5	-	-	-	2.7
	Mean	440.9	76.6	75.9	1376.6	1423.1	0.6389	0.572	19.1	-	-	-	2.7
	STDEV	-	-	-	-	-	-	-	4.0	-	-	-	-
AG-1	No. of tests	5	5	5	-	-	5	5	6	2	1	1	1
	Min.	196.3	41.0	40.3	-	-	0.563	0.564	13.8	10.5	-	-	-
	Max.	236.9	46.8	46.2	-	-	0.697	0.699	16.6	10.8	-	-	-
	Mean	231.5	43.4	42.4	-	-	0.6349	0.6286	14.5	10.7	46.0	1120.0	4.6
	STDEV	16.8	1.9	2.1	-	-	0.051	0.056	1.2	-	-	-	-
GG-1	No. of tests	5	5	5	-	-	5	5	5	15	1	1	1
	Min.	169.7	42.9	40.3	-	-	0.468	0.377	9.1	3.2	-	-	-
	Max.	184.6	44.1	43.0	-	-	0.500	0.519	16.6	10.1	-	-	-
	Mean	177.1	43.4	41.2	-	-	0.486	0.447	12.0	7.6	48.0	1160.0	4.7
	STDEV	4.7	0.4	1.0	-	-	0.012	0.055	2.9	2.3	-	-	-
PFT-1	No. of tests	20	20	1	20	20	20	2	25	15	2	2	1
	Min.	204.3	35.5	-	749.7	781.8	0.712	0.751	8.8	3.2	60.0	360.0	-
	Max.	333.4	47.2	-	1386.4	1420.3	0.947	0.769	19.9	11.2	78.0	400.0	-
	Mean	245.2	40.0	34.9	965.2	1026.3	0.810	0.760	13.2	8.3	69.0	380.0	3.4
	STDEV	31.9	3.3	-	150.7	148.9	0.058	-	3.7	1.8	-	-	-
KGS-1	No. of tests	7	7	2	7	7	7	3	6	-	2	2	1
	Min.	89.1	27.8	23.2	148.0	151.9	0.289	0.221	6.4	-	60.0	580.0	-
	Max.	100.6	34.2	25.7	234.0	251.1	0.491	0.351	8.7	-	60.0	600.0	-
	Mean	95.0	29.9	24.4	191.8	204.9	0.396	0.306	7.7	-	60.0	590.0	2.1
	STDEV	3.9	2.1	-	35.2	35.9	0.072	0.060	0.7	-	-	-	-
OBM-1	No. of tests	8	8	1	8	8	8	-	3	-	2	2	-
	Min.	319.6	61.2	-	389.6	396.4	0.247	-	8.1	-	26.0	780.0	-
	Max.	402.4	77.4	-	1200.7	1412.9	0.615	-	15.5	-	27.0	800.0	-
	Mean	384.8	71.2	69.4	666.1	709.0	0.404	-	12.9	-	26.5	790.0	-
	STDEV	63.9	5.0	-	266.4	316.8	0.122	-	2.9	-	-	-	-
OBM-2	No. of tests	2	2	1	2	2	2	-	3	-	2	2	-
	Min.	162.5	62.9	-	234.5	262.2	0.218	-	15.7	-	22.0	1040.0	-
	Max.	206.0	64.9	-	346.7	359.2	0.310	-	19.8	-	22.0	1060.0	-
	Mean	184.3	63.8	62.5	290.6	310.7	0.264	-	17.5	-	22.0	1050.0	-
	STDEV	-	-	-	-	-	-	-	1.7	-	-	-	-
OBM-3	No. of tests	5	5	3	5	5	5	3	3	7	-	-	1
	Min.	249.0	69.2	64.3	462.8	469.9	0.329	0.378	15.0	15.1	-	-	-
	Max.	386.4	77.6	70.5	1236.3	1296.2	0.615	0.601	20.9	19.4	-	-	-
	Mean	305.5	72.7	67.9	719.0	750.6	0.482	0.478	18.1	17.7	-	-	3.3
	STDEV	48.4	3.1	2.6	279.2	296.3	0.084	0.081	2.0	1.5	-	-	-

Sample ID		σ_u [MPa]	E_t [GPa]	E_{pl} [GPa]	W_b [kJ/m ³]	W_z [kJ/m ³]	ϵ_u [%]	ϵ_{cd} [%]	σ_t [MPa]	I_s [MPa]	LBC [%]	LAC [g/t]	CAI [-]
OBM-4	No. of tests	3	3	1	3	3	3	-	-	-	-	-	2
	Min.	232.9	64.8	-	539.8	587.8	0.291	-	-	-	-	-	3.4
	Max.	253.4	74.8	-	379.0	617.4	0.336	-	-	-	-	-	3.5
	Mean	244.9	69.6	66.4	564.1	597.9	0.306	-	-	-	-	-	3.5
	STDEV	8.7	4.1	-	17.3	13.8	0.021	-	-	-	-	-	-
HUM-1	No. of tests	5	5	1	5	5	5	1	2	-	2	2	-
	Min.	183.8	39.5	-	606.6	708.7	0.495	-	9.0	-	38.0	760.0	-
	Max.	315.9	51.0	-	1202.7	1237.6	0.737	-	10.6	-	39.0	880.0	-
	Mean	255.4	48.8	48.5	830.7	872.8	0.664	0.681	9.8	-	38.5	820.0	-
	STDEV	8.7	4.1	-	17.3	13.8	0.021	-	-	-	-	-	-
HUM-2	No. of tests	4	4	1	4	4	4	1	3	-	-	-	-
	Min.	181.7	46.0	-	400.2	400.8	0.416	-	8.5	-	-	-	-
	Max.	225.9	49.9	-	691.6	732.9	0.592	-	10.6	-	-	-	-
	Mean	203.4	47.8	41.0	544.9	567.8	0.522	0.510	9.5	-	-	-	-
	STDEV	47.5	6.6	-	206.2	190.5	0.088	-	0.5	-	-	-	-
HUM-3	No. of tests	3	3	1	3	3	3	1	2	-	-	-	-
	Min.	154.9	32.8	-	439.1	481.8	0.522	-	8.5	-	-	-	-
	Max.	238.6	48.4	-	791.6	822.2	0.623	-	9.3	-	-	-	-
	Mean	210.4	41.8	44.1	635.4	673.2	0.562	0.539	8.9	-	-	-	-
	STDEV	39.2	6.6	-	146.8	142.2	0.044	-	-	-	-	-	-
HUM-4	No. of tests	3	3	1	3	3	3	1	2	-	-	-	1
	Min.	191.9	50.0	-	620.4	669.0	0.313	-	8.2	-	-	-	-
	Max.	309.8	54.5	-	1112.3	1143.0	0.598	-	8.3	-	-	-	-
	Mean	250.8	52.4	54.1	826.6	878.3	0.486	0.485	8.3	-	-	-	4.5
	STDEV	48.1	1.9	-	208.5	197.4	0.124	-	-	-	-	-	-
LAM-2	No. of tests	3	3	3	-	-	3	1	-	21	2	2	2
	Min.	87.1	40.5	31.6	-	-	0.247	-	-	3.8	88.0	0.0	1.0
	Max.	88.1	45.3	32.6	-	-	0.315	-	-	5.9	89.0	20.0	1.2
	Mean	87.4	42.9	32.0	-	-	0.277	0.184	-	4.6	88.5	10.0	1.1
	STDEV	0.5	1.9	0.4	-	-	0.028	-	-	0.6	-	-	-
LAM-5	No. of tests	3	3	3	3	3	3	3	3	-	-	-	-
	Min.	88.1	43.3	30.5	133.9	184.3	0.251	0.201	6.6	-	-	-	-
	Max.	88.5	44.8	31.6	141.4	191.8	0.289	0.244	9.1	-	-	-	-
	Mean	88.3	44.1	31.1	137.0	189.2	0.269	0.222	7.8	-	-	-	-
	STDEV	0.2	0.6	0.4	3.2	3.5	0.016	0.018	1.0	-	-	-	-
POS-2	No. of tests	3	3	3	3	3	3	3	3	10	2	2	2
	Min.	53.6	20.8	15.1	140.6	160.3	0.306	0.255	4.3	2.9	99.0	120.0	2.2
	Max.	63.9	22.4	19.0	154.6	165.3	0.329	0.288	4.3	3.5	99.0	160.0	2.4
	Mean	60.0	21.5	17.6	147.6	162.9	0.319	0.272	4.3	3.1	99.0	140.0	2.3
	STDEV	4.5	0.7	1.7	5.9	2.1	0.009	0.014	0.0	0.2	-	-	-

Sample ID		σ_u [MPa]	E_t [GPa]	E_{pl} [GPa]	W_b [kJ/m ³]	W_z [kJ/m ³]	ϵ_u [%]	ϵ_{cd} [%]	σ_t [MPa]	I_s [MPa]	LBC [%]	LAC [g/t]	CAI [-]
ABC-1	No. of tests	8	8	8	-	-	8	8	8	10	1	1	2
	Min.	25.3	5.2	4.6	-	-	0.494	0.306	1.8	1.6	-	-	0.4
	Max.	33.5	6.4	5.1	-	-	0.704	0.537	2.6	2.4	-	-	0.5
	Mean	28.4	5.7	4.8	-	-	0.579	0.404	2.2	2.1	99.0	120.0	0.5
	STDEV	2.9	0.4	0.1	-	-	0.058	0.085	0.2	0.2	-	-	-
WIE-2	No. of tests	3	3	3	3	3	3	3	3	8	2	2	2
	Min.	181.1	34.0	27.5	629.8	630.4	0.623	0.408	10.0	5.3	35.0	0.0	0.7
	Max.	270.9	39.3	38.1	1012.7	1048.1	0.770	0.773	14.6	6.9	36.0	20.0	1.0
	Mean	236.2	37.4	34.3	862.6	880.2	0.702	0.631	11.9	5.9	35.5	10.0	0.9
	STDEV	39.4	2.4	4.8	166.9	180.1	0.060	0.159	2.0	0.6	-	-	-
DK-2	No. of tests	3	3	3	-	-	3	3	3	14	3	3	2
	Min.	143.7	35.9	34.9	-	-	0.419	0.419	8.6	5.3	33.0	20.0	0.9
	Max.	170.0	39.1	38.2	-	-	0.496	0.496	8.9	7.6	35.0	40.0	1.1
	Mean	156.5	37.1	36.3	-	-	0.453	0.458	8.9	6.2	34.0	26.7	1.0
	STDEV	10.8	1.4	1.4	-	-	0.032	0.038	0.1	0.7	0.8	9.4	-
MO-1	No. of tests	8	8	1	8	8	8	1	3	-	2	2	-
	Min.	117.1	50.6	-	161.9	222.4	0.185	-	7.6	-	52.0	40.0	-
	Max.	135.8	57.3	-	273.0	427.1	0.295	-	9.1	-	54.0	40.0	-
	Mean	123.9	53.7	42.2	225.1	427.1	0.242	0.183	8.6	-	53.0	40.0	-
	STDEV	6.5	2.0	-	37.2	55.9	0.043	-	0.7	-	-	-	-
MO-2	No. of tests	4	4	1	4	4	4	1	3	-	2	2	-
	Min.	58.2	27.3	-	96.5	183.2	0.175	-	3.6	-	86.0	20.0	-
	Max.	67.8	40.4	-	138.8	226.3	0.323	-	5.7	-	91.0	20.0	-
	Mean	63.3	35.5	27.2	124.9	199.7	0.197	0.143	4.5	-	88.5	20.0	-
	STDEV	3.4	5.2	-	17.0	17.4	0.016	-	0.9	-	-	-	-
MO-3	No. of tests	3	3	2	3	3	3	2	-	13	-	-	-
	Min.	44.6	27.2	18.4	64.0	98.3	0.192	0.128	-	2.0	-	-	-
	Max.	52.5	34.6	19.5	140.9	209.7	0.234	0.140	-	3.3	-	-	-
	Mean	49.7	31.8	19.0	102.8	150.2	0.217	0.134	-	2.8	-	-	-
	STDEV	3.6	3.2	-	31.4	45.8	0.018	-	-	0.4	-	-	-
MO-5	No. of tests	1	1	1	1	1	1	1	3	-	-	-	3
	Min.	-	-	-	-	-	-	-	7.9	-	-	-	0.7
	Max.	-	-	-	-	-	-	-	10.2	-	-	-	1.2
	Mean	91.5	46.5	37.1	176.7	314.6	0.239	0.190	9.1	-	-	-	0.9
	STDEV	-	-	-	-	-	-	-	0.9	-	-	-	-
MO-6	No. of tests	3	3	3	3	3	3	3	2	-	-	-	-
	Min.	97.2	46.1	41.1	170.6	277.3	0.183	0.128	7.9	-	-	-	-
	Max.	120.9	75.2	57.7	266.8	382.4	0.279	0.245	8.0	-	-	-	-
	Mean	111.9	57.6	46.8	208.0	312.5	0.227	0.189	8.0	-	-	-	-
	STDEV	10.5	12.6	7.7	42.1	49.4	0.039	0.048	-	-	-	-	-